Institute of Astronomy & Clare College
University of Cambridge
June 2020

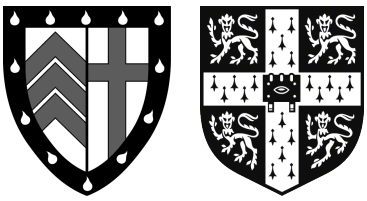

GALAXY-SCALE SIGNATURES
OF
SCREENED MODIFIED GRAVITIES

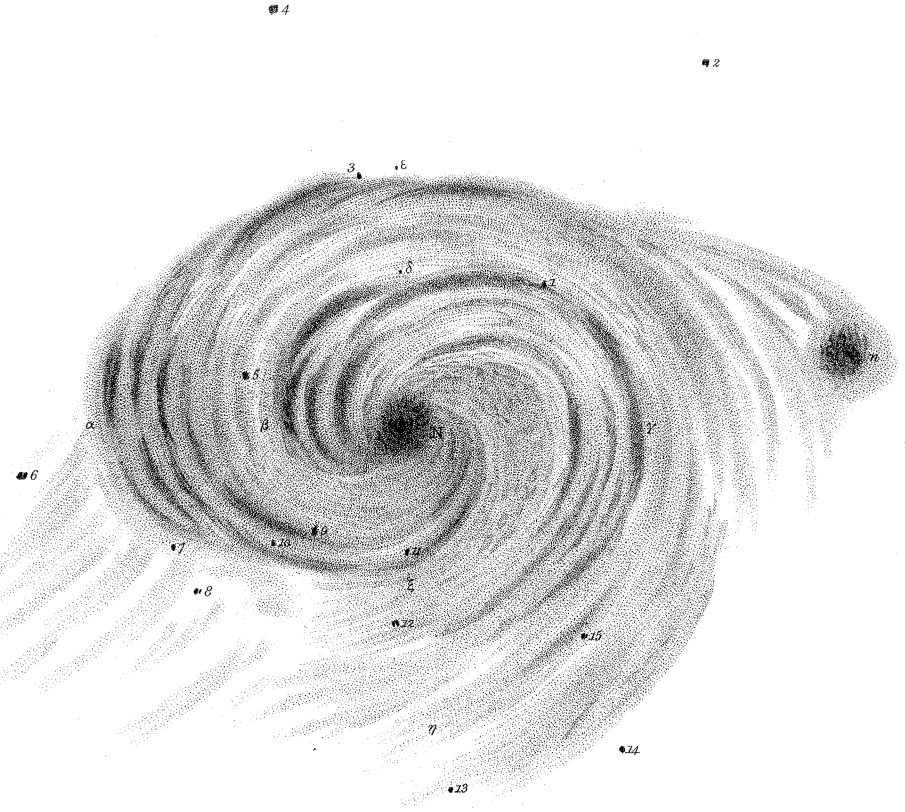

ANEESH P. NAIK

This thesis is submitted for the degree of Doctor of Philosophy.
Illustration: Lord Rosse's hand-drawing of M51, reproduced from Rosse (1850).

To the trees and birds of Cambridge and East Anglia, particularly:
the copper beech overhanging the river at Clare,
the avocets at Welney,
the giant redwood by the Observatory,
and the bluetits in my garden,
for whom this thesis is unlikely to be of the remotest consequence.

Declaration

This thesis is the result of my own work and includes nothing which is the outcome of work done in collaboration except as declared in the preface and specified in the text. It is not substantially the same as any work that has already been submitted before for any degree or other qualification except as declared in the preface and specified in the text. The use of 'we' instead of 'I' throughout various parts of this thesis merely reflects a stylistic choice.

Parts of this thesis are based on articles that have been published or have been submitted for publication. These are:

- Chapter 2:
  A. P. Naik, E. Puchwein, A.-C. Davis, C. Arnold
  Imprints of chameleon f(R) gravity on galaxy rotation curves
  MNRAS, Volume 480, Issue 4, November 2018, Pages 5211–5225

- Chapter 3:
  A. P. Naik, E. Puchwein, A.-C. Davis, D. Sijacki, H. Desmond
  Constraints on chameleon f(R) gravity from galaxy rotation curves of the SPARC sample
  MNRAS, Volume 489, Issue 1, October 2019, Pages 771–787

- Chapter 4:
  A. P. Naik, N. W. Evans, E. Puchwein, H. Zhao, A.-C. Davis
  Stellar Streams in Chameleon Gravity
  Submitted to PRD, preprint available at arXiv:2002.05738

I undertook the majority of the research presented in each of these chapters, and the declaration at the beginning of each chapter explicitly outlines the contributions made by the co-authors of the respective articles.

The Introduction (Chapter 1) does not present any original research.

The length of this thesis does not exceed the limit of 60,000 words specified by the Degree Committee of Physics and Chemistry.

Galaxy-Scale Signatures of Screened Modified Gravities

Aneesh Naik

Summary

In recent years, theories of gravity incorporating a scalar field coupled to gravity—'scalar-tensor' theories—have been subject to increased attention. In these theories, the scalar field mediates gravitational-strength 'fifth forces'.

For such scalar fields to retain cosmological relevance while also evading stringent constraints from high-precision post-Newtonian tests of gravity, 'screening mechanisms' are invoked, in which the fifth force is suppressed in regions of high density or deep gravitational potential. One example of a screening mechanism is the 'chameleon' mechanism, in which the scalar has a density-dependent mass, such that the mass becomes very large in regions of high density, and the fifth force is exponentially suppressed as a consequence. While the primary effect of screening mechanisms is to mask the effects of modified gravity in the Solar System, they can nevertheless give rise to interesting astrophysical signatures elsewhere, searches for which can serve as tests of screened modified gravity. These signatures are the subject of this thesis.

The Introduction of this thesis in Chapter 1 presents some historical background and scientific context, particularly in the fields of cosmology, the astrophysics of galaxies, and screened modified gravity theories. Subsequently, Chapters 2, 3, and 4 present original research regarding two galaxy-scale signatures of screened modified gravity: 'upturns' in galaxy rotation curves and asymmetries in stellar streams.

If a galaxy is partially screened, it will have a 'screening radius', within which the fifth force is suppressed. Outside the screening radius, the fifth force on a test particle will be proportional to the mass enclosed in the shell between the test particle and the screening radius. Thus, the fifth force will contribute to the galaxy's rotation curve, but only outside the screening radius. At the screening radius itself, there will be an upturn in the curve. In Chapter 2, based on an article published in the Monthly Notices of the Royal Astronomical Society (Naik *et al.*, 2018), I give the first prediction of this effect, specifically in the context of Hu-Sawicki $f(R)$ gravity, a widely-studied example of a chameleon theory. By post-processing simulated galaxies of the Auriga Project using the $f(R)$ gravity code MG-Gadget, I produce mock rotation curves for a range of galaxy masses and values of the key theory parameter f_{R0}, forecasting competitive constraints on f_{R0}. In Chapter 3, also based on an article published in the Monthly Notices (Naik *et al.*, 2019), I turn to observational data. Analysing the high-quality rotation curves of the SPARC sample, I find that in certain $f(R)$ parameter regimes there is a strong signal, but it is better explained with standard gravity plus a 'cored' dark matter halo profile than with modified gravity plus a theoretically-predicted 'cuspy' halo. I am thus able to place competitive constraints on $f(R)$ gravity, with

the caveat that if cored haloes can not ultimately be motivated under the standard ΛCDM cosmological paradigm, then screened modified gravity could feasibly ease the tension between observed cores and predicted cusps.

In Chapter 4, I consider the observable imprints of screening on stellar streams around the Milky Way. For reasonable parameter regimes in chameleon theories, main sequence stars will be screened, and thus neither source nor couple to the fifth force. Thus, a situation can arise in which a dark matter dominated dwarf galaxy is unscreened, but the stars within it are screened. If such a galaxy were to be tidally disrupted by the Milky Way, its stars would be preferentially stripped into the trailing stellar stream rather than the leading stream. The streams would therefore be asymmetric about their progenitor. Using a restricted N-body method, I explore this effect for a variety of satellite orbits and modified gravity regimes. Taking $f(R)$ gravity as a fiducial theory, I forecast some of the strongest constraints to date from future data releases of the Gaia satellite. This chapter is based on an article submitted to Physical Review D (Naik *et al.*, 2020).

Finally, Chapter 5 gives some concluding remarks and a discussion of future prospects in this field.

Acknowledgments

This thesis is the culmination of nearly four years of work undertaken in Cambridge, at the Institute of Astronomy. Two pages from here, I make the University-mandated declaration that this work is primarily my own. However, it is certainly not the case that it was performed in isolation, and debts of gratitude are owed to the various people, groups, and institutions who helped me along the way, both directly and indirectly.

The first such debt is due of course to my supervisor, Ewald Puchwein. Throughout my PhD, he has been a profoundly patient and knowledgeable guide. The invaluable role he played in supervising my research and helping me to mature as a scientist has necessitated a considerable investment of his time over these years, and I am enormously grateful. This gratitude extends to my other supervisors, Anne-Christine Davis and Debora Sijacki, both of whom were also very generous with their time and insights. Discussions with them have greatly broadened my knowledge and improved my research immeasurably. I wish to also acknowledge the various contributions made by my other research collaborators: Christian Arnold, Harry Desmond, Wyn Evans, and Hongsheng Zhao, as well as the many helpful discussions I've had with a large number of people in Cambridge and elsewhere. Of particular note are Claudio Llinares, Baojiu Li, Philippe Brax, Harley Katz, Federico Lelli, Cameron Lemon (see below), Girish Kulkarni, Martin Haehnelt, Matt Auger, Vasily Belokurov, Denis Erkal, Sergey Koposov, Jason Sanders, and Paul Hewett.

The research presented in Chapter 2 was facilitated by the Auriga Project team, who allowed me access to their simulations. Similarly, Chapter 3 was made possible by the SPARC team, who have made their rotation curve data publicly available. Acknowledgment is also due to the Science and Technology Facilities Council (STFC), who provided funding for this research. Furthermore, the STFC supercomputing service DiRAC was used extensively in all of my research projects. By extension, this gratitude should lie ultimately with the citizens and tax-payers of the United Kingdom. Even in these times of economic uncertainty and political unrest, a small share of the nation's resources goes towards the funding of abstract scientific research without any apparent industrial or commercial agenda. I don't know the extent to which the proverbial man on the Clapham omnibus is aware of this fact or would necessarily approve of it, but I sincerely hope he is and would.

All of the research presented in this thesis was conducted from a desk in room 35 of the Observatory. This is one of the largest offices in the Institute, and throughout my four years there, it has played host to an ever-changing cast of delightful characters, who were consistently supportive and helpful in a myriad of small ways: Sid, Adam, Laura, Andy, Holly,

and the young'uns. Particular acknowledgment goes to Cameron, with whom I discovered the joy of trees. More generally, the Institute provided a welcoming, collegial working environment, with green spaces and afternoon tea. This was conducive to many fruitful discussions, academic and otherwise. I would particularly like to acknowledge the 'gridzz group': Lewis, Tom, Nick, Douglas, Mia, Cat, *et al.* The thrill of solving a cryptic crossword clue is decidedly much quicker and cheaper (if less meaningful) than anything one can attain through the pursuit of scientific research, and it was a pleasure to share it with others every day. Also the various cruciverbalists at the Guardian, particularly Rufus for easing us in on a Monday. Thanks also to the rest of the Institute for (mostly) tolerating our arcane cult.

Outside of the Institute, my affiliation to Clare College has played a prominent role in my life here, and the College has supported me in many small ways over the years, from the provision of subsidised accommodation to the unmatched privilege of sitting in its fairytale garden. Above all else, however, a Cambridge college is a stimulating environment in which astronomers routinely break bread and sip whisky with philosophers, archaeologists, mathematicians, and the like. This is a unique cauldron, and I am grateful to have been submerged in it. Another institutional presence in my life in Cambridge has been the University Rambling Club, the ideal weekend counterweight to my academic weeks, and the source of many memorable adventures. The Varsity March was particularly miserable. But—in common with many miserable undertakings—glorious in retrospect.

I feel blessed in my life to be supported by my loving friends and family. In the former category, particular mention should go to Rosie and Giles (the Eden St. Logistics Group), whose move to Cambridge last year was extremely welcome. My partner Amy is rightly owed no small share of credit. PhD research presents one with a series of challenges to one's sanity, from unproductive weeks to untraceable bugs in code. It is difficult to envisage how they would have been surmounted without Amy as a wellspring of love, warmth, optimism, and sheer humanity. Finally, my sister Aditi and my parents Rupali and Prakash are an emotional safety net without which embarking on a PhD programme would have been infinitely more daunting. They are the most supportive people I know, in almost every way imaginable. Perhaps most importantly, they instilled in me a sense of the value of education. After all, it is only because of this sense that I have freely and willingly allowed my education to continue into its third decade.

Contents

List of Figures

List of Tables

List of Abbreviations

All acronyms or abbreviations are defined at their first instance in the text. If they occur again later in this thesis, they are not defined again but instead included in the table below.

Acronym	Meaning
AGN	Active Galactic Nucleus (or Nuclei)
BAO	Baryon Acoustic Oscillation
BIC	Bayesian Information Criterion
BOSS	Baryon Oscillation Spectroscopic Survey
CMB	Cosmic Microwave Background
DESI	Dark Energy Spectroscopic Instrument
(C)DM	(Cold) Dark Matter
DC14	Di Cintio *et al.* (2014)
(W/S/E)EP	(Weak/Strong/Einstein) Equivalence Principle (see Footnote 6 in § 1)
FLRW	Friedmann-Lemaître-Robertson-Walker
GR	General Relativity
HS	Hu-Sawicki
LIGO	Laser Interferometer Gravitational-Wave Observatory
LSST	Legacy Survey of Space and Time (see Footnote 51 in § 1)
Mx	Messier x (e.g. Andromeda is M31)
MCMC	Markov Chain Monte Carlo
MG	Modified Gravity
MW	Milky Way
NFW	Navarro-Frenk-White
NGC	New General Catalogue
PPN	Parameterised Post-Newtonian
RAR	Radial Acceleration Relation
RSD	Redshift-Space Distortions
SDSS	Sloan Digital Sky Survey
SHYBONE	Simulating HYdrodynamics BeyONd Einstein
SPARC	Spitzer Photometry and Accurate Rotation Curves
ΛCDM	Lambda Cold Dark Matter

Rufus was hunting one day in the New Forest, when William Tell (the memorable crack-shot, inventor of crossbow puzzles) took unerring aim at a reddish apple, which had fallen on to the King's head, and shot him through the heart. Sir Isaac Walton, who happened to be present at the time, thereupon invented the Law of Gravity.

—W. C. Sellar and R. J. Yeatman (1930)
1066 and All That

Chapter 1

Introduction

1.1 The Cosmological Model

1.1.1 Background

Almost exactly a century before the submission of this thesis, on April 26th 1920, the 'Great Debate' was held at the Smithsonian Museum of National History in Washington DC. The subject of this debate was no less than the nature of our Universe.

The Debate was prompted by the question of the 'spiral nebulae'. The first known example of a spiral nebula was M51, now also known as the 'Whirlpool Galaxy' or NGC 5194,[1] the spiral structure of which was revealed in 1845 by Anglo-Irish astronomer Lord Rosse, using his recently completed 72-inch telescope (Rosse, 1850).[2] Lord Rosse's hand-drawn depiction of M51 is shown on the title page of this thesis.

In the following years, many more of these spiral nebulae were discovered. The compositions of these objects were unclear, as was the cause of their spiral structure. The mystery was deepened in the early twentieth century, when American astronomer Vesto Slipher observed that the spectral lines of these nebulae were strongly shifted, in most cases towards the red end of the spectrum (Slipher, 1917). These 'redshifts' implied large (mostly recessional) radial velocities for these objects, possibly implying that they were situated outside the Milky Way.

On one side of the Debate was American astronomer Harlow Shapley, expounding a theory in which our home galaxy—the Milky Way (MW)—is an "enormous, all-comprehending galactic system."[3] In other words, the Universe is composed of one very large galaxy and everything observable is contained within it, including the mysterious spiral nebulae. This

[1] 'M' and 'NGC' here respectively stand for Messier and New General Catalogue.

[2] The 'Leviathan of Parsonstown' remained the world's largest telescope well into the 20th century.

[3] Quotation from Shapley's correspondence with George Hale (Smith, 1982, p. 62).

'Milky Way Universe' found supporters in various eminent astronomers of the time, such as Sir Arthur Eddington, Henry Norris Russell, and George Hale. Indeed, in one form or another, the Milky Way Universe had been the prevailing conception of the cosmos for the preceding few centuries, since the time of Sir Isaac Newton, who conceived an infinite Universe uniformly populated with stars "so accurately poised one among another, as to stand still in a perfect Equilibrium."[4]

Shapley was opposed in the Debate by his compatriot Heber Curtis, who believed the spiral nebulae to be distant from our galaxy, and to be 'island universes' in their own right, of a similar size and structure to the MW. In this theory, the Universe is composed of a large (possibly infinite) number of such galaxies, separated by large voids. Just as the idea of the Milky Way Universe could trace a lineage back to Newton and beyond, the idea of island universes also had some precedent. The term 'island universe' was first used by the Prussian philosopher Immanuel Kant, who in 1755 imagined an infinite cosmos composed of disc-like island galaxies floating in the vast sea of space. Kant was partly inspired by his English contemporary Thomas Wright, who five years earlier had published his theory of a Universe composed of infinitely many spherical Milky Ways.[5] Thomas Wright's own depiction of his Universe is reproduced in Figure 1.1.

As an interesting aside, in Kant's theory, the Universe would begin as a chaotic soup of particles, the denser regions of which would attract material and slowly coalesce into condensations. These condensations in turn would combine into larger structures, and so on *ad infinitum*. This hierarchical process foreshadows more modern ideas of structure formation, discussed later in this chapter (§ 1.2.2).

The Great Debate provides a telling insight into the *status quo* in cosmology in the early decades of the twentieth century. New theoretical ideas were typically minor variations on centuries-old Kantian or Newtonian themes, and the lack of a clear victor in the Debate demonstrates that observations were not yet at a stage where theories were falsifiable.

The participants and audience at the Great Debate would scarcely have been aware in 1920 that they were on the eve of precipitous change. In the ensuing years and decades, theoretical and empirical advances pursued each other rapidly, and our understanding of the cosmos has inflated with commensurate speed. Now, a century later, cosmology appears to have arrived at a new consensus: the ΛCDM Big Bang cosmology. The remainder of § 1.1 describes the development, over the course of the twentieth century, of the Big Bang cosmology and the ΛCDM model, while also outlining any necessary theoretical formalism. The section ends with a discussion of outstanding problems with the model. It is these unanswered questions that motivate the search for signatures of screened modified gravity (MG) described in this thesis.

[4] Quotation from Newton's famous correspondence with Richard Bentley (Cohen, 1978, p. 278).

[5] The ideas of Kant and Wright have an ancient antecedent in the cosmology of Democritus and the atomistic school, c. fifth century BCE, in which spherical, geocentric 'world systems' float in an infinite chaotic void.

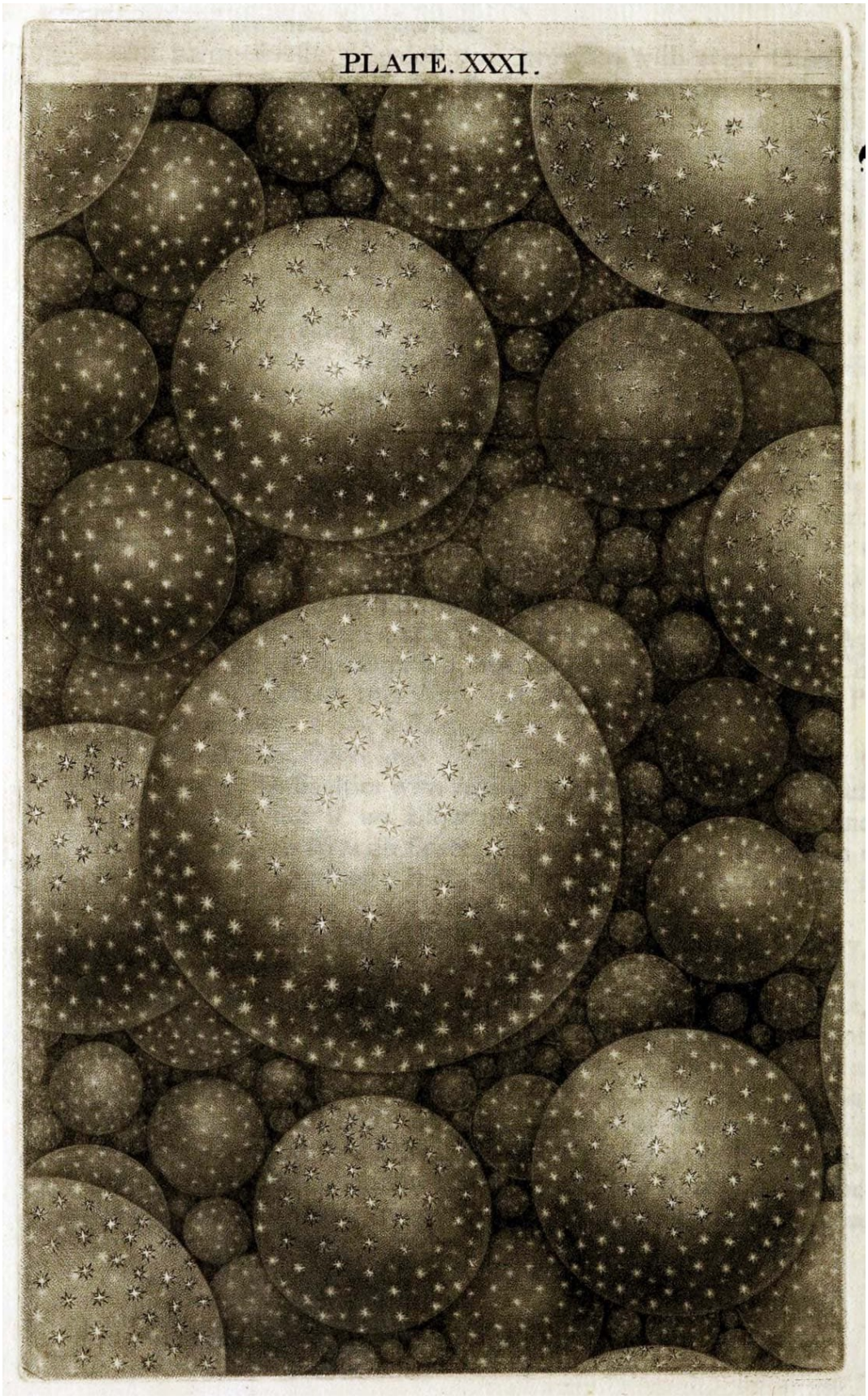

Figure 1.1: Thomas Wright's 1750 depiction of the Universe. Each sphere is an 'island universe', as later described by Immanuel Kant. The stars of each sphere, including the Sun within our own Galaxy, all inhabit the thin outer shell, giving rise to the apparent Milky Way band across the sky. Reproduced from Wright (1750).

1.1.2 General Relativity

Metrics and Geodesics

A key theoretical development that triggered the twentieth century revolution in cosmological understanding was Albert Einstein's 1915 theory of general relativity (henceforth GR; Einstein, 1916).

In conceiving the theory, Einstein's key insight derived from the curious fact that the 'gravitational' mass appearing in Newton's law of gravitation appears to be identical to the 'inertial' mass appearing in Newton's second law. As a consequence, test particles in a gravitational field will experience the same acceleration, regardless of their mass. This is known as the equivalence principle (EP),[6] and there is no reason, *a priori*, why this should hold true for Newtonian physics.

Einstein's realisation was that the EP stemmed from a deep relationship between gravitational acceleration and the geometry of space-time. To be precise, objects travel on geodesics of spacetime,

$$\frac{\mathrm{d}^2 x^\alpha}{\mathrm{d}\tau^2} + \Gamma^\alpha{}_{\mu\lambda} \frac{\mathrm{d}x^\mu}{\mathrm{d}\tau} \frac{\mathrm{d}x^\lambda}{\mathrm{d}\tau} = 0, \tag{1.1}$$

where x^α is the position in spacetime of a given object,[7] τ is its proper time, and Γ is the Christoffel symbol, given by

$$\Gamma^\alpha{}_{\mu\lambda} = \frac{1}{2} g^{\alpha\beta} \left(\frac{\partial g_{\mu\beta}}{\partial x^\lambda} + \frac{\partial g_{\beta\lambda}}{\partial x^\mu} - \frac{\partial g_{\mu\lambda}}{\partial x^\beta} \right). \tag{1.2}$$

Here, the tensor $g_{\alpha\beta}$ is the metric tensor (and $g^{\alpha\beta}$ its inverse). The metric tensor encodes the geometry of the underlying spacetime by specifying the line element

$$\mathrm{d}s^2 = g_{\mu\lambda} \mathrm{d}x^\mu \mathrm{d}x^\lambda. \tag{1.3}$$

Note that the metric tensor is symmetric, $g_{\mu\lambda} = g_{\lambda\mu}$, and so consists of 10 independent components. For a flat (Minkowski) spacetime, $g_{\mu\lambda} = \eta_{\mu\lambda} \equiv \mathrm{diag}\,(-1,1,1,1)$. Consequently, first derivatives of the metric vanish, $\Gamma^\alpha{}_{\mu\lambda} = 0$, and the geodesic equation (1.1) reduces to the equation for a straight line in spacetime. When a spacetime is curved, the Christoffel symbols do not vanish, and geodesics are curved. This manifests as 'acceleration' due to gravity.

[6] This is actually a statement of the Weak Equivalence Principle (WEP). The Einstein Equivalence Principle (EEP) assumes the WEP is true, and states that the laws of special relativistic physics are always recovered in a freely falling frame. The Strong Equivalence Principle (SEP) assumes the WEP and EEP, and generalises them from test particles to small, gravitating test bodies. With the exception of a brief discussion of EP tests in § 1.1.5, the remainder of this thesis will generically use the term 'EP'. However, it is worth noting that different gravity experiments test different statements of the EP, and different modified gravity theories violate different statements of the EP.

[7] $x^\alpha \equiv (c\,t, x, y, z)$.

Einstein's Field Equations

The geodesic equation (1.1) gives a prescription for how objects move in a curved spacetime. This is the GR generalisation of the force law $\ddot{\boldsymbol{x}} = -\boldsymbol{\nabla}\Phi_{\mathrm{N}}$. To complete our picture of GR, we need a prescription for how spacetime curves in the presence of mass, i.e. a GR generalisation of Poisson's equation $\nabla^2\Phi = 4\pi G\rho$.[8] This is given by Einstein's field equations,

$$G^{\alpha\beta} = \frac{8\pi G}{c^4} T^{\alpha\beta}. \tag{1.4}$$

Note that the tensors appearing on each side are symmetric, so Eq. (1.4) represents ten independent equations. A derivation of Eq. (1.4) is beyond the scope of this thesis, but can be found in any standard GR textbook, e.g. Wald (1984). Nonetheless, each side of Eq. (1.4) requires further explanation to give an intuition for the meaning of the equation. On the left-hand side, the tensor $G^{\alpha\beta}$ is known as the Einstein tensor. This is built from first and second derivatives of the metric tensor, and so encodes the curvature of spacetime. To understand this, let us first define the Riemann curvature tensor,

$$R^{\lambda}{}_{\mu\alpha\beta} \equiv \partial_\alpha \Gamma^{\lambda}{}_{\beta\mu} - \partial_\beta \Gamma^{\lambda}{}_{\alpha\mu} + \Gamma^{\lambda}{}_{\alpha\epsilon}\Gamma^{\epsilon}{}_{\mu\beta} - \Gamma^{\lambda}{}_{\epsilon\beta}\Gamma^{\epsilon}{}_{\mu\alpha}. \tag{1.5}$$

Contractions of this tensor give the Ricci tensor and scalar,

$$R_{\alpha\beta} = R^{\mu}{}_{\alpha\mu\beta}; \quad R = g^{\alpha\beta}R_{\alpha\beta}. \tag{1.6}$$

Finally, the Einstein tensor is given by

$$G^{\alpha\beta} \equiv R^{\alpha\beta} - \frac{1}{2} g^{\alpha\beta} R. \tag{1.7}$$

Using symmetries of the Riemann tensor,[9] it can be shown that the Einstein tensor satisfies

$$\nabla_\mu G^{\lambda\mu} = 0, \tag{1.8}$$

regardless of the metric. This statement is more than a mere tensor identity; it carries some physical significance. Eq. (1.8) reduces the number of independent equations in Eq. (1.4) from ten to six; given six components of $G^{\lambda\mu}$, the remaining four could be generated using Eq. (1.8). The metric tensor $g_{\mu\nu}$, however, still carries ten independent components. So, the Einstein field equations (1.4) are not fully able to determine the metric tensor, and four equations-worth of freedom remain. This freedom ensures the coordinate-independence of the metric tensor. In other words, given a metric tensor $g_{\mu\nu}$ that satisfies Eq. (1.4), one can write four arbitrary coordinate transformations $x'^{\mu} = f^{\mu}(x^{\alpha})$, and the transformed metric $g'_{\mu\nu}$ will still satisfy Eq. (1.4).

[8] Throughout this thesis, 3-vectors are bold, e.g. $\boldsymbol{x}$, while 4-vectors carry Greek indices, e.g. x^{α}. Here $\boldsymbol{x}$ is position, Φ_{N} is Newtonian gravitational potential, and ρ is (mass) density.

[9] In particular, the Bianchi identity $\nabla_\gamma R^{\lambda}{}_{\mu\alpha\beta} + \nabla_\beta R^{\lambda}{}_{\mu\gamma\alpha} + \nabla_\alpha R^{\lambda}{}_{\mu\beta\gamma} = 0$

On the other side of Eq. (1.4), $T^{\alpha\beta}$ is the energy-momentum tensor. For a perfect fluid with rest-frame density ρ, rest-frame pressure P, and 4-velocity $u \equiv \mathrm{d}x/\mathrm{d}\tau$, this is

$$T^{\alpha\beta} = \left(\rho + \frac{P}{c^2}\right) u^\alpha u^\beta + P g^{\alpha\beta}. \tag{1.9}$$

Thus, the right-hand side of Eq. (1.4) should be interpreted as the source term, containing information about the density and kinematics of the gravitating matter. Eq. (1.4) can then be understood as the required translation between matter and spacetime curvature.

Cosmological Constant

The cosmological constant Λ plays a central role in our current conception of the Universe. The history and physical significance of the cosmological constant will be discussed in § 1.1.4, but for the present it is worth simply stating how it can be incorporated into GR. Including an explicit cosmological constant term, the field equations (1.4) instead take the form

$$G_{\alpha\beta} = \frac{8\pi G}{c^4} T_{\alpha\beta} - \Lambda g_{\alpha\beta}. \tag{1.10}$$

However, the novel term can be 'absorbed' into the energy-momentum source term by defining

$$T^{\Lambda}_{\alpha\beta} = -\frac{\Lambda c^4}{8\pi G} g_{\alpha\beta}. \tag{1.11}$$

Then, writing $T^{\mathrm{new}}_{\alpha\beta} = T^{\mathrm{old}}_{\alpha\beta} + T^{\Lambda}_{\alpha\beta}$, the original formulation of the field equations (1.4) is recovered.

Note that $T^{\Lambda}_{\alpha\beta}$ is equivalent to a perfect fluid energy-momentum tensor (1.9), with density $\rho = \Lambda c^2/8\pi G$ and $P = -\rho c^2$. We will see later that this negative equation of state leads to the late-time cosmic acceleration for which the cosmological constant is commonly invoked.

GR from Action Principles

Before considering modified theories of gravity, it will prove useful to have first outlined a derivation of GR from action principles. The action underpinning GR—the 'Einstein-Hilbert' action—is given by

$$S_{\mathrm{EH}} = \frac{c^3}{8\pi G} \int d^4x \sqrt{-g} \frac{1}{2} R + S_m[g_{\mu\nu}, \psi_i], \tag{1.12}$$

where g represents the determinant of the metric tensor $g_{\mu\nu}$, R is the Ricci scalar (1.6), S_m is the matter action, i.e. the action representing the various matter components ψ_i. Extremising the above action with respect to the metric tensor yields Einstein's field equations

(1.4), with the energy-momentum tensor $T_{\alpha\beta}$ arising from the matter action S_m via

$$T_{\alpha\beta} \equiv -\frac{2c}{\sqrt{-g}} \frac{\delta\left(\sqrt{-g}\mathscr{L}_m\right)}{\delta g^{\alpha\beta}}, \tag{1.13}$$

where $\mathscr{L}_m$ is the matter Lagrangian, related to the matter action by

$$S_m[g_{\mu\nu}, \psi_i] = \int d^4x \sqrt{-g}\mathscr{L}_m\left(g_{\mu\nu}, \psi_i\right). \tag{1.14}$$

As $T_{\mu\nu}$ stands uncoupled to any external fields, it is covariantly conserved: $\nabla_\mu T^{\mu\nu} = 0$. It can be shown that this conservation law leads to the geodesic equation of GR, which in the Newtonian limit becomes the Newtonian equation of motion $\ddot{\boldsymbol{x}} = -\boldsymbol{\nabla}\Phi_{\rm N}$. We shall see later that the fifth force present in modified gravity theories manifests as an extra term in this equation of motion, arising ultimately from abandoning the $T^{\mu\nu}$ conservation law.

Note that no cosmological constant appears in Eq. (1.12). Including a cosmological constant, the action takes the form

$$S_\Lambda = \frac{c^3}{8\pi G} \int d^4x \sqrt{-g}\left(\frac{1}{2}R - \Lambda\right) + S_m[g_{\mu\nu}, \psi_i]. \tag{1.15}$$

Now, extremising the action leads to the field equations with an explicit Λ term, Eq. (1.10).

The Geodesic Equation Revisited

Before moving on to cosmological applications of GR, it is worth noting that Eq. (1.8), taken together with Eq. (1.4), implies $\nabla_\mu T^{\lambda\mu} = 0$. This is a statement of the conservation of energy-momentum. This conservation law can in turn be used to derive the geodesic equation (1.1). To see this, consider the case of perfect, pressureless dust, $T^{\alpha\beta} = \rho u^\alpha u^\beta$. Plugging this into the conservation law gives

$$0 = \nabla_\alpha\left(\rho u^\alpha u^\beta\right) = u^\beta \nabla_\alpha\left(\rho u^\alpha\right) + \rho u^\alpha \nabla_\alpha u^\beta. \tag{1.16}$$

Using the fact that $g_{\alpha\beta} u^\alpha u^\beta = -c^2$ so that $\nabla_\mu g_{\alpha\beta} u^\alpha u^\beta = 2 g_{\alpha\beta} u^\beta \nabla_\mu u^\alpha = 0$, one can multiply the whole of Eq. (1.16) by $g_{\gamma\beta} u^\gamma$ to show that $\nabla_\mu\left(\rho u^\mu\right) = 0$. Eq. (1.16) then reads

$$0 = u^\alpha \nabla_\alpha u^\beta = u^\alpha\left(\partial_\alpha u^\beta + \Gamma^\beta{}_{\alpha\gamma} u^\gamma\right) = \frac{\mathrm{d}^2 x^\beta}{\mathrm{d}\tau^2} + \Gamma^\beta{}_{\alpha\gamma} \frac{\mathrm{d}x^\alpha}{\mathrm{d}\tau} \frac{\mathrm{d}x^\gamma}{\mathrm{d}\tau}, \tag{1.17}$$

where the first equality has used the definition of a covariant derivative.[10] The geodesic equation (1.1) has thus emerged from the conservation of energy-momentum, which in turn arose from the coordinate-independence encoded within GR.

[10] For a contravariant vector, $\nabla_\alpha V^\beta \equiv \partial_\alpha V^\beta + \Gamma^\beta{}_{\alpha\gamma} V^\gamma$.

1.1.3 An Expanding Universe

Hubble's Law

In the early decades of the twentieth century, an almost universally held belief was that our Universe is (on average) static (Kragh, 2007). For instance, both cosmologies being argued for in the Great Debate of 1920 assumed a static, eternal cosmos. This assumption came to be overturned at the end of the 1920s, as a result of the meticulous observations of Cepheid variable stars in the aforementioned spiral nebulae undertaken by American astronomer Edwin Hubble at the Mount Wilson Observatory in California.

Cepheid variables[11] are stars that exhibit periodicity in their brightness due to pulsations in their outer layers. In 1908, Henrietta Swan Leavitt observed nearly two thousand Cepheid variables in the Magellanic Clouds and demonstrated that a clear relationship exists between the luminosities of these stars and the periods of their pulsations (Leavitt, 1908). This relationship is significant because it allows the distance to a Cepheid variable to be inferred from observations of its apparent brightness and oscillation period. This enables the measurement of cosmic distances far larger than those possible under previous geometric approaches. As a consequence, Cepheid variables have played an immensely important role in the development of modern cosmology.

In 1925, Hubble published the results of an observational study of Cepheid variables in the nearby spiral nebulae M31 and M33 (respectively the Andromeda and Triangulum galaxies; Hubble, 1925). For both of these, he inferred a distance of 285 kpc using Leavitt's period-luminosity relation. This is around a factor of three smaller than current estimates of the distance to M31 (e.g. McConnachie *et al.*, 2005), but was nonetheless around an order of magnitude larger than the widely accepted size of the Milky Way; sufficiently large to convince the vast majority of the astronomical community of the extragalactic nature of M31 and M33. Whereas the Great Debate had ended inconclusively five years earlier, the question of the spiral nebulae appeared to be settled: they are galaxies in their own right, distant from—but similar to—our Milky Way.

As mentioned in § 1.1, Vesto Slipher had made the observation earlier in the century that the majority of galaxies exhibited redshifts. The redshift z of an astronomical object can be related to its motion via the formula for the relativistic (longitudinal) Doppler effect, which states

$$z \equiv \frac{\Delta\lambda}{\lambda_0} = \sqrt{\frac{1+v/c}{1-v/c}} - 1 \approx \frac{v}{c}, \tag{1.18}$$

where λ_0 is the rest-frame wavelength of a given spectral line, $\Delta\lambda$ is the size of its spectral

[11] Named after the prototype δ Cephei, which was first discovered by English astronomer John Goodricke in 1784 (Goodricke, 1786). δ Cephei was actually the second known example of a variable star that would later be classed as a classical Cepheid, the first being η Aquilae, the variability of which was identified by Goodricke's compatriot Edward Pigott one month earlier (Pigott, 1785).

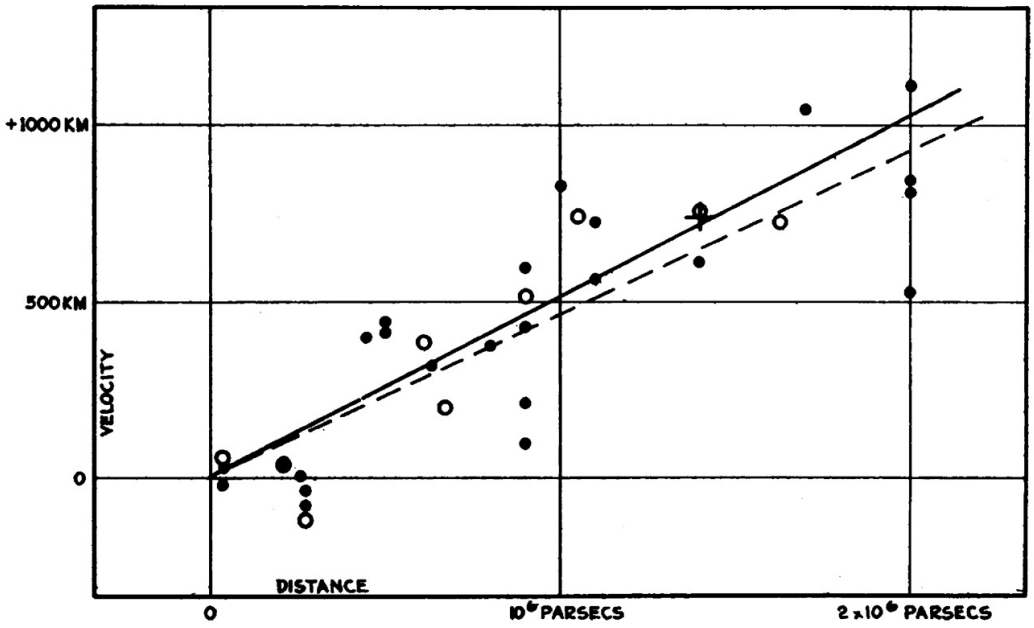

Figure 1.2: Hubble's observed linear relationship between recessional velocity and distance for 24 'extra-galactic nebulae'. The black points represent the 24 galaxies, and the solid line is their linear fit. The unfilled circles (and their corresponding fit represented by the dashed line) result from subdividing the same sample into 9 groups, according to mutual proximity. Despite Hubble's reluctance to draw inferences from this result, it was widely interpreted as proof that our Universe is expanding. Reproduced from Hubble (1929). © AAS. Reprinted with permission.

shift, and v is the speed of the source *away* from the observer. A red spectral shift, i.e. a positive value for z, then indicates that the source is receding. In the years following his publication of the distance to M31/M33, Hubble turned his attention to why, as Eddington phrased it, the galaxies "shun us like a plague".[12]

Using the Cepheid method described above to measure the distances to a number of galaxies for which Slipher's redshifts were available,[13] Hubble (1929) submitted a paper in which he reported an approximately linear relationship between distance d and recessional speed,

$$v = H_0 d. \tag{1.19}$$

The constant H_0 here is known as Hubble's constant. The figure from Hubble's paper showing this result is reproduced in Figure 1.2. This relation is now known as Hubble's law, and the conclusion to be drawn from it is that the Universe is undergoing a uniform expansion.

As an aside, it is worth noting that Hubble's original determination of H_0 was around

[12] Quotation from Eddington (1928, p. 166).

[13] Some redshifts were also measured locally by Hubble's collaborator Milton Humason. Humason's career was sufficiently unusual to warrant a remark. Humason left school in Minnesota at the age of 14, then held a succession of posts at the Mount Wilson Observatory, including the role of mule driver during its construction. His knowledge of astronomy was largely autodidactic, but he nonetheless secured the position of assistant astronomer in 1919 (North, 2008).

500 km/s/Mpc, as is clear in Figure 1.2. This is a drastic overestimate based on a miscalibration of the Cepheid distance, and contemporary values are in the region of 70 km/s/Mpc.[14]

There was some hesitation to the idea of cosmic expansion. Astronomers had long believed in a static cosmos, and Hubble's law seemed to beg a fundamental paradigm shift. In the years following Hubble's publication, a number of astronomers proposed alternative interpretations of Hubble's observed relation. As an example, the 'tired light' hypothesis, first proposed by Swiss-American astronomer Fritz Zwicky (1929), supposed that photons lose energy over the course of their intergalactic journeys, leading to a reddening of distant galaxies. Hubble himself was famously wary of imposing a cosmological interpretation on his observed relation. He insisted on using the term 'apparent velocities' in his paper, and in a 1931 letter to Willem de Sitter, he wrote "We use the term 'apparent' in order to emphasize the empirical features of the correlation. The interpretation, we feel, should be left to you and very few others who are competent to discuss the matter with authority."[15] This reluctance notwithstanding, the idea of cosmic expansion was widely accepted by the early 1930s (Kragh, 2007).

There was some theoretical work that anticipated the discovery of cosmic expansion. Of particular note is the work of Friedmann (1922) and that of Lemaître (1927), both of whom constructed models of a homogeneous Universe undergoing uniform expansion (theoretical details will be covered below). Perhaps due to similar paradigmatic reasons as those discussed above, these works were largely ignored at the time of publication, and only gained widespread recognition after Hubble's discovery.

The Big Bang Cosmology

Over the centuries, the question of whether the Universe has a finite age has been asked many times by cosmologists, astronomers, physicists, and philosophers. In the modern period, debates on this question became especially active in the nineteenth century, when advances in understanding of thermodynamics led many physicists to predict the 'heat death' of the Universe.

Hubble's discovery of the cosmic expansion appeared to impose an 'arrow of time' on the Universe, which reignited such debates. In subsequent years and decades, arguably the preponderance of cosmologists were unwilling to accept a finite age for the Universe, in many cases because of its associated religious connotations (Kragh, 2007). Most famously, English astronomer Sir Fred Hoyle and two Austrian-born Cambridge colleagues of his, Hermann Bondi and Thomas Gold, propounded the idea of a 'Steady State' Universe, in which the recession of galaxies is counteracted by the continuous creation of matter, such that the overall mean density in the Universe remains constant (Bondi & Gold, 1948; Hoyle,

[14] The exact value of H_0 is still not entirely uncontroversial; see § 1.1.5.

[15] Quotation from Smith (1982, p. 192).

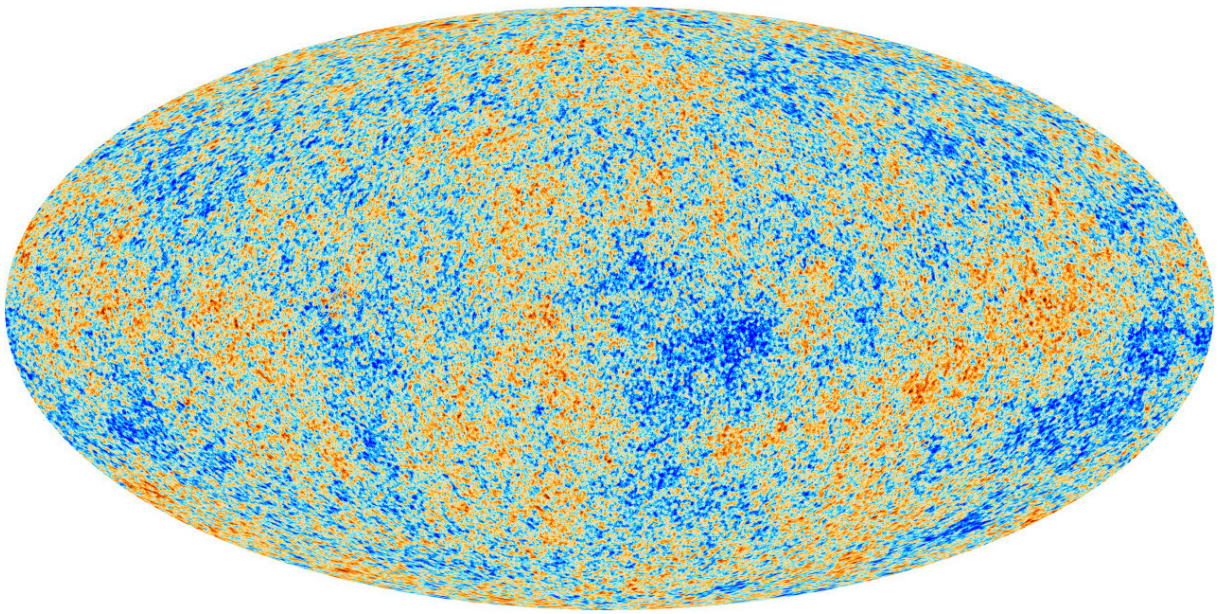

Figure 1.3: A full-sky map of temperature anisotropies of the cosmic microwave background (CMB) as observed by the Planck mission, rendered using a Mollweide projection. The CMB is remarkably isotropic; the colour scale spans ΔT = -300 μK to 300 μK, i.e. $|\Delta T|/T \lesssim 10^{-4}$. Credit: ESA and the Planck Collaboration (2014).

1948). This theory was a realisation of the 'perfect cosmological principle', i.e. humanity occupies a special place in neither space nor time.

On the other hand, theories of an expanding Universe with a finite age also began to appear in these decades. The first such theory was the 'primeval-atom' theory of Lemaître (1931), in which the Universe began in a violent radioactive flash, and has been expanding ever since. Later, in the 1940s and early 1950s, Soviet-American cosmologist George Gamow and his student Ralph Alpher worked on a detailed quantitative theory of a hot, dense early Universe in which the heavy elements were synthesised, a process now known as Big Bang Nucleosynthesis (Alpher, Bethe, & Gamow, 1948[16]). Hoyle famously referred to these theories as hypothesising a 'Big Bang', a term that is now common currency.

Even as late as the early 1960s, the Steady State theory was arguably the prevailing theory among cosmologists (Kragh, 2007). However, the serendipitous 1964 discovery of the cosmic microwave background (CMB) radiation dramatically turned the tide. Predicted by Gamow and colleagues in the late 1940s, the CMB is faint, near-isotropic blackbody radiation with temperature around 2.73 K that pervades all of space. Figure 1.3 shows a map of CMB temperature as obtained by the Planck mission (Planck Collaboration, 2014; see below).

Often described as 'relic radiation' from the Big Bang, the CMB is more accurately de-

[16]This paper is also known as the $\alpha\beta\gamma$ paper. According to Gamow (1952, p. 65), "it seemed unfair to the Greek alphabet to have the article signed by Alpher and Gamow only, and so the name of Dr. Hans A. Bethe *(in absentia)* was inserted in preparing the manuscript for print."

scribed as being relic radiation from the very early Universe, when baryonic matter was in the form of an ionised plasma. Due to frequent Compton scatterings between photons and the free ions, the Universe was macroscopically opaque. At the epoch of recombination, some 380,000 years after the Big Bang (scale factor $a = 1/1100$), the plasma neutralised and the photons were released and embarked upon a (mostly) unimpeded journey to the present.

The first large-scale CMB observation programme was the Cosmic Background Explorer satellite launched in 1989 (COBE; Boggess *et al.*, 1992, and references therein). The different instruments aboard COBE facilitated a measurement of the CMB spectrum (Mather *et al.*, 1994), as well as one of the first detections of CMB anisotropy (Smoot *et al.*, 1992).[17] The ensuing decades have seen a multitude of CMB experiments, including several based on Earth (e.g. ACBAR: Reichardt *et al.* 2009; ACT: Das *et al.* 2011), several borne on balloons (e.g. BOOMERANG: MacTavish *et al.*, 2006), and further satellites (e.g. WMAP: Larson *et al.*, 2011). The most precise measurements to date were obtained by a mission falling in the latter category. The European Space Agency's Planck Satellite (Planck Collaboration, 2018a) recently observed the whole sky in nine microwave frequencies, obtaining detailed maps of the CMB (see Figure 1.3).

The CMB provides invaluable insights into the early Universe, and the cosmological constraints attainable from it will be discussed further below. In addition, the CMB is seen as one of the pillars of proof for the Big Bang cosmology, alongside the Hubble expansion and the successful predictions of Big Bang Nucleosynthesis.

A Metric Tensor for the Universe

One of the central assumptions of modern cosmology is the 'cosmological principle': the idea that on sufficiently large ($\gtrsim$100 Mpc) scales, the Universe is isotropic and homogeneous. The isotropy of the CMB serves as fantastic proof of the former, while large-scale galaxy surveys seem to suggest the latter.

As mentioned above, Friedmann (1922) and Lemaître (1927) both worked on models of an expanding Universe obeying the cosmological principle, even before the discovery of the Hubble expansion. The metric tensor that describes such a Universe is the Friedmann-Lemaître-Robertson-Walker (henceforth FLRW) metric, in which a line element is

$$\mathrm{d}s^2 = -c^2\mathrm{d}t^2 + a^2(t)\left(\mathrm{d}x^2 + \mathrm{d}y^2 + \mathrm{d}z^2\right). \tag{1.20}$$

[17] In fact, the oft-overlooked first detection of CMB anisotropy was reported earlier in the same year by Russian scientists Strukov *et al.* (1992), who announced the detection of a CMB quadrupole with the Relikt-1 experiment on board the Prognoz 9 satellite. This was a monochromatic experiment and the detection had very large error bars, and as such was largely overshadowed by the multi-frequency high-precision detection from COBE later that year.

The quantity a is called the 'scale factor', a time-dependent quantity that determines the expansion of the Universe. By convention, $a = 1$ today, so a region of flat space with physical size R today will have physical size $a(t)R$ at time t. In a Big Bang cosmology, $a < 1$ at all times in the past, and $a \to 0$ as $t \to 0$. It is important to note that this formulation of the metric, in particular the Pythagorean appearance of the spatial part, assumes the Universe has a flat geometry. At present, the evidence (Planck Collaboration, 2018b) appears to favour a flat geometry for the Universe,[18] which will be assumed for the remainder of this thesis.

The spatial coordinates x, y, z appearing in the FLRW metric (1.20) are 'co-moving' coordinates, i.e. time-independent coordinates with the expansion 'divided out'. Consider two galaxies, A and B, situated on the x-axis. If peculiar motions can be neglected for both galaxies, then the cosmic expansion will appear homogeneous and isotropic to observers in either galaxy. The comoving distance separating the galaxies x_{AB} is constant, but the physical distance $d_{AB} = a\,x_{AB}$ expands with the scale factor. The relative recession speed is

$$v_{AB} = \dot{d}_{AB} = \dot{a}\,x_{AB} = \frac{\dot{a}}{a} d_{AB} = H\,d_{AB}, \tag{1.21}$$

where H is the Hubble parameter $H \equiv \dot{a}/a$. The value of the Hubble parameter at the present time is Hubble's constant H_0, so evaluating Eq. (1.21) today yields Hubble's observed relation (1.19) between the recessional speeds and distances of distant galaxies.

As light travels between galaxies, the distance between successive wavecrests expands with space. So, wavelength of light is proportional to the scale factor. If an observer in our Galaxy today ($t = t_0$) receives some light from a distant galaxy emitted some time in the past ($t = t_e$), then the redshift of the light is related to the scale factor at the time of emission $a(t_e)$ by

$$1 + z = \frac{1}{a(t_e)}, \tag{1.22}$$

taking $a(t_0) = 1$.

For the FLRW metric (1.20), the only non-vanishing components of the Einstein tensor (1.7) are the time-time and space-space elements,

$$G_{00} = \frac{3}{c^2}\left(\frac{\dot{a}}{a}\right)^2; \quad G_{ij} = -\frac{a^2}{c^2}\left(\frac{\dot{a}^2}{a^2} + 2\frac{\ddot{a}}{a}\right)\delta_{ij}, \tag{1.23}$$

where a dot indicates a derivative with respect to cosmic time, and δ_{ij} is the Kronecker delta. For a perfect fluid, the corresponding components of the energy-momentum tensor (1.9) are

$$T_{00} = \rho\,c^2; \quad T_{ij} = a^2 P \delta_{ij}. \tag{1.24}$$

[18] Although see recent publications by Park & Ratra (2019); Handley (2019); Di Valentino *et al.* (2020), arguing that evidence favours a closed geometry, and a response by Efstathiou & Gratton (2020).

Thus, the Einstein field equations (1.4) lead to two useful equations,

$$H^2 = \frac{8\pi G}{3}\rho, \tag{1.25}$$

$$\dot{\rho} + 3H\left(\rho + \frac{P}{c^2}\right) = 0. \tag{1.26}$$

The former is known as the Friedmann equation, while the latter is a continuity equation.[19] We have derived two first-order differential equations with three unknowns: a, ρ, and P. To achieve closure, we can assume a polytropic equation of state linking density with pressure,

$$P = w\rho c^2, \tag{1.27}$$

where w is a constant. Different choices for w lead, via Eq. (1.26), to different evolutions of the density ρ over time. This in turn leads, via the Friedmann equation (1.25), to different behaviours of the scale factor a over time. Non-relativistic matter is typically treated as pressureless dust, $w = 0$. For relativistic matter (e.g. CMB photons, neutrinos), statistical physics gives $w = 1/3$. Finally, for a cosmological constant, $w = -1$ as discussed in § 1.1.2. In single-component universes of these types,

$$\rho_m \propto a^{-3}; \qquad a \propto t^{2/3}; \qquad \ddot{a} < 0. \qquad \text{(non-relativistic matter)} \tag{1.28}$$

$$\rho_r \propto a^{-4}; \qquad a \propto t^{1/2}; \qquad \ddot{a} < 0. \qquad \text{(relativistic matter)} \tag{1.29}$$

$$\rho_\Lambda = \text{constant}; \qquad a \propto e^{H_0 t}; \qquad \ddot{a} > 0. \qquad \text{(cosmological constant)} \tag{1.30}$$

From this, it is clear that the composition of the Universe plays a key role in determining the history (and future) of its expansion.

Before moving on to the somewhat more complicated picture of our own multiple-component Universe, it will be useful to write down the Friedmann equation (1.25) in a slightly different fashion. Expanding $\rho = \rho_m + \rho_r + \rho_\Lambda$ and dividing by H_0,

$$\frac{H^2}{H_0^2} = \frac{\Omega_m}{a^3} + \frac{\Omega_r}{a^4} + \Omega_\Lambda, \tag{1.31}$$

where the fractional density parameters Ω are defined by

$$\Omega_X \equiv \frac{8\pi G \rho_{X,0}}{3H_0^2}, \tag{1.32}$$

with $\rho_{X,0}$ the density of component X evaluated today. The three Ω parameters in Eq. (1.31) sum to unity in a flat Universe, and their values give an indication of the importance played by their respective components in the (present-day) cosmic expansion.

1.1.4 The ΛCDM Model

The 'Concordance Cosmology'

The previous section developed a picture of how the cosmic expansion proceeds in various single-component universes. In recent years, evidence has increasingly suggested that

[19] The continuity equation (1.26) could also be derived from the conservation of energy-momentum $\nabla_\beta T^{\alpha\beta} = 0$.

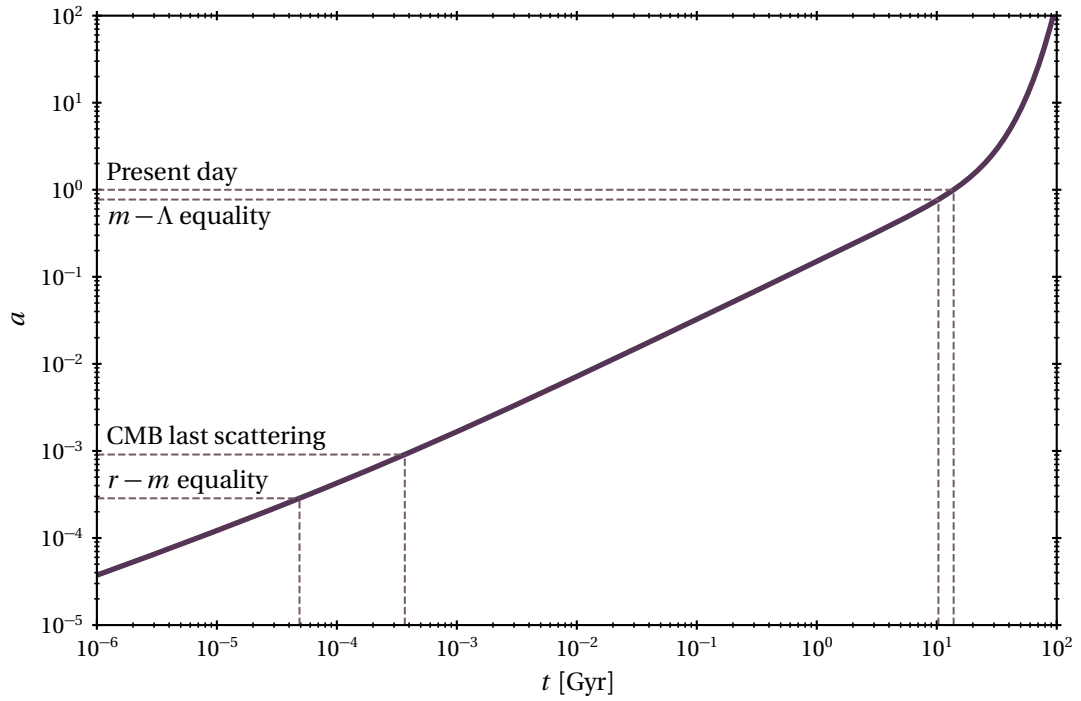

Figure 1.4: The FLRW scale factor as a function of cosmic time in the ΛCDM Universe. Calculated by integrating Eq. (1.31) using cosmological parameter values from Planck (Table 1.1), as well as a radiation density $\Omega_r = 9\times10^{-5}$. The dashed lines indicate various key points in cosmic history: the present day ($a=1$), the time of matter-Λ equality ($a=(\Omega_m/\Omega_\Lambda)^{1/3}$), the time of CMB last scattering ($a\approx 1/1100$), and the time of radiation matter equality ($a=\Omega_r/\Omega_m$).

our own Universe is primarily composed of two components, the cosmological constant ($\Omega_\Lambda \sim 0.7$) and matter ($\Omega_m \sim 0.3$), most of which is in the form of cold dark matter (CDM; $\Omega_{\rm DM} \sim 0.25$, leaving an ordinary, baryonic matter component of $\Omega_b \sim 0.05$). More precise values, obtained from the CMB anisotropy measurements of the Planck satellite (Planck Collaboration, 2018b), are given in Table 1.1. The cosmological parameters shown in the table and the role of CMB measurements in constraining them will be discussed further below.

In addition to the above, there is a small radiation component ($\Omega_r \sim 10^{-4}$). This includes the CMB, as well as the cosmic neutrino background. While this is negligible today, the different scale factor dependences of the radiation (1.29), matter (1.28), and Λ (1.30) densities result in the radiation component being more important in the past.

This cosmic inventory forms the basis for the 'ΛCDM' model of cosmology. Figure 1.4 shows the scale factor a as a function of time in the ΛCDM Universe, calculated by numerically integrating the Friedmann equation (1.31). This procedure also gives a value for the age of the Universe, ∼13.7 billion years, marked on the figure accordingly. Also shown are the times of radiation-matter and matter-Λ equality, i.e. the times in cosmic history when the two relevant components were of equal energy density. It is interesting to note that, at least when viewed on a log-scale, the present day ($a=1$) is very close to the time of matter-Λ equality, i.e. the time when the Universe transitions from the $a \propto t^{2/3}$ matter-dominated

Parameter	Symbol	Planck Value
Hubble's constant	h	0.6727 ± 0.0060
CDM density	$\Omega_{\rm DM} h^2$	0.1202 ± 0.0014
Baryon density	$\Omega_b h^2$	0.02236 ± 0.00015
Scalar spectral amplitude	$\ln\left(10^{10} A_s\right)$	3.045 ± 0.016
Scalar spectral index	n_s	0.9649 ± 0.0044
Optical depth to reionisation	τ_*	$0.0544^{+0.0070}_{-0.0081}$

Table 1.1: ΛCDM cosmological parameters as obtained from the Planck TT+TE+EE+lowE data (Planck Collaboration, 2018b). The values stated are the maximum likelihood values and the errors give the 68% intervals. Note that Hubble's constant h is given in units of 100km/s/Mpc, and the two density parameters $\Omega_{{\rm DM},b}$ carry factors of h^2. A_s and n_s determine the power-law shape of the post-inflationary primordial power spectrum (see the discussion of inflation at the end of § 1.1.4). The optical depth to reionisation τ_* can be approximately understood as the average number of Compton scatterings, per CMB photon, undergone between the present day and the 'epoch of reionisation': the time in the early Universe when the intergalactic medium became macroscopically ionised shortly after the formation of the first stars and galaxies.

period to the $a \propto e^{H_0\sqrt{\Omega_\Lambda}\,t}$ Λ-dominated period.[20] The remaining label on the figure is the time of 'last scattering' (z=1100), when the CMB photons decoupled from baryonic matter.

There is more to the ΛCDM model than the relative energy contents of its components. Perhaps surprisingly however, not a great deal more. Flat ΛCDM is a rather economical model and can be completely described using six parameters. Various parameterisations are possible but one example is listed in Table 1.1; any hitherto undefined quantities are given some physical explanation in the accompanying caption. The only observational probe that can simultaneously constrain all six parameters is the anisotropy distribution of the CMB.

The power spectrum of anisotropies from Planck is displayed in Figure 1.5, along with the best-fitting ΛCDM model. The maximum likelihood parameter values, published in Planck Collaboration (2018b), are reproduced in Table 1.1. This CMB inference is highly consistent internally,[21] i.e. the parameters inferred solely from the Planck temparature-only (TT) power spectrum are able to fit the E-mode polarisation auto- and cross-spectra (EE and TE respectively) with excellent accuracy. The Planck mission and the resulting determination of the cosmological parameters to exquisite precision is rightly considered to be among the chief triumphs of modern cosmology.

While CMB observations are arguably the most informative cosmological probe, it is important to perform independent tests to obtain information from different times and scales, in order to test the consistency of the cosmological model and search for evidence for new physics. Indeed, a number of other cosmological probes are beginning to yield constraints with comparable precision to those of Planck. Of particular note are various

[20] See discussion of the 'coincidence problem' in § 1.1.5.

[21] However, see the discussion of the lensing power spectrum amplitude $A_{\rm L}$ in § 1.1.5.

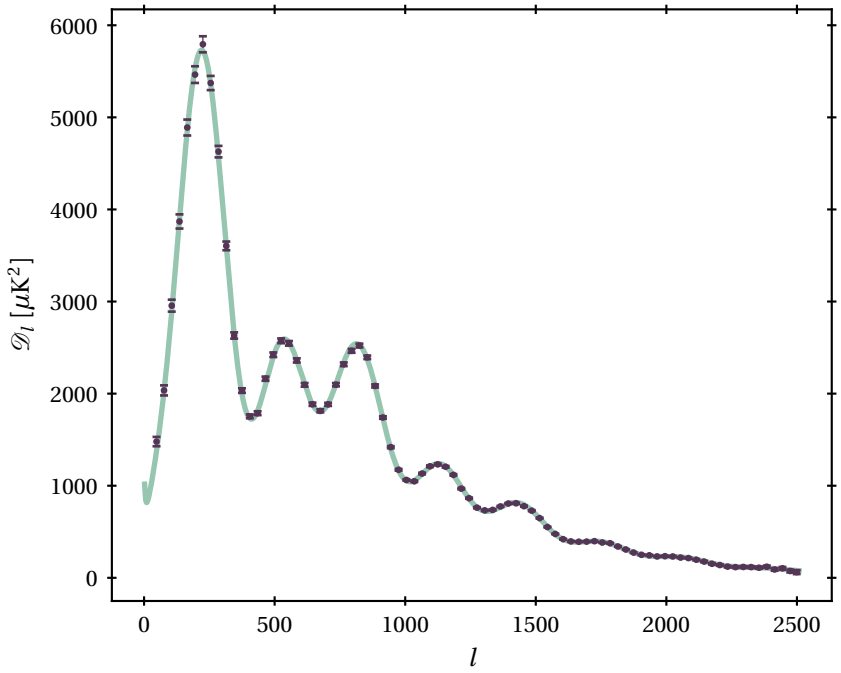

Figure 1.5: The data points give the temperature power spectrum of the CMB as measured by the Planck satellite, while the line gives the maximum likelihood ΛCDM fit with parameter values as given in Table 1.1. The vertical axis plots $\mathscr{D}_l \equiv l(l+1)C_l/(2\pi)$, where l is the multipole (shown on the horizontal axis) and C_l is to be understood as the angular analogue of the power spectrum $P(k)$ defined in Eq. (1.41), i.e. the power spectrum of the spherical harmonic coefficients of the CMB temperature anisotropies depicted in Figure 1.3. Reproduced from Planck Collaboration (2018a) using data from the Planck Legacy Archive.[22]

measurements that probe the large-scale distribution of matter in the late Universe. With the exception of gravitational lensing, such probes are necessarily indirect, because the greater part of the matter distribution (i.e. the dark matter) is unseen, and we must instead rely upon biased tracers of the underlying distribution, such as galaxies or neutral hydrogen.

One of the most important large-scale structure probes is the baryon acoustic oscillation (BAO) feature. This is a preferred length scale imprinted on to the matter distribution arising from acoustic oscillations in the pre-recombination photon-baryon fluid, and can be observed as a peak in correlation functions and power spectra obtained from sufficiently large galaxy surveys (Peebles & Yu, 1970; Eisenstein & Hu, 1998). It can be measured at different redshifts in both the transverse and angular dimensions, giving geometric measurements that lead to constraints on the various parameters that determine the expansion history of the Universe (i.e., particular combinations of Ω_m, Ω_Λ, and H_0). The BAO feature was first measured around the same time in both the power spectrum of the Two-degree-Field Galaxy Redshift Survey (2dFGRS; Cole *et al.*, 2005) and in the real-space correlation function of galaxies from the Sloan Digital Sky Survey (SDSS; Eisenstein *et al.*, 2005), and has most recently been measured by the Baryon Oscillation Spectroscopic Survey (BOSS)

[22] pla.esac.esa.int; accessed May 2020.

part of SDSS-III (Alam *et al.*, 2017). Ongoing and future surveys/missions such as extended BOSS[23] (eBOSS; Dawson *et al.*, 2016), Euclid (Laureijs *et al.*, 2011), and the Dark Energy Spectroscopic Instrument (DESI; DESI Collaboration, 2016a,b) are expected to obtain extremely precise measurements of the signal with unprecedentedly large galaxy samples, at higher redshifts than those currently probed.

Another feature observable in spectroscopic surveys is the phenomenon of redshift-space distortions (RSD), i.e. radial anisotropies in the 3D spatial distributions of galaxies as inferred from redshifts, arising as a result of galaxy peculiar velocities and their consequent Doppler enhancement/diminution of the cosmological redshift (Kaiser, 1987). This feature is sensitive to the density-weighted growth rate $f\sigma_8$.[24] High-precision measurements of redshift-space distortions were also recently obtained by BOSS (Alam *et al.*, 2017).

A third effect worth mentioning is that of weak gravitational lensing; the distortion of apparent shapes of galaxies due to gravitational lensing by the foreground matter distribution (see, e.g., Bartelmann & Schneider, 2001; Kilbinger, 2015, for reviews of weak lensing and its applications to cosmology). Weak lensing gives rise to two related probes: the autocorrelation of observed galaxy shapes ('cosmic shear') and the cross-correlation of lens galaxy positions with source galaxy shapes ('galaxy-galaxy lensing'). Because gravitational lensing is induced by all matter rather than merely the visible matter, cosmic shear does not suffer from the galaxy bias mentioned above. However, various other systematics make the measurement difficult. Nonetheless, measurements of cosmic shear have been obtained, most recently by a number of wide-field imaging surveys, including the Dark Energy Survey (DES; DES Collaboration, 2018a,b, 2019), the Kilo Degree Survey (KiDS; Hildebrandt *et al.*, 2017, 2020), and the Hyper Suprime-Cam Subaru Strategic Program (HSC-SSP; Hikage *et al.*, 2019) giving constraints on Ω_m and the parameter combination $S_8 \equiv \sigma_8(\Omega_m/0.3)^{1/2}$.

In addition to these, there exist many other active fields of research in cosmology, such as distance measurements of Type Ia supernovae (see the discussion below of the discovery of the cosmic acceleration, also the review article by Goobar & Leibundgut (2011) and recent cosmological constraints from Scolnic *et al.*, 2018; Riess *et al.*, 2019), galaxy cluster cosmology (e.g. Bocquet *et al.*, 2019), and the newly inaugurated cosmology of standard sirens (i.e., gravitational waves; see, e.g., the measurement of Hubble's constant from the 'multi-messenger' event GW170817: LIGO Scientific Collaboration *et al.*, 2017a).

With the exception of a number of significant lingering tensions that will be enumerated in § 1.1.5, all of these independent tests lead on the whole to mutually consistent con-

[23] Early data releases from eBOSS have already led to measurements of the BAO signal in both the quasar and red galaxy subsamples (Ata *et al.*, 2018 and Bautista *et al.*, 2018 respectively).

[24] The growth rate of perturbations $f(a)$ is directly related to the matter content Ω_m, while σ_8 is the amplitude of present-day density fluctuations smoothed in a sphere of radius $8h^{-1}$ Mpc and often replaces A_s in parameterisations of ΛCDM adopted by low-redshift investigations.

clusions, and parameter inferences that are consistent with the Planck ΛCDM cosmology sketched above. Moreover, many of them are able to venture beyond estimating ΛCDM parameters and additionally test some of the underlying assumptions of ΛCDM, such as flatness ($\Omega_K = 0$) and the cosmological constant equation of state ($w = 1$). These tests have also largely served to affirm ΛCDM. For example, a combined inference using BOSS and Planck data leads to $\Omega_K = 0.0003 \pm 0.0026$ and $w = -1.01 \pm 0.06$ (Alam *et al.*, 2017).

The six-parameter ΛCDM model is thus rather successful. As a phenomenological theory, it ties together the various puzzling 'dark sector' observations described in the following sections, while its parameters—relatively few in number—are determined by the CMB measurements of Planck Collaboration (2018b) to exquisite precision. Also worth mentioning is the complementary role played by N-body ΛCDM simulations, which are increasingly able to accurately model the physics of non-linear scales and account for the observed properties of galaxies (see § 1.2.2). As such, ΛCDM—sometimes dubbed the 'concordance cosmology'—has become the consensus view in recent years. Indeed, some months after the 1998 discovery of the cosmic acceleration (see below), American cosmologists James Peebles and Michael Turner participated in a debate with the title 'Nature of the Universe Debate: Cosmology Solved?'[25] The debate was held at the Smithsonian Museum of National History and was clearly designed to resemble the Great Debate, which took place in the same auditorium some eighty years prior. Now, however, the subject of the debate was rather different. As the title of the debate suggests, the advent of the ΛCDM cosmology had brought about the very real possibility that cosmology was 'solved', i.e. the twentieth century efforts to understand the makeup and history of the Universe and the values of the key cosmological parameters were at an end.

Such sentiments are undoubtedly somewhat premature, as ΛCDM still has a number of outstanding questions to resolve. These will be discussed in § 1.1.5. First, however, it is worth discussing the two primary ingredients of the model—dark matter and the cosmological constant—both of which are presently elusive, unknown quantities.

Dark Matter

Over the course of the twentieth century, evidence derived from a number of independent sources increasingly suggested that the Universe hosts large amounts of matter other than the visible, luminous matter that occupies the night sky. This 'dark matter' has not been observed directly, but its existence has been inferred indirectly, due to its gravitational effects on visible matter.

Influenced by earlier works by Kapteyn (1922) and Jeans (1922), one of the first such

[25] Both parties in the debate submitted papers to be published in the March 1999 issue of the Publications of the Astronomical Society of the Pacific (Peebles, 1999; Turner, 1999). See also the article by Nemiroff & Bonnell (1999) summarising the proceedings in the same issue.

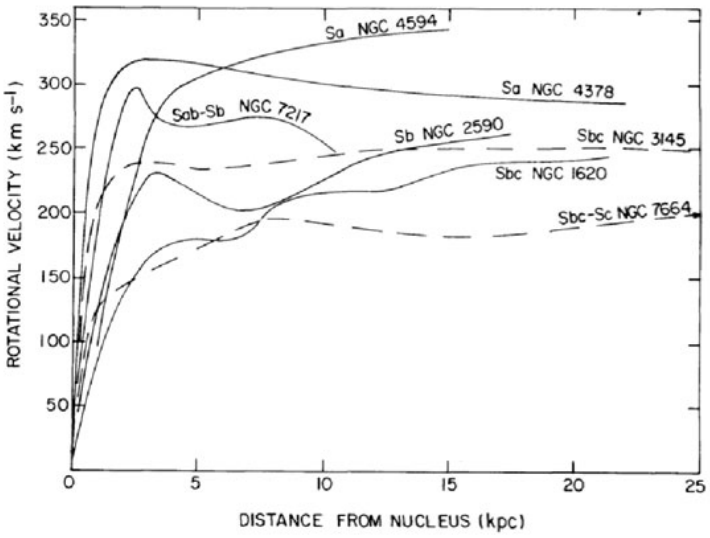

Figure 1.6: Rotation curves (i.e. rotational velocity versus galactocentric distance) of seven nearby galaxies, obtained by Vera Rubin and colleagues using long-slit spectroscopy. The approximate flatness of the curves at large distances implies that the galaxies host large amounts of unseen dark matter. Reproduced from Rubin *et al.* (1978).

inferences was that of Dutch astronmer Jan Oort (1932), who demonstrated by dynamical arguments that the mass density in the Milky Way disc plane is necessarily more than twice that of the observable stars.[26] The following year, Fritz Zwicky (1933) (familiar as the originator of the 'tired light' hypothesis; § 1.1.3) applied the virial theorem to the motions of the Coma galaxy cluster and calculated a dynamical mass that was some fifty times larger than the observed luminous mass. Three years later, American astronomer Sinclair Smith (1936)—Hubble's colleague at the Mount Wilson Observatory—published the results of a similar study in the Virgo cluster, finding an even greater mass-to-light ratio of around one hundred.

Another rich source of evidence for dark matter lay in the internal dynamics of external galaxies. Studying the rotational motion of Andromeda (M31), American astronomer Horace Babcock (1939) inferred a mass-to-light ratio comparable to Zwicky's.[27] For several

[26] As with many ideas and themes in contemporary astronomy and cosmology, antecedents for the idea of dark matter can be found almost arbitrarily far back in the historical record. In the nineteenth century, Lord Kelvin applied arguments derived from the kinetic theory of gases to the Milky Way and demonstrated that "many of our thousand million stars, perhaps a great majority of them, may be dark bodies."(Quotation from an 1884 Baltimore lecture; Kelvin, 1904, p. 274) A century earlier, English and French thinkers John Michell (1784) and Pierre Simon Laplace (1796) speculated about the possible existence of invisible but gravitationally detectable 'dark stars', from which light is unable to escape (these ideas of course resurfaced in twentieth century, with the postulation and discovery of black holes). Much earlier still, in the fifth century BCE, Pythagorean philosopher Philolaus postulated the existence of a dark 'counter-Earth' or *'antichthon'*, orbiting the central fire in opposition to the real Earth (Kragh, 2007).

[27] This was drastically different from mass-to-light ratios accepted at the time for the Milky Way, and Babcock was consequently reluctant to publish his findings. This hesitation was apparently vindicated when, according to North (2008, p. 746), "the critical reception Babcock was given at a meeting of the American Astronom-

decades, the subject of dark matter lay largely dormant, but was picked up again in the 1970s, when independent theoretical studies performed by American and Soviet groups determined that large quantities of dark matter were required for the stability of observed disc galaxies (Ostriker *et al.*, 1974; Einasto *et al.*, 1974). Around the same time, the advent of long-slit spectroscopy enabled American astronomers Vera Rubin and Kent Ford to measure the optical rotation curves of various galaxies in the local Universe. Like Babcock several decades earlier, they inferred total masses of galaxies many times larger than implied by their visible light. Furthermore, the flatness of the rotation curves implied that the dark matter was much more spatially extended than the luminous matter (Rubin & Ford, 1970; Rubin *et al.*, 1978, 1980; also see Figure 1.6, which displays several of Rubin's observed rotation curves). These findings were supported by radio observations of the 21 cm line carried out by Albert Bosma (1978), which allowed observations of neutral hydrogen kinematics to much larger galactocentric distances. Thus, by the end of the 1970s, there began to exist a widespread understanding that galaxies are embedded within much larger and more massive dark matter 'haloes'.

These discoveries prompted a great deal of observational and theoretical work attempting to understand the nature of dark matter; a programme of investigation that continues to the present day. Until relatively recently, a plausible candidate for dark matter was the 'Massive Compact Halo Object', or 'MACHO': an umbrella term including various known, low-luminosity objects, mostly baryonic in composition. Examples of MACHOs are brown dwarfs, planets, and black holes. While these objects emit little or no electromagnetic radiation, they can still be inferred by their gravitational interactions. In particular, various groups have performed systematic surveys searching for gravitational microlensing events caused by large numbers of MACHOs inhabiting the Milky Way and its satellites (Alcock *et al.*, 2000; Tisserand *et al.*, 2007). Such events have been detected, but not in sufficient numbers. The current consensus is therefore that MACHOs alone are unlikely to account for a significant proportion of dark matter.

It is worth noting that aside from the absence of large numbers of microlensing events, there are independent reasons to expect dark matter to be largely non-baryonic in nature. First, calculations of primordial nucleosynthesis suggest a low value for the present-day baryon density. In particular, the abundance of deuterium is sensitive to the baryon density, and observed deuterium densities imply $\Omega_b \sim 0.05$ (Steigman, 2006). Secondly, baryon acoustic oscillations in the CMB imply similar values for Ω_b (Planck Collaboration, 2018b). Given that large-scale galaxy surveys and the CMB also give values for the overall matter density of $\Omega_m \sim 0.3$ (Planck Collaboration, 2018b; Alam *et al.*, 2017), it appears that non-baryonic dark matter necessarily plays a significant role. This $\Omega_b - \Omega_m$ discrepancy inferred independently from nuclear abundances and baryon acoustic oscillations also serves as proof of the existence of dark matter.

---

ical Society was such that he spent the rest of his career in solar astronomy."

For some time in the 1970s and 1980s, a popular non-baryonic candidate for dark matter was the neutrino. Whether neutrinos possessed mass was a matter of considerable debate in that decade, but it was believed that if they did then they could well play the gravitational role of dark matter (Szalay & Marx, 1976). This scenario is an example of a 'hot dark matter' theory. Here, the small assumed masses of the neutrinos ensured that they moved with relativistic speeds throughout much of the history of the Universe. Consequently, their 'free streaming' would wipe out any structures smaller than the largest, super-cluster scales. These very large structures would subsequently fragment into progressively smaller structures. This top-down process of structure formation is the opposite of the CDM picture, in which smaller structures continually merge and accrete into larger structures. Observations of galaxies and small-scale structure at high redshift have largely ruled out hot dark matter theories, and cold dark matter has been the consensus view since the beginning of the 1990s (North, 2008).

Leaving the neutrino behind, particle theorists have proposed a phantasmagoria of hypothetical dark matter candidates; typically new elementary particles beyond the Standard Model of particle physics. Many of these particles additionally have motivations stemming from unsolved problems in particle physics, and predict a variety of detectable signatures. Attempts to detect such signatures have thus far been unsuccessful, but the search continues. An overview of dark matter particle candidates can be found in the review article by Feng (2010).

As an example of a presently popular dark matter candidate, Weakly Interacting Massive Particles (WIMPs) form a generic class of particles that arise naturally in various 'supersymmetric' extensions of the standard model. Dynamically, WIMPs behave like CDM, becoming non-relativistic and 'freezing out' of the baryon-photon plasma in the early Universe. Compellingly, for WIMPs with masses in the GeV-TeV range, the predicted cosmic abundance of dark matter agrees well with the observed abundance: $\Omega_{\rm DM} \sim 0.25$ (e.g. Jungman *et al.*, 1996).[28]

Other particle candidates for DM include QCD axions (Marsh, 2016) and fuzzy dark matter (Hui *et al.*, 2017), both incorporating light, bosonic scalars. The bosonic nature of these particles leads to the formation of solitonic Bose-Einstein condensate 'cores'. For $m \sim 10^{-22}$ eV, these cores can be kpc-sized, leading to interesting phenomenology on galaxy scales and possible solutions to some of the small-scale problems in ΛCDM (§ 1.1.5).

Primordial black holes are a non-particulate candidate for dark matter (Hawking, 1971; Carr & Hawking, 1974). These are hypothetical black holes that formed in the very early Universe, and have recently been the subject of much attention as a result of the unusually large inferred masses of the black holes in the merger event observed at the Laser Interferometer Gravitational-Wave Observatory (LIGO; LIGO Scientific Collaboration & Virgo Collaboration, 2016). However, the expected event rate at LIGO would be significantly higher

[28] This agreement is known as the 'WIMP miracle'.

than observed if primordial black holes accounted for an appreciable fraction of dark matter (Sasaki *et al.*, 2016; Ali-Haïmoud *et al.*, 2017).

The remainder of this thesis assumes that cold dark matter haloes are composed of a diffuse, particulate dark matter. If dark matter were instead comprised of compact objects, the screening properties (§ 1.3.2) of dark matter would change, with self-screening much more likely. In particular, primordial black holes would self-screen under the no-hair theorem (Sotiriou & Faraoni, 2012). Consequently, the galaxy-scale fifth force phenomenology described in this thesis would be altogether different if dark matter were entirely composed of primordial black holes.

As a final note in this section, there are attempts to account for gravitational effects of dark matter without introducing any unseen particles. Perhaps the most well-known of these is Modified Newtonian Dynamics (MOND; Milgrom, 1983). First proposed by Israeli physicist Mordehai Milgrom in 1983, MOND modifies Newton's laws in the low acceleration regime. In a nutshell, MOND is rather successful in reproducing the dynamics of galaxies, but performs less well at the level of galaxy clusters (Clifton *et al.*, 2012). In its initial formulation, MOND was strictly a non-relativistic theory, inapplicable to cosmology, gravitational lensing, or strong-field regimes. However, theories have since been formulated to provide relativistic extensions of MOND (e.g. TeVeS; Bekenstein, 2004).

Cosmological Constant

The dominant component of the ΛCDM model is the cosmological constant, Λ. As shown in Eq. (1.30), $\ddot{a} > 0$ in a Λ-dominated universe; the cosmological constant, if real, is causing the expansion of our Universe to accelerate.

The cosmological constant had a somewhat chequered history throughout the twentieth century. According to the historical account of Λ by Earman (2001, p. 215), "it has been alternately reviled and praised, and it has been counted out many times, only to stage one comeback after another."

In 1917, Einstein introduced the 'cosmological term' $\Lambda g_{\alpha\beta}$ into his field equations (Einstein, 1917). At the time, Einstein's conception of the Universe was decidedly Newtonian; he rejected the notion of the island universes, and believed in a Universe uniformly populated with stars. Most importantly, he believed this Universe was static, and he introduced Λ to bring about this stasis.[29]

To understand this further, consider a Universe consisting of only pressureless matter and the cosmological constant, momentarily relaxing our assumption of a flat geom-

[29] Here also there is some historical antecedent. Some decades prior, German astronomer Hugo von Seeliger (1895) and mathematician Carl Neumann (1896) had introduced Λ-esque repulsive terms into Newton's laws of gravitation, in order to try to resolve the apparent paradox that an infinite homogeneous cosmos would collapse under gravity.

etry. The Friedmann equation (1.25) can then be rewritten, expanding $\rho = \rho_m + \rho_\Lambda = \rho_m + \Lambda c^2/8\pi G$, as

$$H^2 = \frac{8\pi G}{3}\rho_m + \frac{\Lambda c^2}{3} - \frac{kc^2}{a^2}. \tag{1.33}$$

The final term on the right-hand side is the curvature term, with k a constant describing the cosmic curvature; $k > 0$ for a closed universe. Differentiating Eq. (1.33) and using the continuity equation (1.26) gives a cosmic acceleration equation

$$3\frac{\ddot{a}}{a} = \Lambda c^2 - 4\pi G\rho_m. \tag{1.34}$$

A static solution (i.e. $\ddot{a} = 0, \dot{a} = 0, a = 1$) to Eqs. (1.33) and (1.34) is given by

$$\Lambda = k = \frac{4\pi G\rho_m}{c^2}. \tag{1.35}$$

In addition to this desirable static solution, Einstein had two broader—perhaps more metaphysical—reasons for constructing such a model. First, Einstein believed that the cosmological constant brought GR into greater accordance with Mach's principle. According to Einstein's formulation of Mach's principle, matter alone should determine the metric structure of spacetime, and so no metric solutions to the field equations should exist if $T_{\alpha\beta} = 0$. However, flat Minkowski spacetime exists as a solution in this case, unless the Λ term is introduced. Second, the fact that the solution is spatially closed gave it additional appeal in Einstein's eyes: boundary conditions are not needed in a closed universe, and he believed boundary conditions to be "contrary to the spirit of relativity." (Einstein, 1917, p. 183).

These motivations notwithstanding, Einstein was uneasy about Λ since its conception, famously remarking that it was "gravely detrimental to the formal beauty of the theory." (Einstein, 1919, p. 351).[30] His disquiet turned into open denunciation in the subsequent decade, following three developments. First, shortly after Einstein's publication of his cosmological solution, de Sitter (1917) published an alternative cosmology. A de Sitter universe is spatially flat, devoid of matter, and carries a positive cosmological constant. The possibility of an empty-universe solution to his field equations in the presence of Λ greatly devalued the Machian credentials of Λ in the view of Einstein. Second, Eddington (1930) pointed out that Einstein's solution was unstable. Inspecting Eq. (1.34), it is clear that a perturbation that reduced ρ_m would trigger a cosmic expansion that would reduce ρ_m further. Finally, the discovery of Hubble's relation and its implied cosmic expansion of course contradicted Einstein's starting assumption of a static cosmos.

Much of the cosmological community followed Einstein in dropping Λ, but several individuals continued to champion it (Earman, 2001). For instance, Lemaître argued that Λ

[30] Einstein is also widely quoted as having later described Λ as his "biggest blunder". However, all attributions of this remark lead ultimately to George Gamow, who is not unlikely to have been merely paraphrasing Einstein's actual sentiments (Earman, 2001).

could help resolve the 'age paradox': the fact that the apparent ages of the oldest globular clusters were greater than the age of the Universe as inferred from Hubble's relation in the absence of Λ. American physicist Richard Tolman, meanwhile, argued that the left-hand side of the GR field equations (1.4) should host the most general divergence-free, rank-2 symmetric tensor built from the metric tensor and its first and second derivatives, and this should include a term proportional to $g_{\alpha\beta}$. The proportionality constant Λ should only be set to zero if it was empirically determined to be so. Finally, Eddington argued that it was worth keeping Λ because it would provide the Universe with a length scale to act as a 'standard of comparison'.

Throughout the remainder of the twentieth century, Λ made a number of reappearances under various guises. For instance, in the late 1960s, Λ was briefly repopularised as a possible explanation for the apparent overabundance of quasars at $z = 2$ (Petrosian *et al.*, 1967; Kardashev, 1967). Again, in the 1980s and early 1990s, several groups increasingly started to consider the idea of a non-zero Λ, in part as a way to reconcile the variety of observations of a low Ω_m with a flat Universe (e.g. Turner *et al.*, 1984; Efstathiou *et al.*, 1990; Ostriker & Steinhardt, 1995). This time the idea did not die back, and instead hit the mainstream towards the end of the 1990s, due to observations of Type Ia supernovae.

A Type Ia supernova is a highly luminous event, in which an accreting white dwarf detonates in a runaway nuclear fusion process. This takes place when the mass of the white dwarf exceeds a fixed ceiling of approximately $1.44 M_\odot$. The light curves of Type Ia supernovae rise and fall rather quickly, and the timescales of these rises and falls are tightly correlated with the peak (absolute) luminosities of the supernovae. Therefore, the absolute luminosity and luminosity distance[31] of a Type Ia supernova are calculable from its light curve. Type Ia supernovae are thus 'standardisable' candles not unlike Cepheid variables, but probing much larger ($\gtrsim$100 Mpc) distances.

Writing luminosity distance as a function of redshift for a population of standard candles, the relation is given, up to quadratic terms in z, by

$$d_L \approx \frac{c}{H_0} z \left(1 + \frac{1 - q_0}{2} z \right), \tag{1.36}$$

where q_0 is the 'deceleration parameter',

$$q_0 \equiv -\left(\frac{\ddot{a} a}{\dot{a}^2} \right)_{t=t_0} = \Omega_r + \frac{1}{2}\Omega_m - \Omega_\Lambda. \tag{1.37}$$

The latter equality has used Eqs. (1.34) and (1.31). Thus, $q_0 < 0$ for an accelerating expansion, and Eq. (1.36) implies that luminosity distance will be greater for an object at fixed

[31] Because of the cosmic expansion, 'distance' is not a straightforward concept in cosmology, and several distance measures exist. For a standard candle of intrinsic luminosity L and apparent flux f, the appropriate distance measure is the 'luminosity distance' d_L, given by $d_L = (L/4\pi f)^{1/2}$. In the case of a flat Universe, this relates simply to the time-independent co-moving distance x via $d_L = x(1+z)$.

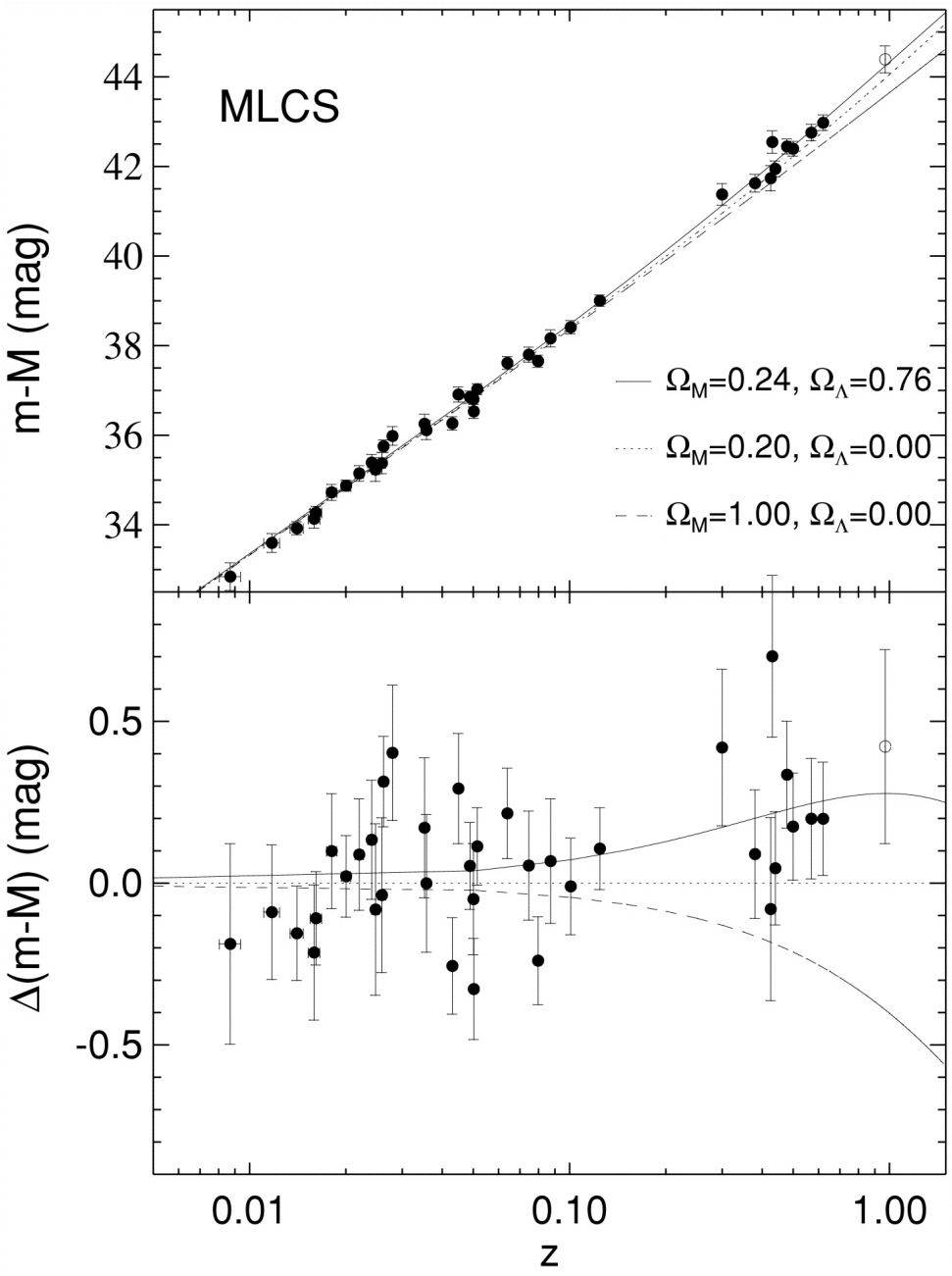

Figure 1.7: The top panel shows distance modulus, $m-M = 5\log_{10}(d_L/10\,\mathrm{pc})$, versus redshift for the Type Ia supernova sample studied by Riess *et al.* (1998). The lines show the predicted relations in various cosmologies, as labelled. The bottom panel shows residuals given a fiducial cosmology with $\Omega_\Lambda = 0$ and $\Omega_m = 0.2$. The authors found statistically significant evidence for $q_0 < 0$ and $\Omega_\Lambda > 0$, i.e. for an accelerated cosmic expansion. Reproduced from Riess *et al.* (1998). © AAS. Reprinted with permission.

redshift than in the cases of coasting ($q_0 = 0$) or decelerating ($q_0 > 0$) expansion. This can be understood by noting that if the expansion of our Universe is accelerating over time, then the expansion will have been slower in the past and the 'lookback time' to an event at a fixed redshift will be larger than would otherwise be the case, and greater lookback time corresponds to greater distance.

Two supernova research groups, the Supernova Cosmology Project led by American

Saul Perlmutter and the High-z Supernova Research Team led by Australian Brian Schmidt, undertook surveys of Type Ia supernovae in the 1990s. Near the end of the decade, both teams published the results of their surveys, finding significant evidence for $q_0 < 0$ and an accelerating expansion (Riess *et al.*, 1998; Perlmutter *et al.*, 1998). One of the key figures from the Riess *et al.* (1998) paper is here reproduced in Figure 1.7.

It remains to discuss the physical meaning of Λ. While early interpretations of it regarded it as something akin to either a physical constant or a constant of integration (Kragh, 2007), from the late 1960s the work of various theorists—most notably Soviet Yakov Zeldovich (1967, 1968)—popularised an alternative interpretation of Λ: the energy density of the vacuum. This idea remains popular today, but it is not unproblematic and will be discussed further in § 1.1.5.

Proof of an accelerating expansion does not equate to proof of a non-zero Λ. Λ is arguably the simplest theory that can account for the acceleration (Amendola & Tsujikawa, 2010), but one could instead imagine a number of alternative mechanisms driving the acceleration. As an example, in quintessence models (Fujii, 1982), a minimally coupled scalar field with a slowly varying potential drives the acceleration. As a second example, modified gravity theories such as those studied in this thesis introduce to the action (1.12) various exotic components coupled to gravity. In some theories these components can 'self-accelerate', but many others effectively rely on Λ terms in their potentials to drive the expansion (Wang *et al.*, 2012). Generically, all such mechanisms fall under the umbrella of 'dark energy' theories.

In addition to the evidence from supernovae discussed above, there are several other sources of evidence of dark energy. First, as Lemaître had correctly argued in the 1930s, the calculated age of a universe without Λ is insufficiently large to account for the oldest globular clusters in the Milky Way. Secondly, the positions of the acoustic peaks in the CMB power spectrum shift in the presence of dark energy. Assuming a flat Universe and that dark energy takes the form of a cosmological constant, analysis of the Planck CMB data indicates $\Omega_\Lambda = 0.6847 \pm 0.0073$ (Planck Collaboration, 2018b), a clear demonstration of the existence of dark energy. Furthermore, these same acoustic peaks are imprinted in the BAO signature detected in large-scale galaxy surveys, giving an independent demonstration of dark energy (Blake *et al.*, 2011). Finally, probes of the large-scale structure of matter, such as the $z = 0$ matter power spectrum, favour a cosmology with non-zero Ω_Λ, as demonstrated by Efstathiou *et al.* (1990) and the other groups in the early 1990s.

Inflation

As mentioned previously, the CMB serves as a remarkable demonstration of the isotropy of the Universe. While this is a pleasing affirmation of the cosmological principle, it also raises a troubling question: why should antipodal points on the CMB display the same

statistical properties despite originating in regions of the Universe that have apparently never been in causal contact? This is known as the 'horizon problem'. To the put the problem on a more quantitative footing, the current physical distance to the last scattering surface is around $d_{\rm LSS}(t_0) \approx 14{,}000$ Mpc. At the time of last scattering, $z_{\rm LSS} \approx 1100$, this corresponded to a region of size $d_{\rm LSS}(t_{\rm LSS}) = d_{\rm LSS}(t_0)/a_{\rm LSS} \approx 13$ Mpc. On the other hand, the horizon distance[32] at $t_{\rm LSS}$—calculated naïvely from the FLRW metric (1.20)—is much smaller: $d_{\rm hor}(t_{\rm LSS}) \approx 0.25$ Mpc. This implies that the CMB is made up of a large number of causally disconnected patches, a fact contradicted by its evident isotropy. The 'initial conditions' of the Universe would require a high degree of fine-tuning to generate this isotropy.

Another problem is the 'flatness problem': *a priori*, there is no clear physical reason to expect the Universe to have a flat spatial geometry, but it is nonetheless observed to be flat or very close to flat, i.e. $\Omega_{\rm tot} \equiv \Omega_r + \Omega_\Lambda + \Omega_m \approx 1$ (Planck Collaboration, 2018b).[33] Furthermore, the departure of $\Omega_{\rm tot}$ from unity grows with scale factor, so Planck bounds of $|\Omega_{\rm tot} - 1| \lesssim 10^{-3}$ become increasingly tight as they are extrapolated back in time. To take this argument to its extreme, at the Planck time $t \sim 10^{-43}$, the flatness is required to be $|\Omega_{\rm tot} - 1| \lesssim 10^{-62}$. This is seemingly another fine-tuning problem.

A third problem is the 'monopole problem': an abundance of magnetic monopoles is a generic prediction of Grand Unified Theories, but none have ever been observed. In the early 1980s, it was the monopole problem that led American particle theorist Alan Guth to the idea of the inflation: a period of extremely rapid exponential expansion in the very early Universe (Guth, 1981).[34]

The inflationary epoch takes place within the first fraction of a second after the Big Bang. If the scale factor at the beginning of the inflationary epoch is $a_i \equiv a(t_i)$, then at its end the scale factor $a_f \equiv a(t_f)$ is given by

$$a_f = e^{H_i\left(t_f - t_i\right)} a_i = e^N a_i, \tag{1.38}$$

assuming a purely exponential growth, with Hubble parameter H_i. The second equality defines N, the number of 'e-foldings' of inflation.

During the inflationary epoch any curvature is strongly suppressed, as $|\Omega_{\rm tot}(t) - 1| \propto e^{-2H_i t}$, so $|\Omega_{\rm tot}(t_f) - 1| = e^{-2N} |\Omega_{\rm tot}(t_i) - 1|$. In this way, inflation explains the present absence of curvature, solving the flatness problem. If strong curvatures existed prior to inflation ($|1 - \Omega_{\rm tot}| \sim 1$), then some $N \approx 60$ e-folds are required to be consistent with today's observed

[32] The particle horizon distance $d_{\rm hor}$ at a given time is the proper distance a photon has travelled from $t = 0$ to that time. This sets a limit to causal contact, as bodies separated by larger distances have had insufficient time to exchange information.

[33] See Footnote 18 in this chapter.

[34] Similar ideas were earlier proposed by Soviet cosmologist Alexei Starobinsky (1980), but were not discussed in terms of the horizon/flatness/monopole problems and did not initially gain widespread attention across the iron curtain.

flatness, allowing for the regrowth of curvature after the inflationary epoch. Similarly, inflation solves the monopole problem by exponentially rarefying the number density of magnetic monopoles, $n(t_f) = e^{-3N} n(t_i)$.

Because of the exponential expansion, small, causally connected regions of the pre-inflationary Universe correspond to larger regions of space today than would otherwise be the case in a universe without an inflationary period. It is possible then to explain the isotropy of the CMB if the last scattering surface originated from a region of the pre-inflationary Universe small enough to be causally connected. In other words, horizon distance increases exponentially during the inflationary epoch, and it is therefore possible to construct an inflation scenario in which $d_{\rm hor}(t_{\rm LSS}) > d_{\rm LSS}(t_{\rm LSS})$. Inflation can therefore also solve the horizon problem.

It is clear from this discussion that inflation is a useful construction that solves a number of problems, but as with dark matter and dark energy, a physical realisation remains to be identified. A popular *ad hoc* model is that of a scalar 'inflaton' field ϕ with a shallow 'slow-roll' potential. If (in natural units) $\dot{\phi}^2 \ll V(\phi)$, then the inflaton acts as a cosmological constant, i.e. $w \approx -1$, driving an exponential expansion. However, the literature hosts a vast smörgåsbord of variations on—and alternatives to—this idea, in addition to a range of ideas for how to relate the inflaton to ideas from particle theory.

An early success for inflationary theory came about as a result of the Nuffield workshop in Cambridge in 1982.[35] Here, it was calculated that a generic prediction of inflation was a (nearly) scale-invariant spectrum of density perturbations (Bardeen *et al.*, 1983). These perturbations arise from quantum fluctuations in the inflaton field which are then amplified during the inflationary epoch. It had previously been shown by Edward Harrison (1970) and Yakov Zeldovich (1972) that the large scale structures of the present Universe should have their 'initial conditions' in just such a spectrum of perturbations. This theoretical derivation of this Harrison-Zeldovich spectrum was widely seen as a triumph for inflationary theory (Kragh, 2007).

A second triumph could well be on the horizon. Another generic result of inflationary theories is the prediction of a primordial gravitational wave background (Starobinsky, 1979; Rubakov *et al.*, 1982). While a direct detection of this background is well beyond the sensitivity level of current and planned gravitational wave detectors, an indirect detection is possible through a 'B-mode' polarisation signature in the CMB (Kamionkowski *et al.*, 1997; Seljak & Zaldarriaga, 1997). This is a key goal of current and future CMB experiments, as

[35] This workshop was attended by many well-known names: as well as Guth and Starobinsky, participants included Stephen Hawking, Gary Gibbons, Dennis Sciama, Martin Rees, Paul Steinhardt, James Bardeen, John Barrow, Andrei Linde, and Michael Turner. With some exceptions (particularly within the local Cambridge cohort), the majority of attendees came from a background of particle theory rather than cosmology (Longair & Smeenk, 2019). This is possibly a reflection of the origin of inflationary theory as a solution to the monopole problem arising in Grand Unified Theories, which would have seemed irrelevant or abstruse to many astronomers of the day (Kragh, 2007).

it would provide a 'smoking gun' signature of inflation, as a well as a source of valuable information about inflation (Kamionkowski & Kovetz, 2016).

Despite its unknown nature and controversies about its predictivity and falsifiability (Rothman & Ellis, 1987; Ijjas *et al.*, 2017[36]), inflation is widely regarded today as a linchpin of modern cosmology. Not only does it solve the monopole, flatness, and horizon problems, it sows the seeds in the early Universe for all subsequent astrophysical structure.

1.1.5 Beyond ΛCDM?

The previous section discussed the ΛCDM model and its empirical successes; chiefly the broad agreement between a number of independent cosmological probes. These successes notwithstanding, a number of outstanding questions still exist under the ΛCDM paradigm. The biggest elephants in the room are the unknown natures of dark matter and dark energy.[37] For dark matter, the problem lies in identifying a suitable candidate, whether a hypothesised particle or otherwise. Efforts in this field were discussed in the previous section and will not be mentioned further here. For dark energy, the problem is more complex. Here, a candidate has been identified: the cosmological constant. However, there are significant problems with using Λ to drive the cosmic acceleration, and solving the dark energy problem will require either solutions to these problems or a suitable alternative to Λ.

This section will discuss these issues surrounding Λ, as well as other outstanding questions under ΛCDM, before closing with a discussion of our current understanding of gravity.

Problems with Λ

If the physical interpretation of Λ is that of a vacuum energy as described in § 1.1.4, then Λ is in principle calculable. Summing zero-point contributions over all modes of an arbitrary massive field and truncating the integral at the Planck scale, the expected vacuum energy density is (in natural units) $\epsilon_\Lambda \sim 10^{74}$ GeV^4 (Amendola & Tsujikawa, 2010). By contrast, the observed value of the cosmological constant from Planck is $\Lambda = 1.1056 \times 10^{-52}\mathrm{m}^{-2}$ (Planck Collaboration, 2018b). Converting this to an energy density via $\epsilon_\Lambda = \rho_\Lambda c^2 = \Lambda c^4/8\pi G$ gives

[36]The latter reference, an article published in the popular science magazine Scientific American, made particularly provocative assertions, including that inflationary cosmology "cannot be evaluated using the scientific method" (*ibid.*, p. 39). This was especially remarkable given one of the authors was Paul Steinhardt, one of the original architects of inflation. It prompted a response by several of the other architects: Guth, Linde, David Kaiser and Yasunori Nomura, further co-signed by 29 other eminent scientists. This response, along with a rebuttal by the authors of Ijjas *et al.* (2017), can be found on the Scientific American website (blogs.scientificamerican.com/observations/a-cosmic-controversy; accessed April 2020).

[37]A tongue-in-cheek encapsulation of the *status quo* has been attributed to Durham cosmologist Tom Shanks: "There are only two things wrong with ΛCDM: Λ and CDM." (Bull *et al.*, 2016, p. 89).

$\epsilon_\Lambda \sim 10^{-47}$ GeV^4; a mammoth discrepancy of 121 orders of magnitude.[38] This huge conflict between theory and observation is known simply as the 'cosmological constant problem' or 'vacuum catastrophe', attention to which was first drawn by American cosmologist Steven Weinberg (1989), even before the widespread acceptance of a non-zero Λ.[39]

Another problem to do with the observed value of the cosmological constant is the 'coincidence problem'. This was first alluded to in § 1.1.4, where Figure 1.4 showed that the era of matter-Λ equality is rather close to the present day. Given that $\Omega_\Lambda \approx 0$ since the Big Bang until relatively recently, and $\Omega_\Lambda \approx 1$ in the relatively near future and forever after, it is somewhat surprising that we inhabit the singular period in which matter and the cosmological constant have comparable energy densities.

There exists a number of approaches to solving these problems. For instance, anthropic arguments have been invoked as a possible solution to both problems (Efstathiou, 1995). While such arguments are compelling, they are widely seen as somewhat unsatisfactory and a measure of last resort (Bull *et al.*, 2016). Alternatively, there is a myriad of dark energy theories which postulate new dynamical degrees of freedom or modifications of gravity. Overviews of these theories can be found in e.g., Amendola & Tsujikawa (2010); Clifton *et al.* (2012); Joyce *et al.* (2015).

Small-scale Issues

Another bone of contention within the ΛCDM paradigm is a number of apparent discrepancies between observation and prediction on small scales.[40] An overview of these small-scale issues can be found in the article by Bullock & Boylan-Kolchin (2017).

There are two 'classic' small-scale problems in particular that have been the subject of intense study, the 'core/cusp' and 'missing satellites' problems, both of which have been known since the early days of ΛCDM simulations.

A key prediction of DM-only ΛCDM simulations is that of 'cuspy' density profiles for dark matter haloes, i.e. profiles with steep central slopes (Navarro *et al.*, 1997), roughly $\propto r^{-1}$. On the other hand, some observations (Moore, 1994; Flores & Primack, 1994; Walker & Peñarrubia, 2011; Oh *et al.*, 2015), e.g., of galaxy rotation curves, have been found to suggest flatter, 'cored' profiles in the inner regions of haloes. An example is given in Figure 1.8, which shows the rotation curve of the nearby dwarf galaxy NGC 3109, taken from the

[38] A slightly more sophisticated calculation than the one described here gives much lower values, in the region of $\epsilon_\Lambda \sim 10^8$ GeV^4 (Martin, 2012; Bull *et al.*, 2016). Of course, this still represents an unacceptably large gap of 55 orders of magnitude.

[39] Weinberg (1989) was not equipped with an empirical value for Λ, but he did have an empirical upper bound, so he could still pose the question: "why is Λ so low?"

[40] 'Small scales' here meaning $R \lesssim 1$ Mpc.

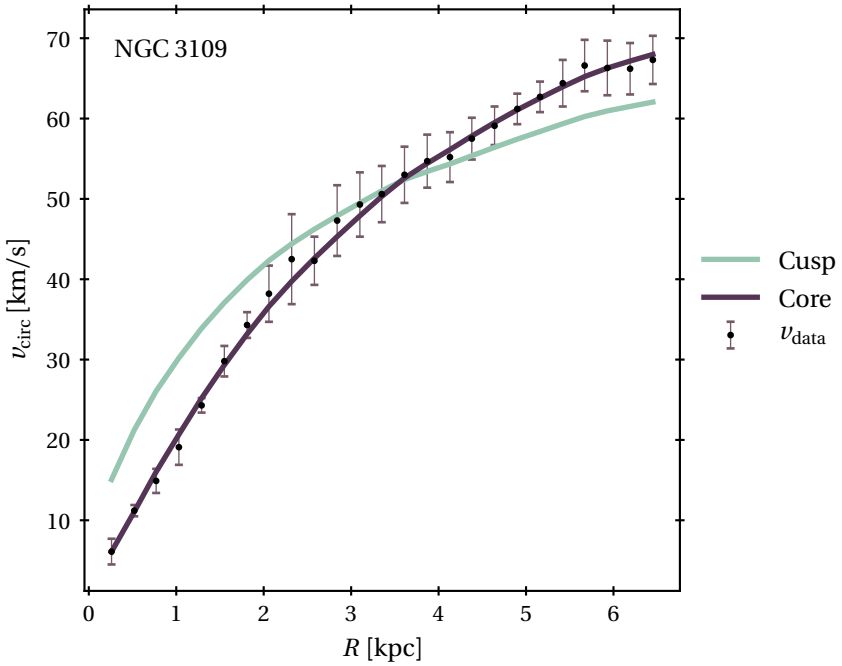

Figure 1.8: The data points give the rotation curve of NGC 3109, taken from the SPARC sample. The green curve is the maximum-likelihood model using a 'cuspy' NFW halo profile, while the purple is that for a 'cored' DC14 profile, both obtained using the methodology described in Chapter 3. This Figure illustrates the 'core/cusp' problem described in the text.

Spitzer Photometry and Accurate Rotation Curves sample (SPARC; Lelli *et al.*, 2016). Alongside the observed data are two fits obtained using the procedure described in Chapter 3. One incorporates the cuspy Navarro-Frenk-White halo profile (NFW; Eq. (1.45); Navarro *et al.*, 1996, 1997), and the other the cored halo profile of Di Cintio *et al.* (DC14; 2014). The goodness-of-fit of the cored halo model is rather better than that of the cuspy halo. The cuspy model puts far too much mass in the galactic centre, and is unable to reduce this without a commensurate reduction in the overall halo mass, and consequently a reduction in the predicted rotation speeds in the outer part of the galaxy, which it is already underpredicting.

As a possible resolution, some simulations including the effects of baryonic feedback have suggested that such mechanisms can induce cored central density distributions in dark matter haloes (Mashchenko *et al.*, 2008; Governato *et al.*, 2010; Pontzen & Governato, 2012; Di Cintio *et al.*, 2014). This is thought to happen when feedback, e.g. from supernovae, pushes around large amounts of gas in the central region of a galaxy, and the resulting fluctuation in the gravitational potential of the gas then also affects the dark matter distribution. Other simulations, however, find no such effect (e.g, Bose *et al.*, 2019). In addition, the recent work of Genina *et al.* (2018) found that the inference of a cored profile from observations might be the result of an incorrect assumption of spherical symmetry, and that observed galaxies are consistent with cusps, while Oman *et al.* (2015) argue that the issue is better characterised as a problem of mass deficit in the inner regions of dwarf

galaxy haloes rather than a core/cusp problem. The core/cusp debate thus remains far from resolved.

Meanwhile, the missing satellites problem relates to the mismatch between the observed number of satellite galaxies of the Milky Way and that expected from much larger numbers of substructures in ΛCDM cosmological simulations (Moore *et al.*, 1999; Klypin *et al.*, 1999). In particular, ΛCDM simulations predict thousands of satellites around the Milky Way (Springel *et al.*, 2008; Garrison-Kimmel *et al.*, 2014; Griffen *et al.*, 2016), while the observed number is around fifty (Kim *et al.*, 2018; Drlica-Wagner *et al.*, 2020). There are two possible mitigating factors, both of which likely play a role. The first is that observational catalogues are likely to be highly incomplete (Drlica-Wagner *et al.*, 2020). Second, baryonic processes may again be important. For instance, photoionising ultraviolet background radiation would prevent the cooling of protogalaxies (Efstathiou, 1992), while supernova feedback might expel their star-forming gas (Shen *et al.*, 2014), in both cases preventing the formation of observable galaxies. The real number of satellite galaxies would then be lower than that predicted by DM-only simulations. Thus, by attacking the problem from both ends, i.e. increasing the observed number and reducing the predicted number, the problem might be solved. Indeed, Kim *et al.* (2018) apply a carefully calculated correction factor to the satellite counts from SDSS to account for their incompleteness, and in doing so bring them into agreement with predicted numbers from state-of-the-art ΛCDM abundance matching techniques. The authors thus claim to have solved the missing satellites problem.

A third problem, the 'too-big-to-fail' problem (Boylan-Kolchin *et al.*, 2011), is related to the first two. ΛCDM simulations (e.g., those of Springel *et al.*, 2008; Diemand *et al.*, 2008) suggest that the central densities (or central masses) of the brightest MW satellites should be much higher than observed.[41] If the classical MW satellites[42] are associated with simulated satellites of comparable central mass, then there should exist around ten satellites with larger central mass (Bullock & Boylan-Kolchin, 2017). These subhaloes would be sufficiently massive to resist the suppressive effects described above. In other words, they would be 'too big to fail' to form a galaxy. Their apparent absence in the MW halo is therefore somewhat puzzling. Rather than accounting for these missing galaxies, one could instead approach the problem by associating the classical satellites with the largest simulated satellites and attempting to explain the discrepancy in central masses. Here, one could imagine baryonic effects being of greater assistance; they could act to reduce the pre-

[41] While the too-big-to-fail problem is often discussed in the context of MW satellites, the problem has also been shown to exist in the Andromeda satellites (Tollerud *et al.*, 2014) and in the field dwarf population (Kirby *et al.*, 2014).

[42] The 'classical' MW satellites are the collection of 11 brightest satellites of the Milky Way, and the only satellites known before the turn of the millennium. Of these, the Large and Small Magellanic Clouds have been known since prehistory, while the remainder are twentieth century discoveries: the Fornax, Carina, Sextans, Leo I, Leo II, Sculptor, Ursa Minor, Draco, and Sagittarius dwarfs.

dicted central densities, e.g. by inducing the formation of cores as described above. Indeed, if the central densities of the highest-mass simulated subhaloes could be reduced in such a way as to match those of the classical MW satellites, this could simultaneously address the too-big-to-fail and core/cusp problems. On the other hand, it has been shown (Bullock & Boylan-Kolchin, 2017) that even in simulations in which baryonic feedback processes induce core formation, the mass scales at which this takes place are not those of most of the classical satellites. Alternatively, environmental processes are often invoked (i.e. satellite-MW interactions; Sawala *et al.*, 2016; Tomozeiu *et al.*, 2016; Wetzel *et al.*, 2016), but these do not solve the problem in the context of field dwarfs (see Footnote 41 in this chapter). As with the core/cusp problem, it would be premature to claim that baryonic feedback processes have solved the too-big-to-fail problem.

There have been other puzzling observations at small scales. For instance, the classical MW satellites appear to approximately inhabit a great circle around the Milky Way (Kunkel & Demers, 1976; Lynden-Bell, 1976; Pawlowski *et al.*, 2014).[43] Furthermore, galaxies exhibit surprisingly consistent relations between their baryonic content and dynamical properties. One example is the 'baryonic Tully-Fisher relation', a simple scaling relation between the baryonic masses of galaxies and the amplitudes of the flat parts of their rotation curves (McGaugh *et al.*, 2000). Another example is the radial acceleration relation (RAR), the tight correlation between total dynamical acceleration (as inferred from rotation curves) and acceleration due to the visible baryonic mass. These observations would not be naïvely expected under the ΛCDM paradigm, and reconciling them with theory is a challenge, although progress has been made on all fronts (Bullock & Boylan-Kolchin, 2017).

As discussed, baryonic physics provides a hope for resolving most of these small-scale tensions under the ΛCDM paradigm. However, 'new physics' solutions also exist. For example, 'self-interacting' (Spergel & Steinhardt, 2000) and 'fuzzy' (Hu *et al.*, 2000) dark matter theories have both been proposed as resolutions to the core/cusp problem. Chapter 3, based on Naik *et al.* (2019), will demonstrate that the screened modified gravity theories discussed in § 1.3 could also alleviate the core/cusp problem, as predicted previously by Lombriser & Peñarrubia (2015).

Parameter Tensions

A tension that has particularly been the focus of attention in recent years is the H_0 tension. Recent measurements of the Hubble constant as inferred from direct distance ladder measurements (i.e. from the low-z slope of the redshift-distance relation in e.g. Figure 1.7) are in the region of 74 km/s/Mpc (e.g. Riess *et al.*, 2019). By contrast, the CMB-derived Planck

[43] This is sometimes known as the 'Vast Polar Structure', or 'VPOS'. Compounding the mystery, Andromeda also seems to host its satellites on co-planar orbits (the 'Great Plane of Andromeda' or 'GPoA'; Conn *et al.*, 2013; Ibata *et al.*, 2013).

value for H_0 is around 67 km/s/Mpc (Planck Collaboration, 2018b). The uncertainties on both values are sufficiently small that this is a rather significant tension. Taking the value of H_0 from Riess *et al.* (2019), the discrepancy is at a level of 4.4 σ.

A possible resolution is unaccounted-for sources of systematic error at either end. For example, Rigault *et al.* (2015) argue that Type Ia supernovae in star-forming environments are intrinsically dimmer than those in passive environments. A failure to allow for this bimodality when 'standardising the candles' could lead to systematic bias in the measurement of H_0. In particular, they find that the tension can be reduced to a level of $\sim$1 σ when accounting for the effect.

On the other hand, another possibility is again that of new physics. Screened modified gravity theories can again serve as an example here. Desmond *et al.* (2019b) showed recently that if the 'calibration' cepheids within the Milky Way are screened while cosmological cepheids are not, the resulting miscalibration would lead one to systematically overestimate H_0. At the other end, the CMB-derived value for H_0 is highly model-dependent; it depends on the sound horizon at the time of recombination, and also on the angular diameter distance to the last scattering surface. The former depends in turn on the energy budget of the early Universe, while the latter depends on the expansion history of the late Universe. The discrepant value of H_0 assumes ΛCDM, but one can instead imagine a number of alternatives to ΛCDM in which either an altered expansion history or an altered early Universe energy budget changes the inference of H_0 from the CMB, and consequently alleviates the tension (for example, 'early dark energy'; Mörtsell & Dhawan, 2018; Poulin *et al.*, 2019).

Other parameter tensions also exist. For instance, the Planck value of the amplitude of the matter power spectrum σ_8[44] is higher than that measured by various other experiments, particularly those measuring matter fluctuations at late times, e.g. via surveys of weak lensing (MacCrann *et al.*, 2015; Raveri, 2016; Hildebrandt *et al.*, 2017) or redshift-space distortions (Macaulay *et al.*, 2013). A second example is $A_{\rm L}$, the amplitude of the CMB lensing power spectrum, by construction equal to unity for the best-fitting cosmological model. If instead allowed to vary freely, it can be inferred from CMB data in two different ways: from the lensing-induced smoothing of the temperature power spectrum, or by using the maps to reconstruct the lensing potential. With Planck data, the value obtained from the lensing reconstruction is consistent with 1, while the smoothing of the temperature power spectrum gives $A_{\rm L} = 1.243 \pm 0.095$, a discrepancy of $\sim$3 σ (Planck Collaboration, 2018b).

Gravity

One of the underpinnings of the ΛCDM model is GR, from which it ultimately derives. Where ΛCDM has had a number of empirical successes, GR is arguably even more impres-

[44] See Footnote 24 in this chapter for a more precise definition of σ_8.

Figure 1.9: The widely publicised image of the shadow of the super-massive black hole in M87. Details of the observation were published in Event Horizon Telescope Collaboration (2019). Credit: Event Horizon Telescope Collaboration.

sive, having effortlessly passed all tests since its conception more than a century ago.

Arguably the first success of GR was Einstein's exact calculation of the anomalous precession of the perihelion of Mercury, then a long-known outstanding problem in astronomy. First described in Einstein (1915), this was one of the three 'classical' tests of GR that Einstein described in his 1916 paper consolidating his numerous articles on GR from the previous year (Einstein, 1916). However, the prediction of a new effect is perennially more impressive than the explanation of a known one, and the other two tests were just such predictions. The first related to the gravitational deflection of light, the magnitude of which in GR is twice that in Newtonian physics. The second prediction was that of gravitational redshift, i.e. the redshifting of light as it passes through (or is emitted from) from gravitational wells.

The total solar eclipse of May 1919 provided an ideal opportunity to test the prediction of gravitational deflection. The darkening of the sun allowed the measurement of apparent positions of nearby stars, which could then be compared with their apparent positions at other times of year, when their light does not pass in the close vicinity of the sun. Einstein's predicted deflection for light grazing the surface of the sun was 1.75 arcseconds. Two British expeditions, organised jointly by the Royal Society (RS) and Royal Astronomical Society (RAS) and spearheaded by then Astronomer Royal Frank Watson Dyson, journeyed to the island of Principe (in the Gulf of Guinea) and Sobral (Brazil) to observe the eclipse and make the requisite measurements. The Principe exhibition was led by Eddington, while the Sobral exhibition was led by A. C. Crommelin, from the Royal Observatory in Greenwich.[45] Upon their return, Eddington performed a great deal of data reduction and arrived

[45]The story of the expeditions and their historical context in the immediate aftermath of the First World War is very interesting in its own right. Fascinating accounts are given in Crelinsten (2006) and Stanley (2003). The latter work focuses in particular on the role and motivations of Eddington, for whom the expedition had a socio-political dimension as well as its obvious scientific one. Guided by his Quaker beliefs in pacifism and humanitarianism, he believed that a British expedition to verify a 'German theory' would do much to rebuild

at a weighted mean deflection of 1.64 arcseconds, agreeably close to the GR value.[46] The announcement of this result at a joint meeting of the RS and RAS in November 1919 had an immediate and prodigious effect on both the public at large and the scientific community, where the main outcome was to convince the vast majority of scientists of the validity of GR (Kragh, 2007).

The verification of the third prediction, that of gravitational redshifts, came some years later. In 1924, Eddington predicted that light from the nearby white dwarf Sirius B would be strongly redshifted due to its own deep gravitational potential. In correspondence with American astronomer Walter Adams, Eddington predicted a redshift corresponding to a radial velocity of 20 km/s (Holberg, 2010). Adams (1925a,b) then measured a redshift of 21 km/s, in excellent agreement with the prediction.[47]

Following this activity in the years immediately following the conception of GR, Will (2014) describes a period of 'hibernation', spanning the years 1920-1960. There appears to have been a loss of appetite in that period for testing GR, and expertise in GR more generally also seems to have decayed. Presumably this is because of an absence at the time of observable regimes in which GR was relevant. This changed in the 1960s, with observations of pulsars, quasars and the cosmic microwave background. These discoveries ushered in a new 'golden age' of GR, spanning 1960-1980, in which opportunities to apply and test GR in astronomy and cosmology proliferated. One notable example was the discovery of the Hulse-Taylor binary (Hulse & Taylor, 1975), a pulsar-neutron star binary system in which the observed decay of the orbital period agreed with the GR calculation of the energy loss due to gravitational wave radiation.

During this period, the 'Parameterised Post-Newtonian' (PPN) formalism was developed (Nordtvedt, 1968a; Will, 1971; Will & Nordtvedt, 1972). Here, perturbations are added to the weak-field Newtonian limit of GR to account for the lowest-order GR corrections.

---

bridges between the British and German academies. Such an objective flew counter to the prevailing views in British society, even within the scientific community, much of which was in favour of a vindictive post-war treatment of Germany, and a permanent exclusion of its scientists from international collaborations. Incidentally, Eddington could well have missed the expedition had he been enlisted in the army following his conscription hearing in 1918. His plan in this event had been to continue his conscientious objection, which would have landed him in prison. Fortunately, Dyson successfully intervened and procured an exemption for Eddington, arguing that Eddington's role in the expedition was indispensable.

[46] Sadly, in the years and decades following the eclipse of 1919, an unflattering narrative has developed, in which Eddington is thought to have somehow 'fudged' the data, downweighting some of the Sobral plates which contradicted the GR prediction, presumably because of his sympathy for Einstein and his political agenda (see e.g. Earman & Glymour, 1980). This idea, however, does not hold under quantitative scrutiny (Stanley, 2003).

[47] As it happens, both Eddington's prediction and Adams' measurement are equally wrong, by a factor of $\sim$4. The agreement, and its vindication of GR, was therefore highly fortuitous. However, as noted by Holberg (2010), Adams' observation was also a milestone in the study of degenerate stars, and this underestimate of the Sirius B redshift impeded progress in that field for several decades.

There are a number of dimensionless PPN parameters—each of which carries some physical intuition—which can be experimentally constrained and compared to their GR expectations (all either 1 or 0). For instance, the PPN γ parameter (= 1 in GR) quantifies the space-time curvature generated by a unit mass at rest. This parameter is probed by experiments such as the gravitational deflection and redshift tests described above. The strongest constraint, however, comes from measurements of the 'Shapiro time delay': the apparent time delay of light arriving at an observer after having passed through a gravitational well. In 2003, Doppler tracking of the Cassini spacecraft as it passed very near to superior conjunction with the Sun enabled a measurement of this time delay, which was found to be very close to the GR expectation: $\gamma - 1 = (2.1 \pm 2.3) \times 10^{-5}$ (Bertotti *et al.*, 2003). A table of other current PPN constraints—along with their experimental sources—is given in the review article by Will (2014, Table 4). Most constraints come either from Solar System tests such as those described, or from observations of pulsars. The constraints are all rather stringent; indeed, the Cassini bound seems comparably lenient when juxtaposed with the others.

Partly independent from these efforts, there have also been many tests of the validity of different statements of the equivalence principle (EP; see 1.1.2, and Footnote 6 for definitions of the different statement of the EP). The most stringent constraints on the WEP have come from the Eöt-Wash group at the University of Washington, who use rotating torsion balances to measure relative accelerations towards the Earth of very small test masses of different compositions. These experiments are conceptually similar to those conceived and undertaken around the turn of the twentieth century by Hungarian physicist Baron Roland von Eötvös (Eötvös *et al.*, 1922), from whom the group take their name. Defining the Eötvös parameter,

$$\eta \equiv 2\frac{|a_1 - a_2|}{|a_1 + a_2|}, \tag{1.39}$$

where a_1 and a_2 are the accelerations of the two test bodies, the Eöt-Wash group find $\eta_{\rm WEP} = (0.3 \pm 1.8) \times 10^{-13}$ (Adelberger, 2001; Schlamminger *et al.*, 2008; Wagner *et al.*, 2012). Current and future space-based experiments are forecast to give more precise constraints by up to four orders of magnitude (Worden *et al.*, 2000; Touboul *et al.*, 2001; Nobili *et al.*, 2012).[48] In the Solar System context, the Earth and Moon cannnot be treated as non-gravitating test particles, so measurements of their relative accelerations toward the Sun test the SEP. Such tests are carried out using 'lunar laser ranging' experiments which repeatedly measure the Earth-Moon separation by reflecting laser light from mirrors on the lunar surface. Such

[48] Preliminary results from the MICROSCOPE satellite, in orbit from 2016 to 2018, already give constraints at the level of $\eta_{\rm WEP} \lesssim 10^{-14}$, an improvement of one order of magnitude, with a forecast of even stronger constraints following a more complete analysis of systematic error (Touboul *et al.*, 2017).

experiments have given the constraint $\eta_{\rm SEP} = (-1.0 \pm 1.4) \times 10^{-13}$ (Williams *et al.*, 2004).[49,50]

Baker *et al.* (2019) claim that the present times are a second golden age of GR. Indeed, a number of observations have grabbed headlines and the public imagination. First, there was the announcement in early 2016 of a direct detection of gravitational waves at LIGO, generated during a merging event of two black holes (LIGO Scientific Collaboration & Virgo Collaboration, 2016). Gravitational waves are a fundamental prediction of GR, but their direct detection is only now possible using high precision laser interferometers such as LIGO and Virgo. Another ground-breaking observation was announced in 2019 by the Event Horizon Telescope collaboration, who had observed the nucleus of the galaxy M87 and obtained the first direct image of a black hole shadow (see Figure 1.9; Event Horizon Telescope Collaboration, 2019). For the purposes of testing gravity, perhaps the most important event of recent years was the observation of the 'multi-messenger' event GW170817 (LIGO Scientific Collaboration & Virgo Collaboration, 2017; LIGO Scientific Collaboration *et al.*, 2017b). Here, a neutron star merger generated a gravitational wave signal detected at LIGO and Virgo, as well as an observed gamma-ray burst and cross-spectrum electromagnetic afterglow. The coincidence of arrival times of the gravitational wave and gamma-ray burst signals from a source around ∼40 Mpc away indicates that the propagation speed of gravitational waves is very close to that of light ($|\Delta c|/c \lesssim 10^{-15}$), greatly restricting the space of allowed modified gravity theories (Baker *et al.*, 2017; Creminelli & Vernizzi, 2017; Ezquiaga & Zumalacárregui, 2017).

Another key recent development in the testing of gravity has been the advent of probes of 'precision cosmology', such as Planck. At cosmological scales, there are a number of probes that can test gravity, such as the expansion history as constrained by the CMB, BAO and Type Ia supernovae, the late-time matter distribution as constrained by weak lensing surveys, and the growth rate of structure as constrained by galaxy surveys. Investigations into these cosmological probes of gravity have proliferated in recent years, and reviews can be found in the articles by Clifton *et al.* (2012) and Ferreira (2019). Approaches have varied from individual model tests to model-independent parameterised approaches, both at the level of the background and at the level of linear perturbations, but a number of such parameterisations exist. One commonly used parameterisation is the pair of functions $\mu(a,k)$ and $\eta(a,k)$, respectively the modification to Poisson's equation, and the anisotropic stress

[49] Note that a relative acceleration between the Earth and Moon due to a hypothetical SEP-violation is known as the Nordtvedt effect, after the American astronomer Kenneth Nordtvedt, who conceived the experiment (Nordtvedt, 1968b). Nordtvedt was also the originator of the PPN formalism described above.

[50] The PPN formalism assumes the WEP and EEP, so the Eötvös tests described here do not give any PPN constraints. The lunar laser ranging tests, however, constrain a PPN parameter combination known as the 'Nordvedt parameter', $\eta_{\rm N} \equiv 4\beta - \gamma - 3 - (10\xi + 3\alpha_1 - 2\alpha_2 + 2\beta_1 + \beta_2)/3$. Most 'conservative' alternative gravity theories set all the PPN parameters to their GR values except β and γ (although ξ can sometimes be an exception). Imposing this along with the Cassini bound on γ, constraints on $\eta_{\rm N}$ become constraints on β, the PPN parameter quantifying the non-linearity of the superposition principle. From Williams *et al.* (2004), $\beta - 1 = (1.2 \pm 1.1) \times 10^{-4}$.

(e.g., Planck Collaboration, 2016, 2018b). Both functions are unity in GR. Using the Planck data in conjunction with BAO and RSD data, the Planck team calculate constraints on μ and η, finding no significant deviation from GR (Planck Collaboration, 2018b, Figure 31). Compared to the PPN constraints described above, these are rather weak, $\mathcal{O}(1)$ constraints, exemplifying cosmological constraints on gravity more generally. Nonetheless, cosmological probes of gravity are tremendously valuable because they test gravity at markedly different length scales and curvature scales than the (mostly Solar System) PPN tests. Such tests check the validity of extrapolating our locally derived theory of gravity to vast cosmological scales, and provide a much-needed observational 'anchor' at such scales. Furthermore, future surveys such as those to be produced by Euclid, DESI, LSST (Legacy Survey of Space and Time[51]; Ivezić *et al.*, 2019), and SKA (Square Kilometre Array; Carilli & Rawlings, 2004) are forecast to give significantly tighter constraints.

The history of alternative theories of gravity has largely paralleled that of GR, with a flurry of activity in the former field accompanying each period of renewed interest in the latter. One example of a well-studied alternative gravity theory from the early days of GR is the 'Kaluza-Klein' theory. First conceived by German theorist Theodor Kaluza (1921) and given a quantum mechanical interpretation by Swede Oskar Klein (1926), the Kaluza-Klein theory was a 5D generalisation of GR. Alternative gravity theories were again resurgent during the golden age of GR. A representative example from this period is Brans-Dicke gravity (Brans & Dicke, 1961), the prototypical scalar-tensor theory (see § 1.3). Over the last two decades, a renewed interest in modified gravity theories has again arisen, driven in part by rapid developments in cosmology and the outstanding questions surrounding the ΛCDM model. Compendia of modified gravity theories that are the subject of active research can be found in, e.g. Amendola & Tsujikawa (2010); Clifton *et al.* (2012); Joyce *et al.* (2015); Koyama (2016). A key development in this period has been the study of screening mechanisms (e.g. Khoury & Weltman, 2004; Hinterbichler & Khoury, 2010), whereby modifications to gravity can be rendered undetectable in dense regions such as the Solar System while remaining active elsewhere. With these mechanisms, new dynamical fields can retain cosmological relevance while also evading the stringent PPN tests described above. Screening mechanisms are discussed further in § 1.3.2.

Given the numerous successes of GR described above, it is inevitable that one should question the merit of devising and testing alternatives. This question becomes particularly acute upon noting that GR is more than simply one theory in a field of competitors, GR is *special*. This is formalised in Lovelock's theorem: the only second-order, local gravitational field equations derivable from an action containing solely the 4D metric tensor are the Ein-

[51] To many, the acronym 'LSST' will have the more familiar meaning of 'Large Synoptic Survey Telescope'. The observatory itself, currently under construction in Chile, was renamed earlier this year as the Vera C. Rubin Observatory, to honour the pioneering astronomer discussed in Chapter 1.1.4. Concomitantly, the planned survey to be undertaken there was named as the 'Legacy Survey of Space and Time', perhaps to avoid retroactively invalidating the many existing literature references to 'LSST'.

stein field equations with a cosmological constant (Lovelock, 1971, 1972). In other words, to modify GR one must, at the very least, introduce new fields or dimensions. Nonetheless, a number of arguments for doing so spring to mind, the relative weightings of which are of course highly subjective. One compelling argument is the discomfiting existence of a mysterious dark sector, along with its theoretical and observational difficulties as enumerated above. All evidence for the dark sector is in some sense gravitational, so the idea that the existence of a dark sector is a result of a misunderstanding of gravity on astrophysical and cosmological scales is rather tempting and warrants investigation, especially if an alternative theory of gravity that obviates the need for the dark sector also explains some of the other ΛCDM tensions, such as the small scale issues or the Hubble tension.

A more basic argument is that generating predictions from alternative theories of gravity leads to novel ways to test GR. For example, § 1.3.5 lists a number of tests of screened gravity theories. These tests have been devised as a result of recent research into screening mechanisms, and search for signatures of plausible, weak-field deviations from GR that would not be captured in further PPN-style testing.

It is also relevant to consider the scales on which gravity has been tested. In terms of the curvature $\xi \sim GM/r^3c^2$, Baker *et al.* (2015)[52] identify a large 'desert' of unexplored regimes spanning the range $\xi \sim 10^{-30} - 10^{-50}$ m^{-2}, between the PPN and cosmological probes respectively. Considering instead the potential $\phi \sim GM/r$, no probes to date have directly tested the 'strong-field' regime, $\phi \sim c^2$. These concerns are particularly relevant today; the newly emerging fields of gravitational wave detection and black hole imaging will provide the first probes of the strong-field regime. Similarly, the curvature desert is uniquely probed by galaxy-scale tests of gravity. Upcoming galaxy surveys are unprecedented in their ambition, and will be able to place constraints on gravity within the curvature desert. For this reason, Baker *et al.* (2019) have launched the 'Novel Probes' project, aimed at connecting theorists with observers in order to devise galaxy-scale tests to probe this parameter regime.

Such galaxy-scale tests of screened modified gravity theories are the subject of this thesis, and screened modified gravity and its application at galaxy scales will be discussed further in § 1.3. First, however, the next section gives a brief, general introduction to the physics and astronomy of galaxies.

[52] More specifically, Baker *et al.* (2015) quantify the curvature using the Kretschmann scalar, which for the Schwarzchild metric is $\xi = \sqrt{48}GM/r^3c^2$.

1.2 Galaxies

1.2.1 Background

The previous section described how our conception of the cosmos was revolutionised several times in the 1920s, first following Hubble's confirmation of the extragalactic nature of the spiral nebulae, and second after his discovery of a relation between their distance and their recession speed, suggesting a cosmic expansion. Another effect of these discoveries was an effective division of astronomy into Galactic and extragalactic subfields.

The former science has progressed prodigiously in the twentieth century. Around the time of the Great Debate, the best empirical model of the Milky Way was that of Dutch astronomer Jacobus Kapteyn, first published along with his student Pieter van Rhijn (Kapteyn & van Rhijn, 1920). The model was constructed using measurements of proper motions, and posited an ellipsoidal mass distribution for the Milky Way, with a radius of twenty kiloparsecs in the Galactic plane. Tellingly, the model was heliocentric.[53] This is to be contrasted with the present day, where high-quality observations have led to a detailed understanding of the structure and composition of the Milky Way, e.g. Figure 1.13.

Extragalactic astronomy has also come along in leaps and bounds. Following the discovery of the Hubble expansion, the application of the spiral nebulae to cosmology remained a field of active research, as demonstrated by the collaboration between Hubble and Tolman (e.g., Hubble & Tolman, 1935). However, the classification, distribution, and formation of the new galaxies also became active research efforts which continue to this day. Figure 1.10 shows Hubble's widely cited map of around 4000 spiral nebulae observed at Mount Wilson (reproduced from Hubble, 1934), to be contrasted with Figure 1.11, depicting a fraction of the huge galaxy sample from SDSS-III BOSS (Alam *et al.*, 2017).

A more detailed overview regarding the current state of Galactic and extragalactic astronomy is given below. First, however, it is worth linking galaxies to the cosmological model described above by briefly describing how astrophysical structure forms in our Universe.

1.2.2 Cosmic Structure Formation

From Figure 1.11, it is clear that while the Universe might be homogeneous and isotropic on its largest scales ($\gtrsim$100 Mpc), the picture is much richer on smaller scales, where an intricate network of overdense nodes is connected by filaments and walls, interspersed with underdense voids. This structure is known as the 'cosmic web'. Its richness is seemingly in stark contrast to the simplicity of the CMB (Figure 1.3), but in actuality the statistical

[53] To give full credit to Kapteyn, the final version of his model, published two years later, shifted the Sun to a position around two kiloparsecs from the Galactic centre (Kapteyn, 1922).

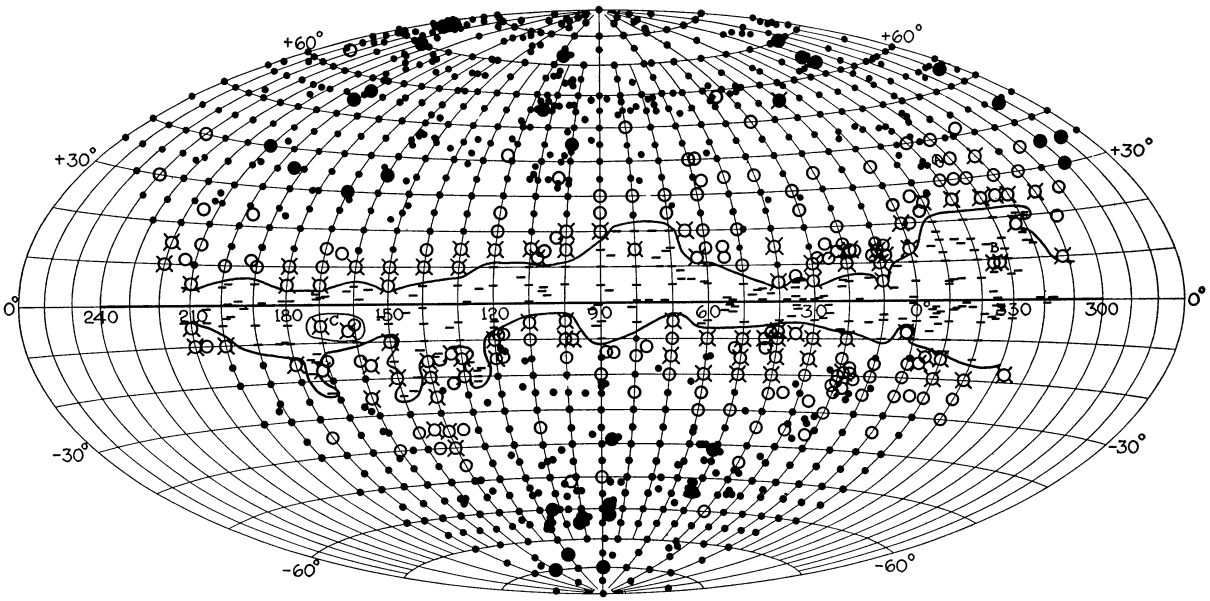

Figure 1.10: Hubble's 'distribution of extra-galactic nebulae.' All marks represent numbers of galaxies in a given patch of sky. Small dots represent a 'normal' number of galaxies ($1.63 < x < 2.22$, where $x \equiv \log_{10} N$), while filled circles represent 'excesses' ($2.22 < x < 2.52$) and unfilled circles represent 'deficiencies' ($1.33 < x < 1.63$). Crosses are superimposed on these circles for N beyond these ranges (i.e. $x > 2.52$ and $x < 1.33$). Dashes represent no galaxies. The central region bounded by the solid line is the Galactic zone of avoidance, in which dust obscuration prevented detection of any galaxies. The total galaxy sample depicted here comprises around 4000 galaxies. Reproduced from Hubble (1934).

properties of present-day large-scale structure can be very well explained by using linear perturbation theory to describe the temporal evolution of small primordial density fluctuations against a homogeneous background. The CMB gives us a snapshot of the very early Universe, before the fluctuations (visible in the CMB as temperature anisotropies) had undergone any significant growth or collapse under gravity.

The following is a largely qualitative account of this process. A more detailed perturbation theory calculation of structure formation can be found in many graduate-level cosmology textbooks, e.g. Dodelson (2003).

Linear perturbation theory holds in the 'linear' regime $\delta \ll 1$, where δ is the (matter) density contrast, defined as

$$\delta(\boldsymbol{x}) \equiv \frac{\rho_m(\boldsymbol{x}) - \bar{\rho}_m}{\bar{\rho}_m}. \tag{1.40}$$

The linear approximation breaks down when perturbations grow to the level of $\delta \sim 1$, at which point structures start to collapse under the gravitational instability.

A useful statistical object in studies of large-scale structure is the matter power spectrum, given by

$$(2\pi)^3 P(k)\delta_D(\boldsymbol{k}' - \boldsymbol{k}) \equiv \langle \delta(\boldsymbol{k})\delta^*(\boldsymbol{k}') \rangle, \tag{1.41}$$

where δ_D is the delta function and the Fourier component $\delta(\boldsymbol{k})$ is obtained via Fourier

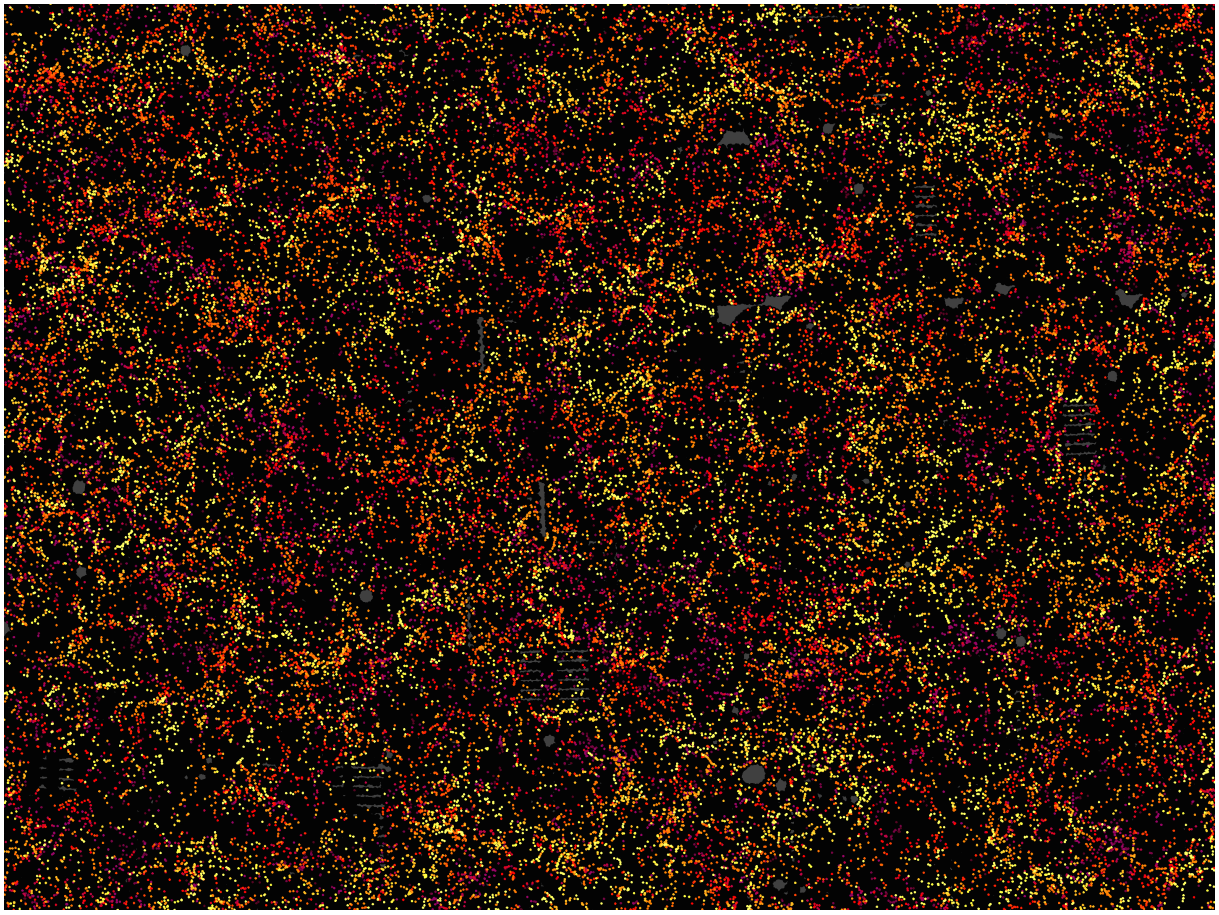

Figure 1.11: A small slice of the final galaxy sample of SDSS-III BOSS (Alam *et al.*, 2017). The total sample consisted of ∼1.2 million galaxies between redshifts 0.2 and 0.75 covering around one quarter of the sky, with accompanying spectroscopic information. Each dot in this image represents a galaxy and the colours indicate redshift (yellow is $z = 0.2$ and purple is $z = 0.75$). Grey patches indicate regions without survey data. The image represents roughly four percent of the survey sample (48,741 galaxies). Image credit: Daniel Eisenstein and the SDSS-III collaboration.

transform of the density contrast,

$$\delta(\boldsymbol{k}) = \frac{1}{V}\int \delta(\boldsymbol{x}) e^{i\boldsymbol{k}.\boldsymbol{x}} d^3\boldsymbol{x}. \tag{1.42}$$

Note that the power spectrum depends only on $k \equiv |\boldsymbol{k}|$, a reflection of the assumption of isotropy.

In the discussion of inflation in § 1.1.4, it was mentioned that a key prediction of inflationary theory was the form of the matter power spectrum at the end of the inflationary period. Given a power law spectrum, $P(k) \propto k^n$, $n = 1$ corresponds to a 'scale-invariant' spectrum, also known as a Harrison-Zeldovich spectrum (Harrison, 1970; Zeldovich, 1972). The prediction from inflation is that of a nearly scale-invariant spectrum, i.e. $n \approx 1$ (Bardeen *et al.*, 1983). This power spectrum of matter fluctuations can be taken as the effective 'initial conditions' for subsequent growth of structure.

Considering only pressureless dark matter, during the initial radiation-dominated era

perturbations on scales larger than the horizon $k \lesssim (c\,t)^{-1}$ grow while the growth of sub-horizon perturbations is suppressed. After radiation-matter equality, this suppression is ended and perturbations grow on all scales throughout the matter-dominated era.

For the baryons, the picture is somewhat more complicated. Prior to decoupling, the baryons were tightly coupled to the photons in the baryon-photon plasma. The Jeans length of such a fluid is very large, and any baryonic structure could not grow. After decoupling, however, the baryons were able to fall into the pre-existing gravitational wells of the dark matter.

Once the density perturbations become non-linear, they undergo a process of gravitational collapse, forming virialised haloes. With CDM, this happens at the smallest scales first. This process of virialisation is a rather violent one, with baryonic clumps repeatedly colliding and creating shocks that heat the gas. At the end of this process, the dark matter is in the form of an approximately spherical 'halo'. Meanwhile, the shock-heated gas—also ending in a roughly spherical distribution—finds hydrostatic equilibrium, i.e. it is supported by pressure against further gravitational collapse. If this gas can cool efficiently (e.g. via line radiation), it will collapse further into a dense, star-forming structure at the centre of the dark matter halo: a galaxy.

The largest, most massive (and thus latest-forming) haloes host the hottest gas; above a certain temperature (depending on metallicity, $\sim 10^7$ K), the gas can only cool inefficiently via bremmstrahlung radiation. For this reason, the most massive haloes in the Universe ($\gtrsim 10^{15}\ M_\odot$) do not host correspondingly enormous galaxies, but instead continue to carry large quantities of the shock-heated gas. These haloes also typically incorporate a number of 'subhaloes', smaller dark matter haloes that formed earlier in the same region of space, which *do* host galaxies. These galaxies occupy a negligible proportion of the overall mass budget of the parent halo, but are nonetheless the most visible component optically. For this reason, these largest of structures are known as galaxy clusters.

This process of virialisation and galaxy formation cannot be described using linear perturbation theory, but a number of analytic methods do exist, such as the spherical collapse model (Gunn & Gott, 1972) and the related Press-Schechter formalism (Press & Schechter, 1974). However, these do not capture the full complexities of the physics involved. To that end, an industry has developed in recent decades, aiming to understand the physics of galaxy formation via N-body computer simulations: astrophysical experiments *in silico* (see Figure 1.12). A major source of uncertainty in this field is the modelling of baryonic processes, such as magnetic fields, radiative hydrodynamics, and feedback from supernovae and active galactic nuclei (AGN; see § 1.2.3). Because of the finite resolution available to simulators, many of these processes are necessarily incorporated using sub-resolution implementations, models that aim to recreate the effects of the relevant physics in a coarse-grained manner. These can sometimes be rather crude, such as mechanical injections of energy. Nonetheless, galaxy formation simulations are nowadays able to create visually

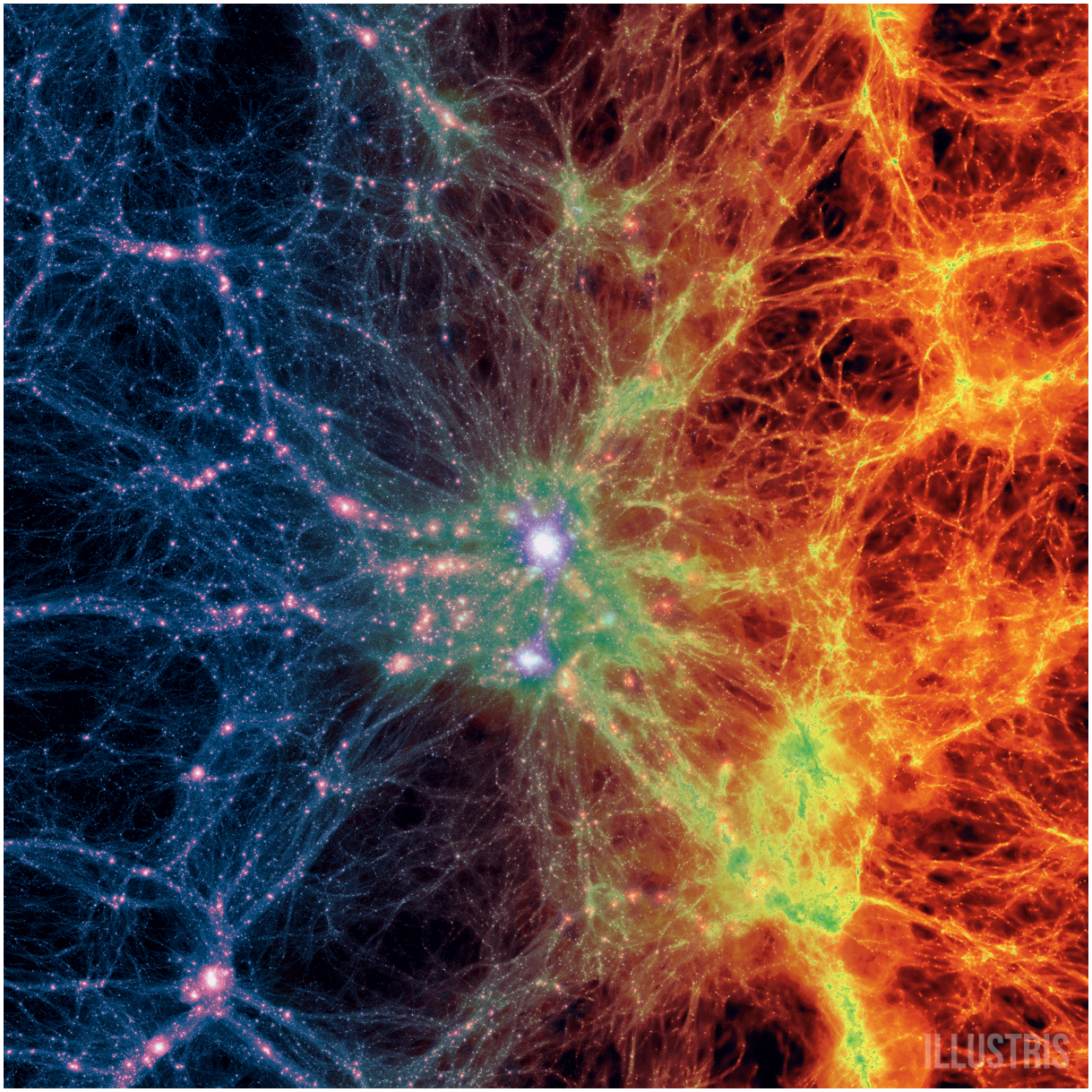

Figure 1.12: Image from the Illustris simulation (Genel *et al.*, 2014; Vogelsberger *et al.*, 2014a,b; Sijacki *et al.*, 2015), depicting a projection through the simulation volume at $z = 0$, centred on the most massive galaxy cluster. The projection box is sized 15Mpc/h to a side, and the depicted quantity transitions from dark matter density (left) to gas density (right). Image Credit: Illustris Collaboration.

realistic galaxies and reproduce a range of galaxy observables (e.g. Dubois *et al.*, 2014; Vogelsberger *et al.*, 2014b; Schaye *et al.*, 2015; Pillepich *et al.*, 2018), and the field can be said to have reached a stage of maturity (see, e.g., the review article by Vogelsberger *et al.*, 2020).

1.2.3 Galaxies in the Universe

Galaxies are a fantastically diverse class of astronomical object. On the one hand, there is the example of Messier 87 (M87; alternatively NGC 4486), mentioned earlier because of the recent direct imaging of the shadow of its central black hole. M87 is one of the largest

galaxies in the local Universe, several times more massive and more luminous than the Milky Way (Murphy *et al.*, 2011). At the other extreme, we could consider the example of Segue 1, a faint satellite galaxy of the Milky Way. It has a detected membership of fewer than 100 stars and a mass of $\sim 10^6\ M_\odot$, some six orders of magnitude smaller than that of the Milky Way (Simon *et al.*, 2011). In addition to these stark contrasts in mass and luminosity, M87 and Segue 1 also differ greatly in their physical size, morphology, composition, kinematics, formation history, and environment.

This large range of observed luminosities is encoded in the empirical Schechter luminosity function,

$$\Phi(L)dL = \Phi^* \left(\frac{L}{L^*}\right)^\alpha e^{-L/L^*} \frac{dL}{L^*}, \tag{1.43}$$

where $\Phi(L)dL$ gives the number density of galaxies in the luminosity range $[L, L+dL]$ (Schechter, 1976). The normalisation Φ^* is around 0.05 Mpc^{-3}, the faint-end slope $\alpha \approx -1$, and the characteristic luminosity L^* is typically quoted instead as an absolute magnitude, $M^* \sim -20$, comparable to that of the Milky Way (e.g. Cole *et al.*, 2001). The exact values of these parameters—and the goodness-of-fit of the functional form of Eq. (1.43)—vary depending on the redshift, the wavelength band of observation, and the characteristics (environments, morphologies, etc.) of the population under consideration. Nonetheless, the assumption of Eq. (1.43) as a universal luminosity function is certainly sufficient for illustrative purposes here.

The decreasing power-law form of Eq. (1.43) accords with our intuition of a hierarchical Universe, with many small, faint objects and comparably fewer massive, luminous ones. The reason for the exponential cutoff at the high-luminosity end is partly the inefficient cooling discussed in § 1.2.2, and partly AGN feedback (e.g. Croton *et al.*, 2006; also see below).

A classic system for classifying the morphologies of galaxies is that of Hubble (1926), still popular today albeit under altered and expanded forms, notably that of de Vaucouleurs *et al.* (1991). Under these schemes, the two main classes of galaxies are 'ellipticals' (E) and 'spirals' (S). Elliptical galaxies are rather featureless, smooth systems with contours of equal brightness (isophotes) that are elliptical in shape. A given elliptical galaxy is subclassified according to the eccentricity of its isophotes. The subcategories are En, with $n \in \{0,1,2,3,4,5,6,7\}$, corresponding to axis ratio $b/a = 1 - n/10$. In other words, an E0 galaxy is approximately spheroidal, while an E7 galaxy is rather elongated.[54] M87 is a classic example of an elliptical galaxy (classification E0; Sandage & Tammann, 1981).

Spiral galaxies, such as the spiral nebulae discussed at the start of this chapter, have prominent stellar discs exhibiting spiral arms of varying prominence. The spirals are sub-

[54] The axis ratio of a galaxy's isophotes typically varies with radius. In this case, the axis ratio used for categorisation is taken at the isophote containing half of the galaxy's total luminosity (Binney & Tremaine, 2008). Note also that this subcategorisation scheme neglects any triaxiality of elliptical galaxies, although in fact this is likely to be widespread.

classified into groups Sa, Sb, Sc, and Sd according to how tightly their spiral arms are wound around the centre of the galaxy, with Sa the most tightly wound. Intermediate cases between two subcategories are indicated by, e.g., Sab. Spiral galaxies also often have a central 'bulge', a concentrated system of stars at the centre of the galaxy, resembling a small elliptical galaxy. Sa-type galaxies have the most prominent bulges, while Sd-types typically have no detectable bulges. In addition, many spiral galaxies have prominent 'bar' features in their central regions. In the Hubble classification scheme, barred spirals are denoted SB, i.e. SBa, SBb etc.

As well as these visually distinguishing features, spirals and ellipticals also vary in their environments, compositions and kinematics. First, cluster galaxies are disproportionately ellipticals while void galaxies are disproportionately spirals (e.g. Bamford *et al.*, 2009). Elliptical galaxies have older stars and very little star-forming gas in their interstellar media, while the spiral arms of spiral galaxies are sites of present-day star-forming gas (e.g. Bell *et al.*, 2012). Finally, elliptical galaxies typically exhibit little rotation, while the discs of spiral galaxies are rotationally supported. Various galaxy surveys have sought to further understand the variation of such galactic properties with morphological type, such as the Calar Alto Legacy Integral Field Area (CALIFA; González Delgado *et al.*, 2015) and ATLAS^{3D} (Cappellari *et al.*, 2011, and subsequent publications).

The rotation speed of a spiral galaxy as a function of distance from the galactic centre is known as the 'rotation curve' of the galaxy. Assuming a circular orbit, the rotation speed of a test particle is given by

$$v_{\rm circ}^2 = R\frac{d\Phi}{dr} = \boldsymbol{a}\cdot\boldsymbol{R}, \tag{1.44}$$

where R is the cylindrical radial coordinate of the particle (the corresponding cylindrical radial vector is $\boldsymbol{R}$), Φ and $\boldsymbol{a}$ are respectively the potential and acceleration due to the galaxy. Eq. (1.44) can be used to connect the observed rotation curve of a galaxy to its potential and thence to its mass distribution. Examples of the connection between rotation curves and underlying mass distributions have already been exhibited in this Introduction. First, rotation curves played a pivotal role in the discovery of dark matter (see Figure 1.6 and accompanying discussion). Secondly, observations of rotation curves are among the key sources of evidence for cored central density profiles in dark matter haloes (see Figure 1.8 and accompanying discussion). Rotation curves will also be the central object of study in Chapters 2 and 3.

Recent photometric and spectroscopic galaxy surveys such as SDSS have led to an altogether new classification scheme, based on 'color-magnitude diagrams', i.e. plots of colour (e.g. $U-V$, where U and V are apparent magnitudes of a given galaxy in the U and V bands) versus absolute magnitude for populations of galaxies. Colour-magnitude diagrams show a clear bimodality in galaxies, with a 'blue cloud' and a tight 'red sequence'. The galaxies in the blue cloud are assumed to be sites of active star formation, with the excess blue radiation originating in young, hot stars. The red sequence galaxies, by con-

trast, are largely 'quenched', i.e. their star formation is suppressed. There is a strong correlation between this classification scheme and the Hubble scheme, with elliptical galaxies predominantly on the red sequence and spirals in the blue cloud (Kauffmann *et al.*, 2003; Baldry *et al.*, 2004; Hogg *et al.*, 2004).

In addition to stars and gas, galaxies also host starlight-absorbing cosmic dust (composed mainly of silicon, carbon, oxygen, and their compounds), and central black holes. The black holes are described as 'super-massive', as their masses fall in the range $10^6 - 10^9 M_\odot$. Accretion on to these black holes is believed to be the power source for extremely luminous cross-spectrum radiation observed in many galaxies. These bright sources are known as 'active galactic nuclei' (AGN), or in their most luminous manifestations, quasars.

As discussed in the description of structure formation above, galaxies are formed in dark matter haloes, in which they continue to reside. While these haloes cannot be observed directly, their presence and properties can be inferred through indirect means, such as kinematic tracers or gravitational lensing. Dark matter haloes are often taken to be spherical, and a canonical functional form assumed for the density profile is the simulation-derived Navarro-Frenk-White (NFW) profile,

$$\rho(r) = \frac{\rho_0}{\frac{r}{r_s}\left(1+\frac{r}{r_s}\right)^2}, \tag{1.45}$$

where ρ_0 and r_s are respectively the scale density and scale radius (Navarro *et al.*, 1996, 1997). The steep r^{-1} slope at small radii is the 'cuspy' profile that is possibly at odds with some observations (see the discussion of the core/cusp controversy in § 1.1.5). In terms of total mass, the dark matter halo is typically by far the dominant component of any galaxy. This is particularly true of dwarf galaxies, the very high mass-to-light ratios of which suggest they are very promising probes of dark matter (Mateo, 1998).

1.2.4 The Milky Way

Having detailed the properties of galaxies in the Universe, it is worth discussing how the Milky Way (Figure 1.13), fits within that context. We are in the midst of a revolution in understanding of the Milky Way, due primarily to the ESA mission Gaia, the ambitions and possibilities of which are discussed below. First, however, a brief sketch of established facts in Galactic astronomy at the dawn of the Gaia era, a much more detailed overview of which can be found in the review article of Bland-Hawthorn & Gerhard (2016).

The Galaxy is a barred spiral, classified SBbc. Along with Andromeda (M31), it is one of two large galaxies in the gravitationally bound Local Group, the remaining members of the group being mostly satellites. The MW and M31 are scheduled to collide in roughly six billion years (Cox & Loeb, 2008; van der Marel *et al.*, 2012). The Local Group itself is situated

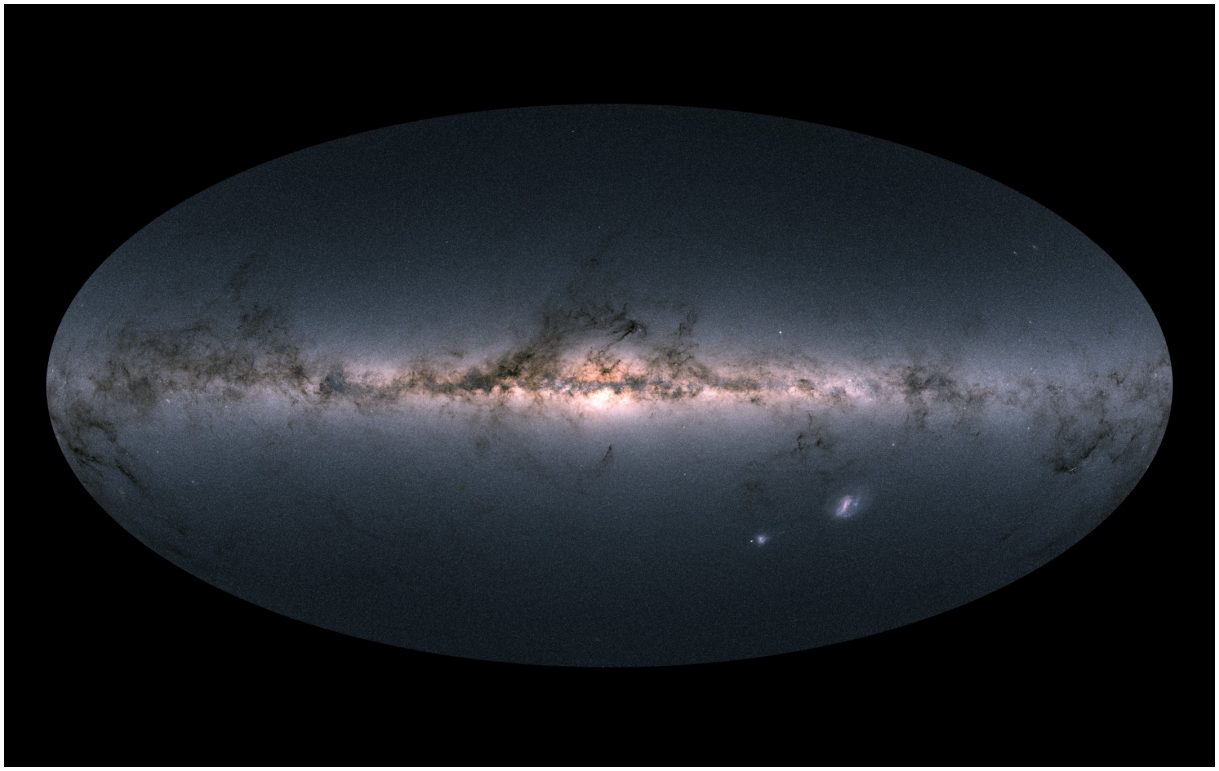

Figure 1.13: Gaia's all sky view of the Milky Way. Brightness indicates stellar density while hue indicates the photometric colour of the starlight. Image Credit: ESA/Gaia/DPAC.

in a low-density filament of the cosmic web, proximate to the Virgo supercluster, in turn a member of the larger Laniakea supercluster (Tully *et al.*, 2014).

In some ways, the MW is an atypical specimen given its type and environment. For instance, it is exceedingly rare for a galaxy of the MW's luminosity to have two infalling galaxies, both actively star forming (cf. the Magellanic Clouds; Robotham *et al.*, 2012). It is also the case that both the MW and M31 appear to inhabit the 'green valley', the relatively sparsely populated region of the colour magnitude diagram inhabited by galaxies making the transition from the blue cloud to the red sequence (Mutch *et al.*, 2011). As such, the MW is much redder and brighter than other galaxies of its morphological type (Licquia *et al.*, 2015). Finally, the mass of the Milky Way's central black hole (given below) is also unusually low (see, e.g., the compendium of central black hole masses of nearby galaxies collected by Tremaine *et al.*, 2002). These facts could be related to another MW anomaly: its unusually quiescent merger history (e.g. Stewart *et al.*, 2008; Deason *et al.*, 2013; Ruchti *et al.*, 2015). On the other hand, various aspects of the MW are perfectly normal, such as its cold gas fraction, stellar mass, and its position on the Tully-Fisher relation (the empirical relation between maximal rotation speed and luminosity; de Rossi *et al.*, 2009; Bland-Hawthorn & Gerhard, 2016).

The MW hosts $\sim 10^{11}$ stars, most of which—including the Sun—inhabit its disc (visible as the central band in Figure 1.13). Upon closer inspection, the disc is found to be composed of two subpopulations of stars: a 'thick disc' and a 'thin disc', distinct in their chemistries,

ages, and vertical extents (Gilmore & Reid, 1983). Radially, both discs have exponentially decaying density profiles, with scale radii of ∼2 kpc (Bland-Hawthorn & Gerhard, 2016). Using SDSS star counts, Jurić *et al.* (2008) find that the Sun lies close to the disc midplane, offset by 25 ± 5 pc.

There are a number of methods of measuring the distance of the Sun from the galactic centre (the 'solar radius', R_0), such as direct measurements of the parallaxes or proper motions of objects near the Galactic centre (e.g. Reid *et al.*, 2009a,b), or indirect measurements estimating the position of the centroid of stars in the Galactic bulge (e.g. Majaess, 2010). Bland-Hawthorn & Gerhard (2016) collect 26 independent measurements of R_0 employing a range of such techniques, and find a carefully weighted consensus value of $R_0 = 8.2 \pm 0.1$ kpc, noting that this is markedly below the International Astronomical Union standard of 8.5 kpc (Kerr & Lynden-Bell, 1986). Such Galactic centre astrometry can also lead to precise measurements of the angular rotation speed of the Sun (e.g. Reid *et al.*, 2009b). Coupled with a value for R_0, this gives a value for the velocity component of the Sun tangential to the Galactic rotation, 248 ± 3 km/s. The Local Standard of Rest (LSR) is the name given to the instantaneous inertial frame centred at the Sun and moving at speed $v_0 \equiv v_{\rm circ}(R_0)$ in the direction tangential to the Galactic rotation, where $v_{\rm circ}$ is the circular velocity given by Eq. (1.44). Stellar orbits are not perfectly circular, and stars in the solar neighbourhood (including the Sun) have small peculiar velocities in the LSR frame, so v_0 need not equal the solar speed stated above (see, e.g., the discussion in Schönrich *et al.*, 2010). In particular, the Sun has peculiar velocity $(U, V, W) \approx (10, 11, 7)$ km/s,[55] leaving $v_0 = 238 \pm 15$ km/s (Bland-Hawthorn & Gerhard, 2016).

The inner Galaxy contains a long bar (Hammersley *et al.*, 1994, 2000), a 'box/peanut'-shaped bulge (McWilliam & Zoccali, 2010; Nataf *et al.*, 2010; Wegg & Gerhard, 2013); likely to be simply an edge-on view of the central part of the bar (Athanassoula, 2005), a nuclear star cluster (Becklin & Neugebauer, 1968), and a super-massive black hole believed to be associated with the radio source Sgr A*, taken to be the Galactic centre (see Reid, 2009, for a review of evidence for the central black hole). The mass of the black hole can be inferred from the orbits of stars within the nuclear star cluster. According to Gillessen *et al.* (2017), $M_\bullet = 4.28 \pm 0.23 \times 10^6\ M_\odot$. The Event Horizon Telescope is expected to produce a direct image of the black hole shadow in Sgr A*, a local counterpart to their widely publicised image from M87 (Figure 1.9; Event Horizon Telescope Collaboration, 2019).

As predicted by the theory of structure formation sketched above, the Milky Way is ensconced in a dark matter halo, the presence of which is indicated by the kinematics of stars and stellar systems in the outer parts of the Galaxy. For the mass and size of the halo, Bland-Hawthorn & Gerhard (2016) calculate a weighted mean of measurements from a

[55] The Galactic (U, V, W) coordinates are defined such that the positive values here for all three components respectively indicate that the Sun is moving toward the Galactic centre, faster than the local rotation speed, and toward the north Galactic pole. Because the Sun is already north of the Galactic disc midplane, the last point means the Sun is currently receding farther from the midplane.

number of stellar kinematic studies in the literature and arrive at a virial mass of $M_{\rm vir} = 1.3 \pm 0.3 \times 10^{12}\ M_\odot$ and a virial radius of 282 ± 30 kpc. This value for the virial mass is consistent with more recent measurements, including those based on Gaia data (see below; Callingham *et al.*, 2019; Posti & Helmi, 2019; Watkins *et al.*, 2019).

Another component of the galaxy worth mentioning is the stellar halo, the site of many stellar streams and substructures. These are the wreckage of dwarf galaxies and globular clusters that have fallen into and are being torn apart by the Milky Way's tidal field. In the past, such substructures have usually been identified as over-densities of resolved stars, as in the 'Field of Streams' image (Belokurov *et al.*, 2006). There, using multi-band SDSS photometry, the stellar halo of the Milky Way was revealed as being composed of criss-crossing stellar streams, the detritus of satellite galaxies. However, streams and substructure remain kinematically cold and so identifiable in phase space long after they have ceased to be recognisable in star counts against the stellar background of the Galaxy (Johnston, 1998). The debris persists for a large fraction of a Hubble time,[56] sometimes longer, so substructures in phase space remain to the present day. Searches in phase space for streams are much more powerful than searches in configuration space.

Just as Baker *et al.* (2019) argued that we have entered a second golden age of GR, it is undoubtedly also the case we have entered a new golden age of observing and understanding the Milky Way. In the past two decades, a variety of photometric and spectroscopic surveys such as RAVE (RAdial Velocity Experiment; Steinmetz *et al.*, 2006), VVV (VISTA Variables in the Via Lactea; Minniti *et al.*, 2010), SEGUE (Sloan Extension for Galactic Understanding and Exploration; Yanny *et al.*, 2009), and APOGEE (Apache Point Observatory Galactic Evolution Experiment; Allende Prieto *et al.*, 2008) have led to significant progress in the field. However, the pivotal development has been the launch and early data releases of the Gaia mission (Figure 1.13; Gaia Collaboration, 2016, 2018). The Gaia satellite (sometimes touted as the 'billion star surveyor') is a scanning satellite of the European Space Agency that is monitoring all objects brighter than magnitude $G \approx 20$ around 70 times over a period of 5 years (though the mission lifetime has recently been extended). Its telescopes are providing magnitudes, parallaxes, proper motions and broad band colours for over a billion stars in the Galaxy (≈ 1 per cent of the Milky Way stellar population) within the Gaia-sphere – or within roughly 20 kpc of the Sun for main sequence stars, 100 kpc for giants.

In constructing this 3D map of an appreciable part of the Milky Way, a key science goal of Gaia is to facilitate a greater understanding of the gravitational potential and underlying matter distribution of the Galaxy. As alluded to above, several recent works have already begun explorations in this direction, inferring the properties of the MW dark matter halo using Gaia data (e.g. Wegg *et al.*, 2019; Posti & Helmi, 2019; Watkins *et al.*, 2019).

Detailed phase space information from Gaia has also led to the discovery of abundant streams and substructures (Myeong *et al.*, 2018; Malhan *et al.*, 2018; Meingast *et al.*, 2019;

[56] The Hubble timescale $t_{\rm Hubble} \equiv 1/H_0 \approx 14$ Gyr is a first order approximation for the age of the Universe.

Koposov *et al.*, 2019). Streams discovered by Gaia are already being followed up spectroscopically to give six-dimensional (6D) phase space data (Li *et al.*, 2019b). Bright tracers such as blue horizontal branch stars or RR Lyraes can be seen out to distances of 250 kpc, assuming Gaia's limiting magnitude of $G \sim 20.5$. Stars near the tip of the red giant branch can be seen even further out to at least 600 kpc. In future, this should enable Gaia to provide astrometry for very distant streams, perhaps near the very edge of the Milky Way's dark halo.

If a stream were a simple orbit, then the positions and velocities of stars would permit the acceleration and force field to be derived directly from the 6D data. Streams are more complex than orbits (Sanders & Binney, 2013; Bowden *et al.*, 2015), but the principle remains the same – their evolution constrains the matter distribution and theory of gravity.

1.3 Screened Modified Gravity

1.3.1 Scalar Tensor Theories

Let us now consider the consequences of introducing a scalar field ϕ to the gravitational sector. In the Einstein frame, the action for a general scalar-tensor theory is given by

$$S_\phi = \frac{c^3}{8\pi G}\int d^4x\sqrt{-g}\left[\frac{1}{2}R - \frac{1}{2}\nabla_\mu\phi\nabla^\mu\phi - V(\phi)\right] + S_m[\tilde{g}_{\mu\nu}, \psi_i]. \tag{1.46}$$

Note that matter does not move on geodesics of the Einstein frame metric $g_{\mu\nu}$, but of the Jordan frame metric $\tilde{g}_{\mu\nu}$. The two metrics are related via

$$\tilde{g}_{\mu\nu} = A^2(\phi)\, g_{\mu\nu}, \tag{1.47}$$

where $A^2(\phi)$ is some coupling function. As a result of its presence in the matter action, the matter energy-momentum tensor $T_{\mu\nu}$ is no longer covariantly conserved. One instead finds

$$\nabla_\mu T^{\mu\nu} = \frac{d\ln A(\phi)}{d\phi} T\nabla^\nu\phi, \tag{1.48}$$

where T is the trace of $T^{\mu\nu}$. Taking the Newtonian limit of (1.48), one finds an altered Newtonian force law

$$\ddot{\boldsymbol{x}} + \boldsymbol{\nabla}\Phi_{\rm N} = -\beta(\phi)c^2\boldsymbol{\nabla}\phi, \tag{1.49}$$

where the coupling β is defined by

$$\beta(\phi) \equiv \frac{d\ln A(\phi)}{d\phi}. \tag{1.50}$$

The novel term on the right-hand side of (1.49) is the 'fifth force', i.e. the weak-field modification to gravity that is the subject of study in the remainder of this thesis.

Extremising the action (1.46) with respect to the scalar field, and assuming an energy-momentum tensor for ideal, non-relativistic matter, one derives the equation of motion for the scalar field,

$$\Box\phi = \frac{dV(\phi)}{d\phi} + \frac{8\pi G\rho}{c^2}\beta(\phi), \tag{1.51}$$

where ρ is the local non-relativistic matter density. As a consequence of the second term on the right-hand side of (1.51), the dynamics of the scalar field are not governed by $V(\phi)$ alone, but are also affected by the local matter environment, via ρ. Indeed, one can recast (1.51) as

$$\Box\phi = \frac{dV_{\rm eff}(\phi)}{d\phi}, \tag{1.52}$$

which introduces an effective potential, defined as

$$V_{\rm eff}(\phi) \equiv V(\phi) + \frac{8\pi G\rho}{c^2}\ln A(\phi). \tag{1.53}$$

The dynamics of ϕ are governed by this effective potential, which (via ρ) encodes information about the local environment.

1.3.2 Screening Mechanisms

At this stage, it may not be obvious how the fifth force introduced in Eq. (1.49) could pass unnoticed in laboratory and Solar System tests. For this, there exist 'screening mechanisms', i.e. mechanisms that suppress the fifth force in dense environments like those of our solar system, but (for interesting, testable theories) unleash it in other environments.

The focus of this thesis is essentially the phenomenology of screening. Chapters 2 and 3 consider the imprint of screening radii (discussed below) on galaxy rotation curves, while Chapter 4 studies the manner in which EP violations arising from screening (also discussed below) would impact the formation of stellar streams around the Milky Way.

One screening mechanism is the 'symmetron' mechanism, named for its Higgs-like effective potential. In this mechanism, the coupling β vanishes when $\phi = 0$, which is the minimum of the effective potential at high densities. The fifth force is therefore suppressed in these environments. Below a critical density however, the potential minimum becomes non-zero, and the fifth force is unleashed.

Another screening mechanism is the 'chameleon' mechanism. Here, $V(\phi)$ and $A(\phi)$ are chosen such that the walls of the effective potential well are very steep in high density regions. The mass of the scalar becomes very large in these regions, and the fifth force is exponentially suppressed as a result. The bulk of this thesis is framed in terms of chameleon theories, but it should be noted that many of the predicted observable signatures would also arise under other screening mechanisms.

The Chameleon: An Example

Let us consider a simple example of a chameleon theory,

$$V(\phi)=\frac{V_0}{\phi};\quad A(\phi)=e^{\beta\phi}, \tag{1.54}$$

where V_0 is a constant, setting the energy scale of the scalar field. Note that the coupling β is also assumed constant, and is equivalent to $\beta(\phi)$ as given by Eq. (1.50). According to Eq. (1.53), the effective potential for this theory is

$$V_{\rm eff}(\phi)=\frac{V_0}{\phi}+\frac{8\pi G\rho}{c^2}\beta\phi. \tag{1.55}$$

The minimum of this effective potential is easily calculable, as is the Compton wavelength of the scalar,

$$\lambda_C\equiv V''_{\rm eff}(\phi_{\rm min})^{-\frac{1}{2}}=\frac{1}{\sqrt{2}}V_0^{\frac{1}{4}}\left(\frac{c^2}{8\pi G\rho\beta}\right)^{\frac{3}{4}}. \tag{1.56}$$

Thus, the wavelength is a decreasing function of ambient density. The Compton wavelength sets the range of the fifth force, so an extremely small wavelength would correspond to an undetectable fifth force. Because many orders of magnitude separate cosmological densities from those found within our Solar System, it is possible to construct a theory wherein λ is undetectably small in a laboratory or space experiment, but relevant elsewhere. This is the power of the chameleon mechanism.

Screened Fifth Forces

To understand screened fifth forces further, let us consider the different ways in which a static, uniform, spherical object (density $\rho=\bar{\rho}+\delta\rho$, mass M, radius R) embedded within a static, uniform background (density $\bar{\rho}$) can source a fifth force. In and around the object, the scalar field equation of motion (1.51) becomes

$$\frac{1}{r^2}\frac{d}{dr}\left(r^2\frac{d\phi}{dr}\right)=\frac{dV(\phi)}{d\phi}+\frac{8\pi G\rho\beta(\phi)}{c^2}. \tag{1.57}$$

If the object is large and dense enough, the scalar field will minimise its effective potential nearly everywhere within the object, i.e., $\phi=\phi_{\rm min}(\bar{\rho}+\delta\rho)$. The field gradients consequently vanish, which in turn kills the fifth force, according to Eq. (1.49). Such an object can be said to be 'screened'. There will be a thin shell at the surface of the object where the scalar field changes from $\phi_{\rm min}(\bar{\rho}+\delta\rho)$ to $\bar{\phi}\equiv\phi_{\rm min}(\bar{\rho})$.

Conversely, one can instead imagine a smaller, less dense body, within which the scalar field is unable to minimise its effective potential. Instead, the scalar field can be written as a linear perturbation against the background: $\phi=\bar{\phi}+\delta\phi$. Then, subtracting background terms from Eq. (1.57) yields

$$\frac{1}{r^2}\frac{d}{dr}\left(r^2\frac{d\delta\phi}{dr}\right)=\frac{1}{\bar{\lambda}_C^2}\delta\phi+\frac{8\pi G\beta(\bar{\phi})}{c^2}\delta\rho+\frac{8\pi G\beta'(\bar{\phi})\bar{\rho}}{c^2}\delta\phi, \tag{1.58}$$

where $\bar{\lambda}_C$ is the Compton wavelength (1.56) evaluated at the background ($\rho = \bar{\rho}$), and quadratic terms have been discarded. Inside the object, the first term on the right-hand side can be discarded because any cosmologically relevant theory will have $R/\bar{\lambda}_C \ll 1$, where R is the characteristic size of the region of interest, taken to be much smaller than cosmological scales. The third term on the right-hand side can also be discarded because we require that $\beta'(\bar{\phi})\delta\phi \ll \beta(\bar{\phi})$, i.e. $\beta(\phi)$ should depend only weakly on ϕ. This ensures, via Eq. (1.50), that $A(\phi)$ is close to unity, which in turn ensures that a small metric perturbation in the Einstein frame is also small in the Jordan frame (cf. Eq. 1.47). One can then integrate to find the gradient of the scalar field

$$\frac{d\delta\phi}{dr} = \frac{2\beta(\bar{\phi})}{c^2}\frac{GM(r)}{r^2}; \quad r \leq R, \tag{1.59}$$

where $M(r)$ is the mass enclosed within radius r. Outside the object, however, $\delta\rho$ vanishes so that the $1/\bar{\lambda}_C^2$ term in Eq. (1.58) can no longer be disregarded. The equation is then a screened Poisson equation, with solution

$$\frac{d\delta\phi}{dr} = \frac{2\beta(\bar{\phi})}{c^2}\frac{GM}{r^2}e^{-(r-R)/\bar{\lambda}_C}; \quad r > R, \tag{1.60}$$

where Eq. (1.59) evaluated at $r = R$ has been used as a boundary condition, as has the requirement that $\delta\phi \to 0$ as $r \to \infty$.

Equations (1.59) and (1.60), taken together with Eq. (1.49), give an expression for the acceleration due to the fifth force,

$$a_5 = \begin{cases} -2\beta(\bar{\phi})^2\dfrac{GM(r)}{r^2}; & r \leq R. \\ -2\beta(\bar{\phi})^2\dfrac{GM}{r^2}e^{-(r-R)/\bar{\lambda}_C}; & r > R. \end{cases} \tag{1.61}$$

The minus signs indicate that the fifth force is attractive, i.e. it acts to augment standard gravity. An unscreened object thus exerts a fifth force equal to its standard gravitational attraction multiplied by a coupling strength, and exponentially suppressed at distances larger than the Compton wavelength of the scalar field.

We now have a picture of two extremes: screened objects which exert no fifth force, and unscreened objects which enhance their standard gravity by a multiplicative $\mathcal{O}(1)$ factor. However, there is an intermediate regime: partial screening. One can imagine an object in which a central region is screened, but there is an extended region outside of this in which scalar field gradients are non-vanishing. The radius of this central region is known as the 'screening radius', $r_{\rm scr}$, and is essentially the radius within which the linear approximations made in Eq. (1.58) break down.

One can derive an expression for the fifth force exerted by a partially screened object following the same procedure as above, now taking $r_{\rm scr}$ as the lower limit of the integral

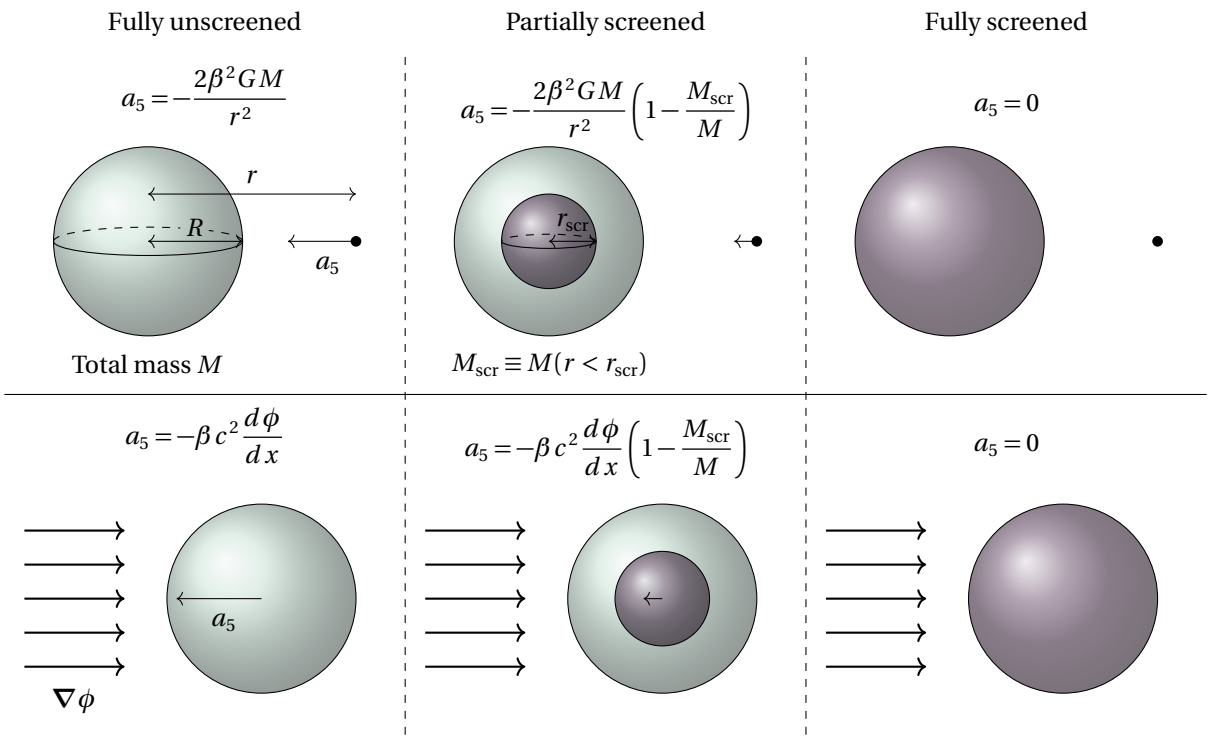

Figure 1.14: The top row shows the acceleration due to the fifth force (1.62) on a test particle (black circle) at distance r from a large spherical body (mass M, radius R) for a variety of screening regimes: unscreened *(left)*, partially screened *(middle)*, or fully screened *(right)*. Note that $\beta \equiv \beta(\bar{\phi})$ is taken as a constant, and it is assumed that $r \ll \lambda_C$, so the exponential factor in Eq. (1.62) can be disregarded. The bottom row instead considers acceleration due to the fifth force (1.64) on the spherical body itself, now situated in an externally sourced field gradient (indicated by the arrows), for the same screening regimes. Note that in both rows, the statement that $a_5 = 0$ in the screened case is in reality an approximation, because the fifth force is sourced and experienced by a thin shell at the surface of the sphere, in which ϕ traverses from its value inside the sphere to its background value.

rather than $r = 0$. This leads to

$$a_5 = \begin{cases} 0; & r \le r_{\rm scr}. \\ -2\beta(\bar{\phi})^2 \dfrac{GM(r)}{r^2}\left(1-\dfrac{M(r_{\rm scr})}{M(r)}\right); & r_{\rm scr} < r < R. \\ -2\beta(\bar{\phi})^2 \dfrac{GM}{r^2}\left(1-\dfrac{M(r_{\rm scr})}{M}\right) e^{-(r-R)/\bar{\lambda}_C}; & r > R. \end{cases} \tag{1.62}$$

Thus, outside the screening radius, the fifth force on a test particle is sourced only by the mass enclosed in the shell between the test particle and the screening radius. The upper row of Figure 1.14 shows a visualisation of the fifth force on a test particle—Eq. (1.62)—for a variety of screening regimes, from screened $r_{\rm scr} = R$ to unscreened $r_{\rm scr} = 0$.

An implicit expression for the screening radius can be derived by integrating $\mathrm{d}\delta\phi/\mathrm{d}r$ again, noting that $\delta\phi \to 0$ as $r \to \infty$. This leads to

$$\frac{\bar{\phi}}{2\beta(\bar{\phi})} = \frac{4\pi G}{c^2}\int_{r_{\rm scr}}^{\infty} \delta\rho(r) r\, dr, \tag{1.63}$$

assuming $\bar{\phi} \gg \phi(r_{\rm scr})$.

Note that the right hand side of this equation is equivalent to the absolute value of the Newtonian potential of all mass outside the screening radius, divided by c^2. If the potential well of a given object is insufficiently deep, then no $r_{\rm scr}$ will satisfy the equality, and the object is unscreened. For any given theory, $\bar{\phi}$ and $\beta(\bar{\phi})$ will typically be input parameters, so the left-hand side of Eq. (1.63) is often written as χ_0, the 'self-screening parameter'. One can then gauge whether an isolated object will be screened in a given theory by comparing the potential depth of the object $|\Phi_{\rm N}|/c^2$ with χ_0. If $|\Phi_{\rm N}|/c^2 < \chi_0$ the object will be unscreened, otherwise it will be partially or fully screened. For instance, a MW-like galaxy has $|\Phi_{\rm N}|/c^2 \sim 10^{-6}$, so will be screened for theories with $\chi_0 \lesssim 10^{-6}$.

As will be demonstrated in Chapters 2 and 3, the situation is more complicated than this for non-spherical or non-isolated objects. 'Environmental screening' is an effect whereby objects that would be unscreened in isolation might be screened if they are in the presence (i.e., within a Compton wavelength) of a larger, screened object.

Equivalence Principle Violation

In the above discussion, we derived an expression (1.62) for the fifth force on a test particle due to an extended object. However, it is also interesting to consider how an extended object responds to an external fifth force.

By integrating the momentum flux on the surface of a sphere around an object (position $\boldsymbol{x}$, mass M, radius R, screening radius $r_{\rm scr}$) embedded in external Newtonian potential $\Phi_{\rm N}$ and scalar field ϕ, Hui *et al.* (2009) derive an expression for the acceleration of the object,[57]

$$\ddot{\boldsymbol{x}} + \boldsymbol{\nabla}\Phi_{\rm N} = -Q\beta(\bar{\phi})c^2\boldsymbol{\nabla}\phi. \tag{1.64}$$

The right-hand side is the acceleration due to the fifth force. Comparing with Eq. (1.49), the only difference is the appearance of the 'dimensionless scalar charge' Q, defined by

$$Q \equiv \left(1 - \frac{M(r_{\rm scr})}{M}\right). \tag{1.65}$$

The effect of Q is to suppress the fifth force acting on an extended object if the object is at all screened. If the object is fully screened $r_{\rm scr} = R$, then $Q = 0$ and the fifth force acting on the object vanishes. Conversely, if the object is fully unscreened $r_{\rm scr} = 0$, then the object falls at the same rate as an unscreened test particle. A visualisation of this is given in the lower row of Figure 1.14.

Because objects of differing compositions (and thus screening levels) fall differently in the same external field, the equivalence principle (EP) is violated. It is interesting to note

[57] The notation of Hui *et al.* (2009) differs somewhat from the notation here: their 'α' is here β, their 'ϵ' is here Q, and their 'Q' is here $Q\beta M$, with M being the total mass of the object.

that this EP-violation is not 'encoded' into the theory at the action level. Indeed, it can be seen in the action (1.46) that all matter species are equivalent in their minimal coupling to the Jordan-frame metric $A^2(\phi)g_{\mu\nu}$. Instead, the EP-violation emerges at a 'higher' level, as a consequence of differences in screening.

1.3.3 $f(R)$ Gravity

Chapters 2 and 3 focus in particular on one species of chameleon theory: Hu-Sawicki $f(R)$ gravity (Hu & Sawicki, 2007). This section covers all of the relevant formalism of that theory.

$f(R)$ Action

First studied by Buchdahl (1970), $f(R)$ theories replace the Ricci scalar R in the Einstein-Hilbert action (1.12) with a generalised $R+f(R)$, allowing for the possibility of higher-order curvature terms.[58] The action is then given by

$$S_{f(R)} = \frac{c^3}{8\pi G}\int d^4x\sqrt{-g}\frac{1}{2}\big[R+f(R)\big]+S_m[g_{\mu\nu},\psi_i]. \tag{1.66}$$

Note that the theory reduces to ΛCDM, i.e. Eq. (1.15), if $f(R)=-2\Lambda$. Extremising the action with respect to the metric gives a set of modified Einstein field equations

$$G_{\mu\nu}+f_R R_{\mu\nu}-\frac{1}{2}f(R)g_{\mu\nu}+g_{\mu\nu}\nabla^\alpha\nabla_\alpha f_R-\nabla_\mu\nabla_\nu f_R=\frac{8\pi G}{c^4}T_{\mu\nu}, \tag{1.67}$$

where $f_R\equiv \mathrm{d}f(R)/\mathrm{d}R$. Taking the trace of these field equations leads to

$$3\Box f_R - R + f_R R - 2f(R) = -\frac{8\pi G\rho}{c^2}, \tag{1.68}$$

adopting the energy-momentum tensor for non-relativistic matter (i.e., $T^{\alpha\beta}=\rho\,u^\alpha u^\beta$).

Equation (1.68) can be interpreted as an equation of motion for the quantity f_R, which plays the role of the scalar field in this theory. Taking the Newtonian limit, one can simplify the equation of motion and also derive a modified Poisson equation

$$\nabla^2 f_R = \frac{1}{3}\left(\delta R-\frac{8\pi G}{c^2}\delta\rho\right), \tag{1.69}$$

$$\nabla^2\Phi = \frac{16\pi G}{3}\delta\rho-\frac{c^2}{6}\delta R, \tag{1.70}$$

[58] There is some variation in the literature regarding the definition of $f(R)$. In some places, the convention adopted is $R\to R+f(R)$, while elsewhere one finds $R\to f(R)$. In this thesis, the former convention has been adopted in order to remain consistent with Puchwein *et al.* (2013) and the internal workings of MG-Gadget, the $f(R)$ simulation code used in Chapter 2.

where δ signifies a perturbation of a quantity from its background value. Implicit in the derivations of these equations is the assumption $|f_R| \ll 1$ and the quasistatic approximation $|\nabla f_R| \gg \frac{\partial f_R}{\partial t}$. The validity of this approximation is discussed in Sawicki & Bellini (2015).

To illustrate some of the physics encapsulated in the above equations, let us assume that we have chosen a functional form of $f(R)$ that exhibits the chameleon mechanism, and consider two regimes. In a screened region, the scalar field would minimise its effective potential everywhere, leaving Eq. (1.69) unsourced, implying $\delta R = 8\pi G \delta\rho$. Substituting this into Eq. (1.70), one recovers the classical Poisson equation

$$\nabla^2\Phi = 4\pi G\delta\rho. \tag{1.71}$$

Conversely, far away from any overdensities, $\delta R \to 0$. Substituting this into Eq. (1.70), one recovers an enhanced Poisson equation

$$\nabla^2\Phi = 4\pi G_{\rm eff}\delta\rho, \tag{1.72}$$

with $G_{\rm eff} = \frac{4}{3}G$. Thus, in $f(R)$ gravity, the unscreened fifth force has a strength 1/3 that of standard gravity, or equivalently $\beta = \sqrt{1/6}$.

$f(R)$ Gravity as a Canonical Scalar-Tensor Theory

Let us connect the $f(R)$ formalism above with the discussion of scalar-tensor theories of gravity in previous sections, by transforming the $f(R)$ action (1.66) into a form equivalent to Eq. (1.46).[59] One can start by defining the scalar field ϕ via

$$f_R \equiv f'(R) = e^{-\frac{2}{\sqrt{6}}\phi} - 1, \tag{1.73}$$

and rescaling the metric

$$\tilde{g}_{\mu\nu} = e^{-\frac{2}{\sqrt{6}}\phi} g_{\mu\nu}. \tag{1.74}$$

The action (1.66) can then be rewritten as

$$S = \frac{c^3}{8\pi G}\int d^4x\sqrt{-\tilde{g}}\left[\frac{1}{2}\tilde{R} - \frac{1}{2}\nabla_\mu\phi\nabla^\mu\phi - V(\phi)\right] + S_m[A^2(\phi)\tilde{g}_{\mu\nu}, \psi_i], \tag{1.75}$$

where

$$A(\phi) = e^{\frac{\phi}{\sqrt{6}}}; \qquad V(\phi) = \frac{Rf_R - f(R)}{2f_R}. \tag{1.76}$$

The form of the action is now equivalent to the canonical scalar-tensor action (1.46). As discussed in the introduction of screening mechanisms (§ 1.3.2), the theory can exhibit chameleon screening if $A(\phi)$ and $V(\phi)$ are chosen such that ϕ gradients are strongly suppressed in regions of high density. In the present context, this is achieved by choosing an appropriate functional form for $f(R)$.

[59] The derivation here follows Brax *et al.* (2008).

Using equations (1.73) and (1.76), one can find an expression for the force law (1.49) now in terms of f_R instead of ϕ,

$$\ddot{\boldsymbol{x}} + \boldsymbol{\nabla}\Phi_{\rm N} = \frac{1}{2}c^2\boldsymbol{\nabla} f_R. \tag{1.77}$$

As before, the fifth force contribution is directly related to gradients in the scalar field f_R.

Hu-Sawicki Model

A widely studied $f(R)$ model known to exhibit chameleon screening is that of Hu & Sawicki (2007, henceforth HS),

$$f(R) = -m^2\frac{c_1\left(\frac{R}{m^2}\right)^n}{1+c_2\left(\frac{R}{m^2}\right)^n}, \tag{1.78}$$

where $m^2 \equiv H_0^2\Omega_m/c^2$. The remainder of this thesis assumes $n=1$, leaving two free parameters: c_1 and c_2. The model can recover an expansion history close to ΛCDM if $c_2R/m^2 \gg 1$, so that

$$f(R) \approx -m^2\frac{c_1}{c_2}\left[1+\mathcal{O}\left(\frac{m^2}{c_2R}\right)\right]. \tag{1.79}$$

Then, one recovers ΛCDM to first order, i.e. $f(R)\approx -2\Lambda$, if

$$\frac{c_1}{c_2} = 6\frac{\Omega_\Lambda}{\Omega_m}. \tag{1.80}$$

With this, we are left with a free choice of just one parameter: either c_1 or c_2.

Differentiating Eq. (1.78), the scalar field f_R is given by

$$f_R = -\frac{c_1}{\left(\frac{c_2R}{m^2}+1\right)^2} \approx -\frac{c_1}{c_2^2}\left(\frac{m^2}{R}\right)^2. \tag{1.81}$$

Using the FLRW metric (1.20), one can get an expression for the background curvature as function of scale factor a,

$$\bar{R}(a) = 3\frac{m^2}{a^3}\left(1+4\frac{\Omega_\Lambda a^3}{\Omega_m}\right). \tag{1.82}$$

Combining equations (1.82) and (1.81), one can derive expressions for the background scalar field $\bar{f}_R$, and the curvature perturbation $\delta R \equiv R - \bar{R}(a)$,

$$\bar{f}_R(a) = a^6\bar{f}_{R0}\left(\frac{1+4\frac{\Omega_\Lambda}{\Omega_m}}{1+4\frac{\Omega_\Lambda a^3}{\Omega_m}}\right)^2, \tag{1.83}$$

$$\bar{f}_{R0} \equiv \bar{f}_R(a=1) = -\frac{2\Omega_\Lambda\Omega_m}{3\left(\Omega_m+4\Omega_\Lambda\right)^2}\frac{1}{c_2}, \tag{1.84}$$

$$\delta R = \bar{R}(a)\left(\sqrt{\frac{\bar{f}_R(a)}{f_R}}-1\right). \tag{1.85}$$

It was seen above that there is only one free parameter remaining in the model, either c_1 or c_2. From Eq. (1.84), it is apparent that choosing c_2 is equivalent to choosing the present-day ($a = 1$) value of the background scalar field, $\bar{f}_{R0}$. The ΛCDM+GR limit corresponds to the limit $\bar{f}_{R0} \to 0$ or $c_2 \to \infty$. Many $f(R)$ studies, including later chapters of this thesis, quote results in terms of constraints on $\bar{f}_{R0}$, which is the key input parameter of the theory. It is interesting to note that $\bar{f}_{R0} \approx -\chi_0$ (see § 1.3.2), so that $\bar{f}_{R0}$ plays a similar role as a 'self-screening parameter', indicating which objects will be unscreened and which will be (fully or partially) screened.

As a final note in this section, it will prove useful in Chapters 2 and 3 to rewrite the modified Poisson equation (1.70) in terms of an 'effective density' that encodes the modified gravity contributions,

$$\delta\rho_{\rm eff} \equiv \frac{1}{3}\delta\rho - \frac{c^2}{24\pi G}\delta R, \tag{1.86}$$

so that the modified Poisson equation (1.70) can be rewritten as

$$\nabla^2\Phi = 4\pi G\left(\delta\rho + \delta\rho_{\rm eff}\right). \tag{1.87}$$

1.3.4 Simulations

As with ΛCDM, in order to generate observable predictions from modified gravity theories, N-body simulations are an invaluable tool at non-linear scales where linear perturbation theory no longer holds (see § 1.2.2). This is particularly the case for theories with screening mechanisms, in which the phenomenology of screening would be expected to lead to non-trivial imprints on exactly these scales. While greater attention has been paid in the last two decades to the construction of simulations of ever finer resolution and ever greater realism under ΛCDM, recent years have also seen a flurry of activity in the field of MG simulations.

Modified gravity simulations are significantly more computationally expensive than ΛCDM ones, for one primary reason: non-linearity. To be precise, at each timestep a modified gravity simulation code needs to solve a modified Poisson equation, as well as some equation of motion for the scalar field.[60] In HS $f(R)$ gravity, these governing equations are (1.87) and (1.69) respectively, supplemented by Eqs. (1.83), (1.85), and (1.86). All taken together, these equations can be solved for the scalar field f_R for a given density distribution $\delta\rho$. For a screening mechanism to even exist, some non-linearity must be built into the scalar field equation of motion. This is manifest in the $f(R)$ case upon substituting Eq. (1.85) into Eq. (1.69), leading to a $f_R^{-1/2}$ term in the equation of motion for the scalar field f_R. As a result of this non-linearity, efficient methods such as Fast Fourier Transforms—used widely in gravity solvers—can no longer be utilised. Instead, the non-linear scalar field

[60] Alternatively, one could solve the standard Poisson equation, and calculate the fifth force separately via gradients of the scalar field, cf. Eqs. (1.49) and (1.77). However, one still needs to first solve for the scalar field via some non-linear equations of motion.

equations such as Eq. (1.69) are directly discretised and solved using relaxation methods. In Chapter 2, the scalar field solver within the $f(R)$ N-body code MG-Gadget (Puchwein *et al.*, 2013) is used extensively, while Chapter 3 describes and employs a 1D analogue.[61]

The first simulations of screened modified gravity were the HS $f(R)$ gravity simulations of Oyaizu (2008) (published in a three part series of articles, alongside Oyaizu *et al.*, 2008; Schmidt *et al.*, 2009).[62] Considering the matter power spectrum, the authors found a enhancement of power on all scales smaller than the Compton wavelength of the theory, as had been predicted previously by Hu & Sawicki (2007). However, it was also demonstrated here for the first time that screening suppresses this enhancement on the smallest scales.

Since then, MG simulation codes have abounded. A highly incomplete list of examples could include the aforementioned MG-Gadget (Puchwein *et al.*, 2013), ECOSMOG (Li *et al.*, 2012), and ISIS (Llinares *et al.*, 2014). The review article by Llinares (2018) gives a more complete overview of modified gravity codes, as well as a description of various commonly used numerical techniques and optimising strategies such as 'multigrid acceleration' (Brandt, 1977). Many codes adopt Hu-Sawicki $f(R)$ gravity, taking it as a representative example of a chameleon theory, while many alternatively or additionally adopt different theories of gravity, incorporating different screening mechanisms. Winther *et al.* (2015) perform a quantitative comparison of several of these codes, finding good agreement between their predictions for key observables, such as the matter power spectrum.

One point worth noting is that a near-universal assumption in these MG codes is the quasistatic approximation, i.e. the assumption that time derivatives of the scalar field can be neglected, as was assumed in the derivation of Eqs. (1.69) and (1.70). The general validity of this approximation in modified gravity theories was discussed in Sawicki & Bellini (2015), and tested explicitly in simulations by Winther *et al.* (2015) and Bose *et al.* (2015) in the symmetron and HS $f(R)$ cases respectively. Both of these tests found the quasistatic approximation to be valid for all practical purposes.

Following the trend established by Oyaizu *et al.* (2008), a key focus of MG simulation works has been on statistics of the large-scale matter distribution such as power spectra, mass and correlation functions, or the Lyman-α forest (Zhao *et al.*, 2010, 2011; Li & Hu, 2011; Lombriser *et al.*, 2013; Puchwein *et al.*, 2013; Arnold *et al.*, 2015; Cataneo *et al.*, 2016; Arnold *et al.*, 2019a). On the other hand, several works have considered various other observables, such as the properties of voids (Zivick *et al.*, 2015; Cautun *et al.*, 2018; Paillas *et al.*, 2019; Davies *et al.*, 2019) and clusters (Lombriser *et al.*, 2012a,b; Arnold *et al.*, 2014), or imprints on galaxy/halo dynamics (Schmidt, 2010; Arnold *et al.*, 2016). With some ex-

[61] And Appendix A describes and employs a 2D analogue.

[62] The simulations of Oyaizu (2008) were not, however, the first modified gravity simulations in general. Earlier studies, such as those of Macciò *et al.* (2004); Kesden & Kamionkowski (2006a,b), typically employed unscreened theories with non-universal couplings. The review article of Baldi (2012) contains a wealth of information about the historical development of modified gravity simulations.

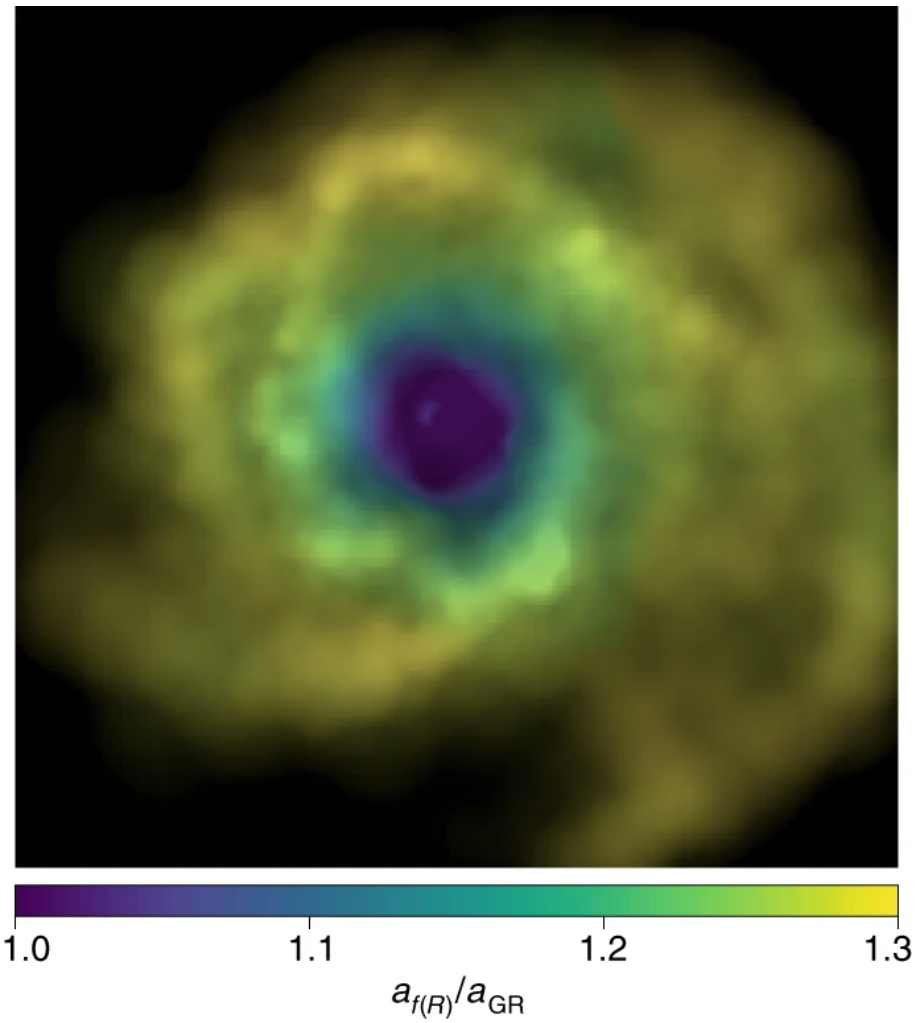

Figure 1.15: Image of a galaxy from the SHYBONE simulations of Arnold *et al.* (2019b), showing the gas density in a thin slice in the galactic disc plane. The colour indicates the fractional strength of the fifth force. The size of the plotted region is 72.5 kpc from the centre of the galaxy to the edge of the image. The central blue region is the screened region of the galaxy. Reproduced from Arnold *et al.* (2019b). © Springer Nature 2019. Reprinted with permission.

ceptions (e.g. Arnold *et al.*, 2014; Hammami *et al.*, 2015; Arnold *et al.*, 2015, 2019a), most of these studies have simulated only the dark matter and scalar field, with baryons absent.

A difficulty in using statistics of large-scale astrophysical structure to test gravity is that the scales on which modified gravity might impart observable signatures are the very same as those in which baryonic processes such as AGN feedback also play a role (Puchwein *et al.*, 2013; Arnold *et al.*, 2019a). In particular, AGN feedback acts to suppress power where a fifth force would enhance it. A degeneracy therefore exists: simplistically, modified gravity plus strong AGN feedback could be mistaken for GR plus mild AGN feedback. In reality, the effects would not precisely cancel (e.g., Arnold *et al.*, 2019a, find a 'sweet spot' at $k \sim 1\mathrm{Mpc}^{-1}$ where the influence of AGN feedback on the power spectrum is significantly smaller than that of modified gravity), but it is nonetheless important to have a thorough understanding of them in order to generate predictions for the next generation of wide-field galaxy surveys

such as LSST (LSST Science Collaboration, 2009) and Euclid. Moreover, the possibility of a complex, non-linear interplay (a 'back-reaction') between the two effects means that to gain this understanding, they ideally need to be simulated together. However, the computational expense of modified gravity simulations makes this very difficult, and so this milestone was only very recently passed for the first time.

Using the state-of-the-art baryonic feedback models of IllustrisTNG (Pillepich *et al.*, 2018), Arnold *et al.* (2019b) ran the first MG galaxy formation simulations: the SHYBONE suite (Simulating HYdrodynamics BeyONd Einstein). Vindicating some of our assumptions in Chapter 2, they demonstrate that disc galaxies are able to form under HS $f(R)$ gravity, even when only their innermost regions are screened (see Figure 1.15). For the matter power spectrum, they find that for $\bar{f}_{R0} = -10^{-6}$, the power spectrum is actually very well estimated by a simple linear sum of the modified gravity enhancement and the AGN feedback suppression, where each is calculated separately (and less expensively) from DM-only $f(R)$ simulations and 'full physics' ΛCDM simulations respectively. However, for $\bar{f}_{R0} = -10^{-5}$, the back-reaction becomes important and this is no longer the case. The reason for this difference between the two cases is possibly to do with whether or not the central regions of AGN-hosting haloes are screened in a given modified gravity scenario.

1.3.5 Galaxy-Scale Tests

Chameleon gravity theories have been subject to a number of tests on a variety of scales, ranging from the laboratory to the cosmic microwave background. However, some of the strongest constraints to date have come from weak-field galaxy-scale probes (e.g., the constraints of Desmond *et al.*, 2018b, described below). At the same time, as I described in § 1.1.5, galaxy scales are actually among the least explored regions of parameter space for tests of gravity in general, but will increasingly be accessible with upcoming datasets (cf. the 'Novel Probes' project of Baker *et al.*, 2019). The coming years therefore hold a great deal of promise for the exploration of chameleon parameter space with galaxy-scale probes.

This section focuses on such galaxy-scale tests of chameleon theories. A more comprehensive review of tests and constraints would venture beyond the scope of this thesis, but such works do exist in the literature. For example, the review article by Burrage & Sakstein (2018) compiles constraints on chameleon theories from all conceivable sources. Moreover, the aforementioned work by Baker *et al.* (2019) and the review article by Sakstein (2018) both describe a number of astrophysical probes of modified gravity theories in great detail.

'Galaxy-scale' here means the scale of individual galaxies, or at most, the distances separating a galaxy from its satellites and near neighbours. This section therefore excludes tests based on galaxy clusters and tests based on intergalactic distance indicators, although both of these regimes provide rather powerful probes of modified gravity.

Interestingly, several of the observable signatures described below arise—directly or indirectly—as a result of the effective EP-violation described in § 1.3.2. These signatures often utilise the fact that for χ_0 (or $|\bar{f}_{R0}|$) $\lesssim 10^{-6}$, main sequence stars will be self-screened. As illustrated in the lower row of Figure 1.14, these stars will not experience any external fifth force. However, if their host galaxies are unscreened then the diffuse dark matter and gas components will feel a fifth force, and interesting phenomenology can arise as a result.

For reasons of convenience, $\bar{f}_{R0}$ is used in the descriptions below as a constraining parameter. However, it should be noted that several of these tests (and chameleon tests in general) derive constraints in a two-dimensional $\beta - \chi_0$ space, or equivalent.

Screening Maps

As discussed in § 1.3.2, 'environmental screening' is a phenomenon whereby an object can be screened by its environment. A galaxy that would be unscreened in isolation could be partially or fully screened if instead it is situated in an overdense environment.

This is a significant hurdle to overcome for observational probes: if a galaxy shows no significant modified gravity signal, it is first necessary to understand whether it is screened by its environment before this can be translated into theory constraints.

In the chameleon context, it has been shown in simulations (e.g. Cabré *et al.*, 2012) that as a first approximation, the degree of environmental screening of a given galaxy can be quantified by the gravitational potential due to external sources $\Phi_{\rm ext}$ within a Compton wavelength of the galaxy. The Compton wavelength λ_C relates to $\bar{f}_{R0}$ via the approximate equation (Cabré *et al.*, 2012)

$$\lambda_C \approx 32\sqrt{\frac{|\bar{f}_{R0}|}{10^{-4}}}\ \mathrm{Mpc}. \tag{1.88}$$

For this very purpose of measuring the impact of environmental screening on tests of gravity, two groups—Cabré *et al.* (2012) and Desmond *et al.* (2018c)—have constructed 'screening maps': 3D maps of $\Phi_{\rm ext}$ throughout the local Universe. Both maps convert observed galaxy catalogues into $\Phi_{\rm ext}$ maps using sophisticated techniques to estimate 'unseen' mass residing in the haloes of the observed galaxies, in unseen haloes, and in the smooth intergalactic density field.

In Chapter 3, we use the screening map of Desmond *et al.* (2018c) which uses updated techniques and catalogues compared to that of Cabré *et al.* (2012). Full details regarding the construction of the map can be found in the original paper.

Galaxy Offsets

Consider a galaxy situated within an external fifth force field. If the galaxy is unscreened but the stars within it are self-screened, then the gas disc will experience the fifth force while

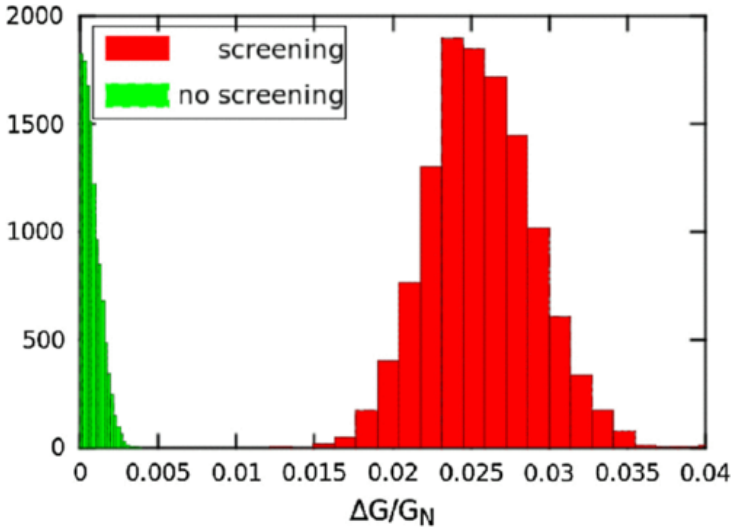

Figure 1.16: Posterior of the fifth force coupling $\Delta G/G_N$ ($\equiv 2\beta^2$ in our notation), obtained by Desmond *et al.* (2018b) from measurements of systematic offsets between gaseous and stellar components of galaxies. The Compton wavelength λ_C here is 1.8 Mpc. The red histogram is the posterior in a chameleon model in which galaxies are screened according to their Newtonian potential, and stars are self-screened against the fifth force. The authors find 6.6 σ evidence for a non-zero screened fifth force. The green histogram is a model in which the galaxy screening is turned off, but stars nonetheless do not feel the fifth force. Reproduced from Desmond *et al.* (2018b). © American Physical Society 2018. Reprinted with permission.

the stellar disc will not. Consequently, one would expect the stellar disc to be offset from the gas disc, and the direction of this offset to align with the direction of the external fifth force vector.

Desmond *et al.* (2018b, 2019a) use a large sample of $\sim$ 11,000 galaxies to search for this offset signature, calculating an upper bound on $|\bar{f}_{R0}|$ of a few $\times 10^{-8}$. These are the strongest reported constraints on $\bar{f}_{R0}$ to date. Away from $f(R)$ gravity (i.e. allowing for a varying β), the study finds a statistically significant signal at $2\beta^2 \approx 10^{-2}$ and $\lambda_C \approx 2$ Mpc, as shown in Figure 1.16. However, the authors add the cautionary note that the signal could well be a result of a number of other effects, including unaccounted-for galaxy formation physics.

The authors find that the signal vanishes when the offsets are artificially rotated in the sky, demonstrating that the signal does indeed arise from a significant correlation between the directions of the galaxy offsets and the calculated directions of the external fifth forces, whether these fifth forces are real or not. The signal also vanishes when all mass is included in the external fifth force calculation, rather than just unscreened mass. This model is shown by the green histogram in Figure 1.16. This suggests that the tentative signal is somehow connected to the complex dynamics of screening.

Galaxy Warps

If a stellar disc is offset from the halo centre as described above, then the stellar disc would be expected to warp as a result of the potential gradient. Moreover, this warping should be

maximised when the rotation axis of the disc aligns with the external fifth force field.

Desmond *et al.* (2018a) search for this signature in data from ~ 4000 galaxies of the NASA Sloan Atlas. Tantalisingly, this study also finds support for a screened modified gravity with $2\beta^2 \approx 10^{-2}$ and $\lambda_C \approx 2$ Mpc, despite the independence of the dataset from that of the offset study described above.

Rotation Curves

Galaxy rotation curves offer a number of observable signatures:

1. If stars are self-screened in an unscreened galaxy, the gas rotation curve will show greater velocities than the stellar rotation curve. Vikram *et al.* (2018) searched for this signal in the rotation curves of 6 low surface-brightness galaxies, yielding an upper bound on $|\bar{f}_{R0}|$ of 10^{-6}.

2. If the rotation axis of a galactic disc is perpendicular the external fifth force field, the stellar-gas offset discussed above will result in asymmetries in the galaxy rotation curves. This effect was studied by Vikram *et al.* (2013), who found no significant deviations from standard gravity.

3. If a galaxy is partially screened, gas rotation curves will display an 'upturn' at the location of the screening radius. This effect is the subject of Chapters 2 and 3.

Stellar Streams

Stellar streams arise from satellite galaxies and globular clusters being tidally disrupted by the central host galaxy. If the Milky Way is partially screened, then a DM-dominated satellite galaxy on an orbit outside the Milky Way screening radius will feel a fifth force. The screened stars within it, however, will not feel the fifth force but will be dragged along by the satellite's halo. As the satellite is tidally disrupted by the Milky Way, the stars will be preferentially disrupted into the trailing stream, rather than the leading stream, leading to an asymmetry about the progenitor.

This effect was first predicted by Kesden & Kamionkowski (2006a,b) for an intrinsically EP-violating "dark matter force." Chapter 4 studies this effect in the context of chameleon theories, where the EP-violation emerges as a result of screening.

Chapter 2

Upturns in Simulated Rotation Curves

Summary

In this chapter, I use the kinematics of galaxies to constrain screened modified gravity theories. I focus on HS $f(R)$ gravity and predict its impact on galaxy rotation curves and radial acceleration relations. This is achieved by post-processing state-of-the-art galaxy formation simulations from the Auriga Project, using the MG-Gadget code. For a given galaxy, the surface dividing screened and unscreened regions adopts an oblate shape, reflecting the galaxy's disc morphology. At the 'screening radius', where screening is triggered in the disc plane, characteristic 'upturns' are present in both rotation curves and radial acceleration relations. The locations of these features depend on various factors, such as galaxy mass, concentration of the density profile, and the background field amplitude $\bar{f}_{R0}$. Self-screening of stars and environmental screening also play a role. For Milky Way-size galaxies, models with $|\bar{f}_{R0}| = 10^{-7}$ result in rotation curves that are indistinguishable from ΛCDM, while for $|\bar{f}_{R0}| \geq 2 \times 10^{-6}$ the galaxies are entirely unscreened, violating Solar System constraints. For intermediate values, distinct upturns are present. I conclude by predicting that with a careful statistical analysis of existing samples of observed rotation curves, including lower mass objects, constraints on $f(R)$ gravity with a sensitivity down to $|\bar{f}_{R0}| \sim 10^{-7}$ should be possible.

This chapter is based on the article:

A. P. Naik, E. Puchwein, A.-C. Davis, C. Arnold

Imprints of chameleon f(R) gravity on galaxy rotation curves

MNRAS, Volume 480, Issue 4, November 2018, Pages 5211–5225

In § 2.2.2, we validate some of the assumptions underlying our post-processing approach by studying a suite of $f(R)$ simulations. These simulations were run by Christian Arnold, one of the co-authors of the above article. The remainder of the work presented in this chapter is my own, informed and guided by discussions with the other authors.

2.1 Background

The Introduction of this thesis included a section (§ 1.3) giving a general outline of screened modified gravity theories, particularly their weak-field limit and applications to galactic scales, as well as a discussion of the *status quo* in modified gravity N-body simulations. Increasingly, such simulations are the tool of choice for predicting the observational signatures of these theories on scales where non-linear effects (i.e., both baryonic physics and screening phenomenology) are important. Winther *et al.* (2015) present an overview and comparison of different simulation codes and find good agreement between the results of different groups, indicating that the field has reached a significant degree of maturity. This is best exemplified by the recent SHYBONE simulations of Arnold *et al.* (2019b), the first galaxy formation simulations under modified gravity. When the article that forms the basis for this chapter was first written, perhaps the most sophisticated modified gravity simulations to date were those of Arnold *et al.* (2016): the first high resolution, dark matter-only, zoom-in simulations of Milky Way-sized halos in $f(R)$ gravity. The work presented in this chapter built upon that work by providing the first simulated galaxy rotation curves in $f(R)$ gravity for Milky Way-sized galaxies.

There is a key difference worth emphasising between the work of Arnold *et al.* (2016) and this chapter. The former work provides fully self-consistent, DM-only simulations of $f(R)$ dark matter halos. The halos simulated therein are evolved under $f(R)$ gravity from high redshift initial conditions in the linear regime to the present day. As discussed in § 1.3.4, the extreme non-linearity of the governing equations of $f(R)$ gravity make these simulations significantly more computationally expensive than in standard gravity. Nonetheless, dark matter-only simulations such as those of Arnold *et al.* (2016) are significantly less computationally expensive than the 'full physics' simulations of, e.g., the SHYBONE suite, which additionally incorporates the complex hydrodynamics and baryonic physics of galaxies at high resolutions. So, in order to investigate the effects of chameleon $f(R)$ gravity in galaxies, we have not performed self-consistent $f(R)$ simulations, and instead calculated the $f(R)$ effects in 'post-processing'.

Taking galaxy mass distributions from the state-of-the-art ΛCDM disc galaxy formation simulations of the Auriga Project (Grand *et al.*, 2017), the modified gravity solver aboard the MG-Gadget code was then used to numerically compute the scalar fields and fifth forces across these galaxies, leading to derivations of their rotation curves. Our models are thus not full dynamical models encapsulating the evolution of $f(R)$ galaxies, but simply rotation curves calculated for galaxies with mass distributions believed to be closely resembling those of real galaxies. The basic underlying assumption—justified *a posteriori* by Arnold *et al.* (2019b)—is that disc galaxies should have a rotationally supported disc component even in the presence of modifications of gravity, so that the radial gravitational acceleration in the disc plane can be inferred from measurements of gas and/or stellar velocities, which allows the presence of a fifth force to be constrained.

Galaxy	r_{200} [kpc]	M_{200} [10^{10} $M_\odot$]	M_* [10^{10} $M_\odot$]	v_{200} [km/s]	$v_{\rm peak}$ [km/s]
Au1	192.09	77.38	3.61	159.44	197.19
Au2	260.51	193.01	11.19	184.02	246.64
Au9	232.25	104.69	6.26	149.87	261.36
Au11	212.45	149.28	8.67	179.93	241.95
Au13	239.14	122.03	7.30	158.59	282.63
Au20	223.59	127.58	5.89	162.43	219.51
Au21	226.93	146.53	9.13	169.01	252.30
Au22	237.64	91.74	6.20	144.70	284.38
Au24	203.31	147.29	8.11	177.37	239.34
AuL1	238.07	51.70	2.47	120.19	165.94
AuL4	168.67	52.39	2.52	111.91	143.13
AuL5	184.34	68.38	3.43	128.57	189.64
AuL8	197.83	84.52	5.36	140.34	223.09

Table 2.1: Basic properties of the simulated galaxies used in this work. Columns are 1) Auriga ID: the identifying number of the galaxy in the Auriga Project, 2) r_{200}: the virial radius, here taken as the radius enclosing a region of average density equal to 200 times the cosmic critical density, 3) M_{200}: the mass contained within r_{200}, 4) M_*: the total stellar mass within r_{200}, 5) v_{200}: the circular velocity in the disc plane at r_{200}, and 6) $v_{\rm peak}$: the peak circular velocity.

This chapter directly foreshadows the next chapter, which turns to the observed rotation curves of the SPARC sample (Lelli *et al.*, 2016).

The remainder of this chapter is structured as follows. First, § 2.2 describes the methodology, describing both the scalar field solver that is employed and the simulated galaxies that are analysed. Results are then presented in § 2.3 and discussed in § 2.4, followed by concluding remarks in § 2.5.

2.2 Methodology

2.2.1 The Auriga galaxy formation simulations

The simulated galaxies studied in this work were not evolved *ab initio* using MG-Gadget, but were instead formed in hydrodynamical ΛCDM simulations with state-of-the-art baryonic physics performed in the Auriga Project (Grand *et al.*, 2017), and post-processed using the scalar field solver of MG-Gadget. The validity of this post-processing approach is discussed in § 2.2.2.

The Auriga Project employed magnetohydrodynamics and a sophisticated galaxy formation prescription—including sub-resolution implementations of radiative cooling, star formation, chemical enrichment, supernovae and AGN feedback—to perform zoom sim-

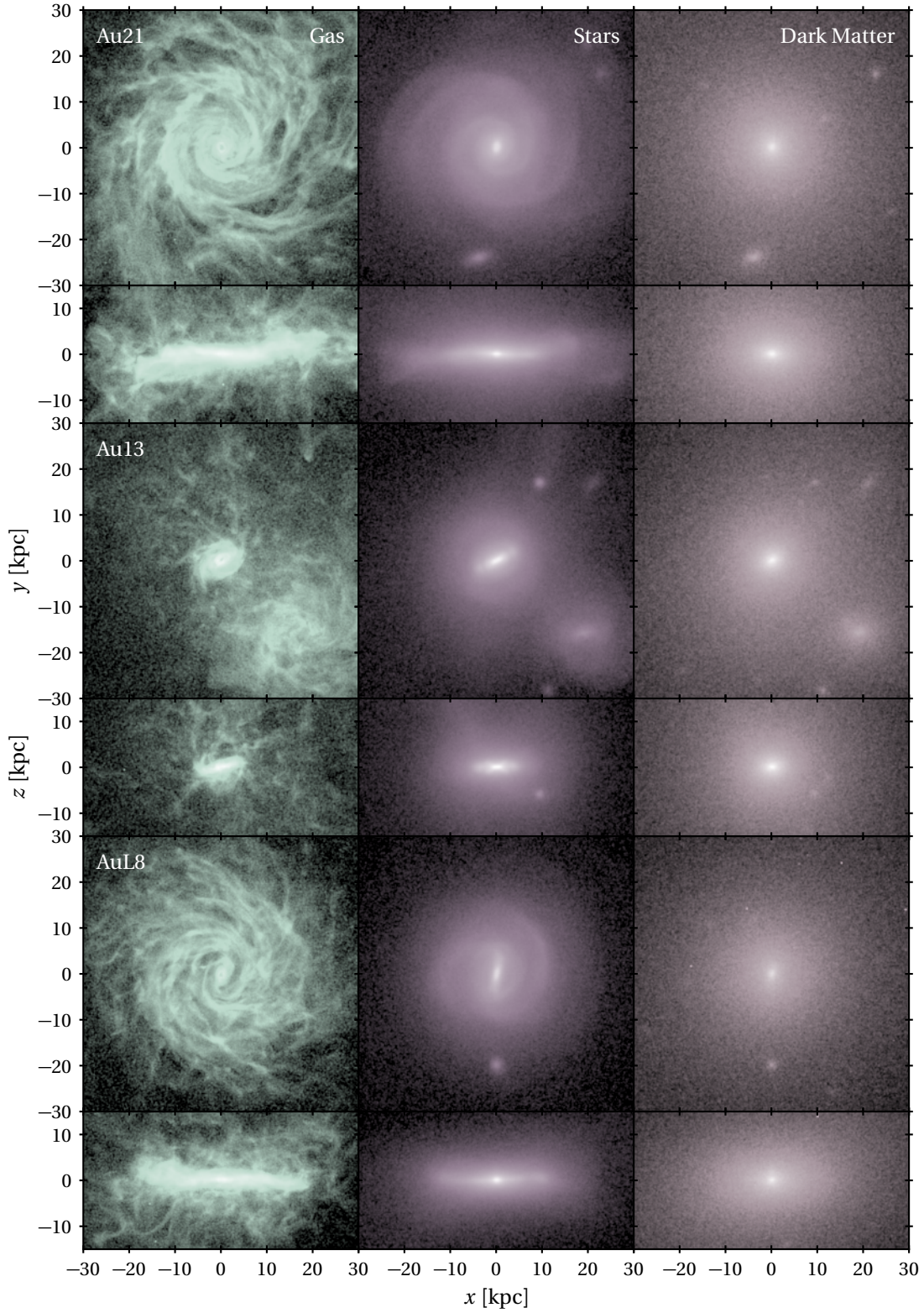

Figure 2.1: Projected gas (left), stellar (middle) and dark matter (right column) density of the Auriga galaxies Au21 (top), Au13 (middle), and AuL8 (bottom row). For each object and component, face-on and edge-on projections are shown. The mass distributions of these and other simulated galaxies were used as an input for the MG-Gadget modified gravity solver.

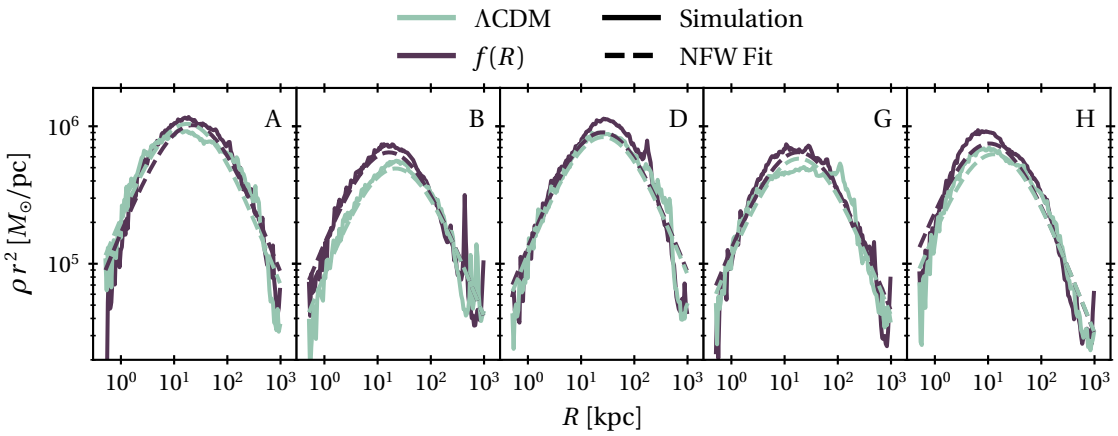

Figure 2.2: Density profiles of five dark matter haloes. The purple curves represent haloes from the full $f(R)$ simulations of Arnold *et al.* (2016), while the green curves are their ΛCDM counterparts from the original Aquarius simulations of Springel *et al.* (2008). The corresponding dashed lines are NFW fits to the density profiles. Density is multiplied by a factor of r^2 for improved readability.

ulations of 30 isolated MW-size galaxies using the moving mesh code AREPO (Springel, 2010).

The Auriga galaxies reproduce a range of observables of Milky Way-like galaxies, including masses, sizes, rotation curves, star formation rates, and metallicities. Furthermore, the simulated galaxies have clear Milky Way-like late-type morphologies, featuring bars and spiral arms.

Thirteen such galaxies have been studied here, and an overview of their basic properties is provided in Table 2.1. 9 of these galaxies are from the original Auriga Project (Au1, Au2, Au9, Au11, Au13, Au20 Au21, Au22, Au24), a further 4 lower-mass galaxies (AuL1, AuL4, AuL5, and AuL8) were taken from a follow-up project.

Projections of the various components, i.e. gas, stellar, and dark matter surface density, of galaxies Au21, Au13, and AuL8 are shown in Figure 2.1. These 3 galaxies have been chosen to represent a range of galaxy morphologies. Au21 is a grand design spiral galaxy, AuL8 has a prominent bar, and Au13 a slightly less well-defined disc.

The particle, and hence mass, distributions of these galaxies were extracted from the Auriga simulation snapshots, and fed to MG-Gadget's modified gravity solver, which is discussed in the following sub-section and computes the scalar field f_R and the modified gravity accelerations throughout the simulation volume.

2.2.2 Calculation of modified gravity effects

The modified gravity solver used in this work is part of the MG-Gadget simulation code (Puchwein *et al.*, 2013), which is itself based on the P-Gadget3 code (see the description of its predecessor Gadget-2 in Springel, 2005), but incorporates a reworked gravity solver,

which enables the simulating of models with highly non-linear force laws such as HS $f(R)$ gravity.

In the base P-Gadget3 code, gravitational accelerations are calculated using a 'TreePM' method: long-range forces are calculated using Fourier (Particle Mesh) methods, while short-range forces are calculated using a hierarchical oct-tree, which gives higher spatial resolution. MG-Gadget also utilises these methods to solve the modified Poisson equation (1.87), but in addition the scalar field f_R is computed and stored on a space-filling adaptive mesh, which is constructed from the oct-tree structure. More precisely, f_R is obtained by solving Eq. (1.69) with a multi-grid accelerated, iterative Newton-Gauss-Seidel relaxation method on the adaptive mesh. This allows calculating f_R everywhere in the simulation volume, as well as the MG acceleration on each particle. A much more detailed description of the algorithm can be found in the original code paper (Puchwein *et al.*, 2013), while scientific applications of the code are presented in, e.g., Arnold *et al.* (2014, 2015, 2016, 2019a). See also § 1.3.4 for a discussion of modified gravity simulations more generally.

The modified gravitational forces are calculated in post-processing from ΛCDM simulations, rather than by performing full galaxy formation $f(R)$ simulations, which would be computationally much more expensive. This means that modified gravity effects on the evolution of galaxies will not be captured. We assume that galaxies with rotationally supported discs are able to form under $f(R)$ gravity[1], so that observed galaxy morphologies are consistent with either ΛCDM or $f(R)$. Given also that the gas and stellar components of the Auriga galaxies match observations well, they can thus be assumed to provide realistic mass models for galaxies in either cosmological paradigm. The primary uncertainty is therefore the dark matter, specifically whether the density profiles of the Auriga dark matter haloes resemble those that would form in an $f(R)$ cosmology.

Arnold *et al.* (2016) investigated the effect of HS $f(R)$ gravity on the formation of dark matter halos. In that work, computationally cheaper dark matter-only $f(R)$ gravity simulations were performed using MG-Gadget in order to investigate the effects of $f(R)$ gravity on Milky Way-mass dark matter halos. The simulations were performed from identical initial conditions to the Aquarius simulations (Springel *et al.*, 2008). Figure 2.2 compares the density profiles of five haloes in these full $f(R)$ simulations (for $|\bar{f}_{R0}| = 10^{-6}$) with those of the corresponding haloes in the ΛCDM simulations. It can be seen in this figure that the shapes of the density profiles from the $f(R)$ simulations are qualitatively similar to those of the ΛCDM simulations. While the presence of the chameleon fifth force might change the total mass and concentration of a given halo somewhat, it does not significantly affect its morphology. In particular, the NFW profile (1.45) can fit both ΛCDM and $f(R)$ haloes equally well. When fitting observed rotation curves along with measured stellar and gas

[1] Since the original undertaking of this research, Arnold *et al.* (2019b) have carried out the first galaxy formation simulations in HS $f(R)$ gravity. One of the results of that work was to demonstrate that disc galaxies are indeed able to form (see Figure 1.15), vindicating our earlier assumption.

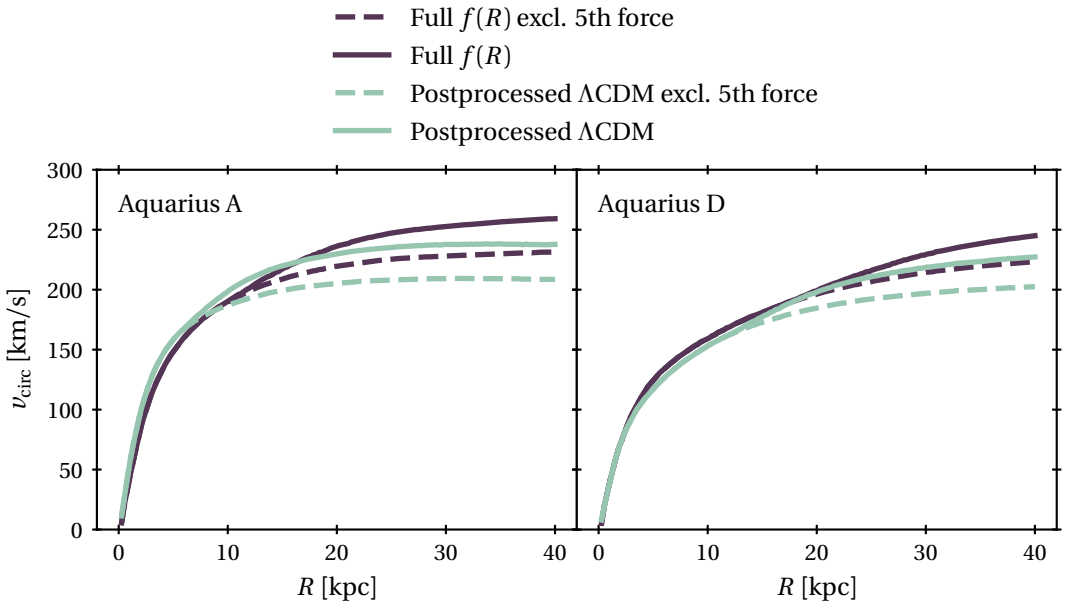

Figure 2.3: Circular velocity profiles for two Aquarius dark matter haloes, labelled A *(left)* and D *(right)*. The purple curves show the circular velocity calculated from particle accelerations in the full $f(R)$ simulations, while the green curves are calculated analogously from their post-processed ΛCDM counterparts from the original Aquarius simulations. In all cases, $|\bar{f}_{R0}| = 10^{-6}$. Solid lines include the fifth force contribution, while the dashed lines ignore it.

densities, the mass and concentration of the dark matter halo would be free parameters, so that changes in these parameters due to modified gravity would be captured.

Figure 2.3 shows rotation curves for two of the five haloes. These two were chosen by virtue of being the only ones partially screened, rather than fully unscreened, for $|\bar{f}_{R0}| = 10^{-6}$. The purple curves show rotation curves from the original full $f(R)$ simulations, while the green curves show post-processed rotation curves from the ΛCDM simulations. The key point of this figure is that both sets of rotation curves are qualitatively the same, with similar upturns[2] at the screening radii. The differences in the heights of the curves and locations of the screening radii can be ascribed to the differences in halo mass and concentration. That is to say, employing the fully self-consistent approach of full $f(R)$ simulations would have changed the exact masses and density profiles of the galaxies, and therefore the resulting rotation curves, but the qualitative features, particularly the upturns, would still be present at the screening radii.

Another complication is the potential effect of baryonic feedback on the dark matter density profile (see the discussion of the 'core/cusp' problem in the Introduction; § 1.1.5). In the following we assume that such effects (e.g., the potential formation of a core) happen in a very similar way under both $f(R)$ gravity and ΛCDM. This should certainly hold in objects in which the central region, which is most prone to baryonic effects, is screened. Using the assumption of similar baryonic effects, it is then possible to describe both $f(R)$

[2] See § 2.3.2 for a definition and further description of rotation curve 'upturns'.

and ΛCDM halo profiles with the same functional form.

In principle it would be interesting to test the effect of modified gravity on the baryonic feedback. This is, however, very difficult due to the wide range of scales involved and due to our limited understanding of the relevant astrophysics. As an example of how these processes might differ under modified gravity, Davis *et al.* (2012) find that unscreened stars are typically brighter in modified gravity scenarios, which implies higher supernova rates than in ΛCDM.

It is also worth noting that baryonic feedback is typically implemented in galaxy formation simulations not via detailed models of all the relevant physics, but via strongly simplified subgrid models which need to be calibrated to observational constraints. Hence, even when evolving such simulations fully under modified gravity, changes in the baryonic effects due to the fifth force would likely be partially offset by re-calibrating the model parameters to observations. Furthermore, as shown in Davis *et al.* (2012), these differences between modified gravity and ΛCDM feedback mechanisms can be expected to be negligible at the small field amplitudes considered in this work $|\bar{f}_{R0}| \leq 10^{-6}$, at which many galactic baryons inhabit screened regions. Thus, our assumptions should remain robust.

These considerations, together with the assumption that rotationally supported disc components are present in both chameleon $f(R)$ gravity and in ΛCDM, suggest that our post-processing approach is valid for illuminating the impact of fifth forces on galaxy rotation curves. That is, qualitatively similar rotation curve upturns and radial acceleration relation bumps would have been seen in the Auriga galaxies had they instead been simulated fully self-consistently under $f(R)$ gravity. The exact location of the features might be slightly different due to modified gravity effects on the dark matter density profiles. However, the parameters describing the dark matter profiles would be free parameters when fitting observed rotation curves, so that these effects would be taken into account.

It is worth restating an assumption mentioned in the Introduction (§ 1.1.4): we assume that dark matter is cold and diffuse, i.e. not comprising potentially self-screening compact objects such as primordial black holes.

2.2.3 Rotation Curves

The rotation curves displayed in the following section are calculated from post-processed simulation snapshots as follows.

Firstly, only particles in the disc plane are considered. In order to isolate these, the total angular momentum vector of the galaxy (within a sphere of radius 30 kpc around the centre) is calculated, and the disc plane is then the plane perpendicular to this vector. Particles within 0.5 kpc of this plane are admitted.

For each particle, the snapshot contains a standard gravity acceleration vector and a separate fifth force acceleration vector. According to Eq. (1.44), taking the inner product

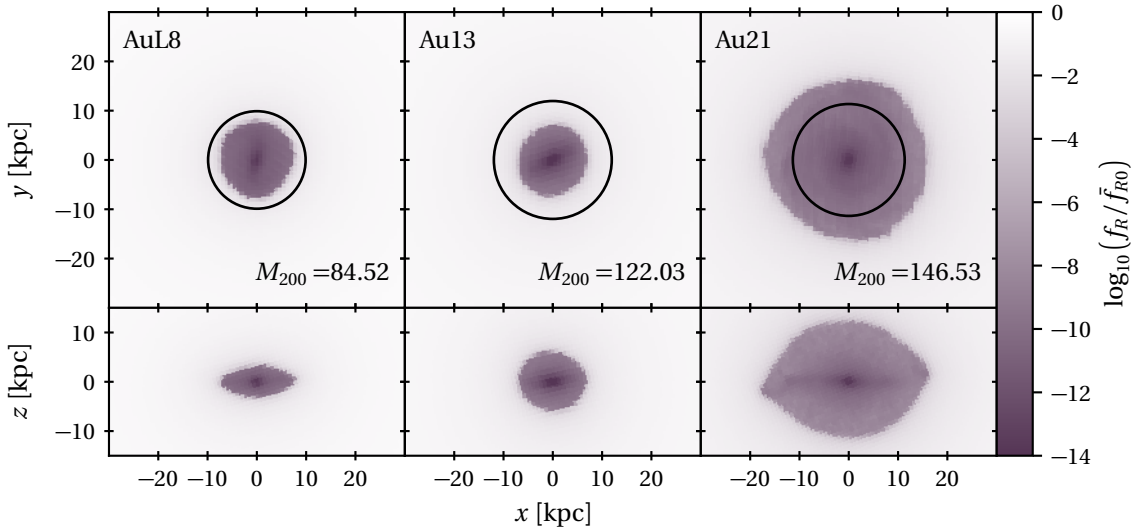

Figure 2.4: Face-on *(top)* and edge-on *(bottom)* scalar field maps of galaxies AuL8, Au13, and Au21, for a background field amplitude of $|\bar{f}_{R0}| = 8 \times 10^{-7}$. The black circle marks $0.05\,R_{200}$. At the screening surfaces, the field amplitude drops by many orders of magnitude. The edge-on views demonstrate that the screening surface is typically compressed towards the disc plane, reflecting the density distribution of the galaxy. The virial mass (M_{200}) of each galaxy is labelled in each case, in units of $10^{10} M_{\odot}$.

of the acceleration vector for a given particle (either including or excluding the modified gravity contribution) with the radial vector then gives an estimate of the square of the circular velocity at the particle position. The particles are then divided into radial bins, and the average circular velocity is calculated in each bin, giving the final rotation curve.

As a final note, the cosmological Compton wavelength in Hu & Sawicki $f(R)$ gravity (for $n = 1$) is approximately given by Eq. (1.88). On scales larger than this, the fifth force would be suppressed even if the chameleon mechanism is not triggered. However, even for the smallest scalar field amplitude considered in this chapter, $|\bar{f}_{R0}| = 10^{-7}$, this wavelength is approximately 1 Mpc, well beyond the size of any galaxy. Outside the screening radius, fifth forces will thus affect the rotation curve out to the largest observed radii.

2.3 Results

2.3.1 Screening in Disc Galaxies

As described in § 2.2.2, we use the modified gravity solver from the MG-Gadget code to post-process $z = 0$ simulation snapshots from the Auriga Project and calculate the scalar field f_R everywhere in the simulation volume. Figures 2.4 and 2.5 show examples of the results of these calculations.

Figure 2.4 shows face-on and edge-on maps of the scalar field f_R, calculated across planes going through the galaxy centres, for galaxies AuL8, Au13 and Au21, and for $|\bar{f}_{R0}| =$

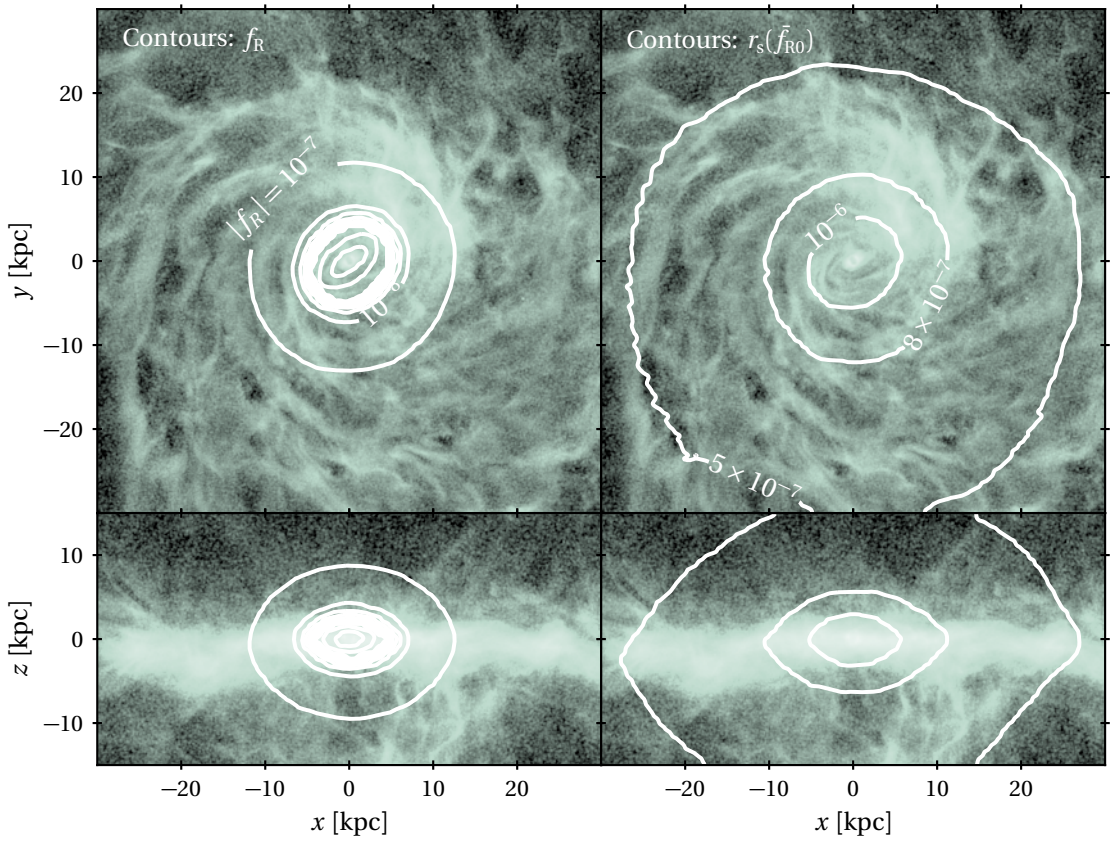

Figure 2.5: *Left*: Face-on *(top)* and edge-on *(bottom)* contour maps of the scalar field, for Au20 and a background field amplitude of $|\bar{f}_{R0}| = 10^{-6}$, evaluated in planes passing through the galaxy centre. *Right*: Face-on and edge-on contours showing the location of the screening surface for three *different* values of the background field amplitude, $|\bar{f}_{R0}|$: 10^{-6}, 8×10^{-7}, and 5×10^{-7}. The screening surface is here defined as the surface on which $f_R = 10^{-4}\bar{f}_{R0}$. The contours are superimposed on maps of the projected gas density.

8×10^{-7}. As in Figure 2.1, these three galaxies are chosen to represent a range of galaxy masses and morphologies. The resulting scalar field maps are qualitatively representative of the sample. In Figure 2.4, it can be seen that in the outer regions of the galaxies (i.e. $R \gtrsim 10$ kpc), the scalar field hovers roughly within an order of magnitude of the cosmic background value $\bar{f}_{R0}$. The scalar field in the innermost regions (i.e. $R \lesssim 5$ kpc), however, is suppressed by many orders of magnitude, with values as low as 10^{-16}. These regions are respectively the unscreened and screened regions.

A sharp transition can be seen between these regions at ~ 5 kpc for AuL8 and Au13, and ~ 15 kpc for Au21, where $|f_R|$ drops precipitously by many orders of magnitude. This is the screening radius of the galaxy, or more precisely its screening surface as there are clearly deviations from spherical symmetry. In the unscreened region outside the screening surface, particles are subject to a sizeable fifth force, whereas in the screened region enclosed by the screening surface, the gradients of the scalar field are sufficiently small that the fifth force is suppressed, according to Eq. (1.77). Equivalently, the ambient density in the screened region is sufficiently high, leading to an increased chameleon mass, which suppresses the range of the fifth force.

Interestingly, the disc-shaped mass distribution of the galaxy is reflected in the shape of the f_R field, which appears to be compressed into the galactic disc plane as can be seen in the lower panels of Fig. 2.4. These effects can also be seen in the left-hand panels of Fig. 2.5, where face-on and edge-on contour maps of the scalar field f_R for $|\bar{f}_{R0}| = 10^{-6}$ are shown for Au20, overlaid on gas density projections. These findings reflect those of Burrage *et al.* (2015), who analytically investigated the chameleon profiles around ellipsoidal objects.

As we shall see in the following sections, the location of the screening surface depends on a variety of factors: galaxy mass, galaxy density profile, environmental density, and $\bar{f}_{R0}$.

The effect of changing $\bar{f}_{R0}$ can be seen in the right-hand panels of Figure 2.5. The screening surfaces of Au20 (or more precisely the intersection of the screening surface with a plane in or perpendicular to the disc plane) are shown as contours for three values of $|\bar{f}_{R0}|$: 5×10^{-7}, 8×10^{-7}, 1×10^{-6}, overlaid on gas density projections. Note that here, the screening surfaces are defined as the surfaces at which $f_R = 10^{-4}\bar{f}_{R0}$. This was found to consistently fall inside the narrow transition zone. In this figure, it can be seen that larger values of $|\bar{f}_{R0}|$ correspond to smaller screening radii, and vice versa. For stronger background amplitudes of the scalar field, i.e. $|\bar{f}_{R0}| \gtrsim 2\times10^{-6}$, all galaxies investigated are entirely unscreened. Conversely, for most galaxies, weaker values ($\sim 10^{-7}$) lead to screening radii beyond the range over which observed rotation curves are typically measured.

2.3.2 Rotation Curves

The presence of a screening surface and the emergence of a fifth force outside it have an impact on the dynamics of galaxies. Figures 2.6 and 2.7 display the resulting effects on the rotation curves and radial acceleration relations of the studied galaxies. We make the assumption that the disc is rotationally supported everywhere.

The left-hand panel of Figure 2.6 shows the rotation curves calculated in the disc plane, including the fifth force contribution, of Au9 for five different values of $|\bar{f}_{R0}|$: 10^{-7}, 5×10^{-7}, 8×10^{-7}, 10^{-6}, and 2×10^{-6}. In each case, the rotation curve beyond the screening radius[3] is enhanced by the additional presence of the fifth force.

As was found in the previous sub-section, the case of $|\bar{f}_{R0}| = 2\times10^{-6}$ corresponds to the galaxy being entirely unscreened and the rotation curve being enhanced with respect to the standard gravity rotation curve throughout the galaxy. Conversely, the case of $|\bar{f}_{R0}| = 10^{-7}$ gives a screening radius larger than the range shown in the plot, and outside the typical range spanned by observed rotation curves. Thus, the predicted rotation curve is identical to that of standard gravity.

The intermediate cases, however, are the most interesting. At the screening radius, the rotation curve shows an 'upturn' as it transitions between the screened and unscreened

[3]Note that in the remainder of this chapter and the next, screening radius refers to the distance of the screening surface from the galaxy centre in the disc plane.

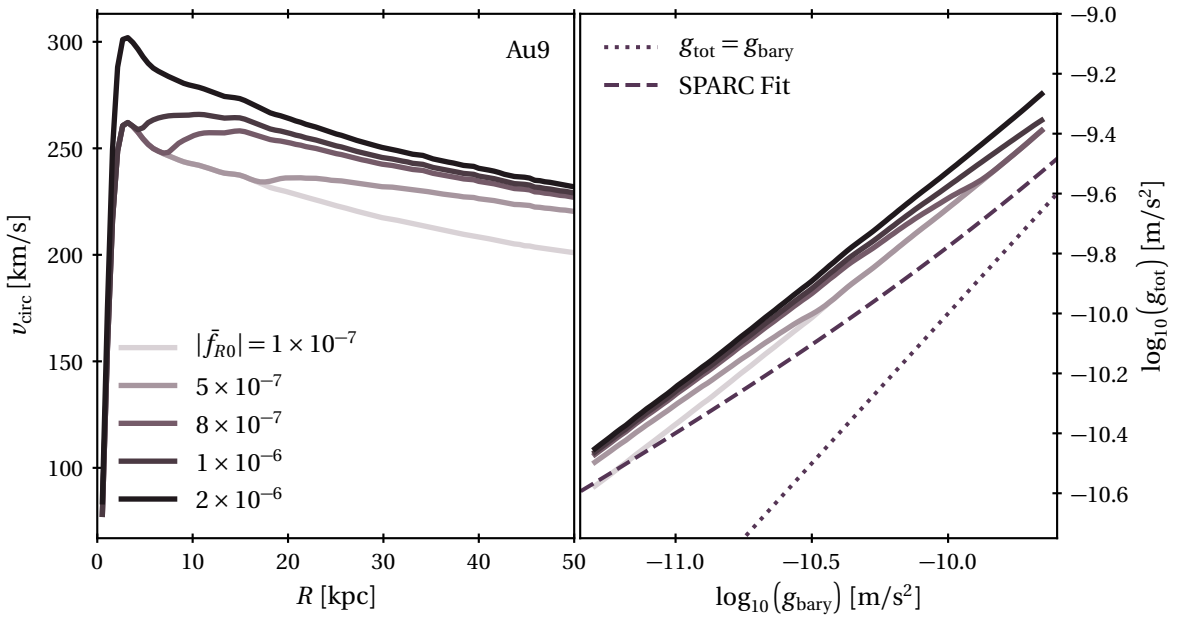

Figure 2.6: *Left:* Rotation curves of Au9 for six different values of $|\bar{f}_{R0}|$, as labelled. As described in the text, $v_{\rm circ}$ is calculated from the full gravitational acceleration, including a potential fifth force. *Right:* Radial acceleration relations for Au9, for the same $|\bar{f}_{R0}|$ values. The dotted line represents $g_{\rm tot} = g_{\rm bary}$, while the dashed line represents the best-fitting function for observed radial acceleration relations from the SPARC sample. $g_{\rm tot}$ is based on the full gravitational acceleration, including a potential fifth force, while $g_{\rm bary}$ is calculated at each radius from the enclosed baryonic mass assuming spherical symmetry and standard gravity, i.e. using $g_{\rm bary} = GM_{\rm bary}(< R)/R^2$.

regimes. Here and throughout the remainder of the thesis, a rotation curve 'upturn' is defined as the point where the modified gravity rotation curve diverges from the standard gravity rotation curve, coinciding with the screening radius of the galaxy. In some cases, such as those in Figure 2.6, the upturn manifests as a distinct kink in the rotation curve, but in other instances (e.g. Figure 2.3) no such kink is predicted. However, even if a real galaxy rotation curve in an $f(R)$ Universe fell into this latter category, the upturn might still be detectable if the dark matter and baryonic contributions to the rotation curve can be accurately modelled. Subtracting these from the full rotation curve would then leave only the fifth force contribution beyond the screening radius.

Studying the galaxies of the SPARC sample (Lelli *et al.*, 2016), McGaugh *et al.* (2016) found a remarkably tight relation between the total acceleration at each point inferred from rotation curves, and the acceleration due to baryonic mass inferred from observed light distributions. We have studied the effect of chameleon $f(R)$ gravity on this 'radial acceleration relation'. The results of this can be seen in the right-hand panel of Figure 2.6. Here, the baryonic acceleration $g_{\rm bary}$ is calculated at a given radius assuming spherical symmetry and neglecting a fifth force, i.e. adopting $GM_{\rm bary}(< R)/R^2$, while the total acceleration $g_{\rm tot}$, which would be measured from rotation curves, is calculated from the actual gravitational accelerations of the simulation particles, including the fifth force contribution.

Observed radial acceleration relations are typically smooth curves with only a small up-

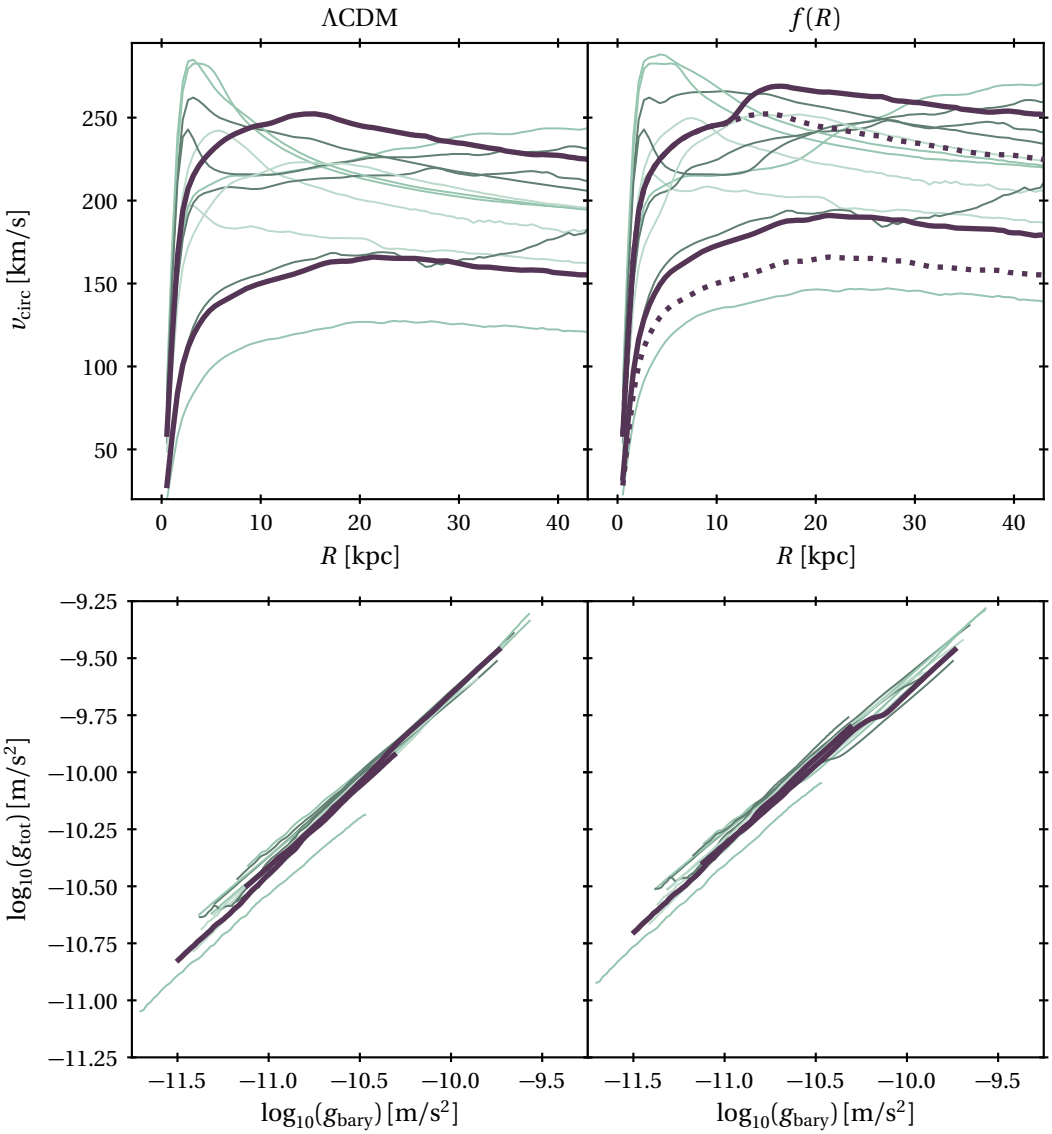

Figure 2.7: Rotation curves *(top)* and radial acceleration relations *(bottom)* for all 13 galaxies in the ΛCDM *(left)*) and $|\bar{f}_{R0}| = 10^{-6}$ *(right)*) cases. As discussed in the text, galaxies Au21 and AuL1 are highlighted in all panels. The dotted lines in the right-hand rotation curve panel shows the standard gravity rotation curves for Au21 and AuL1, to enable more direct comparison with the $f(R)$ curves.

ward curvature. If no screening radius is present in the considered range, the simulation predictions give almost straight lines in this log-log plot. Mirroring the rotation curves in the left-hand panel, the strongest $\bar{f}_{R0}$ values give lines that are consistently enhanced with respect to the standard gravity case, while at the other end, the $|\bar{f}_{R0}| = 10^{-7}$ line is identical to the standard gravity case. The intermediate cases, meanwhile, show marked bumps in the relations, corresponding to the screening radii. This is a promising result: the absence of these easily distinguishable bumps in observed radial acceleration relations could place strong constraints on $\bar{f}_{R0}$.

Also shown in the right panel of this figure is the best-fitting function for the radial acceleration relation from the SPARC galaxies (equation 4 from McGaugh *et al.*, 2016). As

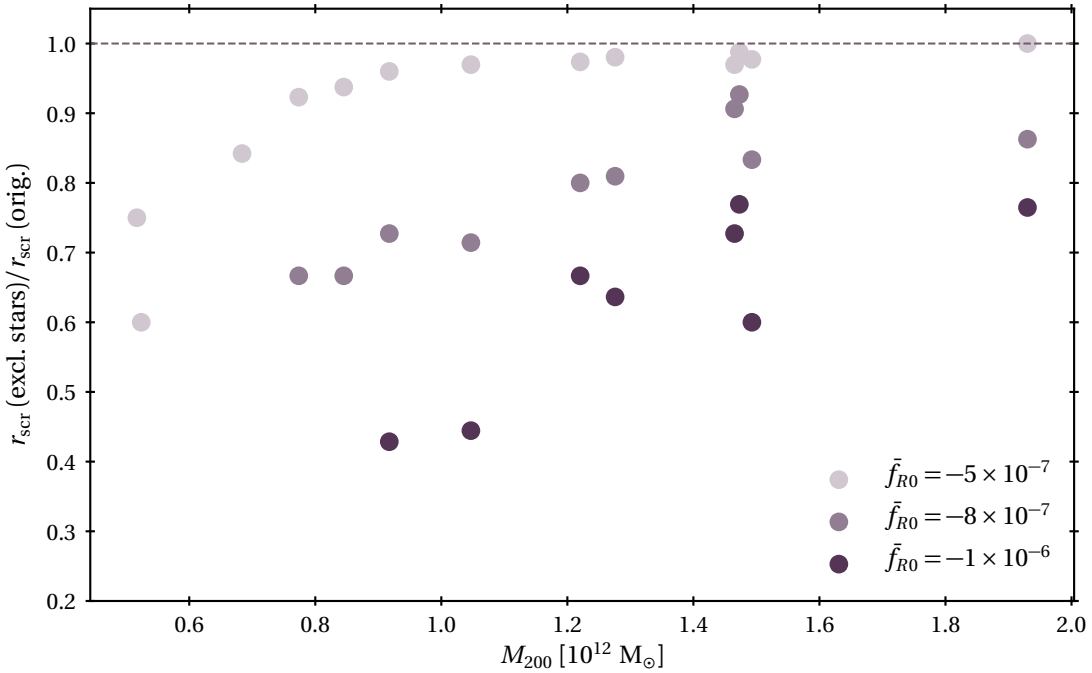

Figure 2.8: Ratio of screening radii including and excluding star particles as a source of the fifth force, as a function of halo mass. The three colours indicate calculations for three different values of $\bar{f}_{R0}$. For smaller $\bar{f}_{R0}$ values, the screening radius is larger and falls in a region in which the density is dominated by dark matter so that the effect of including / excluding stars is reduced. Therefore, the screening is less sensitive to self-screening of stars in this regime.

can be seen here with the case of Au9, the Auriga galaxies are consistently to be found lying above this best-fitting relation. This mirrors the findings of other simulations, e.g. the MassiveBlack-II simulations (Tenneti *et al.*, 2018), and could be related to the central density profile of the dark matter halo.

Figure 2.7 shows the rotation curves and radial acceleration relations of all thirteen galaxies studied, for ΛCDM and $|\bar{f}_{R0}| = 10^{-6}$. Galaxies Au21 and AuL1 are highlighted, in order to illustrate two contrasting cases: the upper rotation curve, that of Au21, shows a clearly distinguishable upturn at its screening radius, ~ 10 kpc, in the upper right panel, while AuL1 is unscreened throughout, yielding no such observable feature.

2.3.3 Stellar Self-Screening

Like all cosmological simulations, modified gravity N-body simulations have limited spatial and mass resolution. Compact bodies such as stars are not resolved in cosmological runs, and are instead treated using simulation particles that represent whole stellar populations.

Ordinarily, this is a sufficient approximation, but in the case of screened modified gravity theories, one might expect some or all of the stars to be sufficiently dense so as to be self-screened, and therefore neither source nor couple to the fifth force, depending on the

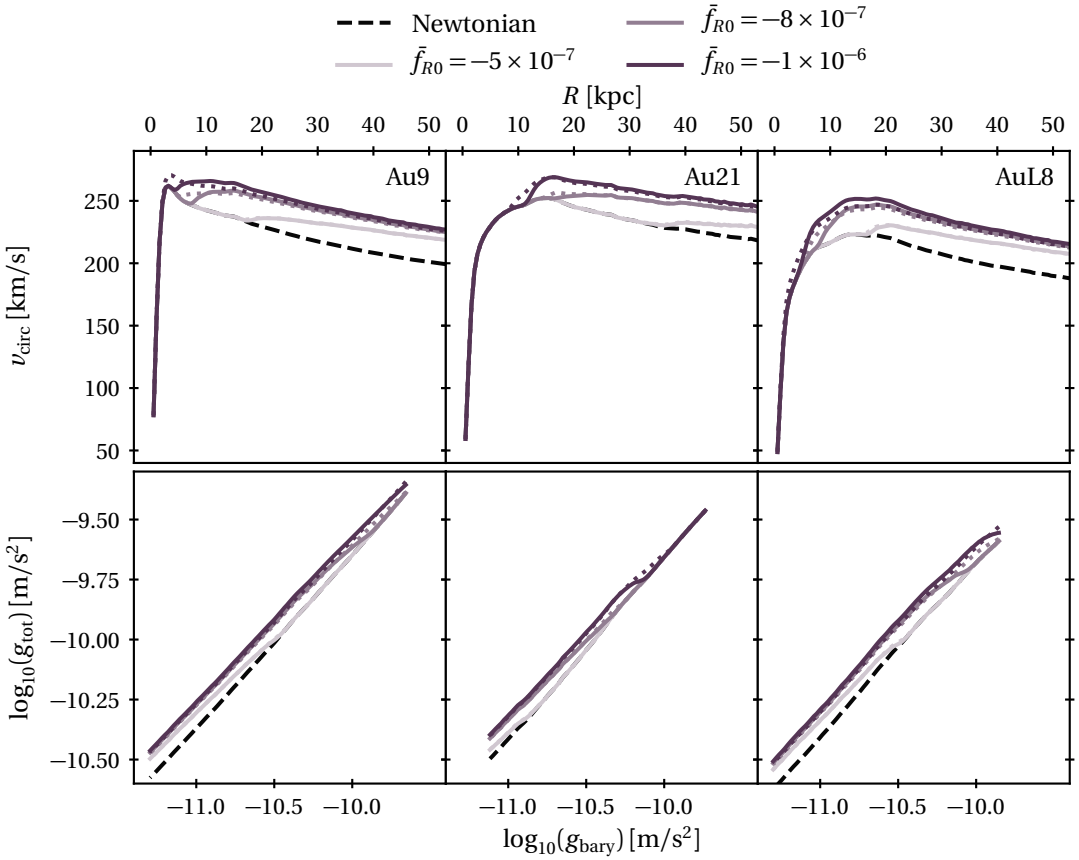

Figure 2.9: Rotation curves *(top)* and radial acceleration relations *(bottom)* for the gas components of Au9, Au21, and AuL8, including *(solid)* and excluding *(dotted)* the contribution of star particles to the fifth force. The dashed lines ignore the fifth force contributions altogether and hence correspond to ΛCDM.

environment of a given star and the background amplitude of the scalar field (Davis *et al.*, 2012).

This is an effective violation of the EP, and gives rise to several of the galaxy-scale tests of screened modified gravity listed in the Introduction (§ 1.3.5). These aside, another effect would be that the fifth force in a given galaxy will be somewhat weaker than those calculated in the previous subsections if stars do not act as sources of the fifth force. In order to quantify this effect, we have trialled an alternative method for post-processing the Auriga simulations. The star particles in the snapshots are included in the calculation of the standard gravitational acceleration, but excluded from the calculation of the scalar field. This corresponds to the extreme scenario, in which every star is fully self-screened, and thus not coupling to the scalar field. In reality, the scalar field would be an intermediate between this solution and the original solution of the previous subsections. In particular, for values of $|\bar{f}_{R0}| \geq 10^{-6}$ we would expect stars to start becoming unscreened and thus recovering our original solution (Davis *et al.*, 2012). However, performing this fully self-consistent calculation would be difficult in practice and we choose instead to show the maximal effect of stellar self-screening.

Figures 2.8 and 2.9 show the results of this test. Figure 2.8 shows, for three different $\bar{f}_{R0}$

values, the ratio of the screening radii for all 13 galaxies in the new and original solutions, as a function of halo mass. One immediately apparent point is that the effect of excluding the stars from the scalar field calculation results in a shrinking of the screening radius. This is to be expected, as the exclusion of stars results in an object of lower *effective* mass,[4] that has a correspondingly smaller screening radius.

Another point is that higher amplitudes for the background scalar field result in greater differences between the two solutions. The reason for this is that, as seen in Figure 2.5, higher values for $|\bar{f}_{R0}|$ give smaller screening radii. At smaller radii, the stellar population becomes an increasingly dominant component of the overall density profile. Indeed, it is typically the case in the Auriga galaxies that the stars dominate over the dark matter component in the central few kpc, and are a significant component for a few kpc beyond. Thus, the effect of excluding them from the scalar field calculation becomes more significant towards the centre. It is also for this reason that lower mass haloes appear to show more of a difference; the lower mass haloes tend to have smaller screening radii than their larger counterparts for a given $\bar{f}_{R0}$.

Figure 2.9 shows the effect of stellar self-screening on the rotation curves and radial acceleration relations of the gas component for three galaxies, and three values of $\bar{f}_{R0}$. As in Figure 2.8, the effect is that of shrinking the screening radii, and thus shifting the locations of the rotation curve upturns and the corresponding bumps in the radial acceleration relations. As before, the magnitude of the shift varies with the galaxy in question, and the value assumed for $\bar{f}_{R0}$. In the most extreme case, the shift in the rotation curve upturn is 2-3kpc. This is a sizeable shift, but it should be borne in mind that this is the most extreme shift caused by the most extreme assumption: that all stars are fully self-screened, and that the screening radius of the galaxy is at a position where the density has a large stellar contribution. To test gravity, it might be preferable to use rotation curves at large radii, where the stellar density contribution is small. Then the effect of stellar self-screening on the rotation curve of the gas component is small as well, as seen for the $|\bar{f}_{R0}| = 5 \times 10^{-7}$ model.

2.3.4 Environmental Screening

The environment of a galaxy is expected to play a role in its screening. For example, a galaxy situated in a dense, group environment should have a larger screening radius than that of a galaxy situated in an underdense void.

One can conceptualise this in the following way: from Eqs. (1.69) and (1.70) one finds that for small perturbations in the unscreened (low-curvature) regime the scalar field perturbation is given by $\delta f_R \equiv f_R - \bar{f}_{R0} \approx -2/3\,\Phi/c^2$, where Φ is the gravitational potential of the considered mass distribution that obeys the modified Poisson equation (1.70). Screening

[4] Recall the definition of effective density, Eq. (1.86)

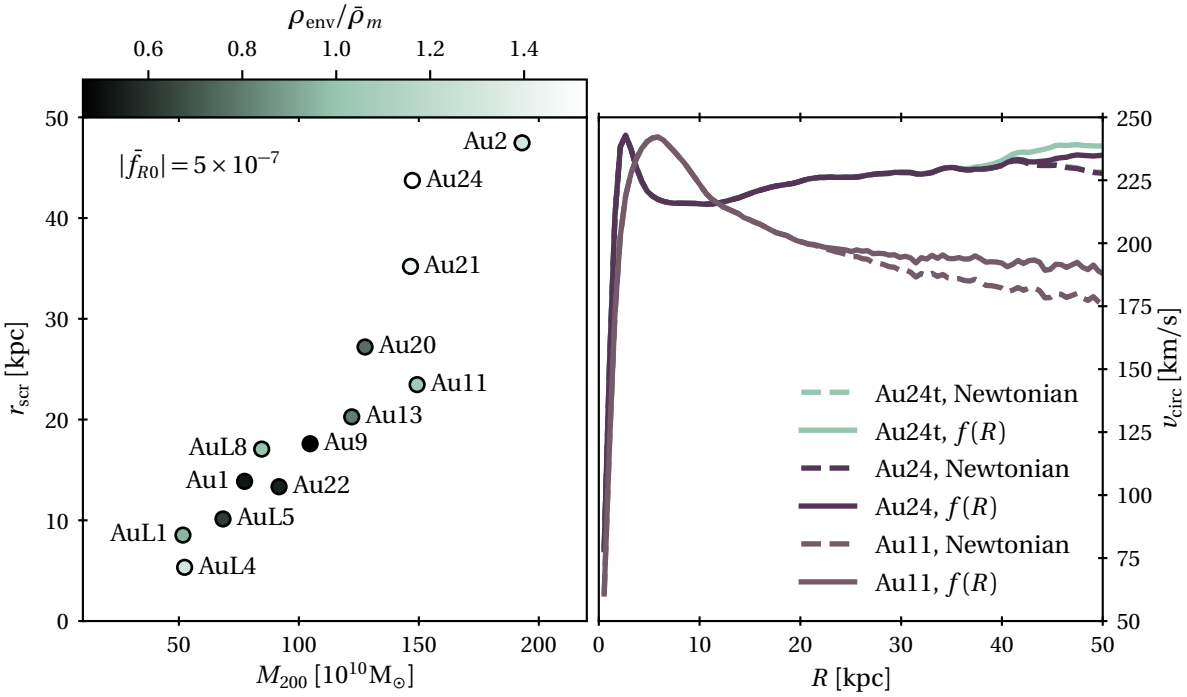

Figure 2.10: *Left:* Screening radius as a function of mass for all 13 galaxies, calculated with $|\bar{f}_{R0}| = 5\times10^{-7}$. The colours of the circles indicate the 'environmental density' of the galaxy: the average density in a spherical shell centred on the galaxy, with inner radius $5R_{200}$, and outer radius $20R_{200}$, in units of the cosmic mean matter density. *Right:* For the same value of $\bar{f}_{R0}$, rotation curves for Au11 and Au24. The 'Au24t' result was obtained by transplanting Au24 into the environment of Au11 as discussed in the text. Solid lines include the fifth force contribution, while the dashed lines ignore it. Au24 and Au11 were chosen for this test because of their similar masses but differing environmental densities (see left panel).

is triggered approximately when $\delta f_R \approx -\bar{f}_R$, as then $f_R \approx 0$ and its gradient which controls the fifth force is also suppressed. Thus, the screening becomes effective roughly when $|\Phi|/c^2 \gtrsim 3/2\,|\bar{f}_{R0}|$ (see, e.g., Hui *et al.*, 2009; Arnold *et al.*, 2014). If an overdense environment contributes to the Newtonian potential at the position of a halo, the halo's own potential does not then have to be as deep to trigger screening.

Figure 2.10 shows the results of a preliminary investigation into the magnitude of this effect. The left-hand panel shows the relation between screening radius and halo mass for all 13 galaxies in our sample, for $|\bar{f}_{R0}| = 5\times10^{-7}$. The colours of the filled circles encode the 'environmental density': the average density in a spherical shell centred around the galaxy, with inner radius $5R_{200}$, and outer radius $20R_{200}$. The inner radius was chosen as we found that for smaller radii the density profiles typically still follows the NFW profile, while the outer radius is comparable to the cosmological Compton wavelength, so that the effect of the environment on even larger scales on f_R should be suppressed.

The left panel of Figure 2.10 indeed suggests that there might be a mild tendency of halos in dense environments having larger screening radii at similar halo mass.

Taking two galaxies with reasonably similar masses but very different environmental densities, Au24 and Au11, we investigated the effect of transplanting the former into the

environment of the latter. A sphere of radius $5R_{200}$ was cut out from the simulation volume of Au24 and placed into that of Au11, in the place formerly occupied by the galaxy Au11. This modified snapshot was then post-processed with MG-Gadget as usual.

The results of this test are shown in the right-hand panel of Figure 2.10, which shows the rotation curves of the three galaxies: the original Au11 and Au24, as well as the transplanted Au24, referred to as 'Au24t'. As in the left-hand panel, $|\bar{f}_{R0}| = 5 \times 10^{-7}$ was assumed. The effect of the differing environments on the scalar field profiles is marginal. Only a small part of the difference in screening radius between Au11 and Au24 is explained by the environmental density. At least in this case, differences in the self-screening, due to different halo concentrations, largely dominate over differences in the environmental screening.

A major factor in the limited effect of environmental screening is likely that the galaxies of the Auriga sample are isolated galaxies; this was a criterion for selecting the galaxies from the parent simulation volume. Environmental screening would likely play a much larger role in the scalar field profiles of cluster galaxies.

When performing observational tests of screened modified gravity with galaxy kinematics, isolated galaxies would also be preferable to those inhabiting dense environments, so as to reduce the degeneracy between environmental screening and background field amplitude. The Auriga simulation sample should hence be a suitable testbed for such studies. Residual environmental effects could likely be further mitigated by taking an estimate of the density of a galaxy's environment into account when using its rotation curve to constrain modified gravity.

2.4 Discussion

We have found in section § 2.3.2 that in HS $f(R)$ gravity galaxy rotation curves exhibit a distinct feature near the screening radius, namely an upturn in the circular velocity. A corresponding bump can be seen in the radial acceleration relation. Here, we discuss the utility of these features to constrain modified gravity models.

While features of the predicted size would be clearly visible in measured rotation curves, great care must be taken in their interpretation. In particular, a potential astrophysical origin of such features as, e.g., a substructure in the galaxy or a complex dynamical state after a merger have to be ruled out.

However, if an observed upturn is indeed due to a screening radius plus fifth force, the position of the upturn implies a specific value for $\bar{f}_{R0}$,[5] which in turn dictates the locations of possible features in the rotation curves of other galaxies. If features are consistently found at these predicted locations, this would lend strong support to $f(R)$ gravity. Conversely, if features are absent at these radii, that would suggest the original upturn was due

[5] Or, for chameleon theories more generally, the self-screening parameter χ_0; cf. Eq. (1.63).

to some other effect. Thus, the strongest conclusions can be drawn by performing fits to large ensembles of rotation curves and testing whether a single $\bar{f}_{R0}$ value allows good fits for the whole sample. In this context, it is however worth considering the two potential complications that we have investigated in Secs. 2.3.3 and 2.3.4, i.e. stellar self-screening and environmental screening which could both affect the exact position of an upturn.

The effect of stellar self-screening on the overall scalar field solution has been neglected in the bulk of the calculations throughout this work. This assumption is dropped in § 2.3.3, where we instead consider the opposite extreme, in which all stars are assumed to be fully self-screened, and not acting at all as source of the fifth force. This typically led to an inward shift of the screening radius, in the most extreme cases by 2-3kpc. A safer option to avoid uncertainties related to this might be to use observed rotation curves at large radii, where the stellar contribution to the mass density is subdominant and a potential shift of an upturn is much smaller.

In addition to potentially preventing stars from acting as a source of the fifth force, self-shielding would also (partly) prevent them from feeling the acceleration by the fifth force. This would result in different rotation curves for stars and gas, as the latter would not self-screen. Rotation curves of the gas component at larger radii may, hence, be the most reliable probe of a fifth force. Alternatively, one can search for differences between stellar and gas rotation curves. This approach has been adopted by Vikram *et al.* (2018), who analysed the gaseous and stellar rotation curves of dwarf galaxies. Rather than searching for upturns, that work searches for differences in the normalisation between gaseous and stellar rotation curves, caused by stellar self-screening, in galaxies that are likely unscreened otherwise.

In § 2.3.4, it was found that the environment of a galaxy also plays a role in determining the scalar field solution. Galaxies in overdense environments have screening radii further from their centre than they would have if the environmental density was equal to the cosmic mean. Conversely, void galaxies have screening radii closer in. These environmental effects will therefore also alter the position of upturns in rotation curves. In the case considered in § 2.3.4, the effect of environmental screening was nevertheless found to be marginal. However, Au24 and Au11 are among the most massive galaxies in the sample, and environmental screening might well play more of a role in lower-mass galaxies. The effect of environmental screening should therefore be accounted for when performing a quantitative fit to observed rotation curves. This could either be done statistically, with an additional free parameter for the environmental density with a prior informed by simulations, or by directly studying the environment of galaxies with measured rotation curves. A step in the latter direction is the 'screening map' presented by (Cabré *et al.*, 2012); a three-dimensional map, covering a large portion of the sky, which employs large galaxy and cluster catalogues in order to calculate, at each point, the Newtonian potential due to external objects. If, for a given astrophysical object, $\Phi_{\rm ext}/c^2 \ll |\bar{f}_{R0}|$, then one can assume that

self-screening of the galaxy dominates over environmental screening. Vikram *et al.* (2018) have employed this screening map in their sample selection. Furthermore, Desmond *et al.* (2018c) have built upon the above work by creating an updated screening map, featuring more sophisticated techniques and a more complete sky map.

As an alternative to searching for upturns, one could also use completely smooth sections of rotation curves to rule out the presence of a screening radius in those regions. Using such sections in a sample of galaxies of different masses should allow the ruling out of large parts of the modified gravity parameter space.

For our roughly Milky Way-sized halos we find that the galaxies are typically screened at the galactocentric distance of the Solar System of ~ 8kpc for background field amplitudes of $|\bar{f}_{R0}| \lesssim 8 \times 10^{-7}$, suggesting that $|\bar{f}_{R0}|$ cannot be much larger than this value. Searching for evidence of screening in rotation curves at larger radii and/or lower mass galaxies will allow probing even smaller field amplitudes. In the SPARC sample, accurate rotation curves have been measured for objects with rotational velocities down to ~ 50 km/s, roughly four times smaller than that of the Milky Way. The square of the circular velocity is expected to be roughly proportional to the depth of the Newtonian potential. The latter can be used to estimate the maximum background field amplitude at which chameleon screening is triggered in an object (see Sec. 2.3.4). Together, this suggests that using rotation curves of lower mass galaxies, it should be possible to constrain $f(R)$-gravity down to $|\bar{f}_{R0}|$ values of $\sim 10^{-7}$, which would be very competitive compared to other techniques.

2.5 Conclusions

We have studied the impact of HS $f(R)$ gravity on rotation curves and radial acceleration relations of disc galaxies. To this end, we have post-processed state-of-the-art ΛCDM simulations of disc galaxy formation from the Auriga Project with the modified gravity solver of the MG-Gadget code. This is numerically much cheaper than performing full physics, galaxy formation simulations with $f(R)$ gravity, which remains very challenging. The validity of this post-processing approach is established in Sec. 2.2.2.

In addition to investigating the kinematic structure, we have studied the scalar field morphology and the transition from the screened to the unscreened region. Our main findings are:

- In HS $f(R)$ gravity, the scalar field iso-contours in disc galaxies inherit an oblate shape from the mass distribution. This results in a discoid screening surface (rather than a simple screening radius). This needs to be taken into account when predicting modified gravity effects on rotation curves.

- At the position where the galactic disc penetrates the screening surface, a distinct upturn is present in the rotation curve. The rotational velocity in the unscreened region is enhanced by the fifth force by up to a factor $\sim \sqrt{4/3}$.
- A corresponding distinct bump is present in the radial acceleration relation.
- Lower values of the comic background scalar field, $|\bar{f}_{R0}|$, lead to larger screening radii, and therefore rotation curve upturns that are more distant from the galactic centre. Conversely, more massive objects have smaller screening radii at fixed $|\bar{f}_{R0}|$.
- Stellar self-screening and environmental screening can also affect the position of the upturn in the rotation curve. The former effect is negligible for upturns at large radii where the stellar contribution to the mass density is small. Environmental screening is a sub-dominant effect for the Milky Way-sized galaxies considered here, but may be more important in lower mass galaxies.
- Stellar self-screening will also result in different rotation curves of stars and gas. Since the gas will not self-screen, its rotation curve might be easier to interpret.
- The predicted rotation curve upturns are qualitatively similar to upturns seen in at least some observed galaxies. These signatures, provide a potentially promising avenue toward strong constraints on $f(R)$ gravity. However, as discussed in Sec. 2.4, a careful statistical analysis of galaxy samples will be needed to unambiguously distinguish modified gravity effects from astrophysical effects on rotation curves and radial acceleration relations.
- In the model with the smallest background scalar field amplitude, $|\bar{f}_{R0}| = 1 \times 10^{-7}$, the rotation curves and radial accelerations of all galaxies considered were indistinguishable from the ΛCDM case. Conversely, at the other end of the spectrum, all galaxies were unscreened for $|\bar{f}_{R0}| = 10^{-5}$ and 2×10^{-6}, and therefore their rotation curves were enhanced with respect to ΛCDM throughout the entire disc. The intermediate values of $\bar{f}_{R0}$ are hence the most interesting. It is at these values that rotation curves and radial acceleration relations display upturns and bumps that would be visible in observational data. Note, however, that lower mass galaxies will be sensitive to correspondingly smaller $|\bar{f}_{R0}|$ values. Sensitivities down to $|\bar{f}_{R0}| \sim 10^{-7}$ should be achievable with existing data.

Our results indicate that rotation curves and radial acceleration relations can provide constraints on screened modified gravity that are very competitive with constraints from larger scales, e.g., employing the next generation of galaxy clustering and weak lensing surveys. Furthermore, they are complementary to these surveys as they test gravity on different scales. The following chapter presents an analysis of the observed rotation curves of the SPARC sample, with a view towards searching for the upturn signature predicted in this chapter and deriving such constraints.

Chapter 3

Upturns in Observed Rotation Curves

Summary

The previous chapter demonstrated that in chameleon theories such as HS $f(R)$ gravity, the fifth force will lead to 'upturns' in galaxy rotation curves near the screening radius. The location of the upturn depends on the cosmic background value of the scalar field $\bar{f}_{R0}$, as well as the mass, size and environment of the galaxy. In this chapter, I search for this signature of modified gravity in the SPARC sample of measured rotation curves, using an MCMC technique to derive constraints on $\bar{f}_{R0}$. Assuming NFW dark matter haloes and with $\bar{f}_{R0}$ freely varying for each galaxy, most galaxies prefer $f(R)$ gravity to ΛCDM, but there is a large spread of inferred $\bar{f}_{R0}$ values, inconsistent with a single global value. Requiring instead a global $\bar{f}_{R0}$ value for the whole sample, models with $\log_{10}|\bar{f}_{R0}| > -6.1$ are excluded. On the other hand, models in the range $-7.5 < \log_{10}|\bar{f}_{R0}| < -6.5$ seem to be favoured with respect to ΛCDM, with a significant peak at -7. However, this signal is largely a result of galaxies for which the $f(R)$ signal is degenerate with the core/cusp problem, and when the NFW profile is replaced with a cored halo profile, ΛCDM gives better fits than any given $f(R)$ model. Thus, I find no convincing evidence of $f(R)$ gravity down to the level of $|\bar{f}_{R0}| \sim 6\times10^{-8}$, with the caveat that if cored halo density profiles cannot ultimately be explained within ΛCDM, a screened modified gravity theory could possibly provide an alternative solution for the core/cusp problem. However, the $f(R)$ models studied here fall short of achieving this.

This chapter is based on the article:

A. P. Naik, E. Puchwein, A.-C. Davis, D. Sijacki, H. Desmond

Constraints on chameleon f(R) gravity from galaxy rotation curves of the SPARC sample

MNRAS, Volume 489, Issue 1, October 2019, Pages 771–787

The evaluation of the screening map at the locations of the SPARC galaxies (see § 3.3.3) was undertaken by Harry Desmond, one of the co-authors of the above article. The remainder of the work presented in this chapter is my own, informed and guided by discussions with the other authors.

3.1 Background

The previous chapter demonstrated that the presence of a chameleon fifth force would lead to observable imprints on galactic rotation curves. Specifically, there will be a 'screening radius' beyond which the fifth force is active. Within the radius, standard gravity is restored. This has the consequence that an 'upturn' appears in the rotation curve at this screening radius, with a fifth force enhancement beyond the screening radius. The location of this screening radius within a given galaxy depends on the global value of $\bar{f}_{R0}$ and the environment of the galaxy, as well as its mass and size.

In this chapter, we use the Spitzer Photometry and Accurate Rotation Curves (SPARC; Lelli *et al.*, 2016) sample of high-quality rotation curve measurements to search for this signature. After several cuts to the sample, 85 galaxies remain, each of which we model with a gaseous disc, a stellar disc, a dark matter halo, and where appropriate, a stellar bulge. Using these components, we solve the $f(R)$ scalar field equations for the fifth force contribution, thereby constructing a forward model for the galaxy's rotation curve. With these models, we then employ an MCMC technique to explore the posterior probabilities for the parameters for each galaxy, looking in particular at the inferred values for the background value of the scalar field $\bar{f}_{R0}$. We also perform model comparisons between $f(R)$ and ΛCDM using the likelihood ratios calculated for our best-fitting models.

Several recent studies have worked with the SPARC sample, e.g. McGaugh *et al.* (2016); Desmond (2017a,b); Lelli *et al.* (2017); Li *et al.* (2018); McGaugh *et al.* (2018); Li *et al.* (2019a). Of particular relevance to this chapter, however, is the study of Katz *et al.* (2017). In that work, the SPARC galaxies were used to investigate the core/cusp problem (see § 1.1.5). The authors found that fits to the rotation curves typically improved when cuspy 'NFW' haloes (Navarro *et al.*, 1997) were replaced with the cored 'DC14' haloes of Di Cintio *et al.* (2014), derived empirically from ΛCDM simulations incorporating subgrid stellar feedback mechanisms.

We argued in Chapter 2 that the NFW profile provides not only a good fit to dark matter haloes in ΛCDM simulations, but also in $f(R)$ simulations. In fact in $f(R)$ gravity, depending on halo mass, a higher concentration of the NFW profile is needed (e.g. Arnold *et al.*, 2019a). Thus, $f(R)$ gravity does not reduce the central densities of haloes and consequently does not offer a direct solution to the core/cusp problem. However, Lombriser & Peñarrubia (2015) made an interesting observation: a chameleon fifth force in the outer regions of a cuspy halo can mimic the observational signature of a cored halo profile in measurements of the kinematics of galaxies. We will discuss this possibility further in § 3.4 and § 3.5.

Baryonic feedback mechanisms that could in principle lead to the formation of a halo core, would likely be as able to do so under modified gravity as under ΛCDM. We, therefore explore the impact of a cored density profile by computing results both for NFW and DC14 haloes (similar to Katz *et al.*, 2017). We utilise a model in which $\bar{f}_{R0}$ is allowed to vary freely

for each galaxy, as well as a grid of models covering a range of $\bar{f}_{R0}$ values fixed for the whole sample. In the former case, we analyse the marginal posteriors on $\bar{f}_{R0}$ for each galaxy to find any evidence of significant clustering around a single preferred value. In the latter case, we are able to compare each model with ΛCDM, and thus search more directly for any evidence of a globally preferred value for $\bar{f}_{R0}$.

We also explore several different prescriptions for the mass-to-light ratios, and the impacts of stellar and environmental screening.

All of the code, analysis tools, and plotting scripts used in this chapter have been made publicly available.[1]

This chapter is structured as follows. § 3.2 describes the SPARC data set and § 3.3 describes our methodology. Results are then outlined in § 3.4, before discussion and concluding remarks in § 3.5.

3.2 Data

For this investigation, we have used the rotation curves from the SPARC sample (Lelli *et al.*, 2016). The SPARC sample consists of 175 high-quality HI/Hα rotation curves, along with accompanying 3.6μm photometry from Spitzer. The sample is diverse, spanning 5 orders of magnitude in mass, and encompassing a variety of morphologies. 3.6μm surface brightness is believed to be a good tracer of stellar mass, so its pairing with rotation curve data enables detailed modelling of the different components of a given galaxy.

For each galaxy, the SPARC sample includes a wealth of information. Most relevant is $v_{\rm circ}(R)$, the rotation speed as a function of radius, along with its corresponding error bars. In addition to this, the photometry information is converted into contributions to the rotation speed due to the stellar disc and stellar bulge, $v_{\rm disc}$ and $v_{\rm bulge}$. The bulge component is only included for galaxies for which the photometry profile departs significantly from an exponential disc profile in the central regions, a minority of the overall sample (13 of our final 85 galaxies). The quantities $v_{\rm disc}$ and $v_{\rm bulge}$ are based on a mass-to-light ratio of $1\,M_\odot/L_\odot$, and therefore need re-scaling for any other assumed ratio. Finally, for each galaxy, gas surface brightness information has been converted into a gas contribution $v_{\rm gas}$. A more detailed description of the data and the derivation of the velocity components can be found in Lelli *et al.* (2016).

From the original sample of 175 galaxies, we make a series of cuts, yielding a final sample of 85 galaxies. The cuts are summarised below, along with numbers in parenthesis indicating how many galaxies were removed at each successive cut.

We include galaxies for which:

[1] github.com/aneeshnaik/spam

Model	Theory	$\bar{f}_{R0}$	Halo	$\rho_{\rm env}$	$a_{5,*}$	Υ	Parameters
A	ΛCDM	-	NFW	-	-	1	$v_{\rm vir}$, $c_{\rm vir}$, Υ, σ_g
B	$f(R)$	Varying	NFW	×	×	1	$\bar{f}_{R0}$, $v_{\rm vir}$, $c_{\rm vir}$, Υ, σ_g
C	$f(R)$	Varying	NFW	✓	×	1	$\bar{f}_{R0}$, $v_{\rm vir}$, $c_{\rm vir}$, Υ, σ_g
D	$f(R)$	Varying	NFW	×	✓	1	$\bar{f}_{R0}$, $v_{\rm vir}$, $c_{\rm vir}$, Υ, σ_g
E	$f(R)$	Varying	NFW	×	×	0	$\bar{f}_{R0}$, $v_{\rm vir}$, $c_{\rm vir}$, σ_g
F	$f(R)$	Varying	NFW	×	×	2	$\bar{f}_{R0}$, $v_{\rm vir}$, $c_{\rm vir}$, $\Upsilon_{\rm disc}$, $\Upsilon_{\rm bulge}$, σ_g
G	ΛCDM	-	DC14	-	-	1	$v_{\rm vir}$, $c_{\rm vir}$, Υ, σ_g
H0-19	$f(R)$	Imposed	NFW	×	×	1	$v_{\rm vir}$, $c_{\rm vir}$, Υ, σ_g
I0-19	$f(R)$	Imposed	DC14	×	×	1	$v_{\rm vir}$, $c_{\rm vir}$, Υ, σ_g

Table 3.1: Summary of the models investigated in this chapter. Columns are (1) Model: the alphabetical/alphanumerical ID corresponding to a given model, (2) Theory: ΛCDM or $f(R)$, i.e. whether or not a fifth force contribution is included in the rotation curve model, (3) $\bar{f}_{R0}$: for an $f(R)$ model, $\bar{f}_{R0}$ is either left as a freely 'varying' parameter, or in the case of Models H0-19 and I0-19, imposed as a series of 20 fixed values given in Table 3.2 (see discussion in § 3.3.1), (4) DM Halo: NFW or DC14 dark matter halo profile (§ 3.3.1), (5) $\rho_{\rm env}$: whether a large-scale environment is added to the scalar field solver (§ 3.3.3). Note that in all models, we take into account environmental screening effects with the final sample cut discussed in § 3.2, and this additional test is merely to ensure that the remaining sample is largely unaffected by environmental screening. (6) Stellar Screening: whether the stellar component is *excluded* from sourcing a fifth force in the scalar field solver (§ 3.3.4), (7) Υ: Whether the mass-to-light ratio is treated with one free parameter (using the same ratio for disc and bulge),'1', two free parameters (allowing for different values for disc and bulge),'2', or as 'fixed' empirical values,'0' (§ 3.3.1), and (8) Parameters: a list of the free parameters for a given model (see main text for details).

- There are ≥ 5 data points. $(175-4=171)$
- Inclination $i \geq 30°$. $(171-12=159)$
- Quality flag $Q=1,2$. This excludes galaxies with major asymmetries, for which $Q=3$. $(159-10=149)$
- Information about the HI gas distribution is available. This excludes galaxies for which the $v_{\rm gas}$ contribution can only be estimated approximately. $(149-2=147)$
- There is not a significant environmental screening effect. See § 3.3.3 for a more detailed description of this cut. $(147-62=85)$

3.3 Methods

3.3.1 Rotation Curve Models

In this study, we have experimented with a range of different models for galaxy rotation curves, e.g., models with different dark matter halo profiles, fixed or varying $\bar{f}_{R0}$, as well

as different treatments of mass-to-light ratio, environmental effects and a potential self-screening of stars. A summary of the models investigated can be found in Table 3.1. The terms used in this table will be explained over the course of the following few subsections.

Following Eq. (1.44), we construct a circular velocity model $v_{\rm model}$ for each galaxy, given by

$$v^2_{\rm model}(R) = a_{\rm tot} R = (a_{\rm N} + a_5) R, \tag{3.1}$$

where R is the distance in the disc plane from the centre of the galaxy, $a_{\rm N}$ is the component of the standard gravity (Newtonian) acceleration evaluated in the disc plane at radius R and pointing radially inwards, and a_5 is the analogous acceleration component due to the fifth force.

The Newtonian acceleration $a_{\rm N}$ is sourced by the various components of the galaxy: the gas, stellar disc, stellar bulge, and dark matter. This relationship can be written as

$$a_{\rm N}(R) = \frac{v^2_{\rm gas} + v^2_{\rm DM} + \Upsilon_{\rm disc} v^2_{\rm disc} + \Upsilon_{\rm bulge} v^2_{\rm bulge}}{R}, \tag{3.2}$$

where v_x is the contribution of component x to the overall velocity curve as a function of radius R, and $\Upsilon_{\rm disc}$ and $\Upsilon_{\rm bulge}$ are the mass-to-light ratios for the stellar disc and bulge. The gaseous and stellar contributions ($v_{\rm gas}$, $v_{\rm disc}$, and $v_{\rm bulge}$) have been calculated by the SPARC team and are included within the SPARC data. Note also that the bulge term only applies to galaxies for which the SPARC team have found evidence for a stellar bulge, and have included a corresponding $v_{\rm bulge}$ contribution in the data; this corresponds to 13 of the 85 galaxies in our final sample.

All that remains to complete the model is to calculate the dark matter contribution $v_{\rm DM}$, the mass-to-light ratios Υ, and the acceleration due to the fifth force a_5.

Firstly, we calculate the dark matter contribution $v_{\rm DM}$ by modelling the dark matter halo as a 2-parameter profile. We consider two different choices for the profile: the NFW profile (1.45), as well as the 'DC14' profile of Di Cintio *et al.* (2014). The latter profile is derived empirically from ΛCDM simulations incorporating baryonic feedback, and provides a more 'cored' profile than NFW for galaxies with a significant stellar component. It was found by Katz *et al.* (2017) to provide a better fit to the SPARC galaxies than NFW. As indicated in Table 3.1, Models A-F and H0-19 all use NFW haloes, while Models G and I0-19 employ DC14 haloes. Note that as in the previous chapter, we assume cold dark matter. However, it is worth noting that cored halo profiles can also arise in other dark matter theories, such as fuzzy dark matter (Hui *et al.*, 2017). Furthermore, we again assume that dark matter is a diffuse particle fluid.

In either case, the profile is determined by 2 parameters, which we adopt as free parameters in our models: the concentration parameter $c_{\rm vir}$ and the virial velocity $v_{\rm vir}$. $c_{\rm vir}$ is defined by

$$c_{\rm vir} = \frac{r_{\rm vir}}{r_{-2}}, \tag{3.3}$$

Model	$\log_{10}\lvert\bar{f}_{R0}\rvert$	Model	$\log_{10}\lvert\bar{f}_{R0}\rvert$
H0 (or I0)	-7.806	H10	-6.697
H1	-7.695	H11	-6.586
H2	-7.584	H12	-6.475
H3	-7.473	H13	-6.364
H4	-7.362	H14	-6.253
H5	-7.252	H15	-6.143
H6	-7.141	H16	-6.032
H7	-7.030	H17	-5.921
H8	-6.919	H18	-5.810
H9	-6.808	H19	-5.699

Table 3.2: Values of $\log_{10}|\bar{f}_{R0}|$ used in Models H0-19 and I0-19. They form a sequence of values that are uniformly spaced in the logarithm from $\log_{10}\left(1.563\times10^{-8}\right)$ to $\log_{10}\left(2\times10^{-6}\right)$.

where $r_{\rm vir}$ is the (spherical) virial radius, the radius enclosing a region of average density 93.6 times the cosmic critical density, and r_{-2} is the radius at which the logarithmic slope of the halo density profile is -2, which in the case of NFW is the same as the scale radius. The virial velocity, $v_{\rm vir}$ is in turn given by

$$v_{\rm vir} = \sqrt{\frac{GM_{\rm vir}}{r_{\rm vir}}}, \tag{3.4}$$

where $M_{\rm vir}$ is the virial mass: the mass contained within the virial radius. Details of the translation between these parameters and $v_{\rm DM}$ can be found in, e.g., the appendix of Katz *et al.* (2018).

Secondly, we have experimented with three approaches for the mass-to-light ratios $\Upsilon_{\rm disc}$ and $\Upsilon_{\rm bulge}$. In the most general case, we treat them as two free parameters for each galaxy. Alternatively, we treat them as a single free parameter (taking $\Upsilon_{\rm disc}=\Upsilon_{\rm bulge}$), mirroring the approach of Katz *et al.* (2017). The final option is to treat them as fixed values ($\Upsilon_{\rm disc}=0.5M_\odot/L_\odot$ and $\Upsilon_{\rm bulge}=0.7M_\odot/L_\odot$). This was the approach taken in McGaugh *et al.* (2016). As indicated in Table 3.1, we mostly adopt the middle approach, that of a single free parameter (denoted as '1' in the Υ column of Table 3.1). However, Model E takes the fixed values for the mass-to-light ratios (denoted as '0'), while Model F treats them as two free parameters (denoted as '2'). As mentioned previously, only 13 of the galaxies have a bulge component. For the remaining 72 galaxies, Models F and B are identical.

Finally, the fifth force contribution a_5 is given by gradients of the $f(R)$ scalar field f_R via Eq. (1.77). In order to compute this, the scalar field f_R needs to be calculated across the galactic disc by solving Eq. (1.69). For this purpose, we use a spherical 1D scalar field solver, which takes as an input the mass distribution and the parameter $\bar{f}_{R0}$. The details of this solver are discussed in the next subsection.

We adopt two different, but complementary approaches for the parameter $\bar{f}_{R0}$:

- $\bar{f}_{R0}$ is a free parameter in the fit of the rotation curve for each galaxy. The resulting spread of marginal $\bar{f}_{R0}$ posteriors values across the galaxies of the sample can then be inspected for any significant clustering around a single preferred global value. This option is denoted as 'varying' under the $\bar{f}_{R0}$ column in Table 3.1, and is used for all $f(R)$ models except H0-19 and I0-19.

- By contrast, Models H0-19 and I0-19 take a log-space grid of 20 values of $|\bar{f}_{R0}|$, ranging from $\log_{10}\left(1.563\times10^{-8}\right)$ to $\log_{10}\left(2\times10^{-6}\right)$. These values are given in Table 3.2. Each of these 20 values are in turn globally imposed over the whole sample, for example Model H17 imposes a global $\log_{10}|\bar{f}_{R0}|$ value of -5.921. These 20 models can then be compared with each other and with ΛCDM, providing constraints on $\bar{f}_{R0}$.

3.3.2 Scalar Field Solver

This subsection describes the calculation of the scalar field f_R for a given mass distribution and cosmic background value $\bar{f}_{R0}$. The technique is essentially a 1D version of the Newton-Gauss-Seidel scalar field solver implemented in the $f(R)$ N-body code MG-GADGET (Puchwein *et al.*, 2013) which was used in the previous chapter.

Given the finding in the previous chapter that the scalar field profiles within galaxies typically adopt a discoid shape, the spherically symmetric 1D approximation is not ideal but is made for reasons of computational cost; the jump to 2D corresponds to roughly two orders of magnitude in computational time, typically making it prohibitively expensive to perform a sufficient number of iterations to achieve MCMC convergence.

On the other hand, an analytic calculation of the screening radius and fifth force for a spherical body, such as Eqs. (1.62) and (1.63), would make the computation instantaneous. However, this prescription was found to be too inaccurate and sensitive to the (somewhat arbitrary) choice of outer limit of integration. Thus, the 1D numerical computation described in this subsection represents a reasonably accurate and reasonably fast compromise. The robustness of this 1D approximation is examined in detail in Appendix § A, where a comparison to an axisymmetric 2D solver is presented.

To avoid unphysical positive values of the scalar field f_R (e.g., due to finite numerical step sizes), the calculation is performed in terms of the quantity $u \equiv \ln\left(f_R/\bar{f}_R(a)\right)$. The equation of motion for the scalar field (1.69) can then be written as

$$\nabla^2 e^u + \frac{1}{3c^2\bar{f}_R(a)}\left[\bar{R}(a)\left(1-e^{-\frac{u}{2}}\right)+8\pi G\delta\rho\right]=0. \tag{3.5}$$

Note that the curvature perturbation δR has been eliminated using Eq. (1.85).

The role of the scalar field solver is to solve Eq. (3.5) for f_R across the galaxy, given an input density profile $\delta\rho$. This scalar field profile can then be used to calculate the fifth force contribution to the rotation curve via Eq. (1.77).

Equation (3.5) is discretised assuming spherical symmetry on a 1D radial grid. The outer edge of the grid needs to be at a radius larger than the Compton wavelength of the theory. For all of the $\bar{f}_{R0}$ values within the bounded prior (see § 3.3.6), 5 Mpc is a sufficiently large value. Finer resolution is required at smaller radii than at these large radii, so it is appropriate to use logarithmically spaced grid cells, i.e. the radial gridlines are equally spaced in the coordinate $x \equiv \ln r$, with constant grid spacing h_x. It was found that 175 cells between $r_{\rm min} = 0.05$kpc and $r_{\rm max} = 5$Mpc gave sufficiently accurate, converged results.

Defining

$$\mathscr{L}_i \equiv \left(\nabla^2 e^u\right)_i + \frac{1}{3c^2\bar{f}_R(a)}\left[\bar{R}(a)\left(1-e^{-\frac{u_i}{2}}\right)+8\pi G\delta\rho_i\right], \tag{3.6}$$

where the index i denotes the radial grid cells, Eq. (3.5) is then

$$\mathscr{L}_i = 0. \tag{3.7}$$

This is solved, as in MG-GADGET, with an iterative Newton-Gauss-Seidel approach, where at iteration n the scalar field is updated via

$$u_i^{n+1} = u_i^n - \frac{\mathscr{L}_i^n}{\frac{\partial\mathscr{L}_i^n}{\partial u_i^n}}. \tag{3.8}$$

In order to do this, we need discretised expressions for the Laplace operator on our grid, as well as the quantity $\partial\mathscr{L}_i/\partial u_i$. The Laplace operator in the coordinate $x \equiv \ln r$ is given by

$$\nabla^2 f = \frac{1}{r^3}\frac{\partial}{\partial x}\left(r\frac{\partial f}{\partial x}\right), \tag{3.9}$$

which is discretised as

$$\left(\nabla^2 f\right)_i = \frac{1}{r_i^3 h_x^2}\left(r_{i+\frac{1}{2}}(f_{i+1}-f_i) - r_{i-\frac{1}{2}}(f_i-f_{i-1})\right), \tag{3.10}$$

where r_i indicates the radial position of the cell centre of cell i, while $r_{i-\frac{1}{2}}$ and $r_{i+\frac{1}{2}}$ are the positions of the inner and outer cell boundaries. Finally, the quantity $\partial\mathscr{L}_i/\partial u_i$ is given by

$$\frac{\partial\mathscr{L}_i}{\partial u_i} = \frac{\bar{R}(a)}{6c^2\bar{f}_R(a)}e^{-\frac{u_i}{2}} - e^{u_i}\left(\frac{r_{i+\frac{1}{2}}+r_{i-\frac{1}{2}}}{r_i^3 h_x^2}\right). \tag{3.11}$$

Iterations of Eq. (3.8) are performed until $\Delta u_i \equiv |u_i^{n+1} - u_i^n| < 10^{-7}$ at all grid cells i. Through experimentation, this tolerance level has been found to give sufficiently accurate, converged results.

All that remains now is to provide a density profile ρ_i for Eq. (3.6). For a given galaxy, the density profile depends on the parameter choices for the mass-to-light ratio(s) and the two dark matter halo parameters. Density data for the baryonic components are not provided with the SPARC data, so we have instead fitted $v_{\rm gas}$ and $v_{\rm disc}$ with exponential disc profiles and $v_{\rm bulge}$ with a Hernquist profile. In the cases of the 2D exponential discs, we spherically average the profiles for use in the 1D solver. These density profiles are then fed to the scalar field solver (multiplied by the mass-to-light ratio in the case of the stellar disc and bulge), along with the spherical dark matter halo profile, either NFW or DC14.

3.3.3 Environmental Screening

The environment of an object plays a role in its scalar field profile. As verified in Chapter 2, a galaxy embedded within a large-scale overdensity experiences an effective $|\bar{f}_{R0}|$ that is lower than the cosmic background value, and as a result will have a larger screening radius than that of a galaxy occupying a region of cosmic mean density.

It has been shown in simulations (e.g. Cabré *et al.*, 2012) that as a first approximation, the degree of environmental screening of a given galaxy can be quantified by the gravitational potential due to external sources $\Phi_{\rm ext}$. The Introduction (§ 1.3.5) described the 'screening maps' of Cabré *et al.* (2012) and Desmond *et al.* (2018c): 3D maps of $\Phi_{\rm ext}$ throughout the local universe, created for this very purpose of measuring the impact of environmental screening on tests of screened modified gravity. In this chapter, we use the screening map of Desmond *et al.* (2018c) which uses updated techniques and catalogues compared to that of Cabré *et al.* (2012). Full details regarding the construction of the map can be found in the original paper, but it is worth noting that the value of $\Phi_{\rm ext}$ given by the screening map at a given point in space depends on the adopted value for $\bar{f}_{R0}$, because the map sums contributions from all mass within the Compton wavelength λ_C of the considered point, which relates to $\bar{f}_{R0}$ via Eq. (1.88).

We use the screening map of Desmond *et al.* (2018c) to find $\Phi_{\rm ext}$ for each of the 147 galaxies that remain in the sample after making the first four cuts described in § 3.2. The screening map uses a Bayesian methodology to reconstruct full posteriors on $\Phi_{\rm ext}$ at any point in space within ~ 200 Mpc, by propagating uncertainties on the various inputs. For each of these galaxies, the posterior distribution for $\Phi_{\rm ext}$ is calculated for a log-spaced sequence of 20 values of $\bar{f}_{R0}$, the same values used in Models H0-19 (see Table 3.2). This information is then used in two ways.

First, we exclude from the sample any galaxy for which the 1σ upper bound on $|\Phi_{\rm ext}|/c^2$ is greater than $3|\bar{f}_{R0}|/2$ (which is an approximate criterion for environmental screening, see Cabré *et al.* 2012), for *any* of the 20 considered values of $\bar{f}_{R0}$. This is tantamount to removing from the sample any galaxies for which we believe environmental screening would be a significant effect in an $f(R)$ Universe. As indicated in § 3.2, this cuts 62 of the 147 remaining galaxies once the other sample cuts have already been performed, leaving our final sample of 85 galaxies.

Secondly, we investigate the effect of the environmental contribution to the scalar field profile of the remaining galaxies in our sample. We consider a spherical top hat model, with a radius equal to the Compton wavelength λ_C, and a gravitational potential equal to the maximum posterior value of $\Phi_{\rm ext}$. As indicated by the quantity $\rho_{\rm env}$ in Figure 3.1, this structure is added to the overall density profile before it is fed to the scalar field solver. As shown in Table 3.1, this change is only made in the case of Model C, which is otherwise identical to Model B, i.e. $f(R)$+varying $\bar{f}_{R0}$+NFW. The results of Model C can be compared

to those of Model B to check the robustness of our results against the residual effects of environmental screening in our final sample. Note that because $\Phi_{\rm ext}$ is a function of $\bar{f}_{R0}$, and $\bar{f}_{R0}$ is a free parameter in Model C, the mass and size of this large-scale structure needs to be recalculated with each Monte Carlo realisation.

3.3.4 Stellar Self-Screening

An assumption underlying our analysis is that the scalar field f_R is sourced by all of the mass components: the dark matter, gas, and stars. However, in an $f(R)$ universe, one might expect a significant population of stars to be 'self-screened', and thus neither source nor couple to the fifth force (Davis *et al.*, 2012). The impact of this effect on our rotation curve signature was explored in the previous chapter (2.3.3). Furthermore, this effect was the underlying principle for several of the studies mentioned in the Introduction (§ 1.3.5; e.g. Vikram *et al.*, 2018; Desmond *et al.*, 2018a,b, 2019a) which searched for signals predicted to result from this differential coupling of the fifth force to stars and gas.

For the purposes of this chapter, the expected effect of the stellar self-screening is that for a given $\bar{f}_{R0}$, the screening radius will be smaller than if the effect is ignored. This was demonstrated in the previous chapter.

The contribution of a given star depends on its mass, radius, and environment. Thus, performing a fully self-consistent calculation incorporating the detailed contribution of the entire stellar population is difficult. We instead repeat the approach adopted in Chapter 2: we implement the extreme scenario in which all stars are assumed to be fully self-screened, and not sourcing the scalar field at all. In practice, this simply amounts to omitting the stellar input to the scalar field solver.

As in the test for environmental screening in the previous subsection, we employ this technique only for one model, Model D, which is otherwise identical to Model B, i.e. $f(R)+$ varying $\bar{f}_{R0}+$ NFW. The 'true' result should then be bookended by these two extremes, so the results of Model D can be compared to those of Model B in order to gain an understanding of the error induced in our inference by the effects of stellar self-screening.

3.3.5 Markov Chain Monte Carlo (MCMC)

We use an affine-invariant, parallel-tempered[2] Markov chain Monte Carlo (MCMC) technique, using the publicly available Python package emcee (Foreman-Mackey *et al.*, 2013) to explore the posteriors of the free parameters of each model.

[2]Since the research presented in this chapter was first undertaken, emcee has changed significantly and the parallel-tempering functionality has been deprecated. At the time of writing this thesis, I have made some changes to my publicly available code such that the MCMC implementation works with the new version of emcee, but the plotting and analysis scripts will require testing.

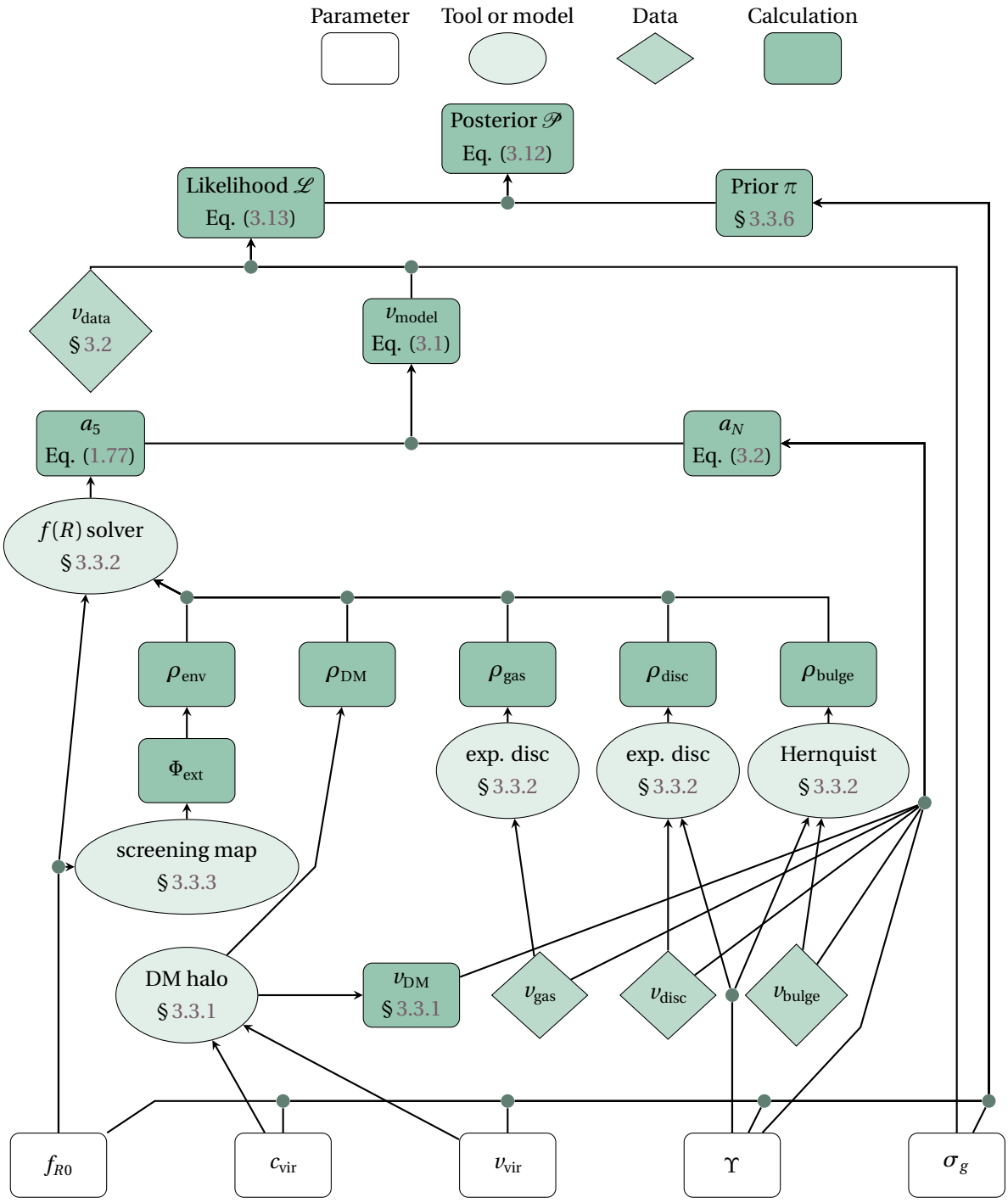

Figure 3.1: Pipeline illustrating the calculation of the posterior probability $\mathscr{P}(\theta|D)$ for parameter values θ and for a given galaxy with rotation curve data D. As indicated in the legend, white rectangles represent free parameters, ellipses represent tools or models, lozenges represent observational data, and green rectangles represent calculated quantities. The model illustrated here is an $f(R)$ model with varying $\bar{f}_{R0}$, a single mass-to-light ratio, an NFW halo and an added large-scale environment (i.e. Model C). Various details of the pipeline would differ in other models. For example, the nodes labelled '$\rho_{\rm env}$', '$\Phi_{\rm ext}$' and 'screening map' would not be present in the case of Model B, which is identical to Model C but does not include a large-scale environment in the scalar field solver. Another example is Model F, which is identical to Model B but has two free parameters for the mass-to-light ratio, and would therefore also lose the environmental screening apparatus and further replace the node marked 'Υ' with two free parameter nodes: '$\Upsilon_{\rm disc}$' and '$\Upsilon_{\rm bulge}$'.

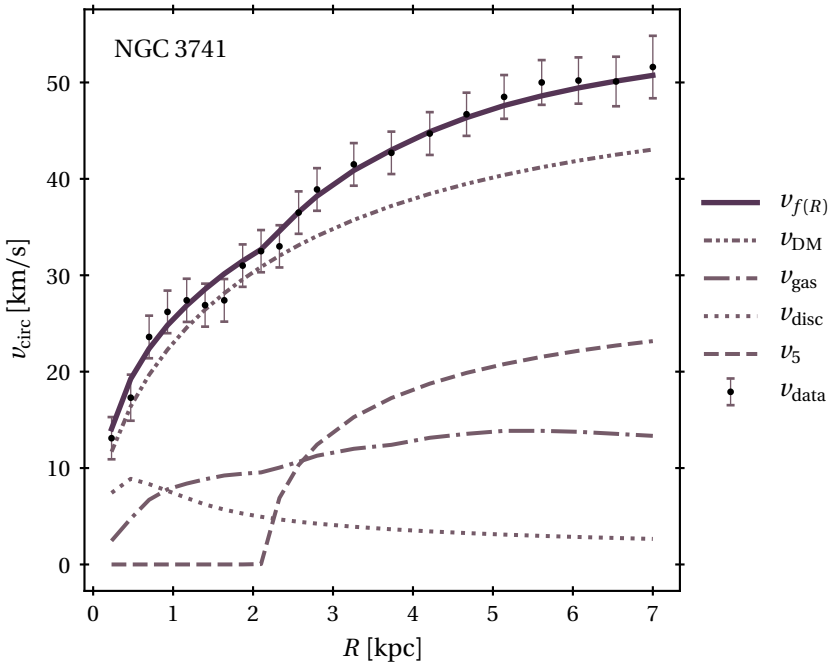

Figure 3.2: Shown as an example, the rotation curve of NGC 3741 and corresponding fit. The black points with errorbars show the observed rotation curve, while the purple curve gives the $f(R)$ (Model B) fit. The grey textured lines show the contributions to the $f(R)$ fit of the various components: gas, stellar disc, dark matter, and fifth force, as labelled. The galaxy does not have a bulge component, so there is no $v_{\rm bulge}$ shown. It should be noted that this fit is unrepresentatively good; it was chosen because there is a clear upturn-like feature that is well fit with a screening radius and fifth force. As is shown in later figures, not all galaxies are so well-fitted.

For a given galaxy with rotation curve data D, the posterior probability $\mathscr{P}(\theta|D)$ for a given set of parameters θ is given by

$$\mathscr{P}(\theta|D) \propto \mathscr{L}(D|\theta)\pi(\theta), \tag{3.12}$$

where $\mathscr{L}(D|\theta)$ represents the likelihood function, and $\pi(\theta)$ represents the prior probability distributions for the parameters θ. The choices of priors will be discussed further in § 3.3.6.

The pipeline for calculating this posterior probability, for a given galaxy and a set of parameters θ, is illustrated heuristically in Figure 3.1. The diagram specifically illustrates the pipeline for an $f(R)$ model with freely varying $\bar{f}_{R0}$ and an environmental contribution (i.e. Model C); some of the details of the diagram would change for other models, and examples of such changes are given in the accompanying caption.

Assuming that the errors σ on the data are Gaussian, the log-likelihood function for a given SPARC galaxy is given by

$$\ln\mathscr{L} = -\frac{1}{2}\sum_j \left[\left(\frac{v_{{\rm data}_j} - v_{\rm model}(r_j)}{\sigma_j} \right)^2 + \ln\left(2\pi\sigma_j^2\right) \right], \tag{3.13}$$

where the sum is over the data points of an individual rotation curve.

In addition to the observational errors provided with the data points, for each galaxy we add in quadrature an additional constant error component σ_g, i.e.,

$$\sigma_j^2 = \sigma_{\mathrm{obs},j}^2 + \sigma_g^2. \tag{3.14}$$

σ_g is then left as a free parameter in the fit for each galaxy. This additional error term is included in order to account for galaxy features not included in the model, e.g. spiral arms and other baryonic features, but a fit is penalised for adopting too large a value of σ_g, via the second term in the log-likelihood Eq. (3.13).

For each MCMC run, we use 30 walkers, 4 temperatures, and 5000 iterations (after burn-in). The chains have all been checked for convergence, both visually and by ensuring that the Gelman-Rubin statistic (Gelman & Rubin, 1992) $\mathscr{R}$ is sufficiently close to 1. In particular, for the overwhelming majority of the fits, $|\mathscr{R}-1|<0.01$, apart from one or two galaxies in some models, which exhibit some bimodality.

An example of a fit generated with this method is shown in Figure 3.2. The figure shows the observed rotation curve of NGC 3741, along with the best-fitting (i.e. maximum a posteriori) rotation curve under the $f(R)$ model with freely varying $\bar{f}_{R0}$ (i.e. Model B). Also shown are the various components: v_{disc}, v_{gas}, v_{DM}, which combine in quadrature via Eq. (3.1) to give the model.

A fourth component is shown in Figure 3.2: v_5. This is the contribution of the fifth force to the rotation curve model, given by

$$v_5(R) = \sqrt{a_5(R)R}. \tag{3.15}$$

The only contribution to the model that is not a function of fit parameters is the gas curve v_{gas}, which is provided with the data as a fixed quantity. v_{disc} is also provided with the data, but its overall normalisation is set by the mass-to-light ratio Υ. It can be seen in the v_5 curve that the fit places a screening radius at around 2 kpc. This results in a mild upturn in the model rotation curve, which visibly appears to give a good fit to the data. It should be noted that this rotation curve was chosen because of this ideal behaviour, and is not necessarily representative of the sample at large.

3.3.6 Priors

As indicated in Table 3.1, different models have different free parameters. For the models with a freely varying $\bar{f}_{R0}$, we adopt a flat prior in $\log_{10}|\bar{f}_{R0}|$, between $|\bar{f}_{R0}| = 10^{-9}$ and $|\bar{f}_{R0}| = 2\times10^{-6}$. For even larger values of $|\bar{f}_{R0}|$ the model would struggle to screen the Milky Way at the solar radius, while even smaller values would be of limited interest as most galaxies would likely be fully screened.

For any given galaxy, we adopt a flat prior for σ_g, between 0 and twice the maximum observed error for that galaxy.

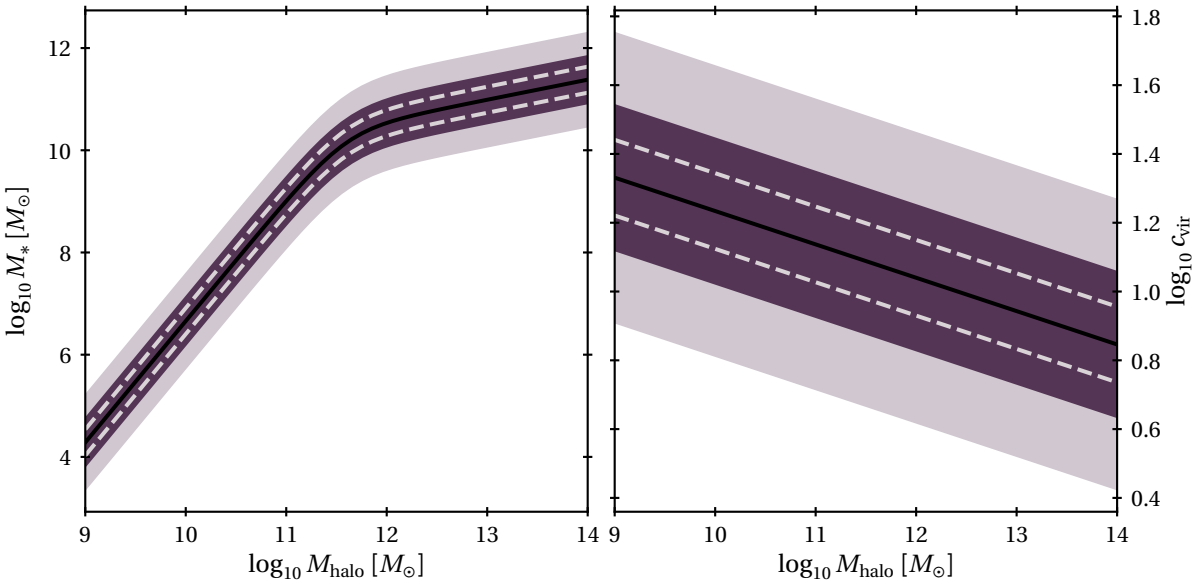

Figure 3.3: *Left:* Stellar mass-halo mass relation based on Moster *et al.* (2013) used as a log-normal prior. The dark and light regions indicate the 1 and 2σ regions respectively, *after* broadening the relation to account for $f(R)$ gravity effects (see text for details). The dashed lines indicate the 1σ region before the broadening. *Right:* As with the left panel, but for the concentration-halo mass relation from Dutton & Macciò (2014).

The priors for the remaining parameters—the two dark matter parameters, $c_{\rm vir}$ and $v_{\rm vir}$, and where applicable, the one or two mass-to-light ratios Υ—are less agnostic. Using flat priors was found to have the result that the fits are able to artificially inflate or deflate their halo masses so as to have a screening radius within the radial range of the rotation curve. As a consequence, unphysical vertical clustering features would appear in the stellar mass-halo mass diagrams and concentration-halo mass relation diagrams of the best-fitting models.

To avoid this undesirable behaviour, we follow the approach of Katz *et al.* (2017) and use empirical stellar mass-halo mass and concentration-halo mass relations from Moster *et al.* (2013) and Dutton & Macciò (2014) respectively as lognormal priors. These relations are depicted in Figure 3.3. For a fixed mass-to-light ratio, these relations translate directly to priors on $v_{\rm vir}$ and $c_{\rm vir}$ respectively. In the case of a freely varying Υ, there is an increased freedom, as the stellar mass depends on the value of Υ.

It should be noted that these relations are derived from ΛCDM simulations, so their applicability in an $f(R)$ universe is not entirely clear. $f(R)$ gravity simulations, such as those of Mitchell *et al.* (2019) suggest that for $|\bar{f}_{R0}| \gtrsim 10^{-6}$, halo concentrations are enhanced by 0.1 dex or so. Taking this into account, we increase the width of our adopted concentration-halo mass relation by 0.1 dex; approximately equivalent to a doubling of the width. The priors should then encompass the 'true' relations of both a ΛCDM and an $f(R)$ universe.

The impact of modified gravity on the stellar mass-halo mass relation is not yet known. However, the work of e.g. Cataneo *et al.* (2016) suggests that the maximum increase to the halo mass function at the level of $|\bar{f}_{R0}| \gtrsim 10^{-6}$ is small; approximately 10% or so. As-

suming baryonic feedback mechanisms to have largely similar effects in an $f(R)$ universe, one might then expect the stellar mass-halo mass relation to be changed by a similar degree. Thus, a doubling of the width of the relation should also comfortably encompass the 'true' relation in the $f(R)$ paradigm. We approximately achieve this by adding 0.2 dex to the width.

As a final note, we follow Katz *et al.* (2017) in imposing some additional constraints. Firstly, we require that the baryon mass fraction is always less than the cosmological value. Furthermore, $\log_{10} c_{\rm vir}$, $\log_{10} v_{\rm vir}/(1{\rm m/s})$, and $\log_{10} \Upsilon/(1 M_\odot/L_\odot)$ are constrained to lie within the bounds (0, 2), (4, 5.7), and (-0.52, -0.1) respectively. The constraints on $c_{\rm vir}$ and $v_{\rm vir}$ are rather loose, while the constraint on Υ is somewhat tighter, but informed by the stellar synthesis models of Meidt *et al.* (2014); McGaugh & Schombert (2014); Schombert & McGaugh (2014).

3.4 Results

3.4.1 Constraints on $\bar{f}_{R0}$

A widely used tool for model comparison is the Bayesian Information Criterion (Schwarz, 1978), given by

$$\mathrm{BIC} = \ln(n)k - 2\ln(\mathscr{L}), \tag{3.16}$$

where n is the number of data points, k is the number of parameters of the model, and $\mathscr{L}$ is the maximised likelihood of the model. The first term acts on behalf of Occam's razor, penalising overcomplicated models with too many parameters. Two models, 1 and 2, can then be compared by calculating the difference in the BIC: $\Delta\mathrm{BIC} \equiv \mathrm{BIC}_1 - \mathrm{BIC}_2$. A positive (negative) value for this quantity indicates a preference for model 2 (1). We define values in the range $|\Delta\mathrm{BIC}| > 2$ as 'mildly significant', and values in the range $|\Delta\mathrm{BIC}| > 6$ as 'strongly significant' (Kass & Raftery, 1995).

Figure 3.4 shows a first comparison of an $f(R)$ model with freely varying $\bar{f}_{R0}$ and a ΛCDM model, in both cases using NFW haloes (i.e. Models B and A respectively). The cumulative distribution function of $\Delta\mathrm{BIC} \equiv \mathrm{BIC}_B - \mathrm{BIC}_A$ is displayed. Model B treats $\bar{f}_{R0}$ as a free parameter and so has one more free parameter than Model A, for which it is penalised by the first term in Eq. (3.16). Nonetheless, the majority of galaxies show *some* preference for $f(R)$, with 64/85 galaxies having $\Delta\mathrm{BIC} < 0$. Perhaps more striking are the numbers of galaxies that have mildly significant ($|\Delta\mathrm{BIC}| > 2$) preferences either way, with 3 galaxies preferring ΛCDM and 49 galaxies preferring $f(R)$. No galaxies have a strongly significant ($|\Delta\mathrm{BIC}| > 6$) preference for ΛCDM, while 27 galaxies do for $f(R)$. It is worth noting that the galaxies with the strongest preferences for $f(R)$ also typically infer much lower values for σ_g under Model B than under Model A; ΛCDM+NFW tries to compensate for a poor fit by increasing the scatter.

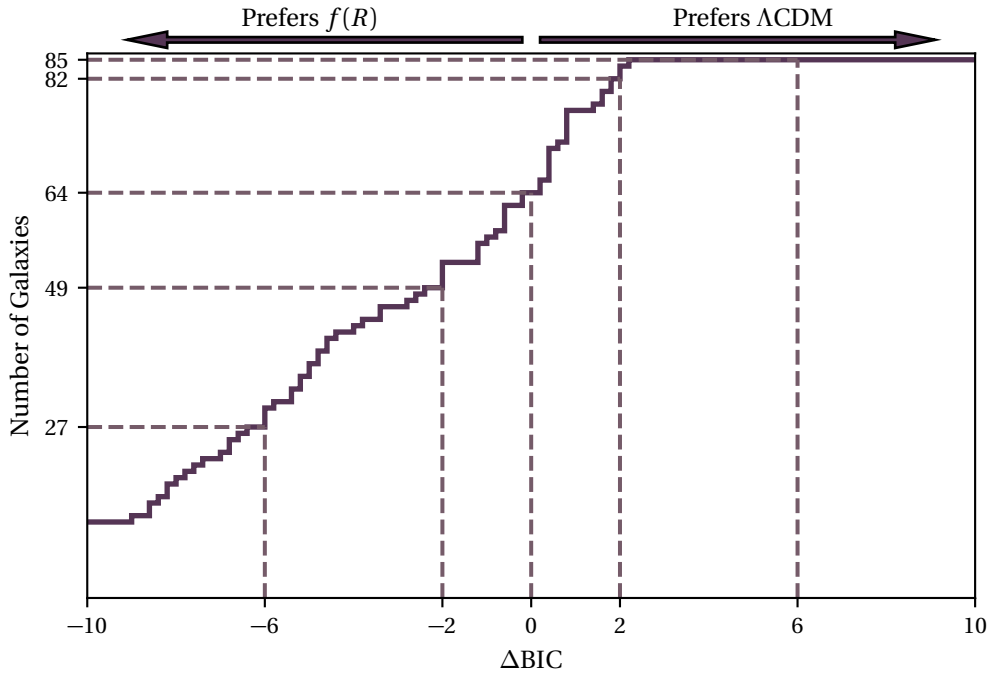

Figure 3.4: Cumulative distribution function of $\Delta\text{BIC} = \text{BIC}_{f(R)} - \text{BIC}_{\Lambda\text{CDM}}$ across SPARC galaxies (total=85), where BIC is the Bayesian Information Criterion, given by Eq. (3.16). The $f(R)$ model here is Model B (freely varying $\bar{f}_{R0}$), while the ΛCDM model is Model A, both of which use NFW haloes and single mass-to-light ratios. As indicated by the arrows at the top of the Figure, a negative value for ΔBIC indicates a preference for $f(R)$, and a positive value for ΛCDM. The grey dashed lines mark the fiducial values of $|\Delta\text{BIC}| = 0, 2, 6$. Corresponding numbers on the y-axis indicate numbers of galaxies *below* the lines. For example, 49 galaxies have a mildly significant preference for $f(R)$, while $85 - 82 = 3$ galaxies have a similar preference for ΛCDM. This figure indicates that the majority of galaxies prefer *some* $f(R)$ model, but it is worth noting that this does not necessarily mean that they all prefer the same $\bar{f}_{R0}$ value.

These numbers, and the preference for $f(R)$ implied by them, is perhaps unsurprising. Given a freely varying $\bar{f}_{R0}$, the fits are able to place a screening radius anywhere within the radial range of the rotation curve, and are thus able to choose a favourable position such that the fit is improved. It is only in a minority of cases that no such position can be found. For these galaxies, a low $|\bar{f}_{R0}|$ is chosen such that the galaxy is fully screened. This results in $\mathscr{L}_{f(R)}/\mathscr{L}_{\Lambda\text{CDM}} \to 1$ and thus $\Delta\text{BIC} \to \ln(n)$. For the SPARC galaxies, this will typically fall in the range $2-5$, and so it is impossible for a galaxy to have a 'strongly significant' preference for ΛCDM over an $f(R)$ model with a freely varying $\bar{f}_{R0}$. This just reflects the fact that ΛCDM is contained within the $f(R)$ model as a limiting case.

Of course, in an $f(R)$ Universe, $\bar{f}_{R0}$ would not vary freely from galaxy to galaxy as we have allowed it to here. Instead, there would be a single global value for $\bar{f}_{R0}$. The natural question then is whether the individually inferred values for $\bar{f}_{R0}$ show any clustering around a single global value. The upper panel of Figure 3.5 addresses this question, showing the marginal posterior distributions for $\bar{f}_{R0}$ across all the galaxies, fitting again with Model B (freely varying $\bar{f}_{R0}$+NFW). The overlaid coloured points show the values of $\bar{f}_{R0}$ for the best-fitting models, which typically coincide with the peaks of the marginal posteriors, except

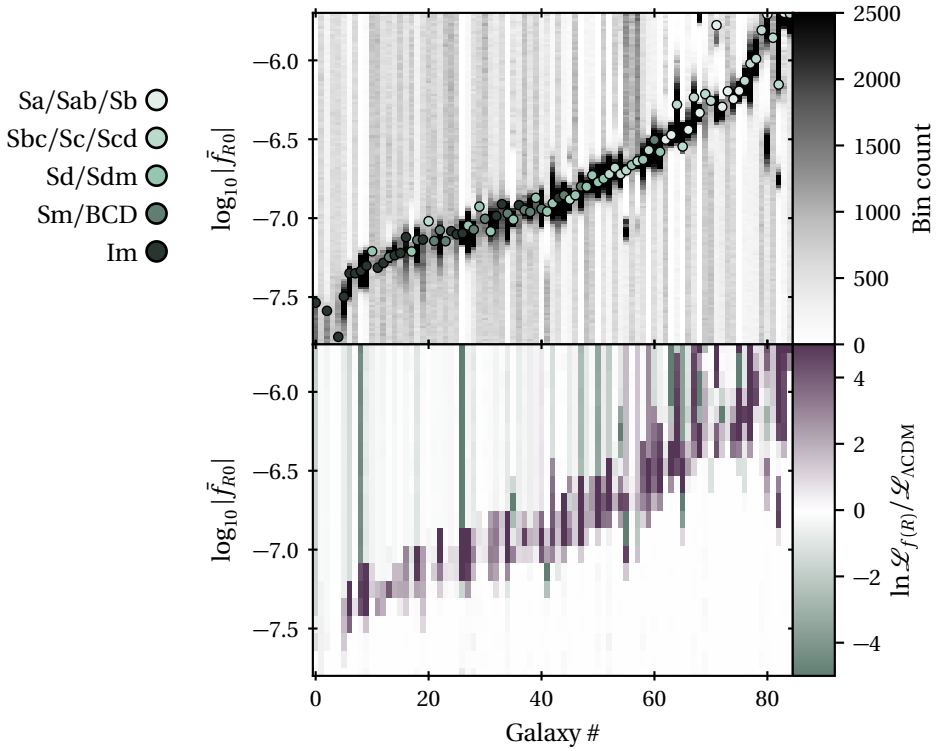

Figure 3.5: *Top:* For all 85 galaxies in the sample, the marginal posterior distributions for $\bar{f}_{R0}$ under the $f(R)$ model with freely varying $\bar{f}_{R0}$ and NFW haloes (i.e. Model B) are shown. Each individual posterior is a histogram with 200 bins, equally log-spaced between the edges of the $\bar{f}_{R0}$ prior. The 85 histograms are then vertically juxtaposed, and ordered by the position of the peak of the histogram. The colourscale is truncated at a bin count of 2500 to allow sufficient contrast in less favoured regions, but actually reaches up to ~ 30000 in some cases. The points show the $\bar{f}_{R0}$ values of the best-fitting models, coloured according to the Hubble classification of the galaxy, as indicated in the legend. The marginal posteriors do not appear to show any significant clustering around a single value for $\bar{f}_{R0}$. *Bottom:* For a series of 20 $f(R)$ models with fixed $\bar{f}_{R0}$ (i.e. Models H0-19), the likelihood ratios $\ln \mathscr{L}_{f(R)}/\mathscr{L}_{\Lambda\mathrm{CDM}}$, where the ΛCDM model used is Model A, and likelihoods are calculated for the best-fitting models. This colourscale is also truncated, at a likelihood ratio of ±5. This panel conveys similar information to the top panel: different galaxies appear to prefer different ranges of $\bar{f}_{R0}$. However, as discussed in the text, the possibility remains of a single global value that is consistent with all galaxies, particularly in the region $|\bar{f}_{R0}| \sim 10^{-7}$, where many of the galaxies are fully screened and therefore insensitive.

in cases where there is some multimodality or $\bar{f}_{R0}$ is not well constrained.

The key result shown in this panel is that there does not appear to be any immediate sign of clustering around a single value of $\bar{f}_{R0}$. For most galaxies, $\bar{f}_{R0}$ values in a reasonably narrow range are preferred, but these inferred values are almost evenly spread across two orders of magnitude, which is inconsistent with a single global value.

As an additional note, the Hubble types of the galaxies are indicated in the upper panel of Figure 3.5. The classifications used are those that accompany the SPARC data, and match the classification scheme of de Vaucouleurs *et al.* (1991): Sa-Sd types are spiral galaxies with spiral arms of decreasing tightness, Sm and Im types are Magellanic spirals and irregulars, and BCD types are 'blue compact dwarfs'. There appears to be a correlation between in-

ferred $\bar{f}_{R0}$ and Hubble type. This is to be expected, as dwarf galaxies would be sensitive to lower values of $|\bar{f}_{R0}|$, for which larger galaxies would be entirely screened. Conversely, larger galaxies would be sensitive to higher values, for which dwarf galaxies would be fully unscreened.

This finding demonstrates an important caveat to the above result that there is no obvious global value for $\bar{f}_{R0}$: different galaxies have different sensitivity ranges for $\bar{f}_{R0}$, so there would naturally be a spread in fitted $\bar{f}_{R0}$ values when comparing across the whole sample. Even in an $f(R)$ Universe, only the galaxies with the true $\bar{f}_{R0}$ within their sensitivity ranges would fit this value, and the other galaxies would instead just choose the incorrect $\bar{f}_{R0}$ values that most improved their fits.

It is important then to invert the question; rather than asking whether all galaxies are consistent with one $\bar{f}_{R0}$ value, we can ask whether one $\bar{f}_{R0}$ value is consistent with all galaxies, i.e. whether a specific $\bar{f}_{R0}$ value can be imposed globally that gives rotation curve models consistent with the observations of all galaxies, even if it is not the most preferred $\bar{f}_{R0}$ value for a significant subpopulation of galaxies, possibly lying outside of their sensitivity range.

To address this question, we consider a series of 20 $f(R)$ models with globally imposed $\bar{f}_{R0}$, i.e. Models H0-19. The $\bar{f}_{R0}$ values utilised are given in Table 3.2. For each of the 20 $\bar{f}_{R0}$ values and each of the 85 galaxies, the lower panel of Figure 3.5 shows the likelihood ratio $\ln \mathscr{L}_{f(R)}/\mathscr{L}_{\Lambda\text{CDM}}$, taking the best-fitting parameters under Models Hx and A. This panel conveys similar information to the top panel; visually, there does not appear to be any obvious global value for $\bar{f}_{R0}$. However, there is additional information to be gleaned. In the higher regions, $\log_{10}|\bar{f}_{R0}| \gtrsim -6.5$, there are several galaxies which prefer such values of $\bar{f}_{R0}$. However, there are also a great many galaxies for which these values provide a worsening of the fit compared with ΛCDM. On the other hand, in the region $\log_{10}|\bar{f}_{R0}| \sim -7$, there are several galaxies which prefer such values, and the galaxies which prefer higher values are indifferent towards it, as a result of being completely screened in this region of $\bar{f}_{R0}$. This region, therefore, appears to be the most promising within our sensitivity range.

A side-note is that the lower panel of Figure 3.5 also gives an understanding of the sensitivity of the sample. Beneath the diagonal green region is a white region, where galaxies are screened and ΛCDM and $f(R)$ are indistinguishable. As we go to progressively lower values of $|\bar{f}_{R0}|$, more galaxies inhabit the white region. We define $\log_{10}|\bar{f}_{R0}| \sim -7.2$ or $|\bar{f}_{R0}| \sim 6\times10^{-8}$ as the 'sensitivity level' of our sample, being the point at which roughly the half of the sample has become insensitive.

Rather than considering each galaxy individually, we can perform a model comparison across the sample as a whole. For each of the Models H0-19, we can perform an overall model comparison with ΛCDM by calculating the total likelihood ratio $\ln \mathscr{L}_{f(R)}/\mathscr{L}_{\Lambda\text{CDM}}$. The log-likelihoods $\ln \mathscr{L}$ are calculated with Eq. (3.13) taking the best-fitted (i.e. maximum a posteriori) parameters for each galaxy, then summing the contributions of all galaxies

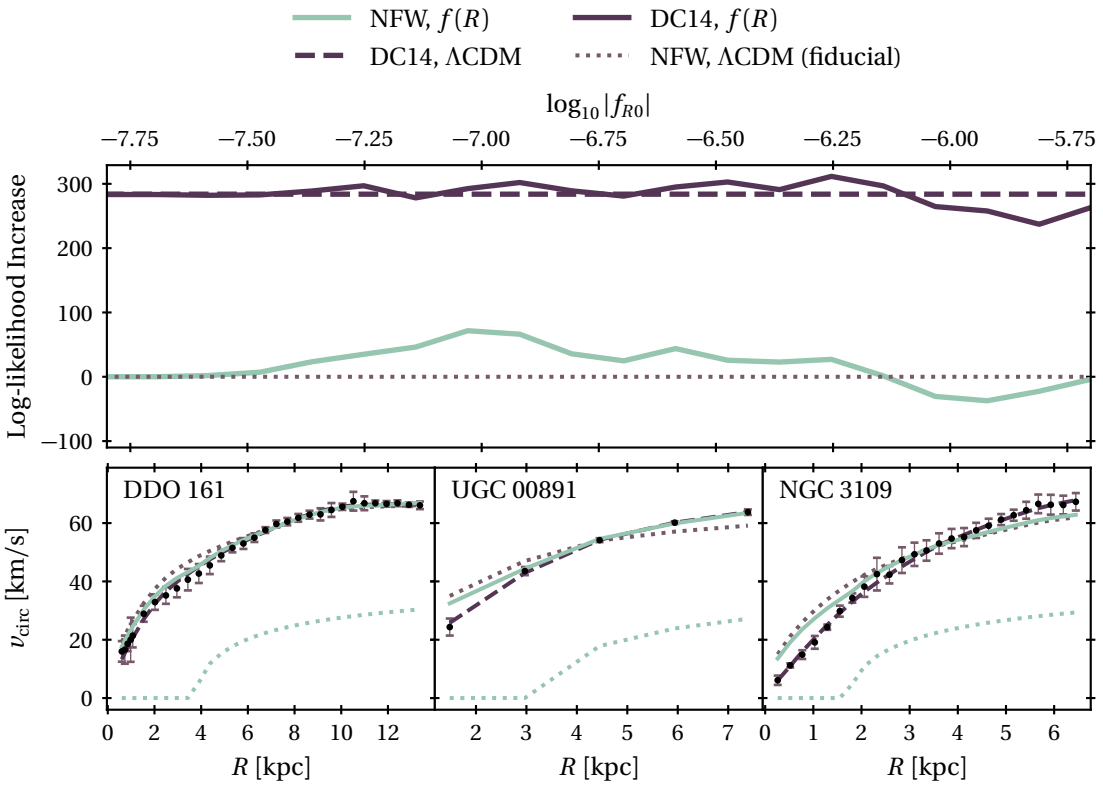

Figure 3.6: *Top:* The coloured lines show model comparisons via the log-likelihood ratio $\ln \mathscr{L}_1/\mathscr{L}_2$. The dashed purple line shows the log-likelihood ratio for DC14+ΛCDM (Model G) versus NFW+ΛCDM (Model A). The green solid line shows the log-likehood ratios for a range of fixed-$\bar{f}_{R0}$ models with NFW haloes (Model H) versus NFW+ΛCDM (Model A), while the purple solid line shows the ratios for another range of fixed-$\bar{f}_{R0}$ models, this time with DC14 haloes (Model I), again versus Model A. The grey dashed line shows where the log-ratio equals zero, i.e. where both models are equally favoured. *Bottom:* Rotation curves and fits of three galaxies: DDO 161 *(left)*, UGC 00891 *(centre)*, and NGC 3109 *(right)*. In each case, the observed rotation curve is shown, as well as 3 fits: NFW+ΛCDM (Model A; grey dotted), DC14+ΛCDM (Model G; purple dashed), and NFW+$f(R)$ imposing $\log_{10}|\bar{f}_{R0}| = -7.03$ (Model H7; green solid). The latter is the model corresponding to the peak of the green likelihood ratio curve in the top panel. The three galaxies chosen are those which contribute the most to this peak. This figure shows the key result of the chapter: the galaxies which most favour $f(R)$ over ΛCDM are those for which NFW provides a poor fit, and using a cored halo profile under ΛCDM gives a better fit to the rotation curves than cuspy haloes with $f(R)$ gravity. Furthermore, when cored haloes are assumed, $f(R)$ gravity does not give any significant improvement in the agreement with the data, as can be seen by comparing the purple solid and purple dashed curve in the top panel.

in our sample. A more fully Bayesian approach would be to marginalise over the full parameter space rather than taking the best-fitted parameters. The likelihoods then become *marginal* likelihoods, and their ratios are known as Bayes factors. The calculation of these Bayes factors, however, is notoriously expensive so we instead consider the more easily calculable likelihood ratios, which are nonetheless robust tools for model comparison. The green curve in Figure 3.6 shows the result of this likelihood ratio calculation for the 20 $\bar{f}_{R0}$ values listed in Table 3.2.

Figure 3.6 shows that $f(R)$ is disfavoured for values $\log_{10}|\bar{f}_{R0}| \gtrsim -6.1$, reaching a decrease

in log-likelihood of ~ 30 at its most extreme. Note that at higher values still, the likelihood for $f(R)$ starts to approach that of ΛCDM again. However, this corresponds to the extreme and unphysical case in which every galaxy is fully unscreened, and so the rotation curve models exactly resemble those of ΛCDM, but with an overall mass reduced to 3/4 of the inferred ΛCDM mass, to account for the gravitational accelerations being 4/3 times that of standard gravity.

At the opposite end of the spectrum, $\log_{10}|\bar{f}_{R0}| \lesssim -7.6$, the likelihood ratios again approach identity. This corresponds to the regime in which every galaxy is fully screened, so the fits are now exactly identical to those of ΛCDM.

At intermediate values of $\bar{f}_{R0}$, $f(R)$ appears to be favourable compared to ΛCDM. The peak of the signal is for the model with $\log_{10}|\bar{f}_{R0}| = -7.03$, where there is a rather significant increase in the log-likelihood of around 66.

The lower panels of Figure 3.6 show the rotation curves and fits of the three galaxies with the highest individual likelihood ratios for Model H7 ($\log_{10}|\bar{f}_{R0}| = -7.03$) compared with Model A. In other words, the three galaxies that contribute the most to the peak in the upper panel of Figure 3.6. These galaxies are DDO 161 ($\ln \mathscr{L}_{f(R)}/\mathscr{L}_{\Lambda\mathrm{CDM}} = 14.96$), UGC 00891 (6.14), and NGC 3109 (6.13).

It is striking that the three galaxies are all rather similar; dwarf galaxies (Hubble types all Im or Sm) with similar radial extents and maximum rotation speeds. Furthermore, in each case, the behaviour of the fits is similar. The observed rotation curves are poorly fit with cuspy NFW profiles, which place too much mass in the inner regions in order to fit the velocity data in the outer regions. The reason the $f(R)$ fits provide a significant improvement is that the presence of the fifth force in the outer regions allows a reduced mass in the inner regions.

The DC14 profile for dark matter haloes Di Cintio *et al.* (2014) is empirically derived from ΛCDM simulations incorporating stellar feedback. The inner slope of the profile depends on the stellar content of the galaxy, giving a more cored profile to galaxies with intermediate ($\sim 0.5\,\%$) stellar mass fractions. Katz *et al.* (2017) found that fitting the SPARC galaxies with a DC14 profile gives a consistent improvement compared to NFW, particularly in cases such as the galaxies depicted in the lower panels of Figure 3.6, i.e. dwarf galaxies requiring a cored profile. Indeed, the rotation curve of NGC 3109—and its dramatically improved fit with a cored halo—was used as an example to illustrate the core/cusp problem in the Introduction (Figure 1.8).

The upper panel of Figure 3.6 also shows a comparison of Models G and A (the dashed purple line), i.e. a model comparison of ΛCDM models with DC14 and NFW haloes. The increase in log-likelihood is nearly 300; a very significant improvement, and far more significant than the increase in log-likelihood for any given $f(R)$ model with an NFW halo. The reason for this improvement is readily apparent in the rotation curve fits in the lower panels of Figure 3.6. Echoing the findings of Katz *et al.* (2017), the DC14 fits to the three

galaxies give consistently better agreement with the data than NFW. We find that this holds for both ΛCDM and $f(R)$ gravity.

The final model comparison shown in the upper panel of Figure 3.6 is between Models I0-19 and Model A, i.e. a comparison of DC14+$f(R)$ and NFW+ΛCDM. Model I does not give a marked improvement to the fits compared to Model G. In other words, when cored halo profiles are assumed, the $f(R)$ signal at $\log_{10}|\bar{f}_{R0}| \sim -7$ largely disappears, so that models with a cored halo profile and a fifth force are not significantly better than those with a cored halo profile and no fifth force.

All of this is not to say, however, that no galaxy prefers an $f(R)$ fifth force to a cored halo. We repeat the analysis shown in Figure 3.4, i.e. the distribution of ΔBIC for a freely varying $\bar{f}_{R0}$ model versus ΛCDM, but replacing the ΛCDM+NFW model with the ΛCDM+DC14 model (i.e. $\Delta\mathrm{BIC} \equiv \mathrm{BIC}_B - \mathrm{BIC}_G$). In this case, we find that it is now only a minority of galaxies that show *some* preference for $f(R)$, with 29/85 galaxies having $\Delta\mathrm{BIC} < 0$, down from 64 in the NFW case. The numbers at the extremes have also shifted, with 14 galaxies showing a strongly significant ($|\Delta\mathrm{BIC}| > 6$) preference for $f(R)$ and 21 for ΛCDM, compared with 27 and 0 respectively in the NFW case. These numbers reinforce the idea conveyed by Figure 3.6: ΛCDM with a cored halo profile appears to be preferable over a cuspy halo and $f(R)$ for most of the galaxies in the sample.

Figure 3.7 shows rotation curve fits of the 3 galaxies with the most extreme preferences for $f(R)$ over ΛCDM+DC14 (i.e. the three galaxies with the most negative values of $\Delta\mathrm{BIC} \equiv \mathrm{BIC}_B - \mathrm{BIC}_G$). These are UGC 11820 ($\Delta\mathrm{BIC} = -22.1$), NGC 2403 (-31.2), and UGC 05253 (-47.1). In the case of UGC 11820, it appears that the $f(R)$ model does indeed do a markedly better job of fitting the rotation curve. There is not a visible 'upturn' feature in the rotation curve, but the overall shape of the rotation curve is much better described by an NFW halo enhanced with a fifth force in the outer regions than by a cored dark matter halo. Indeed, considering the goodness-of-fit in each case, the reduced chi-squared statistic χ^2_ν, drops from 13.4 to 0.8.

However, in the case of UGC 05253, it would appear that there are large-scale features in the rotation curve, both in the central (magnified) region and in the outer stretches, that are not adequately captured by our baryonic models. This picture is borne out by the values of χ^2_ν: 17.7 for Model G, and 9.5 for Model B. The screening radius is being imposed to markedly improve the quality of the fits, but in actuality neither model does particularly well. NGC 2403 shows similar behaviour, although perhaps not quite so starkly. A significant upturn feature at ~ 4 kpc is clearly visible. Both models, with and without a screening radius, approximate this feature. However, the baryonic models are unable to fully fit its magnitude, so a screening radius is imposed to bridge the gap. Again, neither model performs particularly well: χ^2_ν drops from 5.5 to 2.6.

In addition to these caveats, it should be once again borne in mind that the galaxies preferring Model B to Model G are not necessarily showing any preference for a single global

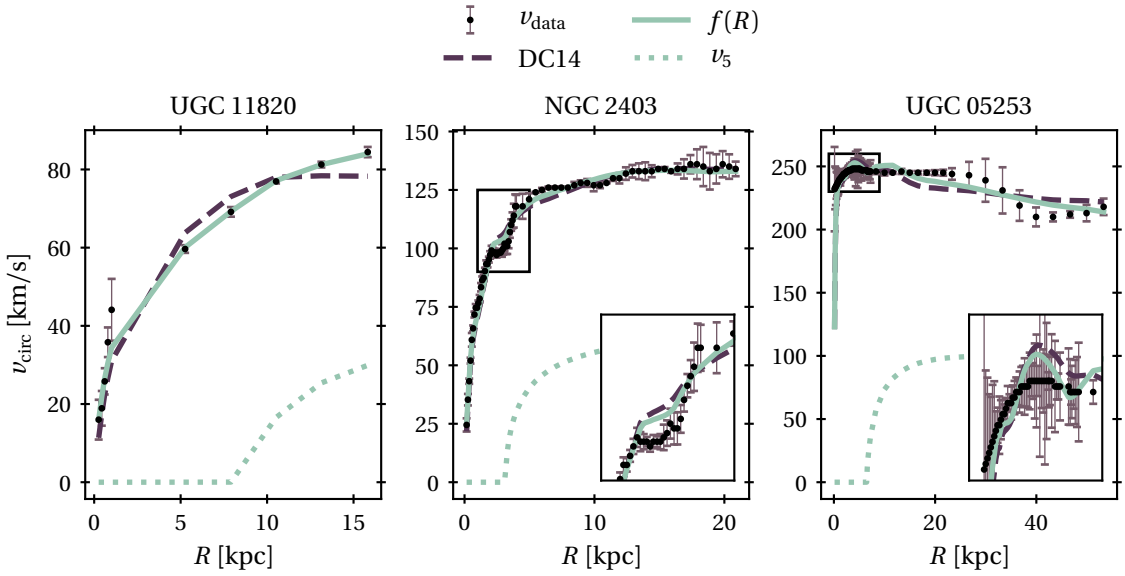

Figure 3.7: Rotation curves and fits of UGC 11820 *(left)*, NGC 2403 *(middle)*, and UGC 05253 *(right)*. These are the three galaxies that have the strongest preference for an $f(R)$ model with an NFW halo and a freely varying $\bar{f}_{R0}$ (i.e. Model B) over a ΛCDM model with a cored DC14 halo (i.e. Model G). The Model B and G fits are consequently the ones shown in the panels, with green solid and purple dashed lines respectively. To give an indication of where the $f(R)$ fit is placing the screening radius, each panel also shows the contribution to the $f(R)$ fit of the fifth force, i.e. v_5, plotted as a green dotted line. The inset panels for NGC 2403 and UGC 05253 give magnified views of crowded areas of the rotation curves. UGC 11820 is a success for $f(R)$, which gives a markedly better fit than the ΛCDM+DC14 model, both visually and formally. In the other two cases, however, neither model does particularly well. From left to right, the best-fitting values of $\log_{10}|\bar{f}_{R0}|$ are -7.07, -6.57, and -6.19.

$\bar{f}_{R0}$ value. In fact, the inferred values of $\log_{10}|\bar{f}_{R0}|$ for the extreme galaxies shown in Figure 3.7 are rather discrepant: -7.07 for UGC 11820, -6.57 for NGC 2403, and -6.19 for UGC 05253. As shown in Figure 3.6, no single, global $\bar{f}_{R0}$ model with a NFW profile is in better agreement with the data than a ΛCDM model with a cored DC14 profile.

3.4.2 Environmental Screening

As described in § 3.3.3, we investigate a model with freely varying $\bar{f}_{R0}$, NFW haloes, and an additional large-scale overdensity to account for the environmental contribution to the scalar field profile. This is Model C, which is identical to Model B in every respect other than the presence of this large-scale overdensity. For a given $\bar{f}_{R0}$ as drawn in the Monte Carlo sampling, the structure will have gravitational potential equal to $\Phi_{\rm ext}$ calculated from the screening maps of Desmond *et al.* (2018c), and size equal to the Compton wavelength calculated using Eq. (1.88).

Figure 3.8 shows a comparison of the $\bar{f}_{R0}$ values inferred from the maximum of the posterior of models Models B and C. Results for the 85 galaxies in our sample are shown, as well as results for the 62 galaxies that were excluded from the sample because of their significant

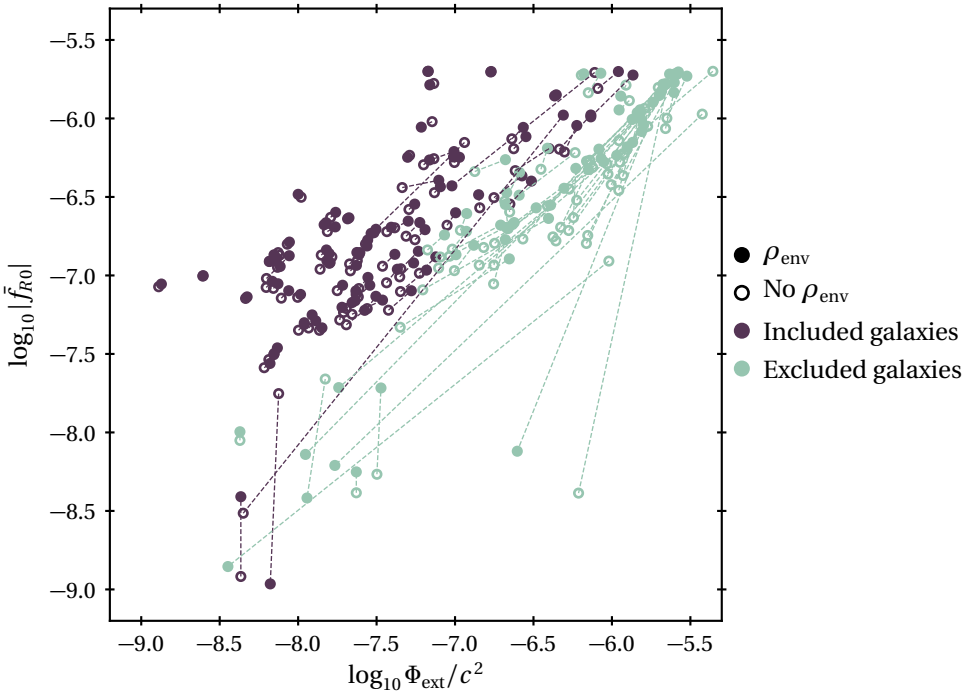

Figure 3.8: Best-fitting $\bar{f}_{R0}$ values for an $f(R)$ model excluding an external large-scale structure (i.e. Model B; unfilled circles) and including one (Model C; filled circles). The two points for a given galaxy are joined by a dashed line to indicate the change caused by including this environmental contribution. Green circles represent the 85 galaxies from our final sample, while purple circles are the 62 galaxies that were cut from the sample due to their overpopulated environment (see text for further details). The x-value for a given point indicates the $\Phi_{\rm ext}$ calculated from the screening map of Desmond *et al.* (2018c) for that given galaxy at the corresponding $\bar{f}_{R0}$ value. This figure indicates that the effect of environmental screening is primarily significant for galaxies that have been cut from the sample, while the environmental effects on our results are small in the galaxies that constitute our final sample.

environmental contribution.

Upon including the environmental contribution, the majority of the galaxies in Figure 3.8 move towards higher $|\bar{f}_{R0}|$ and to higher $\Phi_{\rm ext}$. This makes physical sense: for a given f_{R0}, the addition of an overdense environment will move the screening radius of a galaxy outward. For a rotation curve fit that is improved by a screening radius at a specific location, this effect is compensated by a higher value of $|\bar{f}_{R0}|$, hence the shift towards higher $|\bar{f}_{R0}|$. The shift towards higher $\Phi_{\rm ext}$ is due to the implicit relation between $\bar{f}_{R0}$ and $\Phi_{\rm ext}$: $\Phi_{\rm ext}$ is integrated up to the Compton wavelength, which in turn is determined by Eq. (1.88). A higher $|\bar{f}_{R0}|$ will therefore lead to a higher $\Phi_{\rm ext}$ (note that this is also the reason for the correlation between inferred $\bar{f}_{R0}$ and $\Phi_{\rm ext}$ evident in Figure 3.8). For these cases, this change is visually much larger for the excluded (environmentally screened) galaxies than for the included galaxies.

There is however, also a subset of galaxies for which the jumps are rather large, and these appear to be equally likely to be towards higher or lower $|\bar{f}_{R0}|$. In these cases, f_{R0} is typically very poorly constrained and the marginal posteriors are rather broad, flat distributions (both with and without the environmental contribution). In such scenarios, the peak of the posterior can undergo quite large shifts (in either direction) between models,

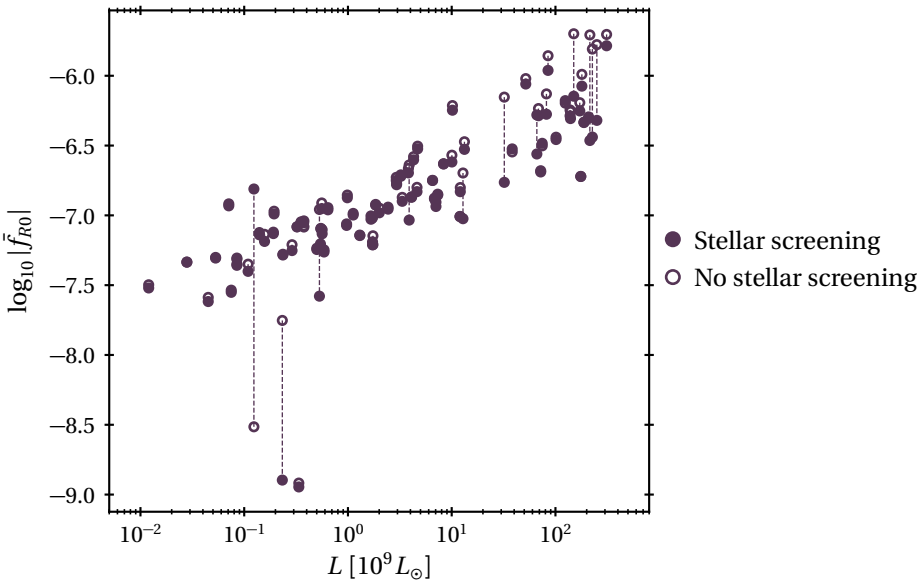

Figure 3.9: Best-fitting $\bar{f}_{R0}$ values for all 85 galaxies, from a model with stellar self-screening (Model D; filled circles) and without (Model B; unfilled circles), as a function of total stellar luminosity. As with Figure 3.8, the small changes shown in this figure indicate that the effect of stellar self-screening on our results is small for the vast majority of the galaxies in our final sample. See the text for a discussion of the few large outliers.

but the distributions are nonetheless mutually consistent.

The finding that the excluded galaxies exhibit a large change in inferred $\bar{f}_{R0}$ (median $|\Delta \log_{10}|\bar{f}_{R0}|| = 0.37$) gives a post hoc justification for their original exclusion from the sample. Meanwhile, the finding that the included galaxies typically do not change their inferred $\bar{f}_{R0}$ values significantly (median $|\Delta \log_{10}|\bar{f}_{R0}|| = 0.04$) gives a post hoc justification for our neglecting the environmental screening effect in most of our models (see Table 3.1).

3.4.3 Stellar Self-Screening

Figure 3.9 shows a comparison of the $\bar{f}_{R0}$ values from the best-fitting models for all galaxies under Models D and B, i.e. $f(R)$ models with and without stellar self-screening, as a function of total stellar luminosity. In Model D, stars do not act as a source of the fifth force, as would be expected if they self-screen completely. Self-screening would also prevent a fifth force from accelerating stars, this is however not relevant here as the measured rotation curves are based on observations of the gas component.

The mean (absolute) change in $|\Delta \log_{10}|\bar{f}_{R0}||$ between Models D and B is 0.11, but this number is dominated by a few outliers. In general, the change is not too large (median $|\Delta \log_{10}|\bar{f}_{R0}|| = 0.02$), with a larger change taking place for more luminous galaxies.

The galaxies with the two largest changes in inferred $\bar{f}_{R0}$ are UGC 05918 ($|\Delta \log_{10}|\bar{f}_{R0}|| = 1.1$) and UGC 07866 (1.7). In the case of UGC 05918, under both Models B and D, the best-fitting models are those in which the galaxy is fully screened. In such a scenario, $\bar{f}_{R0}$ is

poorly constrained as any $|\bar{f}_{R0}|$ value below a certain threshold will fully screen the galaxy, and all such values have equal posterior probability.

Meanwhile, in the case of UGC 07866, the posterior in both Models B and D is bimodal. In one mode, the galaxy is fully screened, while in the other mode, the galaxy is fully unscreened, and the mass of the halo and stellar components are renormalised by a factor of 3/4 to give a very similar rotation curve model. Sellar self-screening causes a slight shift in the relative weights of the two modes, in turn causing the best-fitting model to spontaneously jump from one mode to the other.

Neither of these cases, nor indeed the other outliers with large changes in inferred $\bar{f}_{R0}$, should be causes for concern. In each of these cases, the best-fitting model either fully screens or fully unscreens the galaxy. So, while the best-fitting values are different under the two models, the marginal posterior distributions for $\bar{f}_{R0}$ in both cases are wide, flat distributions that are consistent with each other. The majority of galaxies, however, exhibit the more typical behaviour, where a screening radius in a particular location is favourable, which corresponds to a specific value of $\bar{f}_{R0}$. For these galaxies, the required value of $\bar{f}_{R0}$ is very similar for Models B and D, which is reassuring and justifies neglecting the effect of stellar self-screening in most of the models listed in Table 3.1.

3.4.4 Mass-to-light Ratios

As described in § 3.3.1, Model B (as well as all other models considered besides E and F), performs fits with a single freely varying Υ, which applies to both the bulge and disc components. Model E instead fixes Υ to be equal to $0.5 M_\odot/L_\odot$ for the disc and 0.7 for the bulge, while Model F fits two freely varying ratios: $\Upsilon_{\rm disc}$ and $\Upsilon_{\rm bulge}$.

It should be noted that of the 85 galaxies in the sample, only 13 have a detected bulge component. For the remaining 72 galaxies, Models B and F are identical, and should therefore give identical results.

Figure 3.10 shows a comparison of results from Models B, E, and F. For all 85 galaxies in the sample, the figure shows the $\bar{f}_{R0}$ value for the best-fitting model, for the B, E and F models. The mean (absolute) change is $|\Delta \log_{10}|\bar{f}_{R0}|| = 0.14$ between Models B and E, but this is dominated by a few outliers, and the median change is 0.03. For Models B and F, considering only the 13 galaxies with bulge components, the mean change is 0.07 and the median is 0.01.

These results suggest that fixing the values of the mass-to-light ratios might be too crude an approximation. Indeed, most of the visibly large changes in Figure 3.10 are due to Model E. On the other hand, the reassuringly small changes between Models B and F imply that taking the stellar disc and bulge to have the same mass-to-light ratio is a sufficient approximation.

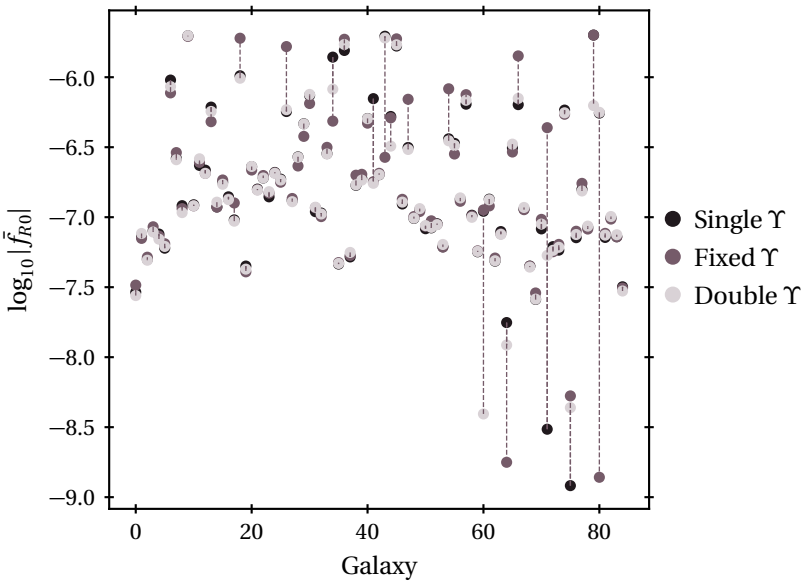

Figure 3.10: For each galaxy in the sample, $\bar{f}_{R0}$ values from the best-fitting model, using three different treatments of the mass-to-light ratio ϒ (i.e., Models B, E, and F). Te darkest points show the results from the model with one free parameter for ϒ (Model B), while the two lighter colours represent Models E and F: models with fixed empirical values, and with two free parameters (for bulge and disc) respectively. Grey dashed lines show the changes in the $\bar{f}_{R0}$ values between models for a given galaxy. This figure indicates that there is no significant change to the results in going from two free parameters to one, but fixing the values as empirical constants induces a more significant change.

3.5 Discussion and Conclusions

In this chapter, we have searched for the potential signatures of HS $f(R)$ gravity predicted in Chapter 2 in the high-quality HI/Hα rotation curve measurements of the SPARC sample. After several cuts to the sample, including an exclusion of all galaxies likely to be environmentally screened, 85 of the original 175 galaxies remained.

Each galaxy is modelled as a stellar disc, gaseous disc, dark matter halo, and (where appropriate) a stellar bulge. Then, for a given $\bar{f}_{R0}$ value, we solve the $f(R)$ equations assuming spherical symmetry, and calculate the implied fifth force contribution to the rotation curve. Assuming a Gaussian likelihood, we are then able to use an MCMC technique to explore suitable models and search for evidence of modified gravity.

Our main findings are:

- In models with an NFW halo and an $\bar{f}_{R0}$ that is allowed to vary freely for each galaxy, most of the galaxy sample (64/85) indicated *some* preference for $f(R)$, according to the Bayesian Information Criterion. Furthermore, 27 galaxies showed a strongly significant ($|\Delta\text{BIC}| > 6$) preference for $f(R)$.

- Looking at the marginal posterior distributions of $\bar{f}_{R0}$ of all galaxies in our final sample, most galaxies have reasonably tight posteriors and $\bar{f}_{R0}$ appears well constrained,

but the spread of these inferred $\bar{f}_{R0}$ values across the sample is very broad, spanning roughly two orders of magnitude. This is inconsistent with a single global value for $\bar{f}_{R0}$.

- This finding is confirmed when analysing models with fixed, globally imposed $\bar{f}_{R0}$ values. Models with $\log_{10}|\bar{f}_{R0}| \gtrsim -6.1$ are highly unfavourable compared to ΛCDM. However, models with lower $|\bar{f}_{R0}|$ appear to be preferred over ΛCDM. This signal reaches a peak at $\log_{10}|\bar{f}_{R0}| \sim -7$, where the log-likelihood ratio $\ln \mathscr{L}_{f(R)}/\mathscr{L}_{\Lambda\mathrm{CDM}} \sim 70$.

- The galaxies that dominate this signal are dwarf galaxies, which have previously been noted to exhibit the core-cusp problem.

- Modelling with cored DC14 haloes without a fifth force, the overall log-likelihood shows an increase of nearly 300, far more significant than any $f(R)$-model with a single, global $\bar{f}_{R0}$ value.

- Modelling with cored DC14 haloes with a fifth force does not provide a significant improvement over the case of DC14+ΛCDM, and the signal at $|\bar{f}_{R0}| \sim 10^{-7}$ has largely vanished.

- There are nonetheless some individual galaxies which show a preference for NFW + $f(R)$ over DC14 + ΛCDM. However, for some of these galaxies it appears to be the case that neither model performs particularly well, as a result of large-scale baryonic features (e.g., due to prominent spiral arms) in the rotation curves inadequately captured by our baryonic models.

- These results appear to be robust to the effects of environmental screening. Having removed a significant fraction of the galaxies for which environmental screening was believed to play a significant role, the results of the $\bar{f}_{R0}$ inference for the remaining 85 galaxies were not affected significantly when a large-scale environment was added to the modelling pipeline.

- Similar analysis was performed to test for the effects of stellar self-screening and a more general treatment of the mass to light ratio. It was also found here that the results of our inference are robust to these effects.

We thus end by reporting an absence of convincing evidence of modified gravity down to the sensitivity level of our sample at $|\bar{f}_{R0}| \sim 6 \times 10^{-8}$, as the improvements to the rotation curve fits due to the $f(R)$ fifth force (which peak at around $|\bar{f}_{R0}| \sim 10^{-7}$) are more readily explained by galaxies having cored dark matter profiles than by a genuine signal of modified gravity.

The only work, to our knowledge, that has previously addressed this degeneracy between cored dark matter profiles and screened modified gravity theories is that of Lombriser & Peñarrubia (2015), which considered the velocity dispersions of the classical MW

satellites Fornax and Sculptor. The radial slopes of their velocity dispersions have previously been shown to be consistent with cored mass profiles (Walker & Peñarrubia, 2011), and Lombriser & Peñarrubia (2015) show that they can alternatively be interpreted as being due to a chameleon fifth force which is unscreened only in the outer parts of these dwarfs.

As discussed in the Introduction (1.1.5), the core/cusp debate remains unsolved. If cored halo profiles ultimately cannot be explained under ΛCDM, we shown that screened modified gravity theories could feasibly ease the tension. However, given that no single $f(R)$ model studied here is able to able to achieve the same likelihood increase as a cored halo profile, it would be interesting to extend the remit of the work presented in this chapter by investigating a wider range of screened modified gravity theories to investigate the constraints that can be derived for them, and whether any such theory can bring cuspy NFW profiles into good agreement with galaxy rotation curve data.

Chapter 4

Asymmetries in Stellar Streams

Summary

If the stars of a Milky Way satellite are screened but the associated dark matter is not, the resulting EP violation can lead to asymmetry between leading and trailing streams if the satellite is tidally disrupted, as stars will be preferentially disrupted into the trailing stream. This chapter provides analytic estimates of the magnitude of this effect for realistic Galactic mass distributions, demonstrating that it is an even more sensitive probe than suggested previously. Additionally, using a restricted N-body code, I simulate 4 satellites with a range of masses and orbits, together with a variety of strengths of the fifth force and screening levels of the Milky Way and satellite. I forecast constraints for streams at large Galactocentric distances, which probe deeper into chameleon parameter space, using the specific example case of HS $f(R)$ gravity. Streams in the outer reaches of the MW halo ($r \sim 100-200$ kpc) provide easily attainable constraints at the level of $|f_{R0}| = 10^{-7}$. Still more stringent constraints at the level of $10^{-7.5}$ or even 10^{-8} are plausible provided the environmental screening of the satellite is accounted for, and screening of the outer halo by the Local Group is not yet triggered in this range. These would be among the tightest astrophysical constraints to date. I note three further signatures of chameleon gravity: (i) the trailing stellar stream may become detached from the dark matter progenitor if all the stars are lost, (ii) in the extreme fifth force regime, striations in the trailing tail may develop from stars liberated at successive pericentric passages, (iii) if the satellite is fully screened, its dark matter is preferentially liberated into the *leading* tidal tail.

This chapter is based on the article:

A. P. Naik, N. W. Evans, E. Puchwein, H. Zhao, A.-C. Davis

Stellar Streams in Chameleon Gravity

Submitted to PRD, preprint available at arXiv:2002.05738

The derivations of the β sensitivities presented in sections § 4.2.2 and § 4.2.3 were primarily undertaken by N. Wyn Evans, one of the co-authors of the above article. These derivations are nonetheless included in this thesis to preserve the completeness of the research project. The remainder of the work presented in this chapter is my own, informed and guided by discussions with the other authors.

4.1 Background

Stellar streams were introduced in the 'Milky Way' section of the Introduction (§ 1.2.4). To recapitulate, stellar streams are the results of dwarf galaxies and globular clusters that have been tidally disrupted by the Milky Way, and the Galaxy's stellar halo is littered with such structures (e.g. Belokurov *et al.*, 2006). Recently, the wealth of data emerging from the Gaia mission has been leading to the discovery and characterisation of abundant streams and substructures (Myeong *et al.*, 2018; Malhan *et al.*, 2018; Meingast *et al.*, 2019; Koposov *et al.*, 2019). In future, Gaia should be able to provide astrometry for very distant streams—at or even beyond the edge of the Milky Way's dark halo—using bright tracers such as stars near the tip of the red giant branch.

The Introduction also discussed the utility of 6D streams data for constraining the acceleration field of the Galaxy. As a result, streams are useful for understanding the underlying mass distribution of the Galaxy, and also for testing gravity. Although this idea has been in the literature for some years, observational tests have been limited primarily by the small number of streams with 6D data before Gaia. However, the field is ripe for further exploitation in the Gaia Era.

Because of their different ages and different positions in phase space, different streams may tell us different things about the theory of gravity. For example, Thomas *et al.* (2018) show that streams from globular clusters are lopsided in Modified Newtonian Dynamics or MOND because the 'external field effect' violates the strong equivalence principle. More relevant for this chapter, Kesden & Kamionkowski (2006a,b) demonstrated that if a fifth force couples to dark matter but not to baryons, this EP violation leads to large, observable asymmetries in stellar streams from dark matter dominated dwarf galaxies. Specifically, the preponderance of stars are disrupted via the outer Lagrange point rather than the inner one, and the trailing stream is consequently significantly more populated than the leading one.

In the years since the work of Kesden and Kamionkowski, the screened modified gravity theories studied in this thesis have become the subject of increasing attention. For reasonable parameter regimes in these theories, main sequence stars will have sufficiently deep potential wells to self-screen against the fifth force. A diffuse dark matter or gaseous component of sufficiently low mass, however, will be unscreened. As a result, the EP is effectively violated. This EP violation was discussed in the Introduction (§ 1.3.2; Figure 1.14) and leads to a number of distinct signatures, such as several of those listed in § 1.3.5.

This chapter explores the idea that the effective EP-violation of chameleon gravity (see § 1.3.2 and Figure 1.14 in particular) should give rise to the stellar stream asymmetries predicted by Kesden & Kamionkowski. We will show that tidal streams in the Milky Way, observable with Gaia, can provide constraints that are comparable to, or stronger than, other astrophysical probes.

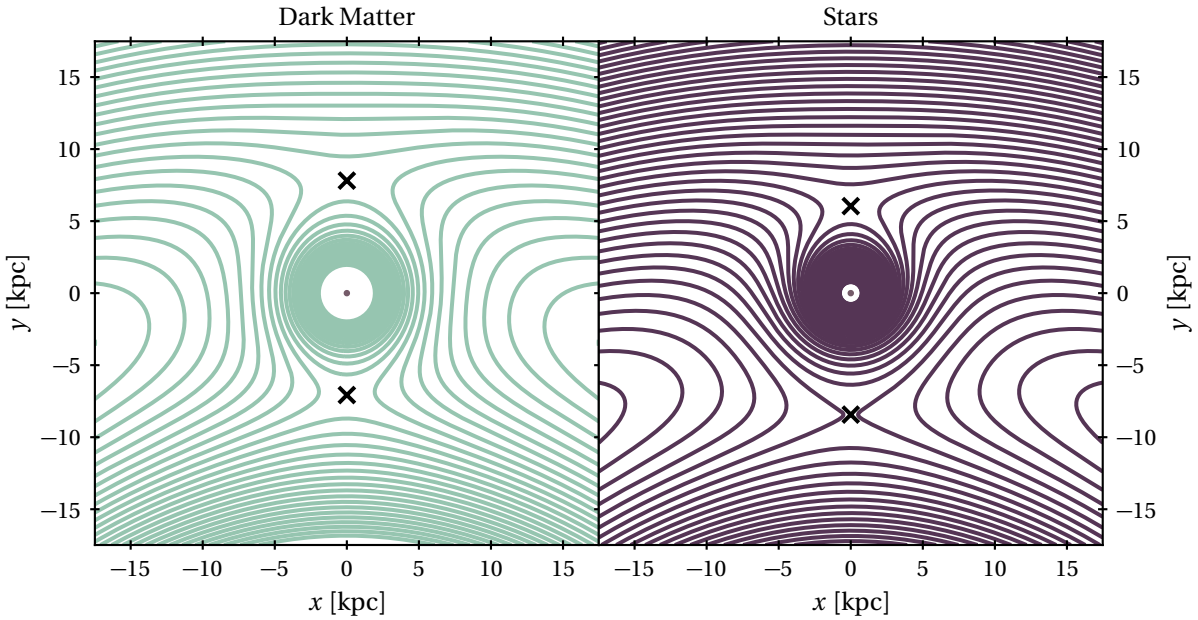

Figure 4.1: *Left:* Contour map of the effective potential for the dark matter $\Phi_{\rm eff,DM}$ as given by Eq. (4.5). *Right:* Contour map of the effective potential for the stars $\Phi_{\rm eff,*}$ as given by Eq. (4.6). In both panels, the satellite (marked by a small circle) is at the origin and the Galactic centre is at $(0,-50,0)$ kpc. The inner and outer Lagrange points are marked by crosses. Note that the circular regions around the satellite centre in which no lines are drawn are due to an artificial cutoff in the contour plotting. Parameters used are: $M = 10^{12} M_\odot$, $m = 10^{10} M_\odot$, and $\beta = 0.5$. The asymmetry of the Lagrange points for the stellar effective potential illustrates the cause of the stream asymmetries under chameleon gravity.

All of the code, analysis tools, and plotting scripts used in this chapter have been made publicly available.[1] Furthermore, animations of various simulations depicted in § 4.6 will be made available online as supplementary material accompanying the article that formed the basis for this chapter: Naik *et al.* (2020).

The following section (§ 4.2) provides a new calculation of the magnitude of the effect, extending the original work of Kesden & Kamionkowski (2006b). Next, § 4.3 describes the Milky Way and satellite models that we use in our simulation code, the methodology and validation of which are in turn described respectively in Sections 4.4 and 4.5. § 4.6 describes results for a range of tidal streams, inspired by examples discovered recently in large photometric surveys or the Gaia datasets. Finally, § 4.7 gives some concluding remarks.

4.2 Stream Asymmetries

4.2.1 A Physical Picture

We begin with a physical picture of the cause of stream asymmetries. Consider a satellite represented by a point mass m. For the moment, let us neglect any fifth forces and assume

[1] github.com/aneeshnaik/smoggy

that the Milky Way and can also be represented as a point mass M, so both satellite and the Milky Way are moving on circular orbits with frequency Ω_0 around their common center of mass.

We use a coordinate system whose origin is at the centre of the satellite. Then, a test particle at position $\mathbf{r}$ moves in an 'effective' gravitational potential given by

$$\Phi_{\rm eff}(\mathbf{r}) = -\frac{Gm}{r} - \frac{GM}{|\mathbf{r}_{\rm MW} - \mathbf{r}|} - \frac{1}{2}\Omega_0^2 |\mathbf{r} - \mathbf{r}_{\rm cm}|^2. \tag{4.1}$$

where r is the position of the point mass representing the Milky Way and $\mathbf{r}_{\rm cm}$ is the position of the centre of mass (e.g. Goldstein, 1951; Binney & Tremaine, 2008). We use the convention $r = |\mathbf{r}|$ to denote the modulus of any vector. The first two terms are the gravitational potentials of the satellite and Milky Way respectively, while the final term provides the centrifugal force due to the frame of reference, which is rotating about the centre of mass with frequency Ω_0, given by

$$\Omega_0 = \sqrt{\frac{G(M+m)}{r_{\rm MW}^3}}. \tag{4.2}$$

In practice, the mass of a typical satellite m is at least two orders of magnitude less than the mass of the Milky Way, and so its contribution to the frequency can be neglected.

The stationary points of the effective potential $\Phi_{\rm eff}$ are the Lagrange points or equilibria at which the net force on a star at rest vanishes. In the circular restricted three-body problem, there are five Lagrange points. Matter is pulled out of the satellite at the 'L1' and 'L2' saddle points, henceforth the 'inner' and 'outer' Lagrange points. These are situated either side of the satellite, co-linear with the satellite and Milky Way. Leading (trailing) streams originate at the inner (outer) Lagrange points, which lie at

$$r_{\rm L} \approx \left(\frac{m}{3M}\right)^{1/3} r_{\rm MW}, \tag{4.3}$$

with respect to the satellite centre (see Section 8.3.1 of Binney & Tremaine, 2008).

Now consider how the system behaves if a fifth force acts on the dark matter. Neglecting any screening, and assuming the satellite is dark matter dominated, the orbit will circle more quickly with frequency given by

$$\Omega_0' = \sqrt{\frac{G'(M+m)}{r_{\rm MW}^3}} \approx \sqrt{\frac{G'M}{r_{\rm MW}^3}}, \tag{4.4}$$

where $G' \equiv (1+2\beta^2)G$. The effective potential experienced by a dark matter particle in this system is

$$\Phi_{\rm eff,DM}(\mathbf{r}) = -\frac{G'm}{r} - \frac{G'M}{|\mathbf{r}_{\rm MW} - \mathbf{r}|} - \frac{1}{2}\Omega_0'^2 |\mathbf{r} - \mathbf{r}_{\rm cm}|^2. \tag{4.5}$$

This is tantamount to a linear rescaling of Eq. (4.1), and the locations of the critical points are therefore unchanged relative to the standard gravity case. However, the effective potential is different for a star which does not feel the fifth force, namely

$$\Phi_{\rm eff,*}(\mathbf{r}) = -\frac{Gm}{r} - \frac{GM}{|\mathbf{r}_{\rm MW} - \mathbf{r}|} - \frac{1}{2}\Omega_0'^2 |\mathbf{r} - \mathbf{r}_{\rm cm}|^2. \tag{4.6}$$

This is not a linear multiple of Eq. (4.1), and the locations of the Lagrange points are consequently altered. The two panels of Figure 4.1 shows contour maps of the effective potentials for dark matter and stars, for $M = 10^{12} M_\odot$, $m = 10^{10} M_\odot$, $r_{\rm MW} = 50$ kpc, and $\beta = 0.5$. Also indicated on the diagram are the locations of the inner and outer Lagrange points of the potentials.

In the dark matter case, the points are approximately equidistant from the satellite centre. However, a significant asymmetry is visible in the stellar effective potential, with the outer Lagrange point being much closer to the satellite and at a lower effective potential. Thus, stars are much more likely to be stripped from the satellite at the outer Lagrange point, and the trailing stream will consequently be more populated than the leading one.

Physically, we can understand this effect in terms of force balance. The stars are being dragged along by the satellite, which is orbiting at an enhanced rotation speed due to the fifth force. This enhanced speed means that the outward centrifugal force on the stars is greater than the inward gravitational attraction by the Milky Way. The consequence of this net outward force is that stars can be stripped from the satellite more easily if they are at larger Galactocentric radii than the satellite, and less easily if they are at smaller radii. This is reflected in the positions of the Lagrange points.

Stars unbound from the satellite will be on a slower orbit around the Milky Way than their progenitor. If β is sufficiently large, then stars that are initially in the leading stream can fall behind and end in the trailing stream.

4.2.2 Circular Restricted Three-Body Problem[2]

We now solve for the stream asymmetries in the circular restricted three-body problem, following and correcting Kesden & Kamionkowski (2006b). This is a useful preliminary before passing to the general case. In Newtonian gravity, the forces balance at the inner and outer Lagrange points, and so

$$-\frac{GM}{(r_{\rm MW}-r_{\rm L})^2}+\frac{Gm}{r_{\rm L}^2}+\frac{G(M+m)}{r_{\rm MW}^3}\left(\frac{M\,r_{\rm MW}}{M+m}-r_{\rm L}\right)=0, \tag{4.7}$$

$$-\frac{GM}{(r_{\rm MW}+r_{\rm L})^2}-\frac{Gm}{r_{\rm L}^2}+\frac{G(M+m)}{r_{\rm MW}^3}\left(\frac{M\,r_{\rm MW}}{M+m}+r_{\rm L}\right)=0. \tag{4.8}$$

We recall that the inertial frame is rotating about the centre of mass, and so the centrifugal terms in Eqs. (4.7) and (4.8) depend on the distance of the Lagrange point to the centre of mass, not the Galactic centre (cf. Eqs. (14) and (15) of Kesden & Kamionkowski, 2006b).

We now define $u = r_{\rm L}/r_{\rm MW}$ and $u' = r'_{\rm L}/r_{\rm MW}$ for the inner and outer Lagrange points

[2]As stated at the beginning of this chapter, the calculations presented in this subsection and the next (§ 4.2.3) were performed by my collaborator N. Wyn Evans.

respectively, and obtain

$$u^3 = \frac{m}{M}\frac{(1-u^3)(1-u)^2}{3-3u+u^2}, \tag{4.9}$$

$$u'^3 = \frac{m}{M}\frac{(1-u'^3)(1+u')^2}{3+3u'+u'^2}. \tag{4.10}$$

Solving, we find that

$$u \approx \left(\frac{m}{3M}\right)^{1/3}\left(1-\frac{u}{3}\right), \tag{4.11}$$

$$u' \approx \left(\frac{m}{3M}\right)^{1/3}\left(1+\frac{u'}{3}\right), \tag{4.12}$$

so the 'natural' asymmetry, i.e. the asymmetry of the inner and outer Lagrange points around the satellite even in standard gravity, is

$$\Delta r_{\rm nat} = (u'-u)r_{\rm MW} \approx \frac{2}{3}\left(\frac{m}{3M}\right)^{2/3} r_{\rm MW}. \tag{4.13}$$

Now introducing a fifth force, the force balance equations for stars not directly coupling to the fifth force become

$$-\frac{GM}{(r_{\rm MW}-r_{\rm L})^2} + \frac{Gm}{r_{\rm L}^2} + \Omega_0^2(1+2\beta^2)\left(\frac{M r_{\rm MW}}{M+m} - r_{\rm L}\right) = 0, \tag{4.14}$$

$$-\frac{GM}{(r_{\rm MW}+r_{\rm L})^2} - \frac{Gm}{r_{\rm L}^2} + \Omega_0^2(1+2\beta^2)\left(\frac{M r_{\rm MW}}{M+m} + r_{\rm L}\right) = 0. \tag{4.15}$$

Proceeding as before

$$u \approx \left(\frac{m}{3M}\right)^{1/3}\frac{1}{(1+2\beta^2)^{1/3}}\left(1-\frac{u}{3}+\frac{2\beta^2}{3}\frac{M}{m}u^2\right), \tag{4.16}$$

$$u' \approx \left(\frac{m}{3M}\right)^{1/3}\frac{1}{(1+2\beta^2)^{1/3}}\left(1+\frac{u'}{3}-\frac{2\beta^2}{3}\frac{M}{m}u'^2\right). \tag{4.17}$$

The last term on the right-hand side produces an asymmetry with opposite sign to the natural asymmetry. Note that as $u \propto (m/M)^{1/3}$, the M/m factor makes this term actually the largest. The condition for the asymmetry due to the fifth force to overwhelm the Newtonian one is then just

$$2\beta^2 \gtrsim 3^{1/3}\left(\frac{m}{M}\right)^{2/3}, \tag{4.18}$$

where only leading terms are kept. This result can be compared with Eq. (29) of Kesden & Kamionkowski (2006b). Although the scaling is the same, the numerical factor is different (remember on comparing results that $2\beta^2$ in our paper corresponds to $\beta^2 f_R f_{\rm sat}$ in theirs). In fact, the changes are very much to the advantage of the fifth force, as smaller values of β now give detectable asymmetries.

The two most massive of the Milky Way dwarf spheroidals are Sagittarius with dark matter mass $2.8\times10^8 M_\odot$ and Fornax at $1.3\times10^8 M_\odot$ (Amorisco & Evans, 2011). These will allow values of $\beta^2 \gtrsim 2\times10^{-3}$ to be probed. For the smallest dwarf spheroidals such as Segue 1 with a mass of $6\times10^5 M_\odot$, then values of $\beta^2 \gtrsim 2\times10^{-4}$ are in principle accessible. It should be noted that the Segue 1 is an ambiguous object, and it is not entirely clear if it is a dark matter dominated dwarf or a globular cluster (Niederste-Ostholt *et al.*, 2009).

4.2.3 General Case

The circular restricted three-body problem is somewhat unrealistic, as the Galaxy's matter distributions is extended. In particular, there is a significant difference in the enclosed host mass within the inner and outer Lagrange points and this plays a role in the strength of the asymmetry. We now proceed to give a mathematical analysis of the general case.

The satellite is now moving on a orbit with instantaneous angular frequency $\mathbf{\Omega}_0$. We work in a (non-inertial) reference frame rotating at $\mathbf{\Omega}_0$ with origin at the centre of the satellite. A test particle at location $\mathbf{r}$ now feels the following forces: (i) a gravitational attraction by the satellite, (ii) a gravitational attraction by the host galaxy; (iii) an inertial force because the satellite is falling into the host and so the reference frame is not inertial and (iv) the Euler, Coriolis and centrifugal forces because the reference frame is rotating. Note that (iii) was not necessary in our earlier treatment of the circular restricted three-body problem because there we chose an inertial frame tied to the centre of mass.

The equation of motion for the test particle is

$$\begin{aligned}\ddot{\mathbf{r}} = &-Gm(r)\frac{\mathbf{r}}{r^3} - GM(|\mathbf{r}-\mathbf{r}_{\rm MW}|)\frac{(\mathbf{r}-\mathbf{r}_{\rm MW})}{|\mathbf{r}-\mathbf{r}_{\rm MW}|^3}\\ &-GM(r_{\rm MW})\frac{\mathbf{r}_{\rm MW}}{r_{\rm MW}^3} - \dot{\mathbf{\Omega}}_0\times\mathbf{r} - 2\mathbf{\Omega}_0\times\dot{\mathbf{r}}\\ &-\mathbf{\Omega}_0\times(\mathbf{\Omega}_0\times\mathbf{r}),\end{aligned} \tag{4.19}$$

Save for the assumption that the matter distributions in the satellite $m(r)$ and the host $M(r_{\rm MW})$ are spherically symmetric, this expression is general.

We now assume that the test particle is following a circular orbit around the satellite with orbital frequency $\mathbf{\Omega}$ and that $r/r_{\rm MW} \ll 1$. By careful Taylor expansion, we obtain

$$\begin{aligned}\ddot{\mathbf{r}} = &-Gm(r)\frac{\mathbf{r}}{r^3} + GM(r_{\rm MW})\frac{(3-n)(\mathbf{r}\cdot\mathbf{r}_{\rm MW})\mathbf{r}_{\rm MW}}{r_{\rm MW}^5}\\ &-GM(r_{\rm MW})\frac{\mathbf{r}}{r_{\rm MW}^3} - \dot{\mathbf{\Omega}}_0\times\mathbf{r} - 2\mathbf{\Omega}_0\times(\mathbf{\Omega}\times\mathbf{r})\\ &+\mathbf{\Omega}_0\times(\mathbf{\Omega}_0\times\mathbf{r}),\end{aligned} \tag{4.20}$$

where $n(r_{\rm MW})$ is the logarithmic gradient of $M(r_{\rm MW})$.

To calculate the tidal radius, we now specialise to the case of a particle whose orbit lies in the same plane as the satellite's orbit. The orbital frequency of the satellite is $\Omega_0^2 = GM(r_{\rm MW})/r_{\rm MW}^3$. The tidal radius is defined as the distance from the centre of the satellite at which there is no net acceleration, i.e., the forces on the particle towards the host and the satellite balance. This gives the tidal radius as

$$r_{\rm L} = \frac{1}{(1-n+2\Omega/\Omega_0)^{1/3}}\left(\frac{m(r)}{M(r_{\rm MW})}\right)^{1/3} r_{\rm MW}. \tag{4.21}$$

When satellite and host are point masses, then $n=0$ and $\Omega_0=\Omega$, and we recover the result previously found in Eq. (4.3).

We now define $u = r_{\rm L}/r_{\rm MW}$ and $u' = r'_{\rm L}/r_{\rm MW}$ for the inner and outer Lagrange points respectively, and obtain

$$u^3 = \frac{m(r)}{M(r_{\rm MW})}\frac{(1-u)^{2-n}u}{1-(1-u)^{2-n}+(1-u)^{2-n}u(2\Omega/\Omega_0-1)}, \tag{4.22}$$

$$u'^3 = \frac{m(r)}{M(r_{\rm MW})}\frac{(1+u')^{2-n}u'}{(1+u')^{2-n}-1+(1+u')^{2-n}u'(2\Omega/\Omega_0-1)}. \tag{4.23}$$

We now solve for the difference in the positions of the Lagrange points with respect to the satellite centre $u'-u$. This is the natural stream asymmetry

$$\Delta r_{\rm nat} \approx (u'-u)r_{\rm MW} = \left(\frac{m(r)}{M(r_{\rm MW})}\right)^{2/3}\frac{(2-n)(3-n)r_{\rm MW}}{3(1-n+2\Omega/\Omega_0)^{5/3}}. \tag{4.24}$$

In the restricted three-body problem, $n=0$ and $\Omega_0=\Omega$, so we recover our previous result in Eq. (4.13).

We wish to compare this asymmetry to the asymmetry produced by adding the modified gravity acceleration of the satellite to the equation of motion. We find the asymmetry due to the fifth force is

$$\Delta r_5 \approx -\frac{4(2\Omega/\Omega_0-1)}{3(1-n+2\Omega/\Omega_0)}\beta^2 r_{\rm MW}. \tag{4.25}$$

So, the requirement that the dark matter asymmetry overwhelms the natural asymmetry is

$$2\beta^2 \gtrsim \frac{(2-n)(3-n)}{2(1-n+2\Omega/\Omega_0)^{2/3}}\left(\frac{m}{M}\right)^{2/3}\frac{1}{2\Omega/\Omega_0-1}, \tag{4.26}$$

which again reduces to Eq. (4.18) in the restricted three body case, as it should. For galactic dynamics, a reasonable choice is $n=1$, which corresponds to a galaxy with a flat rotation curve, isothermal sphere. Assuming the stars in the satellite satisfy $\Omega=\Omega_0$, then tidal streams in galaxies with flat rotation curves are much more sensitive probes of the dark matter asymmetry. As we move from $n=0$ (the point mass case) to $n=1$ (the isothermal sphere), we gain an additional factor of ≈ 2.3 in sensitivity. The changes are again in our favour. The asymmetries in tidal streams are therefore an even more delicate probe of the fifth force than suggested by the analysis of Kesden & Kamionkowski (2006b).

4.3 Milky Way and Satellite Models

In our simulations, we follow the evolution of a large number of tracer particles, stripped from a satellite galaxy and forming tidal tails. The test particles are accelerated by the gravity field of both the Milky Way and the satellite, together with any fifth force contributions. We begin by describing our models for the Milky Way and satellite.

4.3.1 Milky Way Model

We model the Milky Way potential with a static bulge, disc, and halo. For the Galactic bulge, we adopt a Hernquist sphere (Hernquist, 1990) with density-potential pair

$$\Phi = -\frac{GM_b}{r+a_b}; \quad \rho = \frac{M_b a_b}{2\pi r\,(r+a_b)^3}, \tag{4.27}$$

and a_b and M_b give the scale radius and total bulge mass respectively. The mass enclosed in a given radius is

$$M(r) = M_b \frac{r^2}{(r+a_b)^2}. \tag{4.28}$$

For all of our simulations, we adopt the parameter choices of Law & Majewski (2010) and set $a_b = 0.7$ kpc and $M_b = 3.4\times10^{10} M_\odot$.

For the disc, we use a Miyamoto-Nagai profile (Miyamoto & Nagai, 1975),

$$\Phi = -\frac{GM_d}{\sqrt{R^2 + \left(a_d + \sqrt{z^2+b_d^2}\right)^2}}, \tag{4.29}$$

where R and z are cylindrical coordinates. M_d, a_d, and b_d represent the total mass, scale radius, and scale height respectively. For our Milky Way model, we again adopt the choices of Law & Majewski (2010), specifically $M_d = 10^{11} M_\odot$, $a_d = 6.5$ kpc, $b_d = 0.26$ kpc. The mass enclosed with a given spherical radius r does not have an analytic form. When required (see § 4.3.3), we calculate it numerically.

Finally, we adopt an NFW profile (1.45) for the dark matter halo,

$$\Phi = -4\pi G\rho_h r_h^3 \frac{\ln\left(1+\frac{r}{r_h}\right)}{r}, \tag{4.30}$$

where ρ_h and r_h are the halo scale density and scale radius respectively. The enclosed mass within a spherical radius r is given by

$$M(r) = 4\pi\rho_0 r_h^3 \left(\ln\left(1+\frac{r}{r_h}\right) - \frac{\frac{r}{r_h}}{1+\frac{r}{r_h}}\right). \tag{4.31}$$

We adopt the parameters $M_{\rm vir} = 10^{12} M_\odot$ and $c_{\rm vir} = 12$, which can be converted to values of r_h and ρ_h with

$$\begin{aligned} r_h &= \frac{1}{c_{\rm vir}}\left(\frac{3M_{\rm vir}}{4\pi\Delta\rho_c}\right)^{1/3}, \\ \rho_h &= \frac{M_{\rm vir}}{4\pi r_h^3\left(\ln(1+c_{\rm vir}) - \frac{c_{\rm vir}}{1+c_{\rm vir}}\right)}. \end{aligned} \tag{4.32}$$

So, at a given point, the acceleration on a test particle (neglecting any fifth forces for the moment) due to the Milky Way is given by the sum of the accelerations due to the disc, bulge and halo.

4.3.2 Satellite Model

We model the satellite with a truncated Hernquist sphere with the density cut off at a radius r_t. The reason for this sharp truncation will become clear in the discussion of the fifth force in § 4.3.3. Defining a reduced radius $x \equiv r/a_s$ (thus $x_t \equiv r_t/a_s$) where a_s is the scale radius of the profile, the density-potential pair is given by

$$\begin{aligned}
\Phi(x) &= \begin{cases} -\dfrac{Gm}{r_t}\left[1+\dfrac{(1+x_t)^2}{x_t}\left(\dfrac{1}{1+x}-\dfrac{1}{1+x_t}\right)\right]; & x \le x_t. \\ -\dfrac{Gm}{r}; & x > x_t. \end{cases} \\
\rho(x) &= \begin{cases} \dfrac{A}{x(1+x)^3}; & x \le x_t. \\ 0; & x > x_t. \end{cases}
\end{aligned} \tag{4.33}$$

The density normalisation A is related to the total satellite mass m by

$$A = \frac{(1+x_t)^2}{x_t^2}\frac{m}{2\pi a^3}, \tag{4.34}$$

The mass enclosed within a reduced radius x is then

$$m(x) = \begin{cases} m\dfrac{x^2(1+x_t)^2}{x_t^2(1+x)^2}; & \text{if } x \le x_t. \\ m; & \text{otherwise.} \end{cases} \tag{4.35}$$

For all satellites, we adopt truncation radii of $r_t = 10a_s$, or equivalently $x_t = 10$.

The acceleration on any given test particle due to the satellite can then be calculated from the above relations. For self-consistency, the initial phase-space distribution of the tracer particles is that of a truncated Hernquist profile. Of course, this self-consistency is lost as the simulation advances in time, as many of the tracer particles are tidally removed by the Milky Way, but our assumed satellite potential remains unchanged in mass and shape. However, we will show in § 4.5 that this assumption of an unchanging satellite potential is largely harmless.

4.3.3 Fifth Forces

In addition to gravity, the satellite and the tracer particles also experience accelerations due to the fifth force. The satellite feels a fifth force sourced by the Milky Way, while the tracer particles also feel a fifth force sourced by the satellite.

Fifth forces in screened modified gravity theories were described in § 1.3.2. In particular, Figure 1.14 illustrates how an extended body sources a fifth force and couples to an external fifth for a range of given screening radii. We explore a range of screening regimes for both the Milky Way and the satellite.

In order to derive constraints in the chameleon β/χ_0 plane (or the $\bar{f}_{R0}$ space for HS $f(R)$ gravity) from stellar streams around the Milky Way, we would need to adopt some prescription to convert χ_0 of $\bar{f}_{R0}$ to Milky Way and satellite screening radii. Analytical formulae exist in the case of an ideal, isolated spherical body, e.g. Eq. (1.63). However, as discussed in the previous chapter, such a treatment is difficult to apply to realistic astrophysical bodies, as it is sensitive to the arbitrary choice of outer integration limit, and would also neglect the environmental contribution of the Local Group to the Milky Way's screening, the environmental contribution of the Milky Way to the satellite's screening, and the impact of the non-sphericity of the Milky Way. The calculation therefore requires numerical methods in more realistic scenarios. This was the reason for implementing the 1D scalar field solver in rotation curve modelling of the previous chapter. In this chapter, we instead take the fifth force coupling strength β and the Milky Way and satellite screening radii, $r_{\rm scr,MW}$ and $r_{\rm scr,sat}$, as input parameters, thus saving the computational cost of using such a scalar field solver. However, in § 4.6.4, we investigate the connection between f_{R0} and $r_{\rm scr,MW}$ in order to forecast model constraints from future data.

For both the Milky Way and satellite, we assume spherical fifth force profiles. For the satellite, this is consistent with its gravitational potential, although the sphericity of the satellite may be distorted by its tidal disruption. For the Milky Way, the spherical symmetry is inconsistent with the presence of the disc. The scalar field profiles of disc galaxies have correspondingly discoid shapes (see Chapter 2). However, the scalar field profile is roughly spherical when $r_{\rm scr,MW}$ is much larger than the disc scale radius of 6.5 kpc (cf. Figure 4.13). Even when this is not the case, it is unlikely that relaxing the assumption of spherical symmetry will have an appreciable qualitative impact on our results.

Eqs. (1.62) and (1.64) can be rewritten to give the expression for the modified gravity acceleration due to the satellite on tracer particle i, situated at position $\boldsymbol{x}$,

$$\boldsymbol{a}^{i}_{\rm 5,sat}(\boldsymbol{x}) = 2\beta^2 Q_i Q_{\rm sat}(r)\boldsymbol{a}_{\rm N,sat}(\boldsymbol{x}), \tag{4.36}$$

where β is the coupling strength of the fifth force (an input parameter of our simulations), $\boldsymbol{a}_{\rm N,sat}$ is the Newtonian acceleration due to the satellite, and Q_i and $Q_{\rm sat}(r)$ are the scalar charges of particle i and the satellite respectively. The latter is given by

$$Q_{\rm sat}(r) = \begin{cases} 1-\dfrac{m(r_{\rm scr,sat})}{m}; & \text{if } r \geq r_t. \\ 1-\dfrac{m(r_{\rm scr,sat})}{m(r)}; & \text{if } r_t > r \geq r_{\rm scr,sat}. \\ 0; & \text{otherwise.} \end{cases} \tag{4.37}$$

Here, $m(r)$ is the satellite mass enclosed by radius r, and $r_{\rm scr,sat}$ is its screening radius. Note that the third case of 4.37 corresponds to the case in which the tracer particle is within the screening radius of the satellite so the fifth force vanishes. If $r_{\rm scr,sat} = r_t$, then $Q_{\rm sat} = 0$ in all cases and the satellite sources no fifth force anywhere. Also, we have assumed that the Compton wavelength of the theory is much larger than relevant length scales, so the

exponential damping factor in Eq. (1.62) can be neglected. Q_i meanwhile differs between the particle types. As we assume the stars are fully screened against the fifth force, $Q_i = 0$ for the star tracer particles. On the other hand, we take $Q_i = 1$ for the dark matter tracer particles, which we assume to be a diffuse, unscreened component.

Similarly, the modified gravity acceleration due to the Milky Way on particle i (which can now also represent the satellite) at $\boldsymbol{x}$ is given by

$$\boldsymbol{a}^i_{5,\mathrm{MW}}(\boldsymbol{x}) = 2\beta^2 Q_i Q_{\mathrm{MW}}(r)\boldsymbol{a}_{\mathrm{N,MW}}(\boldsymbol{x}), \tag{4.38}$$

where the symbols have analogous meanings to those above. The scalar charge of the Milky Way is given by

$$Q_{\mathrm{MW}}(r) = \begin{cases} 1 - \dfrac{M(r_{\mathrm{scr,MW}})}{M(r)}; & \text{if } r \geq r_{\mathrm{scr,MW}}. \\ 0; & \text{otherwise.} \end{cases} \tag{4.39}$$

If particle i represents the satellite, then we take the limiting value of the satellite scalar charge $Q_i = Q_{\mathrm{sat}}(r = r_t)$. This is valid as long as the Milky Way centre does not fall within the truncation radius of the satellite centre, which does not happen in any of our simulated orbits.

The formalism given in this subsection demonstrates the utility of truncating the mass profile of the satellite. By so doing, we have made it straightforward to model the satellite as being fully screened ($r_{\mathrm{scr,sat}} = r_t$), fully unscreened ($r_{\mathrm{scr,sat}} = 0$), or partially screened ($0 < r_{\mathrm{scr,sat}} < r_t$).

It is worth remarking that by putting in the Milky Way and satellite screening radii by hand, we inevitably explore combinations that would not be realised in any actual physical theories. Nonetheless, by exploring a large range of such combinations, we aim to capture all possible phenomenology that would arise in these theories.

4.4 Methods

Approximate methods for quickly generating realistic streams by stripping stars at the tidal radius of a progenitor are now well established (Lane *et al.*, 2012; Küpper *et al.*, 2012; Gibbons *et al.*, 2014). The methods work as restricted N-body simulations, in which we follow the orbital evolution of a large number of massless tracer particles. The stream particles are integrated in a fixed Galactic potential, together with the potential of the moving satellite. This method robustly reproduces the morphology of streams, in particular the locations of the apocentres of the leading and trailing branches, yet provides two to three orders of magnitude speed-up compared to conventional N-body experiments (Gibbons *et al.*, 2014). The main extension of our code here is that it incorporates an optional fifth force due to the chameleon field.

4.4.1 Tracer Particles

To generate the initial phase space distribution of N tracer particles, we use a Markov Chain Monte Carlo technique to generate $2N$ samples from an equilibrium distribution function for the Hernquist model. The code allows a choice between two possible distribution functions. The first is the isotropic distribution function (Hernquist, 1990)

$$f(\tilde{E}) = \frac{1}{\sqrt{2}(2\pi)^3 (G m' a_s)^{3/2}} \frac{\sqrt{\tilde{E}}}{\left(1-\tilde{E}\right)^2} \left[\left(1-2\tilde{E}\right)\left(8\tilde{E}^2 - 8\tilde{E} - 3\right) + \frac{3\sin^{-1}\sqrt{\tilde{E}}}{\sqrt{\tilde{E}\left(1-\tilde{E}\right)}} \right], \tag{4.40}$$

and the other is the radially anisotropic distribution function (Evans & An, 2006)

$$f(\tilde{E}) = \frac{3}{4\pi^3 a_s} \frac{\tilde{E}}{GL}. \tag{4.41}$$

Here, E is the specific binding energy of a particle, a_s is the scale radius, $m' = (1+x_t)^2 m / x_t^2$ is the untruncated mass of the satellite, while $\tilde{E} = E a_s / G m'$ is the dimensionless binding energy. The two distribution functions differ in the anisotropy of the velocity distributions. Through experimentation, we find that our simulations show extremely similar results for stream generation, irrespective of the choice of distribution function.

Given these $2N$ samples, we integrate the orbits of the particles in the satellite potential (i.e. neglecting fifth forces and the Milky Way) for 10^{17} seconds (≈ 3 Gyr). At the end of this, we randomly downsample N of these particles, excluding any particles for which the orbit ever strayed beyond the truncation radius. This gives a suitable equilibrium distribution of positions and velocities for the test particles in our simulations.

4.4.2 Orbit Integration

To calculate the trajectories of the various particles, we use a second-order leapfrog integrator. Under such a scheme, the velocities $\boldsymbol{v}$ and positions $\boldsymbol{x}$ of the particles are updated at each timestep i via

$$\begin{aligned} \boldsymbol{v}_{i+1/2} &= \boldsymbol{v}_{i-1/2} + \boldsymbol{a}(\boldsymbol{x}_i)\Delta t, \\ \boldsymbol{x}_{i+1} &= \boldsymbol{x}_i + \boldsymbol{v}_{i+1/2}\Delta t, \end{aligned} \tag{4.42}$$

where Δt represents the timestep size, and $\boldsymbol{a}(\boldsymbol{x})$ represents the accelerations calculated using the expressions given in § 4.3.1, § 4.3.2, and § 4.3.3. At the start of the simulation (i.e. timestep $i = 0$), the 'desynchronised' velocities $\boldsymbol{v}_{-1/2}$ are obtained using

$$\boldsymbol{v}_{-1/2} = \boldsymbol{v}_0 - \frac{1}{2}\boldsymbol{a}(\boldsymbol{x}_0)\Delta t. \tag{4.43}$$

From here, Eq. (4.42) can be used repeatedly to advance the system in time.

Our method for choosing the timestep size Δt is as follows. During the relaxation phase in which the orbits are integrated in the satellite potential for 10^{17} seconds, we calculate the

ID	$\boldsymbol{x}_0$ (kpc)	$\boldsymbol{v}_0$ (km/s)	a_s (kpc)	m ($10^8 M_\odot$)	$t_{\rm max}$ (10^{17} s)
A	(7.7, 0.2, 16.4)	(-44, -117, -16)	0.01	0.0003	1
B	(19.0, 2.7, -6.9)	(230, -35, 195)	0.5	5	1
C	(90, 0, 0)	(0, 0, 80)	0.5	2.5	1.5
D	(150, 0, 0)	(0, 0 , 100)	1	5	2.5

Table 4.1: Parameters for each of the 4 progenitors. Here, $\boldsymbol{x}_0$ and $\boldsymbol{v}_0$ respectively give the position and velocity of the satellite at the *end* of the simulations (see discussion in the text), a_s and m are the Hernquist scale radius and total mass of the satellite, and $t_{\rm max}$ is the total time over which each simulation is run; the farther orbits require more time to undergo an appreciable number of orbital periods. Note that 10^{17} seconds is ~ 3 Gyr. The parameters for Satellite A resemble those of the Pal-5 stream, B the Sagittarius stream, C the Orphan stream, and D a hypothetical stream at large distance.

total energies of all particles at the start and end. We repeat this, iteratively reducing the timestep size, until the energies of all particles are conserved to within 2%. Through experimentation, we found that energy conservation is a good proxy for numerical convergence and this 2% criterion gives accurate, converged results. The final timestep size chosen by this process is then used again for the main simulation. In practice, we find $\Delta t \sim \mathcal{O}(10^{11})$ seconds typically.

4.4.3 Simulations

We simulate the generation of streams from 4 progenitors. Satellite A is inspired by the Palomar 5 stream Pearson *et al.* (2017), B the Sagittarius stream Law & Majewski (2010), C the Orphan stream Koposov *et al.* (2019), and D is a hypothetical stream at large Galactocentric distance, of the kind that is likely to be found in the later Gaia data releases. The parameters for these 4 progenitors are given in Table 4.1.

Note that for each simulation, we integrate the orbit of the satellite alone backwards in time starting at $(\boldsymbol{x_0}, \boldsymbol{v_0})$, then forwards again along with the tracer particles. Thus, the simulations end with the satellite at $(\boldsymbol{x_0}, \boldsymbol{v_0})$. This is to reproduce the current observed position of, e.g., the Sagittarius dwarf.

Figure 4.2 shows the evolution of the orbits over ~ 3 Gyr for each of the 4 satellites, under standard gravity. Also shown are lines indicating the disc-plane Milky Way screening radii for a range of values of f_{R0}. These calculations were performed using the scalar field solver within the $f(R)$ N-body code MG-Gadget (§ 2.2.2) for the Milky Way model described in 4.3.1. We demonstrate later that significant stream asymmetries develop when the orbit is mostly outside the Milky Way screening radius, so these lines give a preview of the modified gravity constraints achievable.

For each satellite, we explore a variety of modified gravity scenarios by varying 3 input parameters: the coupling strength β, the satellite screening radius $r_{\rm scr,sat}$, and the Milky Way

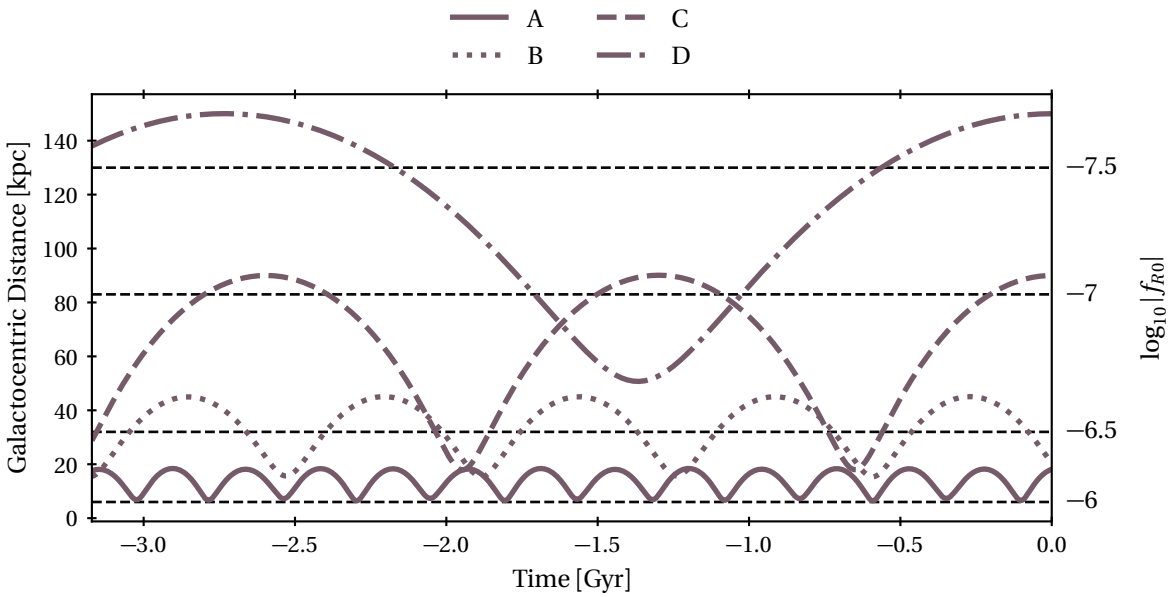

Figure 4.2: For the 4 satellites described in Table 4.1, we show the orbital evolution over 10^{17} seconds (~ 3 Gyr) under standard gravity. The horizontal dashed lines indicate the Milky Way screening radii under Hu-Sawicki $f(R)$ gravity for various different values of the theory parameter f_{R0} (the values of $\log_{10}|f_{R0}|$ are shown at the right hand side of the panel (see Section 4.4.3 for details about the calculation of these screening radii). This Figure illustrates the range of distances probed by tidal streams, and gives an idea of the possible constraints achievable for chameleon gravity theories.

screening radius $r_{\rm scr,MW}$. First, we consider 4 coupling strengths: $\beta = \{0.1, 0.2, 0.3, 0.4\}$. The strength of the fifth force relative to gravity is given by $2\beta^2$, so this corresponds to the range from $2\% - 32\%$. The most extreme case can therefore be used as an approximate analogue for $f(R)$ gravity, where the strength of the fifth force is $1/3$ that of gravity.

For the satellite screening radius, we explore a range of regimes, from fully screened to fully unscreened, and encompassing a variety of partially screened regimes in between. Using the upper case of Eq. (4.37), we recast the screening radius $r_{\rm scr,sat}$ as the scalar charge $Q_{\rm sat}$, and consider a range of values of $Q_{\rm sat}$ from 0 to 1 in steps of 0.1. We recall that $Q_{\rm sat} = 0$ corresponds to the fully screened case, so here $r_{\rm scr,sat} = 10a_s$, where a_s is the Hernquist scale radius of the satellite in question. $Q_{\rm sat} = 1$ is the fully unscreened case, so $r_{\rm scr,sat} = 0$.

Finally, we consider a range of values for the Milky Way screening radius $r_{\rm scr,MW}$. As the orbital distances of each satellite are different, it is useful to select a different range of values for $r_{\rm scr,MW}$ for each satellite. For each satellite, we define a maximum screening radius $r_{\rm scr,max}$, approximately equal to the apocentric distance of the orbit under standard gravity. These values are $r_{\rm scr,max} = 20, 50, 90, 150$ kpc for satellites A, B, C, and D respectively. Then, we choose a range of 11 values such that $r_{\rm scr,MW}/r_{\rm scr,max}$ runs from 0 to 1 in steps of 0.1.

Altogether, we run 485 simulations for each satellite: $4 \times 11 \times 11 = 484$ modified gravity simulations plus one standard gravity ($\beta = 0$) simulation.

4.4.4 Assumptions

The previous subsections have given details about the various parts of our code, but for clarity we provide a list of all of our simplifying assumptions:

1. We neglect self-gravity between the tracer particles, both before and after they are stripped from the satellite, as is typical in Lagrange stripping codes (Gibbons *et al.*, 2014; Bowden *et al.*, 2015). In the context of tidal stream formation, such restricted N-body approaches have previously been shown to accurately reproduce results from full N-body simulations (Küpper *et al.*, 2012).

2. We assume the gravitational attraction on the tracer particles due to the satellite can be approximated as that due to a (truncated) Hernquist sphere, whose orbit is only governed by the Milky Way potential.

3. We assume the depth and radial extent of the satellite potential well does not change over time. While this assumption could be relaxed in the standard gravity case, it is a greatly helpful one in the chameleon case. Thus, to allow a fair comparison between results in the two cases, we make the assumption universally.

4. We assume a static, axisymmetric model for the Milky Way potential, composed of a disc, bulge, and halo. Dynamical friction is therefore not modelled, and previous studies have found that the effect is negligible at these low mass ratios (Boylan-Kolchin *et al.*, 2008). We neglect any effects due to the Large Magellanic Cloud or other Milky Way satellites (cf. Koposov *et al.*, 2019).

5. We assume dark matter to be a diffuse particle fluid. If it were instead comprised of compact objects, it might self-screen in a similar manner to stars.

6. While we typically sample equal numbers of stellar and dark matter particles, we assume the mass profiles of our satellites to be dark matter dominated. So, the satellites feel the full fifth force in the absence of screening.

7. The initial density profile and kinematics of the stellar and dark matter particles in the satellites are assumed to be the same. This simplifies the fifth force calculation, and allows us to ensure any difference in the stellar and dark matter streams is due to the fifth force rather than initial conditions.

Assumptions (1)-(7) apply equally in the standard gravity and modified gravity simulations. The following three assumptions, however, apply only in the simulations including a fifth force.

8. We adopt spherical fifth force profiles around both the Milky Way and the satellite, despite the Milky Way potential being non-spherical.

9. Furthermore, we assume this spherical screening surface of the satellite remains fixed throughout the satellite's orbit. In reality, the radius would vary as the Galactocentric distance of the satellite changes due to environmental screening, and the shape of the screening surface (and surrounding fifth force profile) would likely become aspherical as the satellite approached the Milky Way's screening radius and non-linear effects warp the screening surface.

10. The Compton wavelength of the scalar field is assumed to be much larger than relevant length scales, so that the exponential factor in e.g. Eq. (1.62) can be omitted from our fifth forces calculations. In the context of HS $f(R)$ gravity, the Compton wavelength is given by Eq. (1.88), so this assumption starts to break down at around $|\bar{f}_{R0}| \sim 10^{-8}$.

4.5 Code Validation

As validation, we compare the results of our code for the disruption of the Sagittarius dwarf galaxy under standard Newtonian gravity with the results of Law & Majewski (2010). They simulate the formation of the stream using a full N-body disintegration of the satellite in a static Milky Way potential, so assumptions (1)-(3) in the list in § 4.4 are not made in their work. In other words, the gravitational attractions of the satellite and stream are there treated in fully self-consistent manner.

To set up this test, we adopt the Milky Way potential of Law & Majewski (2010), i.e. the same Hernquist bulge and Miyamoto-Nagai disc described in § 4.3.1, but with a triaxial logarithmic dark matter halo replacing the spherically symmetric NFW halo. The parameters and initial conditions for the satellite are the same as those for Satellite B, given in Table 4.1.

As a first test, we integrate the orbit of the satellite in this potential backwards for 2.5×10^{17} seconds (~ 8 Gyr). The distance of the satellite from the Galactic centre as a function of time is shown in the left-hand panel of Figure 4.3. This shows excellent agreement with Figure 7 from Law & Majewski (2010).

It is also desirable to check the morphology of the streams generated with our method. As a second test, we integrate the orbit of the satellite backwards for 10^{17} seconds (~ 3 Gyr), and then forwards again with 16000 tracer particles. The resulting leading and trailing streams from this simulation are shown in the right-hand pair of panels in Figure 4.3. The detailed morphologies of these streams closely resemble those of the streams depicted in Figure 8 of Law & Majewski (2010), considering only the orange and magenta particles in that figure (i.e., particles liberated within the last 3 Gyr).

This reassuring agreement between the results from our simplified code and those from full N-body simulations validates our methodology, in particular the restricted N-body ap-

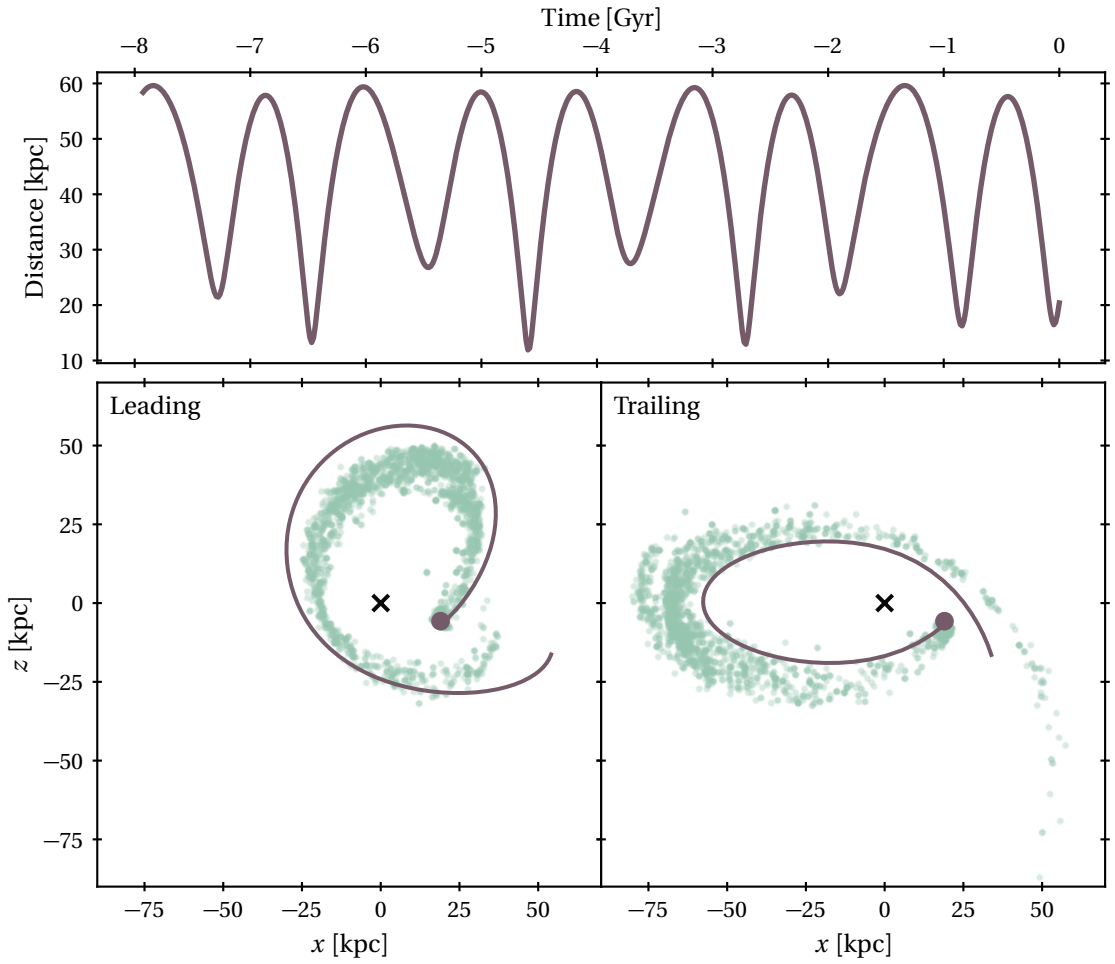

Figure 4.3: Our reproduction of a simulation from Law & Majewski (2010). *Top:* Distance of the simulated Sagittarius dwarf from the Galactic centre over 8 Gyr, to be compared to the results in Figure 7 from Law & Majewski (2010). *Bottom left and right:* First wrap of the leading and trailing streams respectively, to be compared to the results in the two left-hand panels of Figure 8 from Law & Majewski (2010). The curve represents the orbital path of the satellite, culminating in the current position of the Sagittarius dwarf, represented by the filled circle. The green points are the positions of the simulation particles. The satellite orbit has been integrated over 3 Gyr up to the present day, so the morphology of the streams should resemble only the orange and magenta particles from the original figure. This successful reproduction of literature results serves as a test of our code, and checks several of our simplifying assumptions.

proach. However, it is worth noting that the above comparison was standard gravity simulations, so the applicability of the restricted N-body approach in chameleon simulations is not directly addressed.

Ultimately, the restricted N-body approach is a good approximation in the context of stream formation because there is a clear hierarchy of energy scales. Defining $E_{\rm orbit}$ as the energy scale of the MW-satellite orbit (i.e., the specific energy per particle), $E_{\rm tidal}$ as the energy imparted by tidal disruption, and $E_{\rm sat}$ as the binding energy of the satellite, it can be shown that $E_{\rm orbit} \gg E_{\rm tidal} \gg E_{\rm sat}$, provided $m/M \ll 1$ (Kesden & Kamionkowski, 2006b). Meanwhile, the binding energy of the stream $E_{\rm stream}$ is negligible. For these reasons, the only relevant influence on the motion of the stream particles is the attraction from the host

galaxy, and the self-gravity of the stream can be neglected, as can the attraction from the satellite (although we do not make this latter simplification here). With the introduction of a fifth force, these energies would change by $\mathcal{O}(1)$ numerical factors, but the hierarchy of energy scales would be preserved. Thus, it reasonable to expect a restricted N-body approach to be as valid under modified gravity as under standard gravity, so that the above test serves as a more general validation.

On the other hand, several of the assumptions stated in § 4.4.4 are not addressed by this test. In particular, this test does not validate the final three assumptions which pertain to the implementation of the fifth force. However, the aim of the present work is to provide a qualitative understanding of the effects of chameleon gravity on stellar streams. Future work aiming to derive quantitative constraints from observational data will likely require either a relaxation or a more careful justification of some of these assumptions.

4.6 Results

4.6.1 Standard Gravity

Figure 4.4 shows the images from the standard gravity simulations for all 4 satellites listed in Table 4.1. Each of the four quarters of the Figure represents one of the satellites, as labelled in the top corner. The large subpanel in each quarter shows an image of the stream particles at the end of the simulation. As the stellar and dark matter particles are sampled from the same probability distribution initially (see assumption 7 in § 4.4) and there is no EP-violation by a fifth force in these standard gravity simulations, the stars and dark matter particles are indistinguishable and are thus not plotted separately in this Figure. The three smaller subpanels in each quarter show the average velocity along the stream, velocity dispersion along the stream, and velocity dispersion perpendicular to the stream, all as a function of stream longitude and all calculated in bins of particles along the stream. The bins are created adaptively, such that each bin contains 25 particles, including only the particles which have been stripped from the progenitor. Within each bin, the unit vector giving the direction 'along the stream' is taken as the (normed) average velocity vector of all particles in the bin. This Figure illustrates the diversity of our simulated streams, with a variety of morphologies and Galactocentric distances represented.

4.6.2 Unscreened Fifth Force

First, we discuss the results from an unscreened, EP-violating fifth force coupling only to dark matter ($r_{\rm scr,sat} = r_{\rm scr,MW} = 0$). This is the case studied by Kesden & Kamionkowski (2006a,b). This case also applies in screened modified gravity with a (formally) universal coupling if stars self-screen, but screening is not triggered otherwise. In our work, the

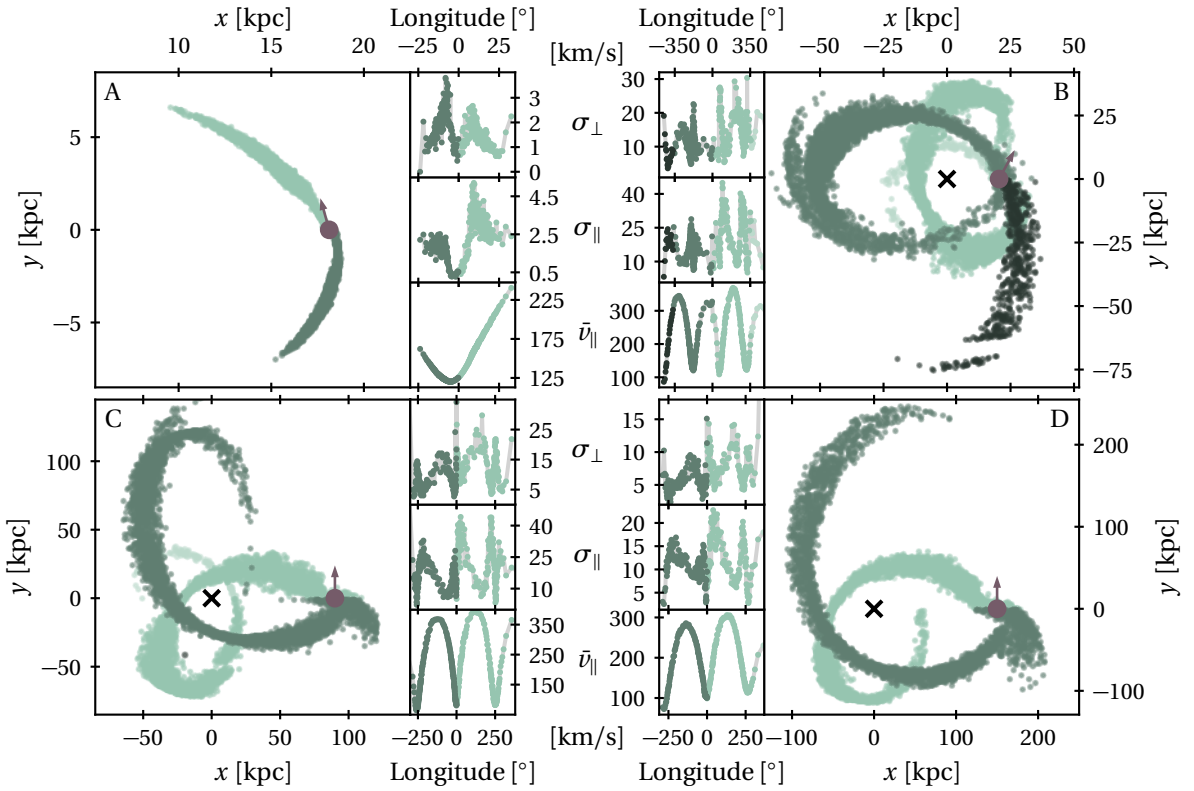

Figure 4.4: The simulated streams under standard gravity. The four quarters represent our 4 satellites: A *(upper left)*, B *(upper right)*, C *(lower left)*, and D *(lower right)*. In each quarter, the largest subpanel shows an image of all stream particles in the orbital plane, at the end of the simulation. No distinction is made between star and dark matter particles. The colours differentiate leading and trailing streams, with the darker shade being the trailing stream. For Satellite B, additional shades are used to distinguish multiple wraps. The black cross shows the position of the centre of the Milky Way, while the filled circle shows the final position of the Satellite, with an arrow indicating its instantaneous direction of travel. The side-panels show three quantities calculated in bins of particles: average velocity along the stream, velocity dispersion along the stream, and velocity dispersion perpendicular to the stream, all in km/s. Here again, the colours differentiate leading and trailing streams. In every case, the orbital plane is defined such that the Satellite is on the x-axis, moving in the positive y-direction.

strength of the fifth force relative to gravity is given by $2\beta^2$, in keeping with the recent modified gravity literature, whereas Kesden and Kamionkowski used β^2. Thus, the simulation depicted in Figure 4.6 for example ($\beta = 0.2$, $F_5/F_N = 0.08$), is most comparable to the '$\beta = 0.3$' ($F_5/F_N = 0.09$) simulation in Kesden & Kamionkowski (2006a,b).

Figure 4.5 shows the shape of Satellite B's orbit for a variety of values of β. In the absence of screening, the introduction of a fifth force as in Eq. (1.61) is tantamount to an overall linear rescaling of the Milky Way mass or gravitational constant by a factor of $1+2\beta^2$. As a consequence, the orbital period of the satellite is shorter and the apocentric distance smaller, as is apparent in Figure 4.5.

Figure 4.6 shows the positions of the dark matter and star particles in the simulation with $r_{\rm scr,sat} = r_{\rm scr,MW} = 0$ and $\beta = 0.2$ for Satellite C, at 11 equally spaced snapshots over

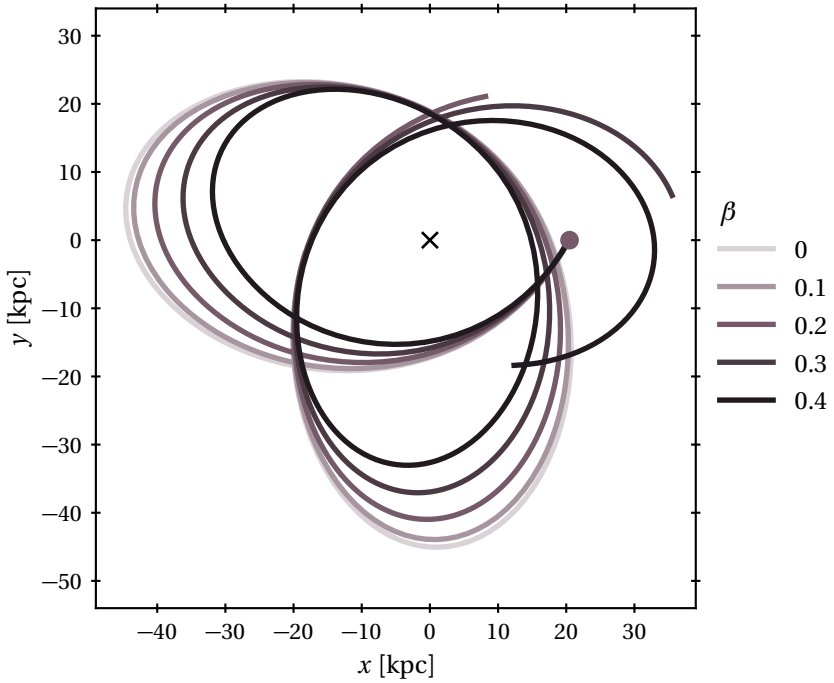

Figure 4.5: Satellite B's orbit in its orbital plane, shown for a range of β with $r_{\rm scr,sat} = r_{\rm scr,MW} = 0$. The cross indicates the Galactic centre and the filled circle shows the final position of the satellite, i.e. the current observed position of the Sagittarius dwarf galaxy. This Figure illustrates the effect of an unscreened fifth force on orbital shapes for a fixed final position.

time. The most striking feature is the asymmetry of the stellar stream. The preponderance of star particles populate the trailing stream, rather than the leading stream. The enhanced rotation speed of the satellite due to the fifth force means that the outward centrifugal acceleration of the stars outweighs the inward gravitational acceleration by the Milky Way. Consequently, stars are more likely to leave the satellite via the outer Lagrange point. Also, even some of the stars which are disrupted from the inner Lagrange point can eventually end up in the trailing stream, once sufficient time has passed for them to be overtaken by the satellite. Meanwhile, the dark matter particles experience the same fifth force as the satellite, and so there is (almost) no preferential disruption via either Lagrange point. The dark matter stream that forms, is consequently almost symmetric around the progenitor.

These effects are also apparent in Figure 4.7, which shows the longitude difference $\Delta\Lambda = \Lambda - \Lambda_{\rm sat}$ as a function of time for all particles in the simulations without screening with β increasing in strength from 0.0 to 0.4 in steps of 0.1 for all 4 satellites. Here, Λ is the longitude in the instantaneous orbital plane of the satellite and increases in the direction of the satellite's motion, so particles in the leading stream have positive $\Delta\Lambda$. The dark matter particles are stripped almost equally into the leading and trailing streams, leading to streams that are nearly symmetric about the progenitor for all values of β. For the stars, however, as β increases, the particles are increasingly disrupted into negative longitudes, i.e. the trailing streams.

Sometimes, the satellite can be stripped completely of all of its stars. Then, the spatial

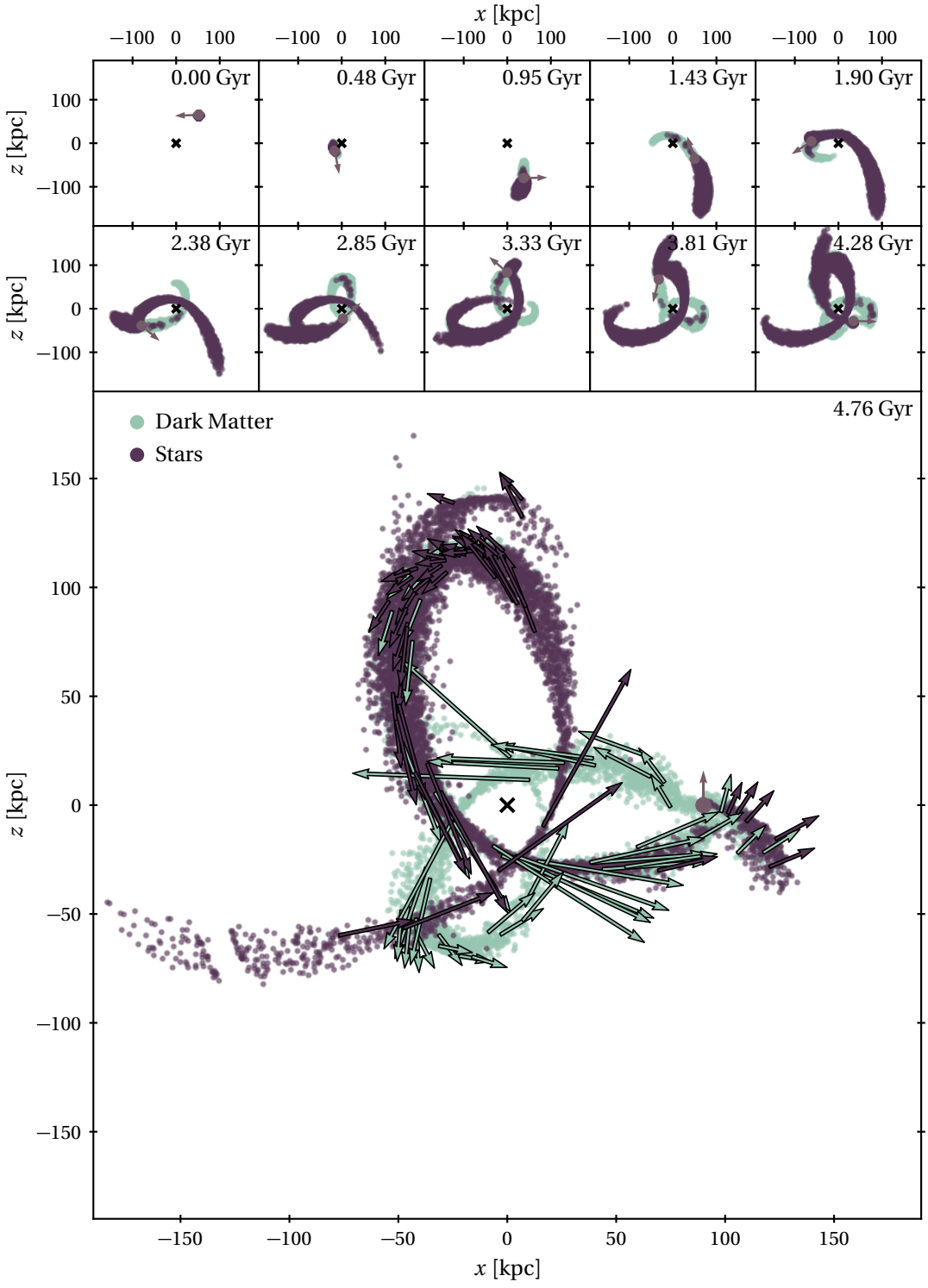

Figure 4.6: The simulation depicted here is Satellite C with no screening and a fifth force coupling only to dark matter with $\beta = 0.2$. The large panel shows an image of the stellar (purple) and dark matter (green) streams at the end of the simulation, while the smaller panels above show the evolution over time. The interval between images is 1.5×10^{16} seconds (~ 0.48 Gyr, as labelled). The cross and large filled circle respectively indicate the positions of the Milky Way and satellite centres. In the large panel, 50 unbound particles have been randomly chosen from each species, and arrows of the corresponding colour are shown indicating their velocities. This Figure shows the formation of an asymmetric stellar stream over time.

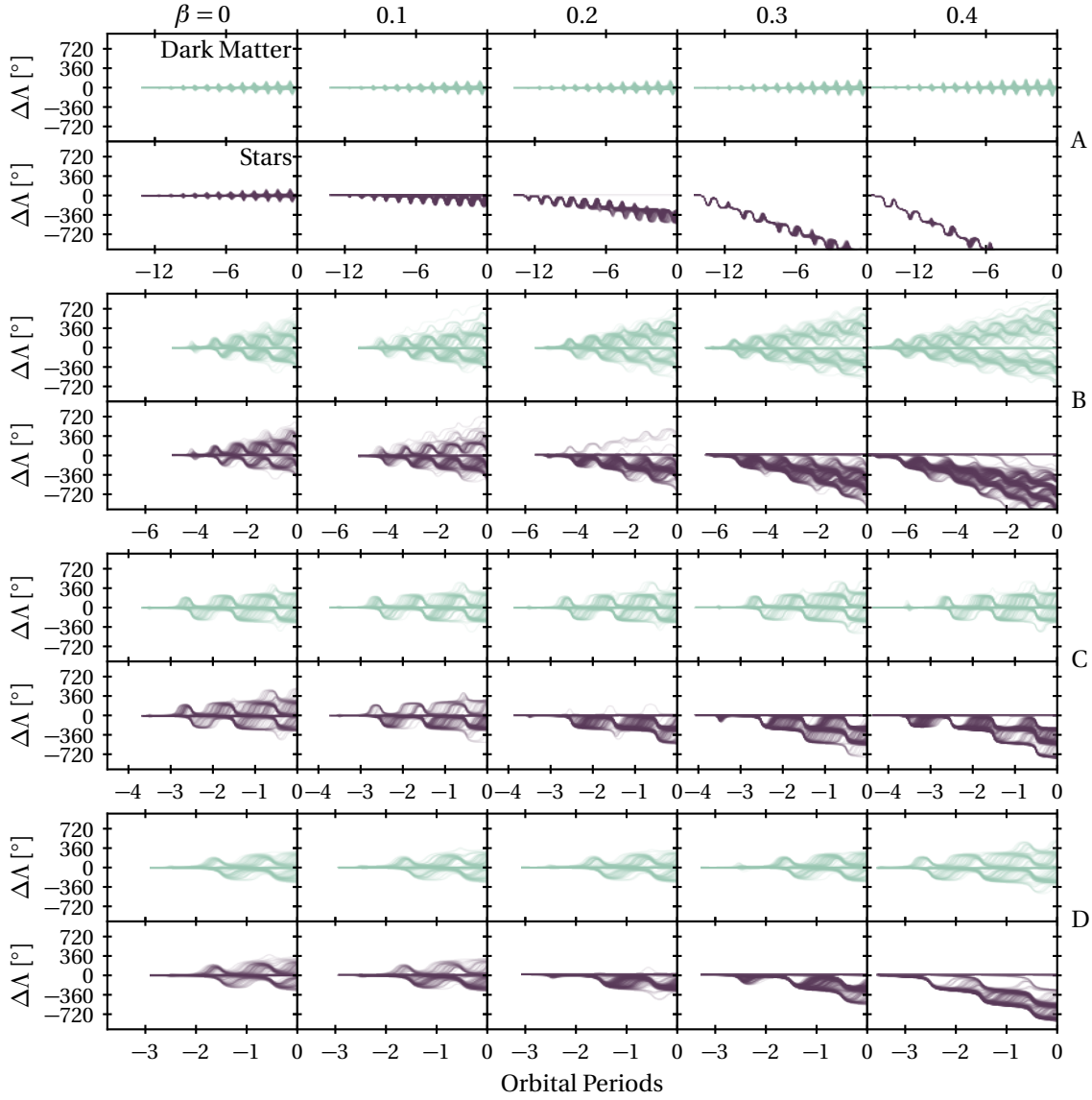

Figure 4.7: The longitude difference $\Delta\Lambda = \Lambda - \Lambda_{\rm sat}$ as a function of time for all 4 satellites without screening. Each column shows a different fifth force coupling from $\beta = 0$ to 0.4 in steps of 0.1. Here, Λ is longitude in the orbital plane of the satellite, increasing in the direction of the satellite's orbit. For each simulation, lines are drawn for 500 star and 500 DM particles (i.e., 1 in 20 particles are randomly sampled). Complementing Figure 4.6, this Figure shows the development over time of the asymmetry of the stellar streams, and the increased magnitude of this effect with β.

separation between satellite and stream can be very large indeed, as no new stars become unbound from the satellite in order to bridge the gap. This occurs in Satellite A for both $\beta = 0.3$ and 0.4, as it loses all of its stars at its first pericentric passage. Satellite A, which is significantly less massive than our other satellites, does not have a sufficiently deep potential well for its stars to remain bound under the enhanced centrifugal force from the Milky Way. Some caution is needed because assumption 3, for example, may begin to break down when the disruption of the satellite due to the Milky Way is so severe. However, all our satellites are, by assumption, dark matter dominated. Even in the simulations where the satellites lose all of their stars, they still retain a large fraction of their dark matter particles,

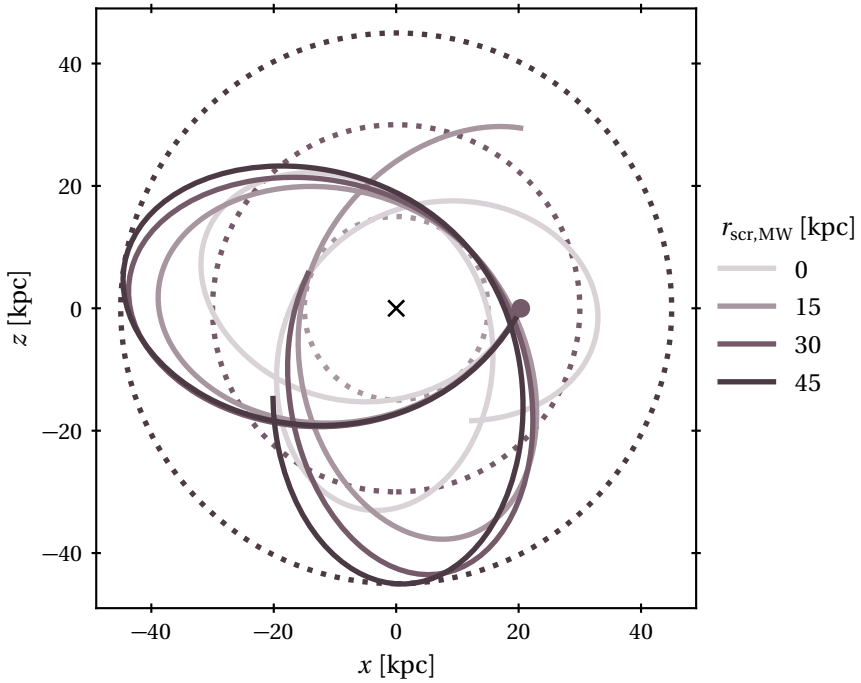

Figure 4.8: Satellite B's orbit in its orbital plane, shown for $r_{\rm scr,MW} = 0, 15, 30, 45$ kpc, and $r_{\rm scr,sat} = 0, \beta = 0.4$. The dotted circles indicate the position of the screening radius in each case. The cross indicates the Galactic centre and the filled circle shows the final position of the satellite, i.e. the current observed position of the Sagittarius dwarf galaxy. This Figure illustrates the effect of a Milky Way screening radius on the satellite orbital shapes.

and thus most of their assumed mass.

4.6.3 Chameleon Screening

We now show results from the chameleon simulations, i.e. the simulations with screening. Unlike the dark matter force investigated in the previous subsection, the fifth force here is universally coupled. However, as discussed in the Introduction (§ 1.3.2), an effective EP-violation arises because main sequence stars are self-screened against the fifth force in parameter regimes of interest.

Figure 4.8 is the analogue of Figure 4.5, now showing the effect on the satellite's orbit of a varying Milky Way screening radius. In the case of the outermost screening radius of 45 kpc, the entire orbit is situated within $r_{\rm scr,MW}$ so this can be taken as equivalent to the standard gravity case. Following along this orbit from plotted position of the progenitor, the other orbits peel away one by one, in order of increasing screening radius. In other words, once the orbit passes outside the screening radius, the fifth force becomes active and the orbit starts to diverge from the standard gravity case. Recalling from Eq. (1.62) that the fifth force is proportional to the mass between the test particle and the screening radius, the divergences do not become noticeable as soon as the orbit passes out of a given screening radius, but some time after, once this enclosed mass is large enough for an appreciable fifth

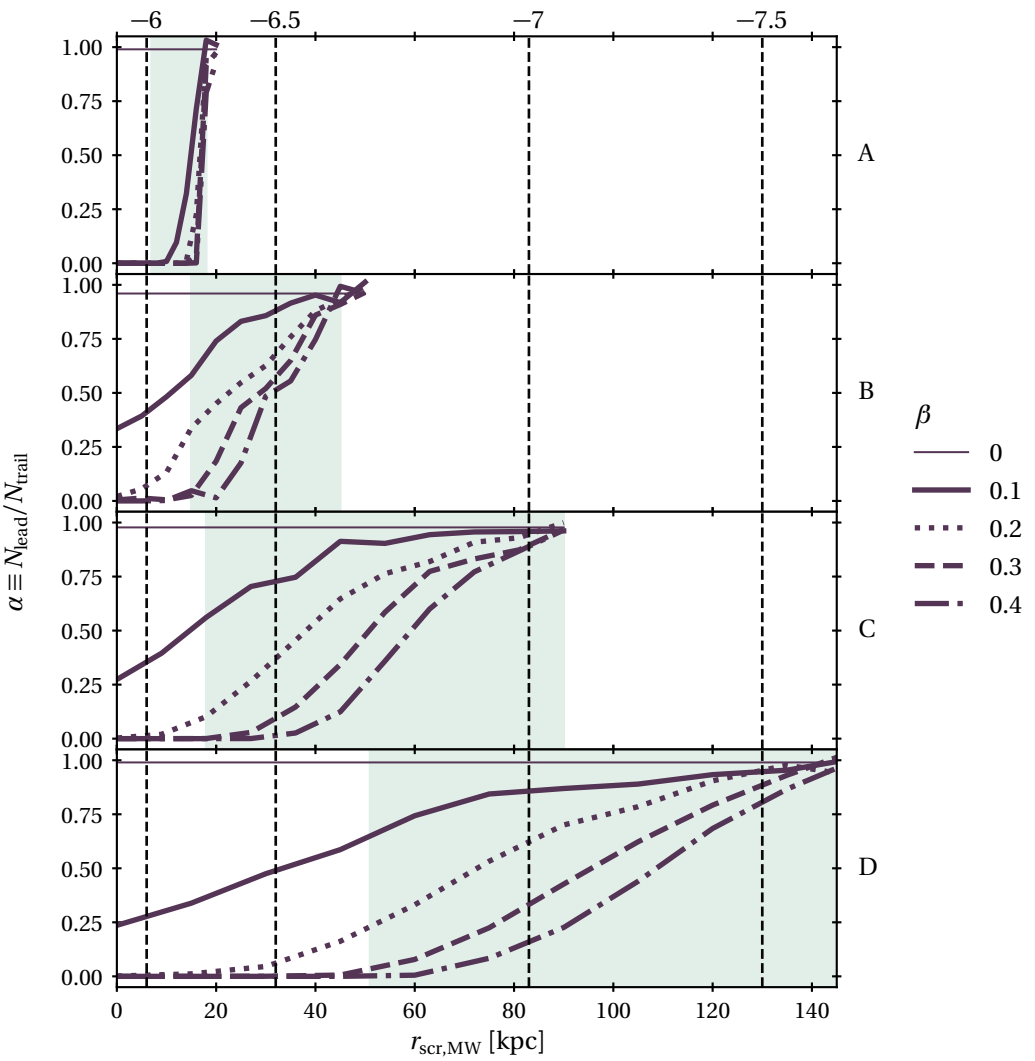

Figure 4.9: The asymmetry parameter $\alpha \equiv N_{\rm lead}/N_{\rm trail}$, for all simulations with $Q_{\rm sat} = 1$. The 4 panels correspond to the 4 satellites and the different textures of line correspond to different values of β. In each panel, the shaded region indicates the radial range of the satellite's orbit. As with the horizontal lines in Figure 4.2, the vertical dashed lines here show the locations of Milky Way screening radii for various values of $\log_{10}|f_{R0}|$. This Figure shows the Milky Way screening radius can affect the stream asymmetry. Streams at larger Galactocentric distances are sensitive to larger screening radii, and therefore weaker modified gravity regimes.

force.

Looking instead at the impact of the Milky Way screening radius on stream asymmetries, one observable quantity is the ratio of the number of stars in the leading to the trailing stream,

$$\alpha = \frac{N_{\rm lead}}{N_{\rm trail}}. \tag{4.44}$$

Figure 4.9 shows this quantity as a function of Milky Way screening radius for all satellites, assuming $Q_{\rm sat} = 1$, i.e. fully unscreened satellites. To ensure a fair comparison between simulations, α is computed in each case at the moment of the satellite's third pericentric passage. As the $r_{\rm scr,MW}$ increases, the asymmetry is progressively reduced. This appears to particularly be the case when $r_{\rm scr,MW}$ lies between the pericentre and apocentre of the

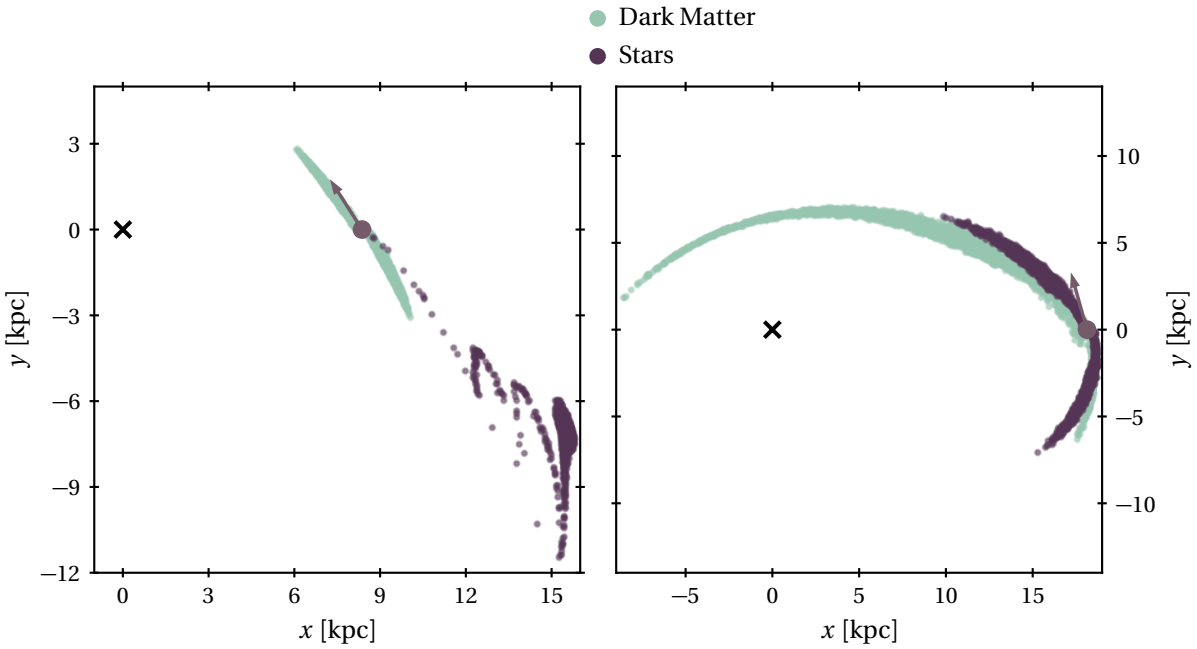

Figure 4.10: *Left:* An image from a simulation of Satellite A, $\beta = 0.4$, $Q_{\rm sat} = 1$, and $r_{\rm scr,MW} = 10$ kpc. *Right:* An image from another simulation of Satellite A, $\beta = 0.1$, $Q_{\rm sat} = 0$, and $r_{\rm scr,MW} = 4$ kpc. This Figure shows some interesting signatures of screened modified gravity other than the stellar asymmetry we have discussed in previous figures.

orbit. This makes sense, as most tidal disruption occurs at and around pericentric passage. Therefore, screening the pericentre has the consequence of reducing the asymmetry of this disruption process. For all of our satellites, the streams are indistinguishable from those in the standard gravity case once $r_{\rm scr,MW}$ exceeds the apocentric distance.

We have observed in our simulations interesting signatures of chameleon gravity other than the stellar asymmetry. Examples of these are depicted in Figure 4.10. First, in the extreme (high β) fifth force regime, the orbital paths of released stars around the Milky Way differ appreciably from their progenitor. However, because stars are released from the progenitor at different times, this also means that the liberated stars can be on different Milky Way orbits from each other. If most releases occur at pericentric passages, this can lead to a 'striping' effect, with neighbouring undulations of stars on the sky, corresponding to streams of stars released at successive pericentric passages. This effect is visible in the left-hand panel of Figure 4.10.

Secondly, if the satellite itself is fully screened or almost so (i.e. low $Q_{\rm sat}$), then it orbits the Milky Way more slowly than the dark matter that has been released and inhabits unscreened space. Then, we observe the opposite asymmetry to that of the stars: the dark matter is preferentially disrupted into the leading stream rather than the trailing stream. This effect is shown in the right-hand panel of Figure 4.10. While interesting, this effect is of course not readily accessible to observations.

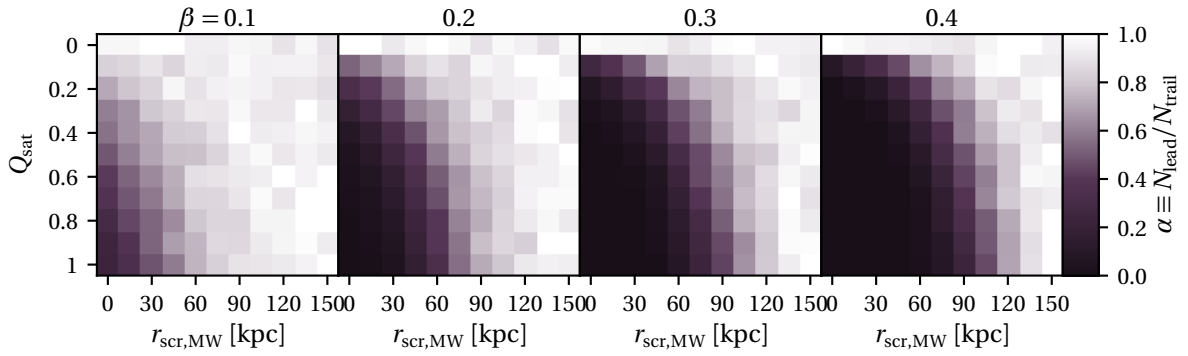

Figure 4.11: The asymmetry parameter $\alpha \equiv N_{\rm lead}/N_{\rm trail}$ for the unbound stellar particles in all simulations of satellite D with screening, shown here as a function of $Q_{\rm sat}$ and $r_{\rm scr,MW}$, with different panels corresponding to different values of β. This Figure shows the effects of varying all of our parameters on the stream asymmetries.

4.6.4 Future Constraints

The later Gaia data releases will likely enable the discovery of stellar streams at large distances from the Galactic centre. As shown in Figure 4.9, such streams are able to probe larger Milky Way screening radii, and therefore 'weaker' (more screened) regions of modified gravity parameter space, potentially down to the level at which screening by our Local Group is triggered.

Figure 4.11 shows α evaluated for all of our simulations of satellite D, as a function of $r_{\rm scr,MW}$, $Q_{\rm sat}$, and β. As with Figure 4.9, α is computed in each simulation at the moment of the satellite's third pericentric passage. This Figure illustrates many of our earlier points; increasing β increases the magnitude of the asymmetry, but the asymmetry is reduced by increasing $r_{\rm scr,sat}$ (reducing $Q_{\rm sat}$) or $r_{\rm scr,MW}$. In the $\beta = 0.4$ case, approximately comparable to $f(R)$ gravity, the asymmetries grow large when $r_{\rm scr,MW} \lesssim 100$ kpc, assuming the satellite is fully unscreened ($Q_{\rm sat} = 1$). Notably, this lies between the apocentre and pericentre of the satellite's orbit. Most tidal disruption occurs at pericentric passage, but here there is still enough disruption outside the screening radius, and sufficient numbers of leading stars lagging behind the satellite, that a large asymmetry develops anyway.

We can again use HS $f(R)$ gravity to give an indication of the kinds of constraints attainable here. Figure 4.12 shows how the Milky Way screening radius depends on the parameter f_{R0}. These calculations were performed using the scalar field solver from MG-Gadget (§ 2.2.2), calculating the fifth forces in the Milky Way model described in 4.3.1. This figure should only be treated as approximate, as the environmental contribution to the scalar field by our Local Group has been neglected.

We see that Satellite D is able to probe the region $\log_{10}|\bar{f}_{R0}| \gtrsim -7.2$. However, if the satellite itself is partially screened, the sensitivity is greatly reduced. It is natural therefore to wonder about the degree to which a satellite would be screened at these values of f_{R0} and this region of the Milky Way's halo.

Figure 4.13 shows the scalar field profile around the Milky Way for $f_{R0} = -10^{-7}$, again

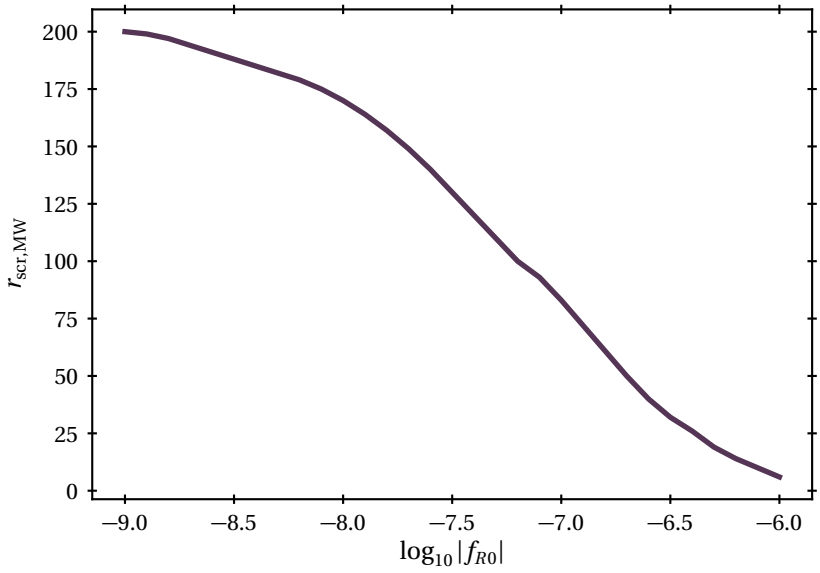

Figure 4.12: The disc-plane Milky Way screening radius as a function of $\log_{10} f_{R0}$. The screening radius is calculated with MG-GADGET, using the Milky Way model described in § 4.3.1.

inferred using MG-Gadget. A Hernquist sphere identical to Satellite D has been inserted at Galactocentric $(X = 100, Y = 0, Z = 100)$ kpc. There is a clear screened region in the centre of the Milky Way halo, with $r_{\rm scr,MW} \approx 80$ kpc. The satellite, however, is unscreened, except for the self-screening of host stars. Therefore, in an $f(R)$ Universe, this satellite would provide very asymmetric streams. This is demonstrated in Figure 4.14, which shows a simulation with a similar setup: Satellite D with $\beta = 0.4$, $r_{\rm scr,MW} = 90$ kpc and conservatively, $Q_{\rm sat} = 0.5$. The left-hand panel shows the stream, while the right-panel shows a more sophisticated observable signature than the asymmetry parameter: the cumulative number function of stars in each stream as a function of longitude in the orbital plane of the satellite. The difference in the two curves is rather striking, and should be clearly discernible in the data.

The examples shown in Figures 4.13 and 4.14 serve as proof of concept, demonstrating that stellar streams in the outer reaches of our Galaxy's halo are a sensitive probe of modified gravity. The observation of highly symmetric streams at large Galactocentric distances would rule out sizeable fifth forces that couple differently to dark matter and stars in the outskirts of the Milky Way. This in turn would provide sensitive constraints on screened modified gravity theories. For instance, looking at Figure 4.12, symmetric streams at distances of $\sim 150-200$ kpc would require $|f_{R0}| \lesssim 10^{-7.5}$ or even $\lesssim 10^{-8}$ to avoid sizeable fifth forces in that radial range. This would be among the tightest constraints on $f(R)$ gravity achievable to date. However, we caution that environmental screening of the satellite may play a more significant role at these levels, but Figure 4.11 suggests that only if the satellite is fully screened does the signal disappear entirely. Even when $Q_{\rm sat} = 0.1$, i.e. 90% of the mass is screened, there is still an appreciable signal. So, given the observation of a large number of symmetric streams, and if there is little environmental screening by the Local Group, then constraints down to these levels are feasible. In practice, the sensitivity may be

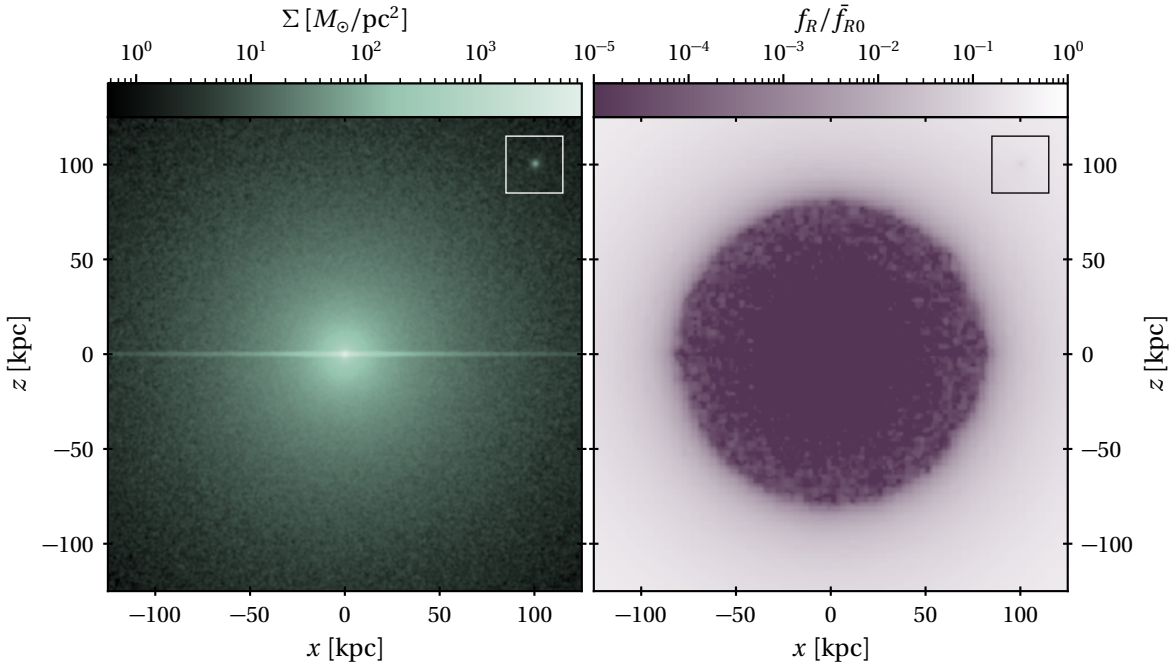

Figure 4.13: *Left:* Edge-on particle density of galaxy+satellite system fed to MG-GADGET to calculate the scalar field profile. The location of the satellite is indicated by the inset box. *Right:* Scalar field profile for $f_{R0} = -10^{-7}$ corresponding to top panel. The Milky Way's screened region is clearly discernible, while the satellite is fully unscreened.

limited if the Local Group screens the whole Milky Way halo at larger $|f_{R0}|$. Detailed studies of the amount of environmental screening expected for the Local Group would be very helpful in this context.

On the other hand, observations of highly asymmetric streams would strengthen the case for screened modified gravity theories. It should be noted, however, that mild asymmetries can arise due to dynamical effects. Indeed, an asymmetry between the leading and trailing streams is expected from Eq. (4.24). This may be compounded by dynamical interactions with dark subhaloes or other satellites (Erkal & Belokurov, 2015), asymmetries in the stellar populations in the progenitor satellite (Peñarrubia *et al.*, 2010; Bonaca *et al.*, 2019), effects of the Galactic bar (Pearson *et al.*, 2017) and regions of chaos in the Galactic potential (Price-Whelan *et al.*, 2016). Such effects would have to be carefully weighed before a modified gravity interpretation could be seriously considered for such observations.

4.7 Conclusions

We have investigated the possible imprints of chameleon gravity on stellar streams from dwarf galaxies around the Milky Way. While canonical chameleon theories are universally coupled, an effective violation of the equivalence principle (EP) arises because of the self-screening of main sequence stars, as noted by Hui *et al.* (2009).

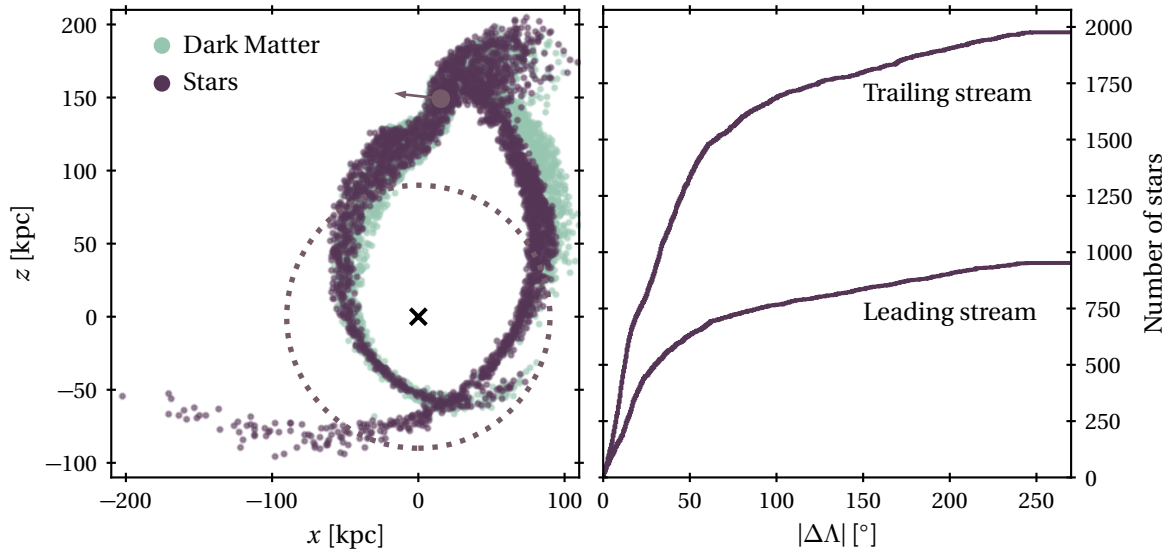

Figure 4.14: *Left:* An image of a simulation of Satellite D, with $r_{\rm scr,MW} = 90$ kpc, $Q_{\rm sat} = 0.5$, $\beta = 0.4$. The dotted circle shows the location of the Milky Way screening radius, while the cross and filled circle show the locations of the Milky Way and satellite centres respectively. The arrow shows the current direction of motion of the satellite. *Right:* Cumulative number of stars in either stream, as a function of longitude in the instantaneous orbital plane of the satellite. This Figure, taken together with Figure 4.13, shows that $f(R)$ gravity with $f_{R0} \sim -10^{-7}$ should give a clear observational signature in stellar streams between 100 and 200 kpc.

As found by Kesden & Kamionkowski (2006a,b), an EP-violating fifth force that couples to dark matter but not baryons causes asymmetries to develop in stellar streams with dark matter-dominated progenitors. The stars are preferentially disrupted via the outer Lagrange points into the trailing streams. We have shown that these asymmetries can also arise in chameleon theories, because of the effective EP-violation described above.

We have corrected and augmented the analytic calculations of Kesden & Kamionkowski (2006b) for point masses so that they are also applicable to extended Galactic mass distributions like isothermal spheres. The effect of these changes is to make the test more sensitive to EP-violating fifth forces. For the most massive dwarf spheroidals, like the Sagittarius or Fornax, the criterion given in Eq. (4.26) suggests values of $\beta^2 \gtrsim 10^{-3}$ can be probed. For the smallest dwarf spheroidals such as Segue 1 with a mass of $6 \times 10^5 M_\odot$, then values of $\beta^2 \gtrsim 10^{-4}$ are in principle accessible. As a rule of thumb for a satellite with mass m at a location enclosing a Milky Way mass M, the form of the criterion suitable for a flat rotation curve galaxy is

$$\beta^2 \gtrsim 2^{-5/3}\left(\frac{m}{M}\right)^{2/3}. \tag{4.45}$$

This asymmetry also occurs in the chameleon context, when screening radii are introduced to the Milky Way and satellite, and with stars self-screening. The magnitude of the asymmetry depends on the coupling strength β, the Milky Way screening radius, as well as the degree of screening of the stream progenitor; large values of β give large asymmetries, but these are reduced with increasing $r_{\rm scr,MW}$ and $r_{\rm scr,sat}$.

We have created a restricted N-body code, and used it to simulate the formation of tidal streams from progenitors, with a variety of masses and Galactocentric distances. We considered a range of modified gravity scenarios (coupling strength, Milky Way screening level, satellite screening level) in each case. Our simulations – the most comprehensive to date for the formation of tidal streams under chameleon gravity – have revealed further interesting effects. First, the trailing stellar stream may become detached from the dark matter progenitor if all the stars are exhausted by earlier pericentric stripping. As an example, this effect is visible in Figure 4.7 and occurs for low mass satellites in the extreme fifth force regime. Second, prominent striations in the stellar trailing tail may exist if stars are stripped at repeated pericentric passages by a strong fifth force. Thirdly, if the satellite is fully screened, its orbital frequency is lower than that of its associated dark matter. This leads to strong asymmetries in the dark matter distribution, which is preferentially liberated into the leading tidal tail.

Taking Hu-Sawicki $f(R)$ gravity with $f_{R0} = -10^{-7}$ as an example, we derive a Milky Way screening radius of around 80 kpc. A massive dwarf spheroidal galaxy at a distance of $\approx$ 150 kpc – such as Fornax – would be fully unscreened (except for self-screening stars) and produce highly asymmetric streams under tidal disruption.

The ratio of the cumulative number function of stars in the leading and trailing stream as a function of longitude from the satellite is computable from simulations, measurable from the observational data and can provide a direct test of theories with screening mechanism, like chameleon gravity. The later Gaia data releases may lead to discoveries of stellar streams at distances $\gtrsim 100$ kpc from the Galactic centre. These streams will be a sensitive probe of modified gravity; such highly asymmetric streams at these distances would be tell-tale signatures of modified gravity.

On the other hand, if the data uncover a number of very symmetric streams, then constraints down to the level of $f_{R0} \sim -10^{-8}$—the tightest constraints to date—could be attainable if the screening of the satellite and other nuisance parameters are carefully taken into account, and assuming that the Local Group does not yet environmentally screen the whole Milky Way halo at these f_{R0} values. Also, our assumption that the Compton wavelength is much larger than relevant length scales begins to break down at such values of f_{R0}, and Yukawa suppression will become appreciable below $f_{R0} \sim -10^{-8}$. Of course, the investigation need not be limited to Hu-Sawicki $f(R)$ gravity. Sensitive constraints will also be attainable in the general chameleon parameter space, and we merely use $f(R)$ gravity as a fiducial theory.

Finally, we note that other screened modified gravity theories can also be probed with stellar streams. For instance, the symmetron screening mechanism has a simple density threshold as a screening criterion (Hinterbichler & Khoury, 2010; Hinterbichler *et al.*, 2011). Consequently, there will necessarily be a region of parameter space in which the stars are screened, but the surrounding diffuse dark matter component is not. In this regime, stream

asymmetries will also be present and are worthy of future investigation.

Chapter 5

Conclusions and Outlook

In this thesis, I have investigated two signatures of screened fifth force theories on galactic dynamics. The first—upturns in the outer regions of rotation curves—is a novel idea, studied for the first time in the two published articles that formed the basis for Chapters 2 and 3 respectively (Naik *et al.*, 2018, 2019). The second signature—asymmetries in tidal streams—is an older idea, first investigated by Kesden & Kamionkowski (2006a,b) in the context of an EP-violating "dark matter force". In Naik *et al.* (2020), this idea was revived and the predicted effect reinvestigated in the context of screened fifth forces. That article formed the basis for Chapter 4. This chapter briefly recapitulates the results and conclusions of these investigations, followed by a discussion of possible future directions, before ending with some final remarks.

Conclusions

Screened modified gravity theories are theories in which additional degrees of freedom (typically scalar fields) couple to gravity in such a way that their mediated fifth forces are suppressed in regions of high density such as our Solar System. In the chameleon screening mechanism, this is achieved with a density-dependent effective mass for the scalar field. An example of a chameleon theory is Hu-Sawicki $f(R)$ gravity, used throughout this thesis as a fiducial theory.

In Chapter 2, I considered the behaviour of Hu-Sawicki $f(R)$ gravity in MW-size spiral galaxies. Using the $f(R)$ N-body code MG-Gadget, I calculated the instantaneous scalar field and fifth force profiles across a number of simulated galaxies, sourced from the Auriga Project simulations. In these galaxies, the scalar field took on a discoid shape, reflecting their mass distribution. In galaxies where screening was triggered in the central regions, the boundaries between screened and unscreened region was an oblate surface.

Calculating the rotation curves of these galaxies in the disc plane, the fifth force contribution beyond the screening radius (defined here as the distance in the disc plane of the

screening surface from the galactic centre) led to upturns in the outer regions of the rotation curves. For a given galaxy, the exact location of the upturn depends on the mass, size, and environment of the galaxy, as well as the cosmic background value of the scalar field, $\bar{f}_{R0}$. This prediction of rotation curve upturns provides a novel signature of screened modified gravity. Another related signature presented in Chapter 2 was found in the radial acceleration relations of the galaxies: the relation, for a given galaxy, between total acceleration at each point in the disc as inferred from the rotation curve and the acceleration at the same points due to baryonic mass inferred from the observed light distribution. Here, kinks appeared in the radial acceleration relations, corresponding directly to the rotation curve upturns.

At $|\bar{f}_{R0}| \lesssim 10^{-7}$, the Auriga galaxies were fully screened, rendering them indistinguishable from ΛCDM. On the other hand, at $|\bar{f}_{R0}| \gtrsim 2 \times 10^{-6}$, the galaxies were fully unscreened, suggesting an incompatibility with Solar System constraints if analogised directly with the Milky Way. Chapter 2 thus ended with a predicted sensitivity level of this rotation curve test of $|\bar{f}_{R0}| \sim 10^{-7}$.

To search for the rotation curve signature in observed rotation curves, in Chapter 3 I turned to the galaxies of the SPARC sample. The SPARC sample is a sample of 175 high-quality HI/Hα rotation curves, spanning five orders of magnitude in galaxy mass. Following a series of cuts to the sample, including a cull of galaxies for which environmental screening was predicted (using 'screening maps' of the local Universe) to play a dominant role, 85 rotation curves remained.

Importantly, the SPARC sample pairs rotation curve measurements with 3.6μm surface brightness profiles, tracing the galaxies' stellar mass profiles. This facilitates the splitting of dynamical models of the galaxies into their individual components: stars, gas, dark matter, and the fifth force. Having constructed a detailed forward model of the rotation curves, I scored the models against the data using a Gaussian likelihood function, and used an MCMC technique to explore the $\bar{f}_{R0}$ parameter space and compare the performance of $f(R)$ against ΛCDM+GR.

Leaving $\bar{f}_{R0}$ as a free parameter for each galaxy, most galaxies showed *some* preference for $f(R)$. Using the Bayesian Information Criterion to compare models, 64 of 85 galaxies gave $\Delta\mathrm{BIC} = \mathrm{BIC}_{f(R)} - \mathrm{BIC}_{\Lambda\mathrm{CDM}} < 0$. In many cases (27 of 85) this was a strong preference, with $\Delta\mathrm{BIC} < -6$. However, the preferred values of $\bar{f}_{R0}$—tightly constrained for most individual galaxies—showed a large spread across the sample of around two orders of magnitude, inconsistent with a single global value.

Globally fitting the sample with a single value of $\bar{f}_{R0}$, $f(R)$ models with $\log_{10}|\bar{f}_{R0}| > -6.1$ are disfavoured with respect to ΛCDM. On the other hand, $f(R)$ models with lower values of $|\bar{f}_{R0}|$ are favoured. The peak signal is at $\log_{10}|\bar{f}_{R0}| \sim -7$, where $f(R)$ gives a huge log-likelihood increase of 70 over ΛCDM. However, it would appear that this signal arises primarily from a well-known problem in near-field cosmology: the core/cusp problem.

The galaxies that dominate the signal are galaxies for which the assumed 'cuspy' NFW halo model appears to provide a poor fit. In the absence of any fifth forces, an alternative 'cored' halo model gives a full-sample log-likelihood increase of 300 compared with NFW+ΛCDM, much larger than any improvement provided by NFW+$f(R)$. Furthermore, adding fifth forces does not appear to add any appreciable further improvement to the cored halo model. The tentative modified gravity signal is therefore much more readily interpreted as a signal of cored haloes, and a greater understanding of dark matter halo shapes under ΛCDM needs to be arrived at before a modified gravity interpretation can be seriously considered.

In Chapter 4, I turned my attention to the stellar streams of the Milky Way's stellar halo. These streams are created when satellite stellar systems—such as dwarf galaxies or globular clusters—are tidally disrupted by the Milky Way, and stars are stripped from the satellite via the L1 and L2 Lagrange points. Under standard gravity, approximately equal numbers of stars are stripped via both Lagrange points, leading to streams that are approximately symmetric about their progenitor. However, if a fifth force couples to dark matter in a dwarf galaxy but not stars, the stars will lag behind the satellite centroid, and will be preferentially disrupted via the L2 point, leading to an asymmetrically engorged trailing stream and diminished leading stream. This effect was first described by Kesden & Kamionkowski (2006a,b) in the context of a generic EP-violating "dark matter force". It was later noted by Hui *et al.* (2009) that although screened modified gravity theories are universally coupled, an effective EP-violation arises when compact objects (e.g. stars) are screened within an unscreened environment (the dwarf galaxy progenitors).

To my knowledge, Chapter 4 gives the first quantitative treatment of stellar streams under chameleon gravity. The first key result was the extension of the calculation of Kesden & Kamionkowski (2006a,b) from point masses to extended mass distributions, leading to the conclusion that stellar streams are a significantly more sensitive probe of EP-violation than originally suggested in that work. Using a realistic Milky Way model and a restricted N-body code, a large number of streams were simulated under chameleon gravity, giving an idea of the kinds of constraints attainable from Gaia data. The final part of the chapter once again used the example of Hu-Sawicki $f(R)$ gravity, with $\bar{f}_{R0} \sim -10^{-7}$. Here, a stellar stream in the Galaxy's outer halo (between 100 and 200 kpc) would show an unambiguous asymmetry in the numbers of stars along each stream: a smoking gun for modified gravity. Conversely, highly symmetric streams at such distances would be able to place very strong constraints on screened modified gravity theories (plausibly down to $|\bar{f}_{R0}| \sim 10^{-8}$), as they would require very large Milky Way screening radii or very weak coupling strengths. An important caveat is that more work needs to be done to understand the Local Group's environmental contribution to the screening of the Galaxy; a factor neglected in Chapter 4.

Outlook

The primary limitation of the rotation curve upturn test was the uncertainty regarding the shapes of the density profiles of dark matter haloes. One way in which this issue could be partially resolved would be via more accurate, higher (spatial) resolution rotation curves. The degeneracy between cored haloes and fifth force upturns is not a true one; the strong implication of Figure 3.6 is that the dark matter haloes of galaxies like UGC 00891 are cored, but an incorrect cuspy halo fit can nonetheless be improved if a fifth force is added in the outer regions, allowing the total mass of the halo to be reduced, thus lessening the discrepancy in the halo centre. A higher resolution rotation curve here would help to determine whether this is the case, or if there is truly an upturn feature at around $R \approx 3$ kpc, as the $f(R)$ fit would require. One possible option would be to search for the signature using spatially resolved galaxy kinematics from an integral field spectroscopic survey such as MaNGA (Mapping Nearby Galaxies at Apache Point Observatory; Bundy *et al.*, 2015).

Ultimately, however, it will remain difficult to perform cast iron model comparisons using this rotation curve test until the theoretical predictions for dark matter halo shapes are better understood, under both ΛCDM and $f(R)$. Given the fast pace of progress in the field of simulations (under both paradigms), this could well be realised soon.

The most obvious future research project suggested by this thesis is the stellar streams test described in Chapter 4. That chapter particularly anticipated the upcoming third Gaia data release which is predicted to lead to the discovery of streams in the outer halo of the Milky Way. The strength of the predicted signal in e.g. Figure 4.14 suggests that even a simple determination of asymmetry from stream observations would rule out significant chunks of theory parameter space. To advance beyond this and achieve the full sensitivity possible would likely necessitate a more detailed calculation, involving a careful determination of stream membership and accounting of selection effects.

As mentioned previously, if one is to use the outer regions of the Milky Way as a probe of screened fifth forces, it will be necessary to understand exactly how theory parameters (e.g. $\bar{f}_{R0}$) translate to screening radii. The result of a crude calculation was displayed in Figure 4.12, but the Local Group will need to be accounted for, and uncertainties about the Milky Way mass marginalised over.

Another idea worth pursuing after Chapter 4 is the measurement of stream asymmetries around other galaxies. Streams have already been observed around other galaxies (e.g. Martínez-Delgado *et al.*, 2008, 2010), and it seems likely that future wide-field surveys such as LSST will be able to observe streams at large distances from their host galaxies. This, combined with a calculation of the host galaxy screening properties (e.g. via the screening maps of Desmond *et al.*, 2018c), could also be a sensitive probe of screened modified gravity.

More generally, the coming years will provide ample opportunities for tests of gravity.

As I noted in § 1.1.5, existing cosmological constraints on gravity, obtained from measurements such as cosmic shear or the BAO scale, are rather weak. These constraints are expected to improve dramatically with data from ongoing and future galaxy surveys, such as Euclid, DESI, and LSST.

In addition to their cosmological merits, these surveys will also improve the sensitivity of the various galaxy-scale tests listed in § 1.3.5. For instance, according to Desmond *et al.* (2018b), a repeat of their search for gas-star offsets using the radio data of SKA will have a sensitivity level of $\Delta G/G \sim 10^{-9}$. This is comparable to Solar System tests of gravity and will easily be able to confirm or rule out their tentative signal (depicted in Figure 1.16). As another example, the aforementioned MaNGA survey has already begun to provide spatially resolved kinematics of both stellar and gas components of a large numbers of galaxies. The gas-star rotation curve test of Vikram *et al.* (2018) was primarily limited by its very small sample size of six galaxies, but was nonetheless able to attain competitive parameter bounds. It would therefore be interesting to apply a similar test—reformulated into 2D kinematics—to MaNGA data.

Finally, the upcoming galaxy surveys mentioned above will improve our ability to identify ideal candidates for fifth force searches. Indirectly, their greatly increased completeness compared with existing galaxy catalogues will aid the identification of unscreened regions of the local Universe by greatly improving the accuracy of screening maps, which are primarily limited by uncertainty about the distribution of 'missing mass'. More directly, they will dramatically increase the known number of faint, low mass galaxies in the more rarefied regions of the Universe. These galaxies will be a final frontier in the search for astrophysical signatures of screened modified gravity.

Final Remarks

This thesis began with an account of the Great Debate that took place a century ago. To the astronomers and natural philosophers of the day, the 'big questions' about our cosmos regarded the extent and shape of the Milky Way, and whether the observed 'spiral nebulae' were 'Milky Ways' in their own right. The stasis and infinite age of the Universe were largely unquestioned axioms. Today, the academic descendants of those thinkers ask an entirely different set of questions. What is the physical reality of the observed dark sector? How does one link general relativity to the quantum theory of fields? How exactly do galaxies form?

Despite talk of a 'concordance cosmology', there is clearly much work to be done, and the community is far from complacent. One imagines that a time will come when cosmologists will be grappling with an entirely new set of questions, our current questions having all been either answered, rendered irrelevant, or demonstrated to have been ill-posed. I can only hope that such a time will come to pass within my lifetime.

Appendix A

1D Approximation

As discussed in § 3.3.2, when solving Eq. (1.69) to calculate the scalar field, we assume spherical symmetry to reduce the computational cost. In Chapter 2, it was found that the scalar field typically takes a discoid shape in galaxies, so assuming spherical symmetry could potentially lead to our calculations differing from the 'true' scalar field profiles, introducing error into our inferences for $\bar{f}_{R0}$. In particular, when a galaxy is partially screened, a given $\bar{f}_{R0}$ might correspond to an appreciably different location for the screening radius when the assumption of spherical symmetry is introduced.

To test the robustness of this 1D approximation, we compare some of our results with those that would have been obtained if the 1D solver was replaced with a 2D solver, in which the assumption of spherical symmetry has been replaced with the assumption of azimuthal symmetry. This 2D solver has been found to give galactic scalar field profiles in excellent agreement with those calculated by the full 3D solver in MG-GADGET.

In the 2D solver that we use for comparison, Eq. (3.5) is discretised on a 2D grid in the spherical polar coordinates r and θ. As in the 1D case, we use logarithmically spaced grid cells for the coordinate r, i.e. the radial gridlines are equally spaced in $x \equiv \ln r$, with constant grid spacing h_x.

For the polar angle θ, we adopt a linear grid, ranging from $\theta = 0$ to $\theta = \pi$, with n_θ grid cells and constant grid spacing h_θ. Through experimentation, it was found that $n_\theta \sim 100$ gave sufficiently accurate results.

Defining

$$\mathscr{L}_{ij} \equiv \left(\nabla^2 e^u\right)_{ij} + \frac{1}{3c^2 \bar{f}_R(a)}\left[\bar{R}(a)\left(1 - e^{-\frac{u_{ij}}{2}}\right) + 8\pi G \delta\rho_{ij}\right], \tag{A.1}$$

where i and j denote grid cells along the radial and polar directions respectively, we can rewrite Eq. (3.5) as

$$\mathscr{L}_{ij} = 0. \tag{A.2}$$

This is then solved, with the same Newton-Gauss-Seidel technique, Eq. (3.8). In order to do this, we need discretised expressions for the Laplace operator on our grid, as well as the

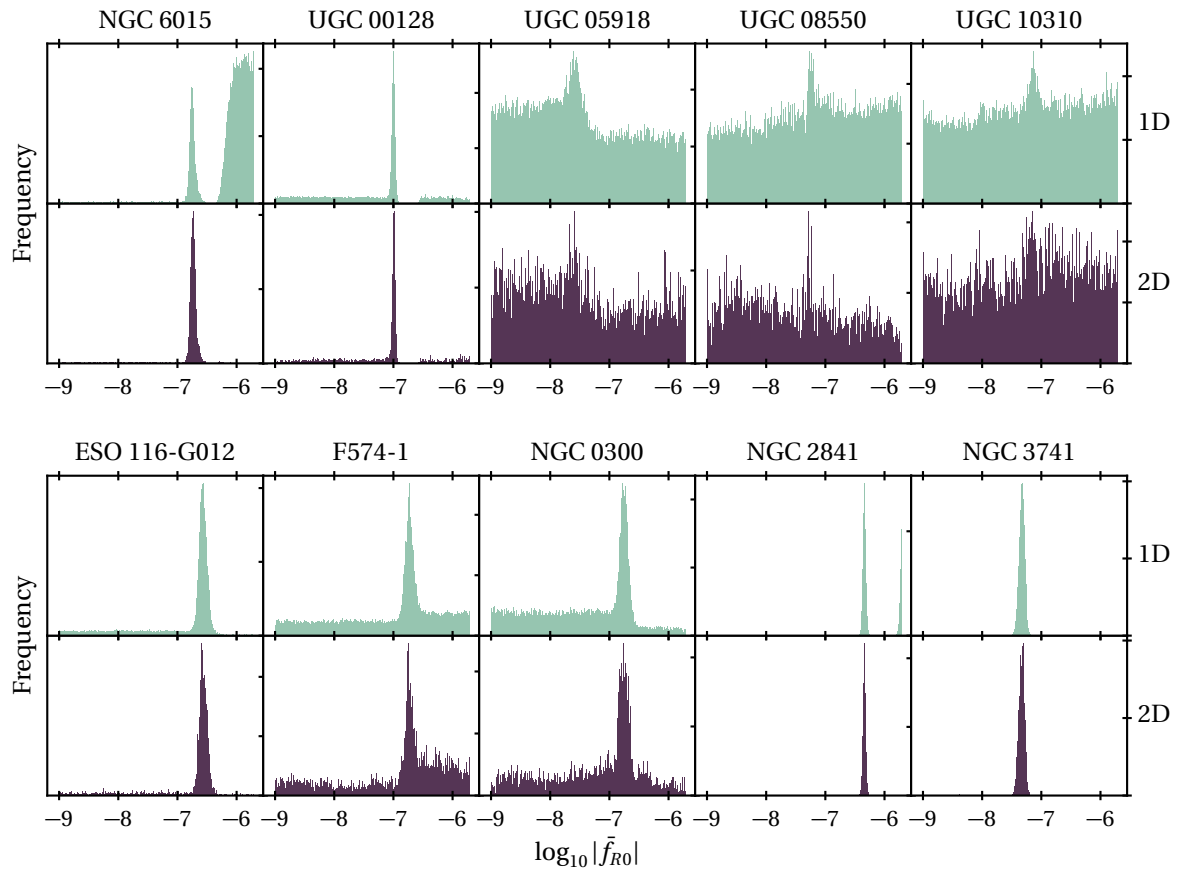

Figure A.1: Marginal posterior distributions of $\bar{f}_{R0}$ for 10 randomly selected galaxies, calculated with both the 1D solver used throughout Chapter 3 *(upper panels)*, and the 2D solver described in this Appendix *(lower panels)*. The results of the two solvers are in remarkably good agreement, with the possible exception of the missing modes associated with NGC 6015 and NGC 2841, which are more likely to be due to convergence issues than the 1D approximation (each walker performed 5000 iterations in the 1D case, and 500 in the 2D case; see discussion in the text).

quantity $\partial \mathscr{L}_{ij}/\partial u_{ij}$. Writing $\sin\theta$ as s, the Laplace operator in our coordinates $x \equiv \ln r$ and θ is given by

$$\nabla^2 f = \frac{1}{r^3}\frac{\partial}{\partial x}\left(r\frac{\partial f}{\partial x}\right) + \frac{1}{r^2 s}\frac{\partial}{\partial \theta}\left(s\frac{\partial f}{\partial \theta}\right), \tag{A.3}$$

which is discretised as

$$\begin{aligned}\left(\nabla^2 f\right)_{ij} = \frac{1}{r_i^3 h_x^2}\left(r_{i+\frac{1}{2}}(f_{i+1,j}-f_{ij}) - r_{i-\frac{1}{2}}(f_{ij}-f_{i-1,j})\right) \\ + \frac{1}{r_i^2 s_j h_\theta^2}\left(s_{j+\frac{1}{2}}(f_{i,j+1}-f_{ij}) - s_{j-\frac{1}{2}}(f_{ij}-f_{i,j-1})\right).\end{aligned} \tag{A.4}$$

Finally, the quantity $\partial \mathscr{L}_{ij}/\partial u_{ij}$ is given by

$$\frac{\partial \mathscr{L}_{ij}}{\partial u_{ij}} = \frac{\bar{R}}{6c^2\bar{f}_R}e^{-\frac{u_{ij}}{2}} - e^{u_{ij}}\left[\frac{r_{i+\frac{1}{2}}+r_{i-\frac{1}{2}}}{r_i^3 h_x^2} + \frac{s_{j+\frac{1}{2}}+s_{j-\frac{1}{2}}}{r_i^2 s_j h_\theta^2}\right]. \tag{A.5}$$

With a solution for f_R everywhere, the fifth force is then given by Eq. (1.77), evaluating the gradients of the scalar field in the disc plane, $\theta = \pi/2$.

We take 10 randomly chosen galaxies from our sample, and rerun our MCMC analysis with this 2D solver for Model B, i.e. the $f(R)$ model with freely varying $\bar{f}_{R0}$, a single mass-to-light ratio, and NFW haloes. As in the 1D case, we use 30 walkers operating at 4 temperatures. With the 1D solver, the walkers each performed 5000 iterations after a burn-in period of 5000 iterations, but here we limit the computation to 500 iterations after a burn-in of 500, for reasons of computational cost. As a consequence, the convergence is more uncertain: whereas the Gelman-Rubin statistic $\mathscr{R}$ was previously confined to the region $|\mathscr{R}-1|<0.01$ for the vast majority of fits, the statistics for several of the galaxies are now in the range $0.01<|\mathscr{R}-1|<0.05$.

Figure A.1 shows the 10 marginal posterior distributions for $\bar{f}_{R0}$, calculated with 2D and 1D solvers. There is remarkably good agreement between the two solvers, demonstrating the validity of our 1D approximation. In two cases, NGC 6015 and NGC 2841, the posterior is bimodal for the 1D solver, but unimodal for 2D. However, as the missing mode in both cases falls within the fully unscreened regime, this is unlikely to be related to any difference between the scalar field solutions of the two solvers, but to the convergence issues described above, which have likely prevented the 2D MCMC from finding the second mode.

Bibliography

Adams, W. S. (**1925a**): *The Relativity Displacement of the Spectral Lines in the Companion of Sirius*
Proceedings of the National Academy of Science, Volume 11, Issue 7 [DOI] [ADS]

Adams, W. S. (**1925b**): *The Relativity Displacement of the Spectral Lines in the Companion of Sirius*
The Observatory, Volume 48 [ADS]

Adelberger, E. G. (**2001**): *New tests of Einstein's equivalence principle and Newton's inverse-square law*
Classical and Quantum Gravity, Volume 18, Issue 13 [DOI] [ADS]

Alam, S., Ata, M., Bailey, S., *et al.* (**2017**): *The clustering of galaxies in the completed SDSS-III Baryon Oscillation Spectroscopic Survey: cosmological analysis of the DR12 galaxy sample*
Monthly Notices of the Royal Astronomical Society, Volume 470, Issue 3 [DOI] [ADS] [arXiv]

Alcock, C., Allsman, R. A., Alves, D. R., *et al.* (**2000**): *The MACHO Project: Microlensing Results from 5.7 Years of Large Magellanic Cloud Observations*
The Astrophysical Journal, Volume 542, Issue 1 [DOI] [ADS] [arXiv]

Ali-Haïmoud, Y., Kovetz, E. D., & Kamionkowski, M. (**2017**): *Merger rate of primordial black-hole binaries*
Physical Review D, Volume 96, Issue 12 [DOI] [ADS] [arXiv]

Allende Prieto, C., Majewski, S. R., Schiavon, R., *et al.* (**2008**): *APOGEE: The Apache Point Observatory Galactic Evolution Experiment*
Astronomische Nachrichten, Volume 329, Issue 9-10 [DOI] [ADS] [arXiv]

Alpher, R. A., Bethe, H., & Gamow, G. (**1948**): *The Origin of Chemical Elements*
Physical Review, Volume 73, Issue 7 [DOI] [ADS]

Amendola, L. & Tsujikawa, S. (**2010**): *Dark Energy: Theory and Observations*
Cambridge University Press, 1st ed. [DOI] [ADS]

Amorisco, N. C. & Evans, N. W. (**2011**): *Phase-space models of the dwarf spheroidals*
Monthly Notices of the Royal Astronomical Society, Volume 411, Issue 4 [DOI] [ADS] [arXiv]

Arnold, C., Fosalba, P., Springel, V., *et al.* (**2019a**): *The modified gravity light-cone simulation project - I. Statistics of matter and halo distributions*
Monthly Notices of the Royal Astronomical Society, Volume 483, Issue 1 [DOI] [ADS] [arXiv]

Arnold, C., Leo, M., & Li, B. (**2019b**): *Realistic simulations of galaxy formation in $f(R)$ modified gravity*
Nature Astronomy, Volume 3 [DOI] [ADS] [arXiv]

Arnold, C., Puchwein, E., & Springel, V. (**2014**): *Scaling relations and mass bias in hydrodynamical $f(R)$ gravity simulations of galaxy clusters*
Monthly Notices of the Royal Astronomical Society, Volume 440, Issue 1 [DOI] [ADS] [arXiv]

Arnold, C., Puchwein, E., & Springel, V. (**2015**): *The Lyman α forest in $f(R)$ modified gravity*
Monthly Notices of the Royal Astronomical Society, Volume 448, Issue 3 [DOI] [ADS] [arXiv]

Arnold, C., Springel, V., & Puchwein, E. (**2016**): *Zoomed cosmological simulations of Milky Way-sized haloes in $f(R)$ gravity*
Monthly Notices of the Royal Astronomical Society, Volume 462, Issue 2 [DOI] [ADS] [arXiv]

Ata, M., Baumgarten, F., Bautista, J., *et al.* (**2018**): *The clustering of the SDSS-IV extended Baryon Oscillation Spectroscopic Survey DR14 quasar sample: first measurement of baryon acoustic oscillations between redshift 0.8 and 2.2*
Monthly Notices of the Royal Astronomical Society, Volume 473, Issue 4 [DOI] [ADS] [arXiv]

Athanassoula, E. (**2005**): *On the nature of bulges in general and of box/peanut bulges in particular: input from N-body simulations*
Monthly Notices of the Royal Astronomical Society, Volume 358, Issue 4 [DOI] [ADS] [arXiv]

Babcock, H. W. (**1939**): *The rotation of the Andromeda Nebula*
Lick Observatory Bulletin, Volume 498 [DOI] [ADS]

Baker, T., Barreira, A., Desmond, H., *et al.* (**2019**): *The Novel Probes Project – Tests of Gravity on Astrophysical Scales*
arXiv e-prints (1908.03430) [ADS] [arXiv]

Baker, T., Bellini, E., Ferreira, P. G., *et al.* (**2017**): *Strong Constraints on Cosmological Gravity from GW170817 and GRB 170817A*
Physical Review Letters, Volume 119, Issue 25 [DOI] [ADS] [arXiv]

Baker, T., Psaltis, D., & Skordis, C. (**2015**): *Linking Tests of Gravity on All Scales: from the Strong-field Regime to Cosmology*
The Astrophysical Journal, Volume 802, Issue 1 [DOI] [ADS] [arXiv]

Baldi, M. (**2012**): *Dark Energy simulations*
Physics of the Dark Universe, Volume 1, Issue 1-2 [DOI] [ADS] [arXiv]

Baldry, I. K., Glazebrook, K., Brinkmann, J., *et al.* (**2004**): *Quantifying the Bimodal Color-Magnitude Distribution of Galaxies*
The Astrophysical Journal, Volume 600, Issue 2 [DOI] [ADS] [arXiv]

Bamford, S. P., Nichol, R. C., Baldry, I. K., *et al.* (**2009**): *Galaxy Zoo: the dependence of morphology and colour on environment*
Monthly Notices of the Royal Astronomical Society, Volume 393, Issue 4 [DOI] [ADS] [arXiv]

Bardeen, J. M., Steinhardt, P. J., & Turner, M. S. (**1983**): *Spontaneous creation of almost scale-free density perturbations in an inflationary universe*
Physical Review D, Volume 28, Issue 4 [DOI] [ADS]

Bartelmann, M. & Schneider, P. (**2001**): *Weak gravitational lensing*
Physics Reports, Volume 340, Issue 4-5 [DOI] [ADS] [arXiv]

Bautista, J. E., Vargas-Magaña, M., Dawson, K. S., *et al.* (**2018**): *The SDSS-IV Extended Baryon Oscillation Spectroscopic Survey: Baryon Acoustic Oscillations at Redshift of 0.72 with the DR14 Luminous Red Galaxy Sample*
The Astrophysical Journal, Volume 863, Issue 1 [DOI] [ADS] [arXiv]

Becklin, E. E. & Neugebauer, G. (**1968**): *Infrared Observations of the Galactic Center*
The Astrophysical Journal, Volume 151 [DOI] [ADS]

Bekenstein, J. D. (**2004**): *Relativistic gravitation theory for the modified Newtonian dynamics paradigm*
Physical Review D, Volume 70, Issue 8 [DOI] [ADS] [arXiv]

Bell, E. F., van der Wel, A., Papovich, C., *et al.* (**2012**): *What Turns Galaxies Off? The Different Morphologies of Star-forming and Quiescent Galaxies since $z\sim2$ from CANDELS*
The Astrophysical Journal, Volume 753, Issue 2 [DOI] [ADS] [arXiv]

Belokurov, V., Zucker, D. B., Evans, N. W., *et al.* (**2006**): *The Field of Streams: Sagittarius and Its Siblings*
The Astrophysical Journal, Volume 642, Issue 2 [DOI] [ADS] [arXiv]

Bertotti, B., Iess, L., & Tortora, P. (**2003**): *A test of general relativity using radio links with the Cassini spacecraft*
Nature, Volume 425, Issue 6956 [DOI] [ADS]

Binney, J. & Tremaine, S. (**2008**): *Galactic Dynamics*
Princeton University Press, 2nd ed. [DOI] [ADS]

Blake, C., Davis, T., Poole, G. B., *et al.* (**2011**): *The WiggleZ Dark Energy Survey: testing the cosmological model with baryon acoustic oscillations at $z = 0.6$*
Monthly Notices of the Royal Astronomical Society, Volume 415, Issue 3 [DOI] [ADS] [arXiv]

Bland-Hawthorn, J. & Gerhard, O. (**2016**): *The Galaxy in Context: Structural, Kinematic, and Integrated Properties*
Annual Review of Astronomy & Astrophysics, Volume 54 [DOI] [ADS] [arXiv]

Bocquet, S., Dietrich, J. P., Schrabback, T., *et al.* (**2019**): *Cluster Cosmology Constraints from the 2500 deg^2 SPT-SZ Survey: Inclusion of Weak Gravitational Lensing Data from Magellan and the Hubble Space Telescope*
The Astrophysical Journal, Volume 878, Issue 1 [DOI] [ADS] [arXiv]

Boggess, N. W., Mather, J. C., Weiss, R., *et al.* (**1992**): *The COBE Mission: Its Design and Performance Two Years after Launch*
The Astrophysical Journal, Volume 397 [DOI] [ADS]

Bonaca, A., Conroy, C., Price-Whelan, A. M., *et al.* (**2019**): *Multiple Components of the Jhelum Stellar Stream*
The Astrophysical Journal Letters, Volume 881, Issue 2 [DOI] [ADS] [arXiv]

Bondi, H. & Gold, T. (**1948**): *The Steady-State Theory of the Expanding Universe*
Monthly Notices of the Royal Astronomical Society, Volume 108, Issue 3 [DOI] [ADS]

Bose, S., Frenk, C. S., Jenkins, A., *et al.* (**2019**): *No cores in dark matter-dominated dwarf galaxies with bursty star formation histories*
Monthly Notices of the Royal Astronomical Society, Volume 486, Issue 4 [DOI] [ADS] [arXiv]

Bose, S., Hellwing, W. A., & Li, B. (**2015**): *Testing the quasi-static approximation in $f(R)$ gravity simulations*
Journal of Cosmology & Astroparticle Physics, Volume 2015, Issue 2 [DOI] [ADS] [arXiv]

Bosma, A. (**1978**): *The distribution and kinematics of neutral hydrogen in spiral galaxies of various morphological types*
Ph.D. thesis, University of Groningen [ADS]

Bowden, A., Belokurov, V., & Evans, N. W. (**2015**): *Dipping our toes in the water: first models of GD-1 as a stream*
Monthly Notices of the Royal Astronomical Society, Volume 449, Issue 2 [DOI] [ADS] [arXiv]

Boylan-Kolchin, M., Bullock, J. S., & Kaplinghat, M. (**2011**): *Too big to fail? The puzzling darkness of massive Milky Way subhaloes*
Monthly Notices of the Royal Astronomical Society, Volume 415, Issue 1 [DOI] [ADS] [arXiv]

Boylan-Kolchin, M., Ma, C.-P., & Quataert, E. (**2008**): *Dynamical friction and galaxy merging time-scales*
Monthly Notices of the Royal Astronomical Society, Volume 383, Issue 1 [DOI] [ADS] [arXiv]

Brandt, A. (**1977**): *Multi-level adaptive solutions to boundary-value problems*
Mathematics of Computation, Volume 31, Issue 138 [DOI]

Brans, C. & Dicke, R. H. (**1961**): *Mach's Principle and a Relativistic Theory of Gravitation*
Physical Review, Volume 124, Issue 3 [DOI] [ADS]

Brax, P., van de Bruck, C., Davis, A.-C., *et al.* (**2008**): *$f(R)$ gravity and chameleon theories*
Physical Review D, Volume 78, Issue 10 [DOI] [ADS] [arXiv]

Buchdahl, H. A. (**1970**): *Non-linear Lagrangians and cosmological theory*
Monthly Notices of the Royal Astronomical Society, Volume 150 [DOI] [ADS]

Bull, P., Akrami, Y., Adamek, J., *et al.* (2016): *Beyond ΛCDM: Problems, solutions, and the road ahead*
Physics of the Dark Universe, Volume 12 [DOI] [ADS] [arXiv]

Bullock, J. S. & Boylan-Kolchin, M. (2017): *Small-Scale Challenges to the ΛCDM Paradigm*
Annual Review of Astronomy and Astrophysics, Volume 55, Issue 1 [DOI] [ADS] [arXiv]

Bundy, K., Bershady, M. A., Law, D. R., *et al.* (2015): *Overview of the SDSS-IV MaNGA Survey: Mapping nearby Galaxies at Apache Point Observatory*
The Astrophysical Journal, Volume 798, Issue 1 [DOI] [ADS] [arXiv]

Burrage, C., Copeland, E. J., & Stevenson, J. A. (2015): *Ellipticity weakens chameleon screening*
Physical Review D, Volume 91, Issue 6 [DOI] [ADS] [arXiv]

Burrage, C. & Sakstein, J. (2018): *Tests of chameleon gravity*
Living Reviews in Relativity, Volume 21 [DOI] [ADS] [arXiv]

Cabré, A., Vikram, V., Zhao, G.-B., *et al.* (2012): *Astrophysical tests of gravity: a screening map of the nearby universe*
Journal of Cosmology & Astroparticle Physics, Volume 2012, Issue 7 [DOI] [ADS] [arXiv]

Callingham, T. M., Cautun, M., Deason, A. J., *et al.* (2019): *The mass of the Milky Way from satellite dynamics*
Monthly Notices of the Royal Astronomical Society, Volume 484, Issue 4 [DOI] [ADS] [arXiv]

Cappellari, M., Emsellem, E., Krajnović, D., *et al.* (2011): *The ATLAS^{3D} project - I. A volume-limited sample of 260 nearby early-type galaxies: science goals and selection criteria*
Monthly Notices of the Royal Astronomical Society, Volume 413, Issue 2 [DOI] [ADS] [arXiv]

Carilli, C. L. & Rawlings, S. (2004): *Motivation, key science projects, standards and assumptions*
New Astronomy Reviews, Volume 48, Issue 11-12 [DOI] [ADS] [arXiv]

Carr, B. J. & Hawking, S. W. (1974): *Black holes in the early Universe*
Monthly Notices of the Royal Astronomical Society, Volume 168, Issue 2 [DOI] [ADS]

Cataneo, M., Rapetti, D., Lombriser, L., *et al.* (2016): *Cluster abundance in chameleon f(R) gravity I: toward an accurate halo mass function prediction*
Journal of Cosmology & Astroparticle Physics, Volume 2016, Issue 12 [DOI] [ADS] [arXiv]

Cautun, M., Paillas, E., Cai, Y.-C., *et al.* (2018): *The Santiago-Harvard-Edinburgh-Durham void comparison - I. SHEDding light on chameleon gravity tests*
Monthly Notices of the Royal Astronomical Society, Volume 476, Issue 3 [DOI] [ADS] [arXiv]

Clifton, T., Ferreira, P. G., Padilla, A., *et al.* (2012): *Modified gravity and cosmology*
Physics Reports, Volume 513, Issue 1-3 [DOI] [ADS] [arXiv]

Cohen, I. B. (1978): *Isaac Newton's Papers & Letters on Natural Philosophy and Related Documents*
Harvard University Press, 1st ed. [DOI]

Cole, S., Norberg, P., Baugh, C. M., *et al.* (2001): *The 2dF galaxy redshift survey: near-infrared galaxy luminosity functions*
Monthly Notices of the Royal Astronomical Society, Volume 326, Issue 1 [DOI] [ADS] [arXiv]

Cole, S., Percival, W. J., Peacock, J. A., *et al.* (2005): *The 2dF Galaxy Redshift Survey: power-spectrum analysis of the final data set and cosmological implications*
Monthly Notices of the Royal Astronomical Society, Volume 362, Issue 2 [DOI] [ADS] [arXiv]

Conn, A. R., Lewis, G. F., Ibata, R. A., *et al.* (2013): *The Three-dimensional Structure of the M31 Satellite System; Strong Evidence for an Inhomogeneous Distribution of Satellites*
The Astrophysical Journal, Volume 766, Issue 2 [DOI] [ADS] [arXiv]

Cox, T. J. & Loeb, A. (2008): *The collision between the Milky Way and Andromeda*
Monthly Notices of the Royal Astronomical Society, Volume 386, Issue 1 [DOI] [ADS] [arXiv]

Crelinsten, J. (2006): *Einstein's Jury: The Race to Test Relativity*
Princeton University Press, 1st ed. [DOI]

Creminelli, P. & Vernizzi, F. (2017): *Dark Energy after GW170817 and GRB170817A*
Physical Review Letters, Volume 119, Issue 25 [DOI] [ADS] [arXiv]

Croton, D. J., Springel, V., White, S. D. M., *et al.* (2006): *The many lives of active galactic nuclei: cooling flows, black holes and the luminosities and colours of galaxies*
Monthly Notices of the Royal Astronomical Society, Volume 365, Issue 1 [DOI] [ADS] [arXiv]

Das, S., Marriage, T. A., Ade, P. A. R., *et al.* (2011): *The Atacama Cosmology Telescope: A Measurement of the Cosmic Microwave Background Power Spectrum at 148 and 218 GHz from the 2008 Southern Survey*
The Astrophysical Journal, Volume 729, Issue 1 [DOI] [ADS] [arXiv]

Davies, C. T., Cautun, M., & Li, B. (2019): *Cosmological test of gravity using weak lensing voids*
Monthly Notices of the Royal Astronomical Society, Volume 490, Issue 4 [DOI] [ADS] [arXiv]

Davis, A.-C., Lim, E. A., Sakstein, J., *et al.* (2012): *Modified gravity makes galaxies brighter*
Physical Review D, Volume 85, Issue 12 [DOI] [ADS] [arXiv]

Dawson, K. S., Kneib, J.-P., Percival, W. J., *et al.* (2016): *The SDSS-IV Extended Baryon Oscillation Spectroscopic Survey: Overview and Early Data*
The Astronomical Journal, Volume 151, Issue 2 [DOI] [ADS] [arXiv]

de Rossi, M. E., Tissera, P. B., De Lucia, G., *et al.* (2009): *Milky Way type galaxies in a ΛCDM cosmology*
Monthly Notices of the Royal Astronomical Society, Volume 395, Issue 1 [DOI] [ADS] [arXiv]

de Sitter, W. (**1917**): *Einstein's theory of gravitation and its astronomical consequences. Third paper*
Monthly Notices of the Royal Astronomical Society, Volume 78, Issue 1 [DOI] [ADS]

de Vaucouleurs, G., de Vaucouleurs, A., Corwin, J., Herold G., *et al.* (**1991**): *Third Reference Catalogue of Bright Galaxies*
Springer, 1st ed. [DOI] [ADS]

Deason, A. J., Belokurov, V., Evans, N. W., *et al.* (**2013**): *Broken and Unbroken: The Milky Way and M31 Stellar Halos*
The Astrophysical Journal, Volume 763, Issue 2 [DOI] [ADS] [arXiv]

DES Collaboration (**2018a**): *Dark Energy Survey year 1 results: Cosmological constraints from cosmic shear*
Physical Review D, Volume 98, Issue 4 [DOI] [ADS] [arXiv]

DES Collaboration (**2018b**): *Dark Energy Survey year 1 results: Cosmological constraints from galaxy clustering and weak lensing*
Physical Review D, Volume 98, Issue 4 [DOI] [ADS] [arXiv]

DES Collaboration (**2019**): *Dark Energy Survey year 1 results: Constraints on extended cosmological models from galaxy clustering and weak lensing*
Physical Review D, Volume 99, Issue 12 [DOI] [ADS] [arXiv]

DESI Collaboration (**2016a**): *The DESI Experiment Part I: Science,Targeting, and Survey Design*
arXiv e-prints (1611.00036) [ADS] [arXiv]

DESI Collaboration (**2016b**): *The DESI Experiment Part II: Instrument Design*
arXiv e-prints (1611.00037) [ADS] [arXiv]

Desmond, H. (**2017a**): *A statistical investigation of the mass discrepancy-acceleration relation*
Monthly Notices of the Royal Astronomical Society, Volume 464, Issue 4 [DOI] [ADS] [arXiv]

Desmond, H. (**2017b**): *The scatter, residual correlations and curvature of the SPARC baryonic Tully-Fisher relation*
Monthly Notices of the Royal Astronomical Society, Volume 472, Issue 1 [DOI] [ADS] [arXiv]

Desmond, H., Ferreira, P. G., Lavaux, G., *et al.* (**2018a**): *Fifth force constraints from galaxy warps*
Physical Review D, Volume 98, Issue 8 [DOI] [ADS] [arXiv]

Desmond, H., Ferreira, P. G., Lavaux, G., *et al.* (**2018b**): *Fifth force constraints from the separation of galaxy mass components*
Physical Review D, Volume 98, Issue 6 [DOI] [ADS] [arXiv]

Desmond, H., Ferreira, P. G., Lavaux, G., *et al.* (**2018c**): *Reconstructing the gravitational field of the local Universe*
Monthly Notices of the Royal Astronomical Society, Volume 474, Issue 3 [DOI] [ADS] [arXiv]

Desmond, H., Ferreira, P. G., Lavaux, G., *et al.* (**2019a**): *The fifth force in the local cosmic web*
Monthly Notices of the Royal Astronomical Society, Volume 483, Issue 1 [DOI] [ADS] [arXiv]

Desmond, H., Jain, B., & Sakstein, J. (**2019b**): *Local resolution of the Hubble tension: The impact of screened fifth forces on the cosmic distance ladder*
Physical Review D, Volume 100, Issue 4 [DOI] [ADS] [arXiv]

Di Cintio, A., Brook, C. B., Dutton, A. A., *et al.* (**2014**): *A mass-dependent density profile for dark matter haloes including the influence of galaxy formation*
Monthly Notices of the Royal Astronomical Society, Volume 441, Issue 4 [DOI] [ADS] [arXiv]

Di Valentino, E., Melchiorri, A., & Silk, J. (**2020**): *Planck evidence for a closed Universe and a possible crisis for cosmology*
Nature Astronomy, Volume 4 [DOI] [ADS] [arXiv]

Diemand, J., Kuhlen, M., Madau, P., *et al.* (**2008**): *Clumps and streams in the local dark matter distribution*
Nature, Volume 454, Issue 7205 [DOI] [ADS] [arXiv]

Dodelson, S. (**2003**): *Modern cosmology*
Academic Press, 1st ed. [DOI] [ADS]

Drlica-Wagner, A., Bechtol, K., Mau, S., *et al.* (**2020**): *Milky Way Satellite Census. I. The Observational Selection Function for Milky Way Satellites in DES Y3 and Pan-STARRS DR1*
The Astrophysical Journal, Volume 893, Issue 1 [DOI] [ADS] [arXiv]

Dubois, Y., Pichon, C., Welker, C., *et al.* (**2014**): *Dancing in the dark: galactic properties trace spin swings along the cosmic web*
Monthly Notices of the Royal Astronomical Society, Volume 444, Issue 2 [DOI] [ADS] [arXiv]

Dutton, A. A. & Macciò, A. V. (**2014**): *Cold dark matter haloes in the Planck era: evolution of structural parameters for Einasto and NFW profiles*
Monthly Notices of the Royal Astronomical Society, Volume 441, Issue 4 [DOI] [ADS] [arXiv]

Earman, J. (**2001**): *Lambda: The Constant That Refuses to Die*
Archive for History of Exact Sciences, Volume 55 [DOI]

Earman, J. & Glymour, C. (**1980**): *Relativity and Eclipses: The British Eclipse Expeditions of 1919 and Their Predecessors*
Historical Studies in the Physical Sciences, Volume 11, Issue 1

Eddington, A. S. (**1928**): *The Nature of the Physical World*
Cambridge University Press, 1st ed. [DOI]

Eddington, A. S. (**1930**): *On the instability of Einstein's spherical world*
Monthly Notices of the Royal Astronomical Society, Volume 90, Issue 7 [DOI] [ADS]

Efstathiou, G. (**1992**): *Suppressing the formation of dwarf galaxies via photoionization*
Monthly Notices of the Royal Astronomical Society, Volume 256, Issue 2 [DOI] [ADS]

Efstathiou, G. (**1995**): *An anthropic argument for a cosmological constant*
Monthly Notices of the Royal Astronomical Society, Volume 274, Issue 4 [DOI] [ADS]

Efstathiou, G. & Gratton, S. (**2020**): *The evidence for a spatially flat Universe*
arXiv e-prints (2002.06892) [ADS] [arXiv]

Efstathiou, G., Sutherland, W. J., & Maddox, S. J. (**1990**): *The cosmological constant and cold dark matter*
Nature, Volume 348, Issue 6303 [DOI] [ADS]

Einasto, J., Kaasik, A., & Saar, E. (**1974**): *Dynamic evidence on massive coronas of galaxies*
Nature, Volume 250, Issue 5464 [DOI] [ADS]

Einstein, A. (**1915**): *Erklärung der Perihelbewegung des Merkur aus der allgemeinen Relativitätstheorie*
Sitzungsberichte der Preußischen Akademie der Wissenschaften [ADS]

Einstein, A. (**1916**): *Die Grundlage der allgemeinen Relativitätstheorie*
Annalen der Physik, Volume 354, Issue 7 [DOI] [ADS]

Einstein, A. (**1917**): *Kosmologische Betrachtungen zur allgemeinen Relativitätstheorie*
Sitzungsberichte der Preußischen Akademie der Wissenschaften [ADS]

Einstein, A. (**1919**): *Spielen Gravitationsfelder im Aufbau der materiellen Elementarteilchen eine wesentliche Rolle?*
Sitzungsberichte der Preußischen Akademie der Wissenschaften [ADS]

Eisenstein, D. J. & Hu, W. (**1998**): *Baryonic Features in the Matter Transfer Function*
The Astrophysical Journal, Volume 496, Issue 2 [DOI] [ADS] [arXiv]

Eisenstein, D. J., Zehavi, I., Hogg, D. W., *et al.* (**2005**): *Detection of the Baryon Acoustic Peak in the Large-Scale Correlation Function of SDSS Luminous Red Galaxies*
The Astrophysical Journal, Volume 633, Issue 2 [DOI] [ADS] [arXiv]

Eötvös, R. V., Pekár, D., & Fekete, E. (**1922**): *Beiträge zum Gesetze der Proportionalität von Trägheit und Gravität*
Annalen der Physik, Volume 373, Issue 9 [DOI] [ADS]

Erkal, D. & Belokurov, V. (**2015**): *Forensics of subhalo-stream encounters: the three phases of gap growth*
Monthly Notices of the Royal Astronomical Society, Volume 450, Issue 1 [DOI] [ADS] [arXiv]

Evans, N. W. & An, J. H. (**2006**): *Distribution function of dark matter*
Physical Review D, Volume 73, Issue 2 [DOI] [ADS] [arXiv]

Event Horizon Telescope Collaboration (**2019**): *First M87 Event Horizon Telescope Results. I. The Shadow of the Supermassive Black Hole*
The Astrophysical Journal Letters, Volume 875, Issue 1 [DOI] [ADS] [arXiv]

Ezquiaga, J. M. & Zumalacárregui, M. (**2017**): *Dark Energy After GW170817: Dead Ends and the Road Ahead*
Physical Review Letters, Volume 119, Issue 25 [DOI] [ADS] [arXiv]

Feng, J. L. (**2010**): *Dark Matter Candidates from Particle Physics and Methods of Detection*
Annual Review of Astronomy & Astrophysics, Volume 48 [DOI] [ADS] [arXiv]

Ferreira, P. G. (**2019**): *Cosmological Tests of Gravity*
Annual Review of Astronomy & Astrophysics, Volume 57 [DOI] [ADS] [arXiv]

Flores, R. A. & Primack, J. R. (**1994**): *Observational and Theoretical Constraints on Singular Dark Matter Halos*
The Astrophysical Journal Letters, Volume 427 [DOI] [ADS] [arXiv]

Foreman-Mackey, D., Hogg, D. W., Lang, D., *et al.* (**2013**): *emcee: The MCMC Hammer*
Publications of the Astronomical Society of the Pacific, Volume 125, Issue 925 [DOI] [ADS] [arXiv]

Friedmann, A. (**1922**): *Über die Krümmung des Raumes*
Zeitschrift für Physik, Volume 10 [DOI] [ADS]

Fujii, Y. (**1982**): *Origin of the gravitational constant and particle masses in a scale-invariant scalar-tensor theory*
Physical Review D, Volume 26, Issue 10 [DOI] [ADS]

Gaia Collaboration (**2016**): *The Gaia mission*
Astronomy & Astrophysics, Volume 595 [DOI] [ADS] [arXiv]

Gaia Collaboration (**2018**): *Gaia Data Release 2. Summary of the contents and survey properties*
Astronomy & Astrophysics, Volume 616 [DOI] [ADS] [arXiv]

Gamow, G. (**1952**): *The Creation of the Universe*
Viking

Garrison-Kimmel, S., Boylan-Kolchin, M., Bullock, J. S., *et al.* (**2014**): *ELVIS: Exploring the Local Volume in Simulations*
Monthly Notices of the Royal Astronomical Society, Volume 438, Issue 3 [DOI] [ADS] [arXiv]

Gelman, A. & Rubin, D. B. (**1992**): *Inference from Iterative Simulation Using Multiple Sequences*
Statistical Science, Volume 7 [DOI] [ADS]

Genel, S., Vogelsberger, M., Springel, V., *et al.* (**2014**): *Introducing the Illustris project: the evolution of galaxy populations across cosmic time*
Monthly Notices of the Royal Astronomical Society, Volume 445, Issue 1 [DOI] [ADS] [arXiv]

Genina, A., Benítez-Llambay, A., Frenk, C. S., *et al.* (**2018**): *The core-cusp problem: a matter of perspective*
Monthly Notices of the Royal Astronomical Society, Volume 474 [DOI] [ADS] [arXiv]

Gibbons, S. L. J., Belokurov, V., & Evans, N. W. (**2014**): *'Skinny Milky Way please', says Sagittarius*
Monthly Notices of the Royal Astronomical Society, Volume 445, Issue 4 [DOI] [ADS] [arXiv]

Gillessen, S., Plewa, P. M., Eisenhauer, F., *et al.* (**2017**): *An Update on Monitoring Stellar Orbits in the Galactic Center*
The Astrophysical Journal, Volume 837, Issue 1 [DOI] [ADS] [arXiv]

Gilmore, G. & Reid, N. (**1983**): *New light on faint stars - III. Galactic structure towards the South Pole and the Galactic thick disc.*
Monthly Notices of the Royal Astronomical Society, Volume 202, Issue 4 [DOI] [ADS]

Goldstein, H. (**1951**): *Classical mechanics*
Addison-Wesley, 1st ed. [ADS]

González Delgado, R. M., García-Benito, R., Pérez, E., *et al.* (**2015**): *The CALIFA survey across the Hubble sequence. Spatially resolved stellar population properties in galaxies*
Astronomy & Astrophysics, Volume 581 [DOI] [ADS] [arXiv]

Goobar, A. & Leibundgut, B. (**2011**): *Supernova Cosmology: Legacy and Future*
Annual Review of Nuclear and Particle Science, Volume 61, Issue 1 [DOI] [ADS] [arXiv]

Goodricke, J. (**1786**): *A Series of Observations on, and a Discovery of, the Period of the Variation of the Light of the Star Marked δ by Bayer, Near the Head of Cepheus. In a Letter from John Goodricke, Esq. to Nevil Maskelyne, D. D. F. R. S. and Astronomer Royal*
Philosophical Transactions of the Royal Society of London Series I, Volume 76 [ADS]

Governato, F., Brook, C., Mayer, L., *et al.* (**2010**): *Bulgeless dwarf galaxies and dark matter cores from supernova-driven outflows*
Nature, Volume 463, Issue 7278 [DOI] [ADS] [arXiv]

Grand, R. J. J., Gómez, F. A., Marinacci, F., *et al.* (**2017**): *The Auriga Project: the properties and formation mechanisms of disc galaxies across cosmic time*
Monthly Notices of the Royal Astronomical Society, Volume 467, Issue 1 [DOI] [ADS] [arXiv]

Griffen, B. F., Ji, A. P., Dooley, G. A., *et al.* (**2016**): *The Caterpillar Project: A Large Suite of Milky Way Sized Halos*
The Astrophysical Journal, Volume 818, Issue 1 [DOI] [ADS] [arXiv]

Gunn, J. E. & Gott, I., J. Richard (**1972**): *On the Infall of Matter Into Clusters of Galaxies and Some Effects on Their Evolution*
The Astrophysical Journal, Volume 176 [DOI] [ADS]

Guth, A. H. (**1981**): *Inflationary universe: A possible solution to the horizon and flatness problems*
Physical Review D, Volume 23, Issue 2 [DOI] [ADS]

Hammami, A., Llinares, C., Mota, D. F., *et al.* (**2015**): *Hydrodynamic effects in the symmetron and $f(R)$-gravity models*
Monthly Notices of the Royal Astronomical Society, Volume 449, Issue 4 [DOI] [ADS] [arXiv]

Hammersley, P. L., Garzon, F., Mahoney, T., *et al.* (**1994**): *Infrared signatures of the inner spiral arms and bar.*
Monthly Notices of the Royal Astronomical Society, Volume 269, Issue 3 [DOI] [ADS]

Hammersley, P. L., Garzón, F., Mahoney, T. J., *et al.* (**2000**): *Detection of the old stellar component of the major Galactic bar*
Monthly Notices of the Royal Astronomical Society, Volume 317, Issue 3 [DOI] [ADS] [arXiv]

Handley, W. (**2019**): *Curvature tension: evidence for a closed universe*
arXiv e-prints (1908.09139) [ADS] [arXiv]

Harrison, E. R. (**1970**): *Fluctuations at the Threshold of Classical Cosmology*
Physical Review D, Volume 1, Issue 10 [DOI] [ADS]

Hawking, S. (**1971**): *Gravitationally collapsed objects of very low mass*
Monthly Notices of the Royal Astronomical Society, Volume 152, Issue 1 [DOI] [ADS]

Hernquist, L. (**1990**): *An analytical model for spherical galaxies and bulges*
The Astrophysical Journal, Volume 356 [DOI] [ADS]

Hikage, C., Oguri, M., Hamana, T., *et al.* (**2019**): *Cosmology from cosmic shear power spectra with Subaru Hyper Suprime-Cam first-year data*
Publications of the Astronomical Society of Japan, Volume 71, Issue 2 [DOI] [ADS] [arXiv]

Hildebrandt, H., Köhlinger, F., van den Busch, J. L., *et al.* (**2020**): *KiDS+VIKING-450: Cosmic shear tomography with optical and infrared data*
Astronomy & Astrophysics, Volume 633 [DOI] [ADS] [arXiv]

Hildebrandt, H., Viola, M., Heymans, C., *et al.* (**2017**): *KiDS-450: cosmological parameter constraints from tomographic weak gravitational lensing*
Monthly Notices of the Royal Astronomical Society, Volume 465, Issue 2 [DOI] [ADS] [arXiv]

Hinterbichler, K. & Khoury, J. (**2010**): *Screening Long-Range Forces through Local Symmetry Restoration*
Physical Review Letters, Volume 104, Issue 23 [DOI] [ADS] [arXiv]

Hinterbichler, K., Khoury, J., Levy, A., *et al.* (**2011**): *Symmetron cosmology*
Physical Review D, Volume 84, Issue 10 [DOI] [ADS] [arXiv]

Hogg, D. W., Blanton, M. R., Brinchmann, J., *et al.* (**2004**): *The Dependence on Environment of the Color-Magnitude Relation of Galaxies*
The Astrophysical Journal Letters, Volume 601, Issue 1 [DOI] [ADS] [arXiv]

Holberg, J. B. (**2010**): *Sirius B and the Measurement of the Gravitational Redshift*
Journal for the History of Astronomy, Volume 41, Issue 1 [DOI] [ADS]

Hoyle, F. (**1948**): *A New Model for the Expanding Universe*
Monthly Notices of the Royal Astronomical Society, Volume 108, Issue 5 [DOI] [ADS]

Hu, W., Barkana, R., & Gruzinov, A. (**2000**): *Fuzzy Cold Dark Matter: The Wave Properties of Ultralight Particles*
Physical Review Letters, Volume 85, Issue 6 [DOI] [ADS] [arXiv]

Hu, W. & Sawicki, I. (**2007**): *Models of $f(R)$ cosmic acceleration that evade solar system tests*
Physical Review D, Volume 76, Issue 6 [DOI] [ADS] [arXiv]

Hubble, E. (**1929**): *A Relation between Distance and Radial Velocity among Extra-Galactic Nebulae*
Proceedings of the National Academy of Science, Volume 15, Issue 3 [DOI] [ADS]
Hubble, E. (**1934**): *The Distribution of Extra-Galactic Nebulae*
The Astrophysical Journal, Volume 79 [DOI] [ADS]
Hubble, E. & Tolman, R. C. (**1935**): *Two Methods of Investigating the Nature of the Nebular Redshift*
The Astrophysical Journal, Volume 82 [DOI] [ADS]
Hubble, E. P. (**1925**): *Cepheids in Spiral Nebulae*
Popular Astronomy, Volume 33 [ADS]
Hubble, E. P. (**1926**): *Extragalactic nebulae.*
The Astrophysical Journal, Volume 64 [DOI] [ADS]
Hui, L., Nicolis, A., & Stubbs, C. W. (**2009**): *Equivalence principle implications of modified gravity models*
Physical Review D, Volume 80, Issue 10 [DOI] [ADS] [arXiv]
Hui, L., Ostriker, J. P., Tremaine, S., *et al.* (**2017**): *Ultralight scalars as cosmological dark matter*
Physical Review D, Volume 95, Issue 4 [DOI] [ADS] [arXiv]
Hulse, R. A. & Taylor, J. H. (**1975**): *Discovery of a pulsar in a binary system.*
The Astrophysical Journal Letters, Volume 195 [DOI] [ADS]
Ibata, R. A., Lewis, G. F., Conn, A. R., *et al.* (**2013**): *A vast, thin plane of corotating dwarf galaxies orbiting the Andromeda galaxy*
Nature, Volume 493, Issue 7430 [DOI] [ADS] [arXiv]
Ijjas, A., Steinhardt, P. J., & Loeb, A. (**2017**): *Pop Goes the Universe*
Scientific American, Volume 316, Issue 2 [DOI] [ADS]
Ivezić, Ž., Kahn, S. M., Tyson, J. A., *et al.* (**2019**): *LSST: From Science Drivers to Reference Design and Anticipated Data Products*
The Astrophysical Journal, Volume 873, Issue 2 [DOI] [ADS] [arXiv]
Jeans, J. H. (**1922**): *The Motions of Stars in a Kapteyn Universe*
Monthly Notices of the Royal Astronomical Society, Volume 82, Issue 3 [DOI] [ADS]
Johnston, K. V. (**1998**): *A Prescription for Building the Milky Way's Halo from Disrupted Satellites*
The Astrophysical Journal, Volume 495, Issue 1 [DOI] [ADS] [arXiv]
Joyce, A., Jain, B., Khoury, J., *et al.* (**2015**): *Beyond the cosmological standard model*
Physics Reports, Volume 568 [DOI] [ADS] [arXiv]
Jungman, G., Kamionkowski, M., & Griest, K. (**1996**): *Supersymmetric dark matter*
Physics Reports, Volume 267 [DOI] [ADS] [arXiv]
Jurić, M., Ivezić, Ž., Brooks, A., *et al.* (**2008**): *The Milky Way Tomography with SDSS. I. Stellar Number Density Distribution*
The Astrophysical Journal, Volume 673, Issue 2 [DOI] [ADS] [arXiv]
Kaiser, N. (**1987**): *Clustering in real space and in redshift space*
Monthly Notices of the Royal Astronomical Society, Volume 227, Issue 1 [DOI] [ADS]
Kaluza, T. (**1921**): *Zum Unitätsproblem der Physik*
Sitzungsberichte der Preußischen Akademie der Wissenschaften [ADS]
Kamionkowski, M., Kosowsky, A., & Stebbins, A. (**1997**): *A Probe of Primordial Gravity Waves and Vorticity*
Physical Review Letters, Volume 78, Issue 11 [DOI] [ADS] [arXiv]
Kamionkowski, M. & Kovetz, E. D. (**2016**): *The Quest for B Modes from Inflationary Gravitational Waves*
Annual Review of Astronomy & Astrophysics, Volume 54 [DOI] [ADS] [arXiv]
Kapteyn, J. C. (**1922**): *First Attempt at a Theory of the Arrangement and Motion of the Sidereal System*
The Astrophysical Journal, Volume 55 [DOI] [ADS]
Kapteyn, J. C. & van Rhijn, P. J. (**1920**): *On the Distribution of the Stars in Space Especially in the High Galactic Latitudes*
The Astrophysical Journal, Volume 52 [DOI] [ADS]
Kardashev, N. (**1967**): *Lemaître's Universe and Observations*
The Astrophysical Journal Letters, Volume 150 [DOI] [ADS]
Kass, R. E. & Raftery, A. E. (**1995**): *Bayes Factors*
Journal of the American Statistical Association, Volume 90, Issue 430 [DOI] [arXiv]
Katz, H., Desmond, H., Lelli, F., *et al.* (**2018**): *Stellar feedback and the energy budget of late-type Galaxies: missing baryons and core creation*
Monthly Notices of the Royal Astronomical Society, Volume 480, Issue 4 [DOI] [ADS] [arXiv]
Katz, H., Lelli, F., McGaugh, S. S., *et al.* (**2017**): *Testing feedback-modified dark matter haloes with galaxy rotation curves: estimation of halo parameters and consistency with ΛCDM scaling relations*
Monthly Notices of the Royal Astronomical Society, Volume 466, Issue 2 [DOI] [ADS] [arXiv]
Kauffmann, G., Heckman, T. M., White, S. D. M., *et al.* (**2003**): *Stellar masses and star formation histories for 10^5 galaxies from SDSS*
Monthly Notices of the Royal Astronomical Society, Volume 341, Issue 1 [DOI] [ADS] [arXiv]
Kelvin, W. (**1904**): *Baltimore Lectures on Molecular Dynamics and the Wave Theory of Light*
C. J. Clay and Sons
Kerr, F. J. & Lynden-Bell, D. (**1986**): *Review of galactic constants.*
Monthly Notices of the Royal Astronomical Society, Volume 221, Issue 4 [DOI] [ADS]

Kesden, M. & Kamionkowski, M. (**2006a**): *Galilean Equivalence for Galactic Dark Matter*
Physical Review Letters, Volume 97, Issue 13 [DOI] [ADS] [arXiv]

Kesden, M. & Kamionkowski, M. (**2006b**): *Tidal tails test the equivalence principle in the dark-matter sector*
Physical Review D, Volume 74, Issue 8 [DOI] [ADS] [arXiv]

Khoury, J. & Weltman, A. (**2004**): *Chameleon cosmology*
Physical Review D, Volume 69, Issue 4 [DOI] [ADS] [arXiv]

Kilbinger, M. (**2015**): *Cosmology with cosmic shear observations: a review*
Reports on Progress in Physics, Volume 78, Issue 8 [DOI] [ADS] [arXiv]

Kim, S. Y., Peter, A. H. G., & Hargis, J. R. (**2018**): *Missing Satellites Problem: Completeness Corrections to the Number of Satellite Galaxies in the Milky Way are Consistent with Cold Dark Matter Predictions*
Physical Review Letters, Volume 121, Issue 21 [DOI] [ADS]

Kirby, E. N., Bullock, J. S., Boylan-Kolchin, M., *et al.* (**2014**): *The dynamics of isolated Local Group galaxies*
Monthly Notices of the Royal Astronomical Society, Volume 439, Issue 1 [DOI] [ADS] [arXiv]

Klein, O. (**1926**): *Quantentheorie und fünfdimensionale Relativitätstheorie*
Zeitschrift für Physik, Volume 37 [DOI] [ADS]

Klypin, A., Kravtsov, A. V., Valenzuela, O., *et al.* (**1999**): *Where Are the Missing Galactic Satellites?*
The Astrophysical Journal, Volume 522, Issue 1 [DOI] [ADS] [arXiv]

Koposov, S. E., Belokurov, V., Li, T. S., *et al.* (**2019**): *Piercing the Milky Way: an all-sky view of the Orphan Stream*
Monthly Notices of the Royal Astronomical Society, Volume 485, Issue 4 [DOI] [ADS] [arXiv]

Koyama, K. (**2016**): *Cosmological tests of modified gravity*
Reports on Progress in Physics, Volume 79, Issue 4 [DOI] [ADS] [arXiv]

Kragh, H. S. (**2007**): *Conceptions of Cosmos*
Oxford University Press, 1st ed. [DOI]

Kunkel, W. E. & Demers, S. (**1976**): *The Magellanic Plane*
Royal Greenwich Observatory Bulletins, Volume 182 [ADS]

Küpper, A. H. W., Lane, R. R., & Heggie, D. C. (**2012**): *More on the structure of tidal tails*
Monthly Notices of the Royal Astronomical Society, Volume 420, Issue 3 [DOI] [ADS] [arXiv]

Lane, R. R., Küpper, A. H. W., & Heggie, D. C. (**2012**): *The tidal tails of 47 Tucanae*
Monthly Notices of the Royal Astronomical Society, Volume 423, Issue 3 [DOI] [ADS] [arXiv]

Laplace, P. S. (**1796**): *Exposition du Système du Monde*
L'Imprimerie du Cercle-Social, 1st ed.

Larson, D., Dunkley, J., Hinshaw, G., *et al.* (**2011**): *Seven-year WMAP Observations: Power Spectra and WMAP-derived Parameters*
The Astrophysical Journal Supplement Series, Volume 192, Issue 2 [DOI] [ADS] [arXiv]

Laureijs, R., Amiaux, J., Arduini, S., *et al.* (**2011**): *Euclid Definition Study Report*
arXiv e-prints (1110.3193) [ADS] [arXiv]

Law, D. R. & Majewski, S. R. (**2010**): *The Sagittarius Dwarf Galaxy: A Model for Evolution in a Triaxial Milky Way Halo*
The Astrophysical Journal, Volume 714, Issue 1 [DOI] [ADS] [arXiv]

Leavitt, H. S. (**1908**): *1777 variables in the Magellanic Clouds*
Annals of Harvard College Observatory, Volume 60 [ADS]

Lelli, F., McGaugh, S. S., & Schombert, J. M. (**2016**): *SPARC: Mass Models for 175 Disk Galaxies with Spitzer Photometry and Accurate Rotation Curves*
The Astronomical Journal, Volume 152, Issue 6 [DOI] [ADS] [arXiv]

Lelli, F., McGaugh, S. S., Schombert, J. M., *et al.* (**2017**): *One Law to Rule Them All: The Radial Acceleration Relation of Galaxies*
The Astrophysical Journal, Volume 836, Issue 2 [DOI] [ADS] [arXiv]

Lemaître, A. G. (**1931**): *Contributions to a British Association Discussion on the Evolution of the Universe.*
Nature, Volume 128, Issue 3234 [DOI] [ADS]

Lemaître, G. (**1927**): *Un Univers homogène de masse constante et de rayon croissant rendant compte de la vitesse radiale des nébuleuses extra-galactiques*
Annales de la Société Scientifique de Bruxelles, Volume 47 [ADS]

Li, B., Zhao, G.-B., Teyssier, R., *et al.* (**2012**): *ECOSMOG: an Efficient COde for Simulating MOdified Gravity*
Journal of Cosmology & Astroparticle Physics, Volume 2012, Issue 1 [DOI] [ADS] [arXiv]

Li, P., Lelli, F., McGaugh, S., *et al.* (**2018**): *Fitting the radial acceleration relation to individual SPARC galaxies*
Astronomy & Astrophysics, Volume 615 [DOI] [ADS] [arXiv]

Li, P., Lelli, F., McGaugh, S. S., *et al.* (**2019a**): *A constant characteristic volume density of dark matter haloes from SPARC rotation curve fits*
Monthly Notices of the Royal Astronomical Society, Volume 482, Issue 4 [DOI] [ADS] [arXiv]

Li, T. S., Koposov, S. E., Zucker, D. B., *et al.* (**2019b**): *The southern stellar stream spectroscopic survey (S^5): Overview, target selection, data reduction, validation, and early science*
Monthly Notices of the Royal Astronomical Society, Volume 490, Issue 3 [DOI] [ADS] [arXiv]

Li, Y. & Hu, W. (**2011**): *Chameleon halo modeling in $f(R)$ gravity*
Physical Review D, Volume 84, Issue 8 [DOI] [ADS] [arXiv]

Licquia, T. C., Newman, J. A., & Brinchmann, J. (**2015**): *Unveiling the Milky Way: A New Technique for Determining the Optical Color and Luminosity of Our Galaxy*
The Astrophysical Journal, Volume 809, Issue 1 [DOI] [ADS] [arXiv]

LIGO Scientific Collaboration & Virgo Collaboration (**2016**): *Observation of Gravitational Waves from a Binary Black Hole Merger*
Physical Review Letters, Volume 116, Issue 6 [DOI] [ADS] [arXiv]

LIGO Scientific Collaboration & Virgo Collaboration (**2017**): *GW170817: Observation of Gravitational Waves from a Binary Neutron Star Inspiral*
Physical Review Letters, Volume 119, Issue 16 [DOI] [ADS] [arXiv]

LIGO Scientific Collaboration, Virgo Collaboration, 1M2H Team, *et al.* (**2017a**): *A gravitational-wave standard siren measurement of the Hubble constant*
Nature, Volume 551, Issue 7678 [DOI] [ADS] [arXiv]

LIGO Scientific Collaboration, Virgo Collaboration, Fermi GBM, *et al.* (**2017b**): *Multi-messenger Observations of a Binary Neutron Star Merger*
The Astrophysical Journal Letters, Volume 848, Issue 2 [DOI] [ADS] [arXiv]

Llinares, C. (**2018**): *Simulation techniques for modified gravity*
International Journal of Modern Physics D, Volume 27, Issue 15 [DOI] [ADS]

Llinares, C., Mota, D. F., & Winther, H. A. (**2014**): *ISIS: a new N-body cosmological code with scalar fields based on RAMSES. Code presentation and application to the shapes of clusters*
Astronomy & Astrophysics, Volume 562 [DOI] [ADS] [arXiv]

Lombriser, L., Koyama, K., Zhao, G.-B., *et al.* (**2012a**): *Chameleon $f(R)$ gravity in the virialized cluster*
Physical Review D, Volume 85, Issue 12 [DOI] [ADS] [arXiv]

Lombriser, L., Li, B., Koyama, K., *et al.* (**2013**): *Modeling halo mass functions in chameleon $f(R)$ gravity*
Physical Review D, Volume 87, Issue 12 [DOI] [ADS] [arXiv]

Lombriser, L. & Peñarrubia, J. (**2015**): *How chameleons core dwarfs with cusps*
Physical Review D, Volume 91, Issue 8 [DOI] [ADS] [arXiv]

Lombriser, L., Schmidt, F., Baldauf, T., *et al.* (**2012b**): *Cluster density profiles as a test of modified gravity*
Physical Review D, Volume 85, Issue 10 [DOI] [ADS] [arXiv]

Longair, M. S. & Smeenk, C. (**2019**): *Inflation, dark matter, and dark energy*
Chapter in Kragh, H. S. & Longair, M. S. (eds.): *The Oxford Handbook of the History of Modern Cosmology*. Oxford University Press, 1st ed. [DOI]

Lovelock, D. (**1971**): *The Einstein Tensor and Its Generalizations*
Journal of Mathematical Physics, Volume 12, Issue 3 [DOI] [ADS]

Lovelock, D. (**1972**): *The Four-Dimensionality of Space and the Einstein Tensor*
Journal of Mathematical Physics, Volume 13, Issue 6 [DOI] [ADS]

LSST Science Collaboration (**2009**): *LSST Science Book, Version 2.0*
arXiv e-prints (0912.0201) [ADS] [arXiv]

Lynden-Bell, D. (**1976**): *Dwarf galaxies and globular clusters in high velocity hydrogen streams.*
Monthly Notices of the Royal Astronomical Society, Volume 174, Issue 3 [DOI] [ADS]

Macaulay, E., Wehus, I. K., & Eriksen, H. K. (**2013**): *Lower Growth Rate from Recent Redshift Space Distortion Measurements than Expected from Planck*
Physical Review Letters, Volume 111, Issue 16 [DOI] [ADS] [arXiv]

Macciò, A. V., Quercellini, C., Mainini, R., *et al.* (**2004**): *Coupled dark energy: Parameter constraints from N-body simulations*
Physical Review D, Volume 69, Issue 12 [DOI] [ADS] [arXiv]

MacCrann, N., Zuntz, J., Bridle, S., *et al.* (**2015**): *Cosmic discordance: are Planck CMB and CFHTLenS weak lensing measurements out of tune?*
Monthly Notices of the Royal Astronomical Society, Volume 451, Issue 3 [DOI] [ADS] [arXiv]

MacTavish, C. J., Ade, P. A. R., Bock, J. J., *et al.* (**2006**): *Cosmological Parameters from the 2003 Flight of BOOMERANG*
The Astrophysical Journal, Volume 647, Issue 2 [DOI] [ADS] [arXiv]

Majaess, D. (**2010**): *Concerning the Distance to the Center of the Milky Way and Its Structure*
Acta Astronomica, Volume 60, Issue 1 [ADS] [arXiv]

Malhan, K., Ibata, R. A., & Martin, N. F. (**2018**): *Ghostly tributaries to the Milky Way: charting the halo's stellar streams with the Gaia DR2 catalogue*
Monthly Notices of the Royal Astronomical Society, Volume 481, Issue 3 [DOI] [ADS] [arXiv]

Marsh, D. J. E. (**2016**): *Axion cosmology*
Physics Reports, Volume 643 [DOI] [ADS] [arXiv]

Martin, J. (**2012**): *Everything you always wanted to know about the cosmological constant problem (but were afraid to ask)*
Comptes Rendus Physique, Volume 13, Issue 6-7 [DOI] [ADS] [arXiv]

Martínez-Delgado, D., Gabany, R. J., Crawford, K., *et al.* (**2010**): *Stellar Tidal Streams in Spiral Galaxies of the Local Volume: A Pilot Survey with Modest Aperture Telescopes*
The Astronomical Journal, Volume 140, Issue 4 [DOI] [ADS] [arXiv]

Martínez-Delgado, D., Peñarrubia, J., Gabany, R. J., *et al.* (2008): *The Ghost of a Dwarf Galaxy: Fossils of the Hierarchical Formation of the Nearby Spiral Galaxy NGC 5907*
The Astrophysical Journal, Volume 689, Issue 1 [DOI] [ADS] [arXiv]

Mashchenko, S., Wadsley, J., & Couchman, H. M. P. (2008): *Stellar Feedback in Dwarf Galaxy Formation*
Science, Volume 319, Issue 5860 [DOI] [ADS] [arXiv]

Mateo, M. L. (1998): *Dwarf Galaxies of the Local Group*
Annual Review of Astronomy & Astrophysics, Volume 36 [DOI] [ADS] [arXiv]

Mather, J. C., Cheng, E. S., Cottingham, D. A., *et al.* (1994): *Measurement of the Cosmic Microwave Background Spectrum by the COBE FIRAS Instrument*
The Astrophysical Journal, Volume 420 [DOI] [ADS]

McConnachie, A. W., Irwin, M. J., Ferguson, A. M. N., *et al.* (2005): *Distances and metallicities for 17 Local Group galaxies*
Monthly Notices of the Royal Astronomical Society, Volume 356, Issue 3 [DOI] [ADS] [arXiv]

McGaugh, S. S., Lelli, F., & Schombert, J. M. (2016): *Radial Acceleration Relation in Rotationally Supported Galaxies*
Physical Review Letters, Volume 117, Issue 20 [DOI] [ADS] [arXiv]

McGaugh, S. S., Li, P., Lelli, F., *et al.* (2018): *Presence of a fundamental acceleration scale in galaxies*
Nature Astronomy, Volume 2 [DOI] [ADS]

McGaugh, S. S. & Schombert, J. M. (2014): *Color-Mass-to-light-ratio Relations for Disk Galaxies*
The Astronomical Journal, Volume 148, Issue 5 [DOI] [ADS] [arXiv]

McGaugh, S. S., Schombert, J. M., Bothun, G. D., *et al.* (2000): *The Baryonic Tully-Fisher Relation*
The Astrophysical Journal Letters, Volume 533, Issue 2 [DOI] [ADS] [arXiv]

McWilliam, A. & Zoccali, M. (2010): *Two Red Clumps and the X-shaped Milky Way Bulge*
The Astrophysical Journal, Volume 724, Issue 2 [DOI] [ADS] [arXiv]

Meidt, S. E., Schinnerer, E., van de Ven, G., *et al.* (2014): *Reconstructing the Stellar Mass Distributions of Galaxies Using S^4G IRAC 3.6 and 4.5 μm Images. II. The Conversion from Light to Mass*
The Astrophysical Journal, Volume 788, Issue 2 [DOI] [ADS] [arXiv]

Meingast, S., Alves, J., & Fürnkranz, V. (2019): *Extended stellar systems in the solar neighborhood . II. Discovery of a nearby 120° stellar stream in Gaia DR2*
Astronomy & Astrophysics, Volume 622 [DOI] [ADS] [arXiv]

Michell, J. (1784): *On the Means of Discovering the Distance, Magnitude, &c. of the Fixed Stars, in Consequence of the Diminution of the Velocity of Their Light, in Case Such a Diminution Should be Found to Take Place in any of Them, and Such Other Data Should be Procured from Observations, as Would be Farther Necessary for That Purpose. By the Rev. John Michell, B. D. F. R. S. In a Letter to Henry Cavendish, Esq. F. R. S. and A. S.*
Philosophical Transactions of the Royal Society of London Series I, Volume 74 [ADS]

Milgrom, M. (1983): *A modification of the Newtonian dynamics as a possible alternative to the hidden mass hypothesis*
The Astrophysical Journal, Volume 270 [DOI] [ADS]

Minniti, D., Lucas, P. W., Emerson, J. P., *et al.* (2010): *VVV: The public ESO near-IR variability survey of the Milky Way*
New Astronomy, Volume 15, Issue 5 [DOI] [ADS] [arXiv]

Mitchell, M. A., Arnold, C., He, J.-h., *et al.* (2019): *A general framework to test gravity using galaxy clusters II: A universal model for the halo concentration in f(R) gravity*
Monthly Notices of the Royal Astronomical Society, Volume 487, Issue 1 [DOI] [ADS] [arXiv]

Miyamoto, M. & Nagai, R. (1975): *Three-dimensional models for the distribution of mass in galaxies*
Publications of the Astronomical Society of Japan, Volume 27 [ADS]

Moore, B. (1994): *Evidence against dissipation-less dark matter from observations of galaxy haloes*
Nature, Volume 370, Issue 6491 [DOI] [ADS]

Moore, B., Ghigna, S., Governato, F., *et al.* (1999): *Dark Matter Substructure within Galactic Halos*
The Astrophysical Journal Letters, Volume 524, Issue 1 [DOI] [ADS] [arXiv]

Mörtsell, E. & Dhawan, S. (2018): *Does the Hubble constant tension call for new physics?*
Journal of Cosmology & Astroparticle Physics, Volume 2018, Issue 9 [DOI] [ADS] [arXiv]

Moster, B. P., Naab, T., & White, S. D. M. (2013): *Galactic star formation and accretion histories from matching galaxies to dark matter haloes*
Monthly Notices of the Royal Astronomical Society, Volume 428, Issue 4 [DOI] [ADS] [arXiv]

Murphy, J. D., Gebhardt, K., & Adams, J. J. (2011): *Galaxy Kinematics with VIRUS-P: The Dark Matter Halo of M87*
The Astrophysical Journal, Volume 729, Issue 2 [DOI] [ADS] [arXiv]

Mutch, S. J., Croton, D. J., & Poole, G. B. (2011): *The Mid-life Crisis of the Milky Way and M31*
The Astrophysical Journal, Volume 736, Issue 2 [DOI] [ADS] [arXiv]

Myeong, G. C., Evans, N. W., Belokurov, V., *et al.* (2018): *Halo substructure in the SDSS-Gaia catalogue: streams and clumps*
Monthly Notices of the Royal Astronomical Society, Volume 475, Issue 2 [DOI] [ADS] [arXiv]

Naik, A. P., Evans, N. W., Puchwein, E., *et al.* (2020): *Stellar Streams in Chameleon Gravity*
arXiv e-prints (2002.05738) [ADS] [arXiv]

Naik, A. P., Puchwein, E., Davis, A.-C., *et al.* (2018): *Imprints of Chameleon f(R) gravity on Galaxy rotation curves*
Monthly Notices of the Royal Astronomical Society, Volume 480, Issue 4 [DOI] [ADS] [arXiv]

Naik, A. P., Puchwein, E., Davis, A.-C., *et al.* (2019): *Constraints on chameleon $f(R)$-gravity from galaxy rotation curves of the SPARC sample*
Monthly Notices of the Royal Astronomical Society, Volume 489, Issue 1 [DOI] [ADS] [arXiv]

Nataf, D. M., Udalski, A., Gould, A., *et al.* (2010): *The Split Red Clump of the Galactic Bulge from OGLE-III*
The Astrophysical Journal Letters, Volume 721, Issue 1 [DOI] [ADS] [arXiv]

Navarro, J. F., Frenk, C. S., & White, S. D. M. (1996): *The Structure of Cold Dark Matter Halos*
The Astrophysical Journal, Volume 462 [DOI] [ADS] [arXiv]

Navarro, J. F., Frenk, C. S., & White, S. D. M. (1997): *A Universal Density Profile from Hierarchical Clustering*
The Astrophysical Journal, Volume 490, Issue 2 [DOI] [ADS] [arXiv]

Nemiroff, R. J. & Bonnell, J. T. (1999): *The Nature of the Universe Debate in 1998*
Publications of the Astronomical Society of the Pacific, Volume 111, Issue 757 [DOI] [ADS]

Neumann, C. (1896): *Allgemeine Untersuchungen über das Newton'sche Princip der Fernwirkungen, mit besonderer Rücksicht auf die elektrischen Wirkungen*
Teubner

Niederste-Ostholt, M., Belokurov, V., Evans, N. W., *et al.* (2009): *The origin of Segue 1*
Monthly Notices of the Royal Astronomical Society, Volume 398, Issue 4 [DOI] [ADS] [arXiv]

Nobili, A. M., Shao, M., Pegna, R., *et al.* (2012): *'Galileo Galilei' (GG): space test of the weak equivalence principle to 10^{-17} and laboratory demonstrations*
Classical and Quantum Gravity, Volume 29, Issue 18 [DOI] [ADS]

Nordtvedt, K. (1968a): *Equivalence Principle for Massive Bodies. II. Theory*
Physical Review, Volume 169, Issue 5 [DOI] [ADS]

Nordtvedt, K. (1968b): *Testing Relativity with Laser Ranging to the Moon*
Physical Review, Volume 170, Issue 5 [DOI] [ADS]

North, J. (2008): *Cosmos: An Illustrated History of Astronomy and Cosmology*
Chicago University Press, 1st ed.

Oh, S.-H., Hunter, D. A., Brinks, E., *et al.* (2015): *High-resolution Mass Models of Dwarf Galaxies from LITTLE THINGS*
The Astronomical Journal, Volume 149 [DOI] [ADS] [arXiv]

Oman, K. A., Navarro, J. F., Fattahi, A., *et al.* (2015): *The unexpected diversity of dwarf galaxy rotation curves*
Monthly Notices of the Royal Astronomical Society, Volume 452, Issue 4 [DOI] [ADS] [arXiv]

Oort, J. H. (1932): *The force exerted by the stellar system in the direction perpendicular to the galactic plane and some related problems*
Bulletin of the Astronomical Institutes of the Netherlands, Volume 6 [ADS]

Ostriker, J. P., Peebles, P. J. E., & Yahil, A. (1974): *The Size and Mass of Galaxies, and the Mass of the Universe*
The Astrophysical Journal Letters, Volume 193 [DOI] [ADS]

Ostriker, J. P. & Steinhardt, P. J. (1995): *The observational case for a low-density Universe with a non-zero cosmological constant*
Nature, Volume 377, Issue 6550 [DOI] [ADS]

Oyaizu, H. (2008): *Nonlinear evolution of $f(R)$ cosmologies. I. Methodology*
Physical Review D, Volume 78, Issue 12 [DOI] [ADS] [arXiv]

Oyaizu, H., Lima, M., & Hu, W. (2008): *Nonlinear evolution of $f(R)$ cosmologies. II. Power spectrum*
Physical Review D, Volume 78, Issue 12 [DOI] [ADS] [arXiv]

Paillas, E., Cautun, M., Li, B., *et al.* (2019): *The Santiago-Harvard-Edinburgh-Durham void comparison II: unveiling the Vainshtein screening using weak lensing*
Monthly Notices of the Royal Astronomical Society, Volume 484, Issue 1 [DOI] [ADS] [arXiv]

Park, C.-G. & Ratra, B. (2019): *Using the Tilted flat-ΛCDM and the Untilted Non-flat ΛCDM Inflation Models to Measure Cosmological Parameters from a Compilation of Observational Data*
The Astrophysical Journal, Volume 882, Issue 2 [DOI] [ADS] [arXiv]

Pawlowski, M. S., Famaey, B., Jerjen, H., *et al.* (2014): *Co-orbiting satellite galaxy structures are still in conflict with the distribution of primordial dwarf galaxies*
Monthly Notices of the Royal Astronomical Society, Volume 442, Issue 3 [DOI] [ADS] [arXiv]

Peñarrubia, J., Belokurov, V., Evans, N. W., *et al.* (2010): *Was the progenitor of the Sagittarius stream a disc galaxy?*
Monthly Notices of the Royal Astronomical Society, Volume 408, Issue 1 [DOI] [ADS] [arXiv]

Pearson, S., Price-Whelan, A. M., & Johnston, K. V. (2017): *Gaps and length asymmetry in the stellar stream Palomar 5 as effects of Galactic bar rotation*
Nature Astronomy, Volume 1 [DOI] [ADS] [arXiv]

Peebles, P. J. E. (1999): *Is Cosmology Solved? an Astrophysical Cosmologist's Viewpoint*
Publications of the Astronomical Society of the Pacific, Volume 111, Issue 757 [DOI] [ADS] [arXiv]

Peebles, P. J. E. & Yu, J. T. (1970): *Primeval Adiabatic Perturbation in an Expanding Universe*
The Astrophysical Journal, Volume 162 [DOI] [ADS]

Perlmutter, S., Aldering, G., della Valle, M., *et al.* (1998): *Discovery of a supernova explosion at half the age of the Universe*
Nature, Volume 391, Issue 6662 [DOI] [ADS] [arXiv]

Petrosian, V., Salpeter, E., & Szekeres, P. (1967): *Quasi-Stellar Objects in Universes with Non-Zero Cosmological Constant*
The Astrophysical Journal, Volume 147 [DOI] [ADS]

Pigott, E. (**1785**): *Observations of a New Variable Star. In a Letter from Edward Pigott, Esq. to Sir H. C. Englefield, Bart. F. R. S. and A. S.*
Philosophical Transactions of the Royal Society of London Series I, Volume 75 [ADS]

Pillepich, A., Springel, V., Nelson, D., *et al.* (**2018**): *Simulating galaxy formation with the IllustrisTNG model*
Monthly Notices of the Royal Astronomical Society, Volume 473, Issue 3 [DOI] [ADS] [arXiv]

Planck Collaboration (**2014**): *Planck 2013 results. I. Overview of products and scientific results*
Astronomy & Astrophysics, Volume 571 [DOI] [ADS] [arXiv]

Planck Collaboration (**2016**): *Planck 2015 results. XIV. Dark energy and modified gravity*
Astronomy & Astrophysics, Volume 594 [DOI] [ADS] [arXiv]

Planck Collaboration (**2018a**): *Planck 2018 results. I. Overview and the cosmological legacy of Planck*
arXiv e-prints (1807.06205) [ADS] [arXiv]

Planck Collaboration (**2018b**): *Planck 2018 results. VI. Cosmological parameters*
arXiv e-prints (1807.06209) [ADS] [arXiv]

Pontzen, A. & Governato, F. (**2012**): *How supernova feedback turns dark matter cusps into cores*
Monthly Notices of the Royal Astronomical Society, Volume 421, Issue 4 [DOI] [ADS] [arXiv]

Posti, L. & Helmi, A. (**2019**): *Mass and shape of the Milky Way's dark matter halo with globular clusters from Gaia and Hubble*
Astronomy & Astrophysics, Volume 621 [DOI] [ADS] [arXiv]

Poulin, V., Smith, T. L., Karwal, T., *et al.* (**2019**): *Early Dark Energy can Resolve the Hubble Tension*
Physical Review Letters, Volume 122, Issue 22 [DOI] [ADS] [arXiv]

Press, W. H. & Schechter, P. (**1974**): *Formation of Galaxies and Clusters of Galaxies by Self-Similar Gravitational Condensation*
The Astrophysical Journal, Volume 187 [DOI] [ADS]

Price-Whelan, A. M., Sesar, B., Johnston, K. V., *et al.* (**2016**): *Spending Too Much Time at the Galactic Bar: Chaotic Fanning of the Ophiuchus Stream*
The Astrophysical Journal, Volume 824, Issue 2 [DOI] [ADS] [arXiv]

Puchwein, E., Baldi, M., & Springel, V. (**2013**): *Modified-Gravity-GADGET: a new code for cosmological hydrodynamical simulations of modified gravity models*
Monthly Notices of the Royal Astronomical Society, Volume 436, Issue 1 [DOI] [ADS] [arXiv]

Raveri, M. (**2016**): *Are cosmological data sets consistent with each other within the Λ cold dark matter model?*
Physical Review D, Volume 93, Issue 4 [DOI] [ADS] [arXiv]

Reichardt, C. L., Ade, P. A. R., Bock, J. J., *et al.* (**2009**): *High-Resolution CMB Power Spectrum from the Complete ACBAR Data Set*
The Astrophysical Journal, Volume 694, Issue 2 [DOI] [ADS] [arXiv]

Reid, M. J. (**2009**): *Is There a Supermassive Black Hole at the Center of the Milky Way?*
International Journal of Modern Physics D, Volume 18, Issue 6 [DOI] [ADS] [arXiv]

Reid, M. J., Menten, K. M., Zheng, X. W., *et al.* (**2009a**): *A Trigonometric Parallax of Sgr B2*
The Astrophysical Journal, Volume 705, Issue 2 [DOI] [ADS] [arXiv]

Reid, M. J., Menten, K. M., Zheng, X. W., *et al.* (**2009b**): *Trigonometric Parallaxes of Massive Star-Forming Regions. VI. Galactic Structure, Fundamental Parameters, and Noncircular Motions*
The Astrophysical Journal, Volume 700, Issue 1 [DOI] [ADS] [arXiv]

Riess, A. G., Casertano, S., Yuan, W., *et al.* (**2019**): *Large Magellanic Cloud Cepheid Standards Provide a 1% Foundation for the Determination of the Hubble Constant and Stronger Evidence for Physics beyond ΛCDM*
The Astrophysical Journal, Volume 876, Issue 1 [DOI] [ADS] [arXiv]

Riess, A. G., Filippenko, A. V., Challis, P., *et al.* (**1998**): *Observational Evidence from Supernovae for an Accelerating Universe and a Cosmological Constant*
The Astronomical Journal, Volume 116, Issue 3 [DOI] [ADS] [arXiv]

Rigault, M., Aldering, G., Kowalski, M., *et al.* (**2015**): *Confirmation of a Star Formation Bias in Type Ia Supernova Distances and its Effect on the Measurement of the Hubble Constant*
The Astrophysical Journal, Volume 802, Issue 1 [DOI] [ADS] [arXiv]

Robotham, A. S. G., Baldry, I. K., Bland-Hawthorn, J., *et al.* (**2012**): *Galaxy And Mass Assembly (GAMA): in search of Milky Way Magellanic Cloud analogues*
Monthly Notices of the Royal Astronomical Society, Volume 424, Issue 2 [DOI] [ADS] [arXiv]

Rosse, T. E. O. (**1850**): *Observations on the Nebulae*
Philosophical Transactions of the Royal Society of London Series I, Volume 140 [ADS]

Rothman, T. & Ellis, G. (**1987**): *Has cosmology become metaphysical?*
Astronomy, Volume 15, Issue 2 [ADS]

Rubakov, V. A., Sazhin, M. V., & Veryaskin, A. V. (**1982**): *Graviton creation in the inflationary universe and the grand unification scale*
Physics Letters B, Volume 115, Issue 3 [DOI] [ADS]

Rubin, V. C., Ford, J., W. K., & Thonnard, N. (**1978**): *Extended rotation curves of high-luminosity spiral galaxies. IV. Systematic dynamical properties, Sa→Sc.*
The Astrophysical Journal Letters, Volume 225 [DOI] [ADS]

Rubin, V. C., Ford, J., W. K., & Thonnard, N. (**1980**): *Rotational properties of 21 Sc galaxies with a large range of luminosities and radii, from NGC 4605 ($R = 4$ kpc) to UGC 2885 ($R = 122$ kpc).*
The Astrophysical Journal, Volume 238 [DOI] [ADS]

Rubin, V. C. & Ford, J., W. Kent (**1970**): *Rotation of the Andromeda Nebula from a Spectroscopic Survey of Emission Regions*
The Astrophysical Journal, Volume 159 [DOI] [ADS]

Ruchti, G. R., Read, J. I., Feltzing, S., *et al.* (**2015**): *The Gaia-ESO Survey: a quiescent Milky Way with no significant dark/stellar accreted disc*
Monthly Notices of the Royal Astronomical Society, Volume 450, Issue 3 [DOI] [ADS] [arXiv]

Sakstein, J. (**2018**): *Astrophysical tests of screened modified gravity*
International Journal of Modern Physics D, Volume 27, Issue 15 [DOI] [ADS] [arXiv]

Sandage, A. & Tammann, G. A. (**1981**): *A Revised Shapley-Ames Catalog of Bright Galaxies*
Carnegie Institution [ADS]

Sanders, J. L. & Binney, J. (**2013**): *Stream-orbit misalignment - I. The dangers of orbit-fitting*
Monthly Notices of the Royal Astronomical Society, Volume 433, Issue 3 [DOI] [ADS] [arXiv]

Sasaki, M., Suyama, T., Tanaka, T., *et al.* (**2016**): *Primordial Black Hole Scenario for the Gravitational-Wave Event GW150914*
Physical Review Letters, Volume 117, Issue 6 [DOI] [ADS] [arXiv]

Sawala, T., Frenk, C. S., Fattahi, A., *et al.* (**2016**): *The APOSTLE simulations: solutions to the Local Group's cosmic puzzles*
Monthly Notices of the Royal Astronomical Society, Volume 457, Issue 2 [DOI] [ADS] [arXiv]

Sawicki, I. & Bellini, E. (**2015**): *Limits of quasistatic approximation in modified-gravity cosmologies*
Physical Review D, Volume 92, Issue 8 [DOI] [ADS] [arXiv]

Schaye, J., Crain, R. A., Bower, R. G., *et al.* (**2015**): *The EAGLE project: simulating the evolution and assembly of galaxies and their environments*
Monthly Notices of the Royal Astronomical Society, Volume 446, Issue 1 [DOI] [ADS] [arXiv]

Schechter, P. (**1976**): *An analytic expression for the luminosity function for galaxies.*
The Astrophysical Journal, Volume 203 [DOI] [ADS]

Schlamminger, S., Choi, K. Y., Wagner, T. A., *et al.* (**2008**): *Test of the Equivalence Principle Using a Rotating Torsion Balance*
Physical Review Letters, Volume 100, Issue 4 [DOI] [ADS] [arXiv]

Schmidt, F. (**2010**): *Dynamical masses in modified gravity*
Physical Review D, Volume 81, Issue 10 [DOI] [ADS] [arXiv]

Schmidt, F., Lima, M., Oyaizu, H., *et al.* (**2009**): *Nonlinear evolution of $f(R)$ cosmologies. III. Halo statistics*
Physical Review D, Volume 79, Issue 8 [DOI] [ADS] [arXiv]

Schombert, J. & McGaugh, S. (**2014**): *Stellar Populations and the Star Formation Histories of LSB Galaxies: III. Stellar Population Models*
Publications of the Astronomical Society of Australia, Volume 31 [DOI] [ADS] [arXiv]

Schönrich, R., Binney, J., & Dehnen, W. (**2010**): *Local kinematics and the local standard of rest*
Monthly Notices of the Royal Astronomical Society, Volume 403, Issue 4 [DOI] [ADS] [arXiv]

Schwarz, G. (**1978**): *Estimating the Dimension of a Model*
Annals of Statistics, Volume 6 [ADS]

Scolnic, D. M., Jones, D. O., Rest, A., *et al.* (**2018**): *The Complete Light-curve Sample of Spectroscopically Confirmed SNe Ia from Pan-STARRS1 and Cosmological Constraints from the Combined Pantheon Sample*
The Astrophysical Journal, Volume 859, Issue 2 [DOI] [ADS] [arXiv]

Seeliger, H. (**1895**): *Über das Newton'sche Gravitationsgesetz*
Astronomische Nachrichten, Volume 137, Issue 9 [DOI] [ADS]

Seljak, U. & Zaldarriaga, M. (**1997**): *Signature of Gravity Waves in the Polarization of the Microwave Background*
Physical Review Letters, Volume 78, Issue 11 [DOI] [ADS] [arXiv]

Sellar, W. C. & Yeatman, R. J. (**1930**): *1066 and All That: A Memorable History of England, comprising all the Parts you can remember, including 103 Good Things, 5 Bad Kings and 2 Genuine Dates*
Methuen & Co.

Shen, S., Madau, P., Conroy, C., *et al.* (**2014**): *The Baryon Cycle of Dwarf Galaxies: Dark, Bursty, Gas-rich Polluters*
The Astrophysical Journal, Volume 792, Issue 2 [DOI] [ADS] [arXiv]

Sijacki, D., Vogelsberger, M., Genel, S., *et al.* (**2015**): *The Illustris simulation: the evolving population of black holes across cosmic time*
Monthly Notices of the Royal Astronomical Society, Volume 452, Issue 1 [DOI] [ADS] [arXiv]

Simon, J. D., Geha, M., Minor, Q. E., *et al.* (**2011**): *A Complete Spectroscopic Survey of the Milky Way Satellite Segue 1: The Darkest Galaxy*
The Astrophysical Journal, Volume 733, Issue 1 [DOI] [ADS] [arXiv]

Slipher, V. M. (**1917**): *Nebulae*
Proceedings of the American Philosophical Society, Volume 56 [ADS]

Smith, R. W. (**1982**): *The Expanding Universe: Astronomy's 'Great Debate', 1900-1931*
Cambridge University Press

Smith, S. (**1936**): *The Mass of the Virgo Cluster*
The Astrophysical Journal, Volume 83 [DOI] [ADS]

Smoot, G. F., Bennett, C. L., Kogut, A., *et al.* (**1992**): *Structure in the COBE Differential Microwave Radiometer First-Year Maps*
The Astrophysical Journal Letters, Volume 396 [DOI] [ADS]

Sotiriou, T. P. & Faraoni, V. (**2012**): *Black Holes in Scalar-Tensor Gravity*
Physical Review Letters, Volume 108, Issue 8 [DOI] [ADS] [arXiv]

Spergel, D. N. & Steinhardt, P. J. (**2000**): *Observational Evidence for Self-Interacting Cold Dark Matter*
Physical Review Letters, Volume 84, Issue 17 [DOI] [ADS] [arXiv]

Springel, V. (**2005**): *The cosmological simulation code GADGET-2*
Monthly Notices of the Royal Astronomical Society, Volume 364, Issue 4 [DOI] [ADS] [arXiv]

Springel, V. (**2010**): *E pur si muove: Galilean-invariant cosmological hydrodynamical simulations on a moving mesh*
Monthly Notices of the Royal Astronomical Society, Volume 401, Issue 2 [DOI] [ADS] [arXiv]

Springel, V., Wang, J., Vogelsberger, M., *et al.* (**2008**): *The Aquarius Project: the subhaloes of galactic haloes*
Monthly Notices of the Royal Astronomical Society, Volume 391, Issue 4 [DOI] [ADS] [arXiv]

Stanley, M. (**2003**): *An expedition to heal the wounds of war. The 1919 eclipse and Eddington as Quaker adventurer*
Isis, Volume 94, Issue 1 [ADS]

Starobinsky, A. A. (**1979**): *Spectrum of relict gravitational radiation and the early state of the universe*
Soviet Journal of Experimental and Theoretical Physics Letters, Volume 30 [ADS]

Starobinsky, A. A. (**1980**): *A new type of isotropic cosmological models without singularity*
Physics Letters B, Volume 91, Issue 1 [DOI] [ADS]

Steigman, G. (**2006**): *Primordial Nucleosynthesis:. Successes and Challenges*
International Journal of Modern Physics E, Volume 15, Issue 1 [DOI] [ADS] [arXiv]

Steinmetz, M., Zwitter, T., Siebert, A., *et al.* (**2006**): *The Radial Velocity Experiment (RAVE): First Data Release*
The Astronomical Journal, Volume 132, Issue 4 [DOI] [ADS] [arXiv]

Stewart, K. R., Bullock, J. S., Wechsler, R. H., *et al.* (**2008**): *Merger Histories of Galaxy Halos and Implications for Disk Survival*
The Astrophysical Journal, Volume 683, Issue 2 [DOI] [ADS] [arXiv]

Strukov, I. A., Brukhanov, A. A., Skulachev, D. P., *et al.* (**1992**): *Anisotropy of the microwave background radiation*
Soviet Astronomy Letters, Volume 18, Issue 5 [ADS]

Szalay, A. S. & Marx, G. (**1976**): *Neutrino rest mass from cosmology.*
Astronomy & Astrophysics, Volume 49, Issue 3 [ADS]

Tenneti, A., Mao, Y.-Y., Croft, R. A. C., *et al.* (**2018**): *The radial acceleration relation in disc galaxies in the MassiveBlack-II simulation*
Monthly Notices of the Royal Astronomical Society, Volume 474, Issue 3 [DOI] [ADS] [arXiv]

Thomas, G. F., Famaey, B., Ibata, R., *et al.* (**2018**): *Stellar streams as gravitational experiments. II. Asymmetric tails of globular cluster streams*
Astronomy & Astrophysics, Volume 609 [DOI] [ADS] [arXiv]

Tisserand, P., Le Guillou, L., Afonso, C., *et al.* (**2007**): *Limits on the Macho content of the Galactic Halo from the EROS-2 Survey of the Magellanic Clouds*
Astronomy & Astrophysics, Volume 469, Issue 2 [DOI] [ADS] [arXiv]

Tollerud, E. J., Boylan-Kolchin, M., & Bullock, J. S. (**2014**): *M31 satellite masses compared to ΛCDM subhaloes*
Monthly Notices of the Royal Astronomical Society, Volume 440, Issue 4 [DOI] [ADS] [arXiv]

Tomozeiu, M., Mayer, L., & Quinn, T. (**2016**): *Tidal Stirring of Satellites with Shallow Density Profiles Prevents Them from Being Too Big to Fail*
The Astrophysical Journal Letters, Volume 827, Issue 1 [DOI] [ADS] [arXiv]

Touboul, P., Métris, G., Rodrigues, M., *et al.* (**2017**): *MICROSCOPE Mission: First Results of a Space Test of the Equivalence Principle*
Physical Review Letters, Volume 119, Issue 23 [DOI] [ADS] [arXiv]

Touboul, P., Rodrigues, M., Métris, G., *et al.* (**2001**): *MICROSCOPE, testing the equivalence principle in space*
Academie des Sciences Paris Comptes Rendus Serie Physique Astrophysique, Volume 2, Issue 9 [DOI] [ADS]

Tremaine, S., Gebhardt, K., Bender, R., *et al.* (**2002**): *The Slope of the Black Hole Mass versus Velocity Dispersion Correlation*
The Astrophysical Journal, Volume 574, Issue 2 [DOI] [ADS] [arXiv]

Tully, R. B., Courtois, H., Hoffman, Y., *et al.* (**2014**): *The Laniakea supercluster of galaxies*
Nature, Volume 513, Issue 7516 [DOI] [ADS] [arXiv]

Turner, M. S. (**1999**): *Cosmology Solved? Quite Possibly!*
Publications of the Astronomical Society of the Pacific, Volume 111, Issue 757 [DOI] [ADS] [arXiv]

Turner, M. S., Steigman, G., & Krauss, L. M. (**1984**): *Flatness of the Universe: Reconciling Theoretical Prejudices with Observational Data*
Physical Review Letters, Volume 52, Issue 23 [DOI] [ADS]

van der Marel, R. P., Besla, G., Cox, T. J., *et al.* (**2012**): *The M31 Velocity Vector. III. Future Milky Way M31-M33 Orbital Evolution, Merging, and Fate of the Sun*
The Astrophysical Journal, Volume 753, Issue 1 [DOI] [ADS] [arXiv]

Vikram, V., Cabré, A., Jain, B., *et al.* (**2013**): *Astrophysical tests of modified gravity: the morphology and kinematics of dwarf galaxies*
Journal of Cosmology & Astroparticle Physics, Volume 2013, Issue 8 [DOI] [ADS] [arXiv]

Vikram, V., Sakstein, J., Davis, C., *et al.* (**2018**): *Astrophysical tests of modified gravity: Stellar and gaseous rotation curves in dwarf galaxies*
Physical Review D, Volume 97, Issue 10 [DOI] [ADS]

Vogelsberger, M., Genel, S., Springel, V., *et al.* (**2014a**): *Introducing the Illustris Project: simulating the coevolution of dark and visible matter in the Universe*
Monthly Notices of the Royal Astronomical Society, Volume 444, Issue 2 [DOI] [ADS] [arXiv]

Vogelsberger, M., Genel, S., Springel, V., *et al.* (2014b): *Properties of galaxies reproduced by a hydrodynamic simulation*
Nature, Volume 509, Issue 7499 [DOI] [ADS] [arXiv]

Vogelsberger, M., Marinacci, F., Torrey, P., *et al.* (2020): *Cosmological simulations of galaxy formation*
Nature Reviews Physics, Volume 2, Issue 1 [DOI] [ADS] [arXiv]

Wagner, T. A., Schlamminger, S., Gundlach, J. H., *et al.* (2012): *Torsion-balance tests of the weak equivalence principle*
Classical and Quantum Gravity, Volume 29, Issue 18 [DOI] [ADS] [arXiv]

Wald, R. M. (1984): *General relativity*
Chicago University Press, 1st ed. [DOI]

Walker, M. G. & Peñarrubia, J. (2011): *A Method for Measuring (Slopes of) the Mass Profiles of Dwarf Spheroidal Galaxies*
The Astrophysical Journal, Volume 742, Issue 1 [DOI] [ADS] [arXiv]

Wang, J., Hui, L., & Khoury, J. (2012): *No-Go Theorems for Generalized Chameleon Field Theories*
Physical Review Letters, Volume 109, Issue 24 [DOI] [ADS] [arXiv]

Watkins, L. L., van der Marel, R. P., Sohn, S. T., *et al.* (2019): *Evidence for an Intermediate-mass Milky Way from Gaia DR2 Halo Globular Cluster Motions*
The Astrophysical Journal, Volume 873, Issue 2 [DOI] [ADS] [arXiv]

Wegg, C. & Gerhard, O. (2013): *Mapping the three-dimensional density of the Galactic bulge with VVV red clump stars*
Monthly Notices of the Royal Astronomical Society, Volume 435, Issue 3 [DOI] [ADS] [arXiv]

Wegg, C., Gerhard, O., & Bieth, M. (2019): *The gravitational force field of the Galaxy measured from the kinematics of RR Lyrae in Gaia*
Monthly Notices of the Royal Astronomical Society, Volume 485, Issue 3 [DOI] [ADS] [arXiv]

Weinberg, S. (1989): *The cosmological constant problem*
Reviews of Modern Physics, Volume 61 [DOI] [ADS]

Wetzel, A. R., Hopkins, P. F., Kim, J.-h., *et al.* (2016): *Reconciling Dwarf Galaxies with ΛCDM Cosmology: Simulating a Realistic Population of Satellites around a Milky Way-mass Galaxy*
The Astrophysical Journal Letters, Volume 827, Issue 2 [DOI] [ADS] [arXiv]

Will, C. M. (1971): *Theoretical Frameworks for Testing Relativistic Gravity. II. Parametrized Post-Newtonian Hydrodynamics, and the Nordtvedt Effect*
The Astrophysical Journal, Volume 163 [DOI] [ADS]

Will, C. M. (2014): *The Confrontation between General Relativity and Experiment*
Living Reviews in Relativity, Volume 17 [DOI] [ADS] [arXiv]

Will, C. M. & Nordtvedt, J., Kenneth (1972): *Conservation Laws and Preferred Frames in Relativistic Gravity. I. Preferred-Frame Theories and an Extended PPN Formalism*
The Astrophysical Journal, Volume 177 [DOI] [ADS]

Williams, J. G., Turyshev, S. G., & Boggs, D. H. (2004): *Progress in Lunar Laser Ranging Tests of Relativistic Gravity*
Physical Review Letters, Volume 93, Issue 26 [DOI] [ADS] [arXiv]

Winther, H. A., Schmidt, F., Barreira, A., *et al.* (2015): *Modified gravity N-body code comparison project*
Monthly Notices of the Royal Astronomical Society, Volume 454 [DOI] [ADS] [arXiv]

Worden, P., Torii, R., Mester, J. C., *et al.* (2000): *The STEP Payload and Experiment*
Advances in Space Research, Volume 25, Issue 6 [DOI] [ADS]

Wright, T. (1750): *An Original Theory or New Hypothesis of the Universe*
H. Chapelle [DOI] [ADS]

Yanny, B., Rockosi, C., Newberg, H. J., *et al.* (2009): *SEGUE: A Spectroscopic Survey of 240,000 Stars with g = 14-20*
The Astronomical Journal, Volume 137, Issue 5 [DOI] [ADS] [arXiv]

Zeldovich, Y. B. (1967): *Cosmological Constant and Elementary Particles*
ZhETF Pisma Redaktsiiu, Volume 6 [ADS]

Zeldovich, Y. B. (1968): *Special Issue: the Cosmological Constant and the Theory of Elementary Particles*
Soviet Physics Uspekhi, Volume 11, Issue 3 [DOI] [ADS]

Zeldovich, Y. B. (1972): *A hypothesis, unifying the structure and the entropy of the Universe*
Monthly Notices of the Royal Astronomical Society, Volume 160, Issue 1 [DOI] [ADS]

Zhao, G.-B., Li, B., & Koyama, K. (2011): *N-body simulations for $f(R)$ gravity using a self-adaptive particle-mesh code*
Physical Review D, Volume 83, Issue 4 [DOI] [ADS] [arXiv]

Zhao, H., Macciò, A. V., Li, B., *et al.* (2010): *Structure Formation by Fifth Force: Power Spectrum from N-Body Simulations*
The Astrophysical Journal Letters, Volume 712, Issue 2 [DOI] [ADS] [arXiv]

Zivick, P., Sutter, P. M., Wandelt, B. D., *et al.* (2015): *Using cosmic voids to distinguish $f(R)$ gravity in future galaxy surveys*
Monthly Notices of the Royal Astronomical Society, Volume 451, Issue 4 [DOI] [ADS] [arXiv]

Zwicky, F. (1929): *On the Red Shift of Spectral Lines through Interstellar Space*
Proceedings of the National Academy of Science, Volume 15, Issue 10 [DOI] [ADS]

Zwicky, F. (1933): *Die Rotverschiebung von extragalaktischen Nebeln*
Helvetica Physica Acta, Volume 6 [ADS]